UNIVERSITY OF LEICESTER

A method for source – depth estimation using a Hybrid Optical / Gamma Camera

A thesis submitted for the degree of Doctoral of Philosophy

By

NUMAN SALMAN DAWOOD

Space Research Centre

Department of Physics and Astronomy

FEBRUARY 2019

A method for source – depth estimation using a Hybrid Optical / Gamma Camera

NUMAN SALMAN DAWOOD

Abstract

This work describes a new imaging technique to estimate the depth of radionuclide accumulations in relation to patient anatomy using a novel small field of view (SFOV) hybrid gamma camera (HGC) which combines optical and gamma imaging. The HGC offers higher spatial resolution and good sensitivity, and allows for greater flexibility for staff and patients than the conventional gamma cameras that are currently in use in nuclear medicine departments. This study aims to optimise the depth estimation technique and to assess the use of the HGC in clinical settings.

Two HGCs were used to estimate the depth of radioisotope sources within a variety of phantoms and over a wide range of operating distances.

Three camera arrangements (perpendicular, convergent and divergent) were investigated to select the best design for estimating the depth of the radioisotope within the phantoms; the perpendicular arrangement was found to be preferable among these arrangements.

In this thesis, prototype anthropomorphic phantoms were designed and used to simulate hot spots in various regions of the human body, such as tumour localisation and sentinel lymph nodes. The HGC was used to image these phantoms with the aim of simulating a number of clinical procedures and assessing the camera performance for each.

The effect of source movement on depth estimation of radiolabelled tissues was studied to simulate the effects of breathing during surgery.

The HGC was used to carry out hybrid gamma-optical imaging procedures on two patients who had attended routine single photon emission computed tomography (SPECT) imaging appointments in the nuclear medicine departments at the Queen's Medical Centre and the Nottingham City Hospital – Nottingham University Hospitals NHS Trust, Nottingham as part of clinical evaluation of the HGC. The results of the first two clinical studies of the HGC to estimate the depth of accumulated radioisotope are presented.

Acknowledgment

I gladly give thanks to Allah Almighty for the grace He offered me to be able to accomplish this Journey.

First and foremost, I want to express my sincere gratitude to my first supervisor John Lees for offering me this great opportunity to join the project. He has provided his expertise and invaluable guidance throughout my research work. I would like to thank him for his patient and support that without him this work would not be completed.

My special thanks go to Dr. Sarah who offers her superb expertise and insight in helping me and endlessly supporting my work.

I am also thankful to my sponsor, the Iraqi government, and specifically the "Ministry of Higher Education and Scientific Research" for providing me with this great opportunity to start my Ph.D. at a universal institution and the Iraqi Cultural Attaché in London for their role during my research.

I would also like to take this opportunity to thank Professor Alan C. Perkins. With his strong medical physics background, he played an important role in criticising my research work, reflecting on the produced results and expanding my research scope. He supported me through recruiting patients at Queen Medical Centre and Nottingham city hospital – Nottingham University Hospitals NHS Trust, Nottingham.

Many thanks goes to my supportive friends who made my PhD experience really special, including but not limited to, Mohammed Saeed M Alqahtani, Layal Jambi, Dr Simon Lindsay, Awad Almarhaby, Aik Ng, Bill McKnight, Bahadar Bhatia and Kjell Koch-Mehrin. I am also grateful to Sharon McMahon and the nuclear medicine team, Leicester Royal Infirmary, for continuing provide me with radioactive material during the course of my research, and to Elaine Blackshaw and Simon Lawes, Nuclear Medicine Department - Queen's Medical Centre, for their technical support and helping in patients' recruitment.

I would also like to express my sincere appreciation to my wife, Um-Yaseen (Ekhlas Mushref Idan), my daughter Oufa and my son Yaseen for their encouragement, support and cooperation during my study. I would like to appreciate the wonderful support of my wife for leaving her family and her beautiful moments and taking the decision to join me during my studies.

For the non-scientific side of my work, I would particularly like to thank my family, my brothers and sisters in Iraq and a special thank you to my dad and Mum who have always stood beside me since my childhood.

I would like to introduce a sincere my heartfelt condolences to the spirit of my dear brother Ali Salman Dawood

Thank you too to my friends Dr khild Ibrahem, Dr Mazin Al Isawi, Dr Ahmed Al heeti and Dr Hamdan O. Mansoor.

List of publications and conferences

Publications

1. Lees, J.E., S.L. Bugby, M.S. Alqahtani, L.K. Jambi, **NS Dawood**, W.R. McKnight, A.H. Ng, and A.C. Perkins, *A Multimodality Hybrid Gamma-Optical Camera for Intraoperative Imaging.* Sensors (Basel), 2017. 17(3).

2. MS Alqahtani, JE Lees, SL Bugby, LK Jambi, BS Bhatia, WR McKnight, **NS Dawood**, AH Ng and AC Perkins. *Capability of a novel small field of view hybrid gamma camera (HGC) for sentinel lymph node and small organ imaging*. Soc. Nuclear Med. 58(Supplement 1): 157, 2017.

3. LK Jambi, JE Lees, SL Bugby, MS Alqahtani, BS Bhatia, WR McKnight, **NS Dawood,** AH Ng and AC Perkins. *A hand-held hybrid gamma-near-infrared fluorescence imaging camera*. Soc. Nuclear Med. 58(Supplement 1): 220, 2017.

4. Layal K. Jambi, John E. Lees, Sarah L. Bugby, Bahadar S. Bhatia, Mohammed S. Alqahtani, **Numan S. Dawood**, Aik H. Ng, Alan C. Perkins. Comparison of columnar and pixelated scintillators for small field of view hybrid gamma camera imaging. IEEE Xplore. 2016 IEEE Nuclear Science Symposium, Medical Imaging Conference and Room-Temperature Semiconductor Detector Workshop (NSS/MIC/RTSD), Strasbourg, France, 2017, p.1-4.

5. Layal K. Jambi, John E. Lees, Sarah L. Bugby, Bahadar S. Bhatia, Mohammed S. Alqahtani, **Numan S. Dawood**, Aik H. Ng, Alan C. Perkins. Comparison of columnar and pixelated scintillators for small field of view hybrid gamma camera imaging. IEEE Xplore. 2016 IEEE Nuclear Science Symposium, Medical Imaging Conference and Room-Temperature Semiconductor Detector Workshop (NSS/MIC/RTSD), Strasbourg, France, 2017, p.1-4.

6. MS Alqahtani, JE Lees, SL Bugby, LK Jambi, BS Bhatia, WR McKnight, **NS Dawood,** AH Ng, AC Perkins. *Investigation of a novel small field of view hybrid compact gamma camera (HCGC) for scintigraphic imaging*. Insights Imaging 7(Supplement 1):162, 2016.

Conferences

1. JE Lees, SL Bugby, MS Alqahtani, LK Jambi, **NS Dawood**, WR McKnight, BS Bhatia, AH Ng and AC Perkins. Hybrid gamma camera for medical applications. PSD11: 11th International Conference on Position Sensitive Detectors, Milton Keynes, UK, 2017.
2. JE Lees, SL Bugby, MS Alqahtani, LK Jambi, **NS Dawood**, WR McKnight, BS Bhatia, AH Ng and AC Perkins. A multimodality camera for intraoperative imaging. Cancer Imaging Conference. London, UK, 2017.

3. **NS Dawood**, JE Lees, SL Bugby, MS Alqahtani, LK Jambi, WR McKnight, AH Ng and AC Perkins. Radionuclide depth estimation using a novel SFOV hybrid gamma-optical camera with an anthropomorphic breast phantom. The 45th Annual Spring BNMS Meeting. Birmingham, UK, 2017.

4. JE Lees, SL Bugby, MS Alqahtani, LK Jambi, AH Ng, **NS Dawood**, AC Perkins. A high-resolution hybrid gamma-optical camera for intraoperative imaging. European Association of Nuclear Medicine (EANM) Annual Congress. Barcelona, Spain, 2016. DOI: 10.1007/s00259-016-3484-4.

5. MS Alqahtani, JE Lees, SL Bugby, LK Jambi, BS Bhatia, WR McKnight, **NS Dawood**, AH Ng, AC Perkins. Investigation of a novel small field of view hybrid compact gamma camera (HCGC) for scintigraphic imaging. European Congress of Radiology (ECR), Vienna, Austria, 2016. Abstract available in: http://dx.doi.org/10.1594/ecr2016/B-0033.

6. LK Jambi, JE Lees, SL Bugby, MS Alqahtani, BS Bhatia, WR McKnight, **NS Dawood**, AH Ng, AC Perkins. Development of a small field of view gamma camera for medical imaging. European Congress of Radiology (ECR), Vienna, Austria, 2016. Abstract available in: http://dx.doi.org/10.1594/ecr2016/C-2206.

7. **NS Dawood**, JE Lees, SL Bugby, LK Jambi, MS Alqahtani, WR McKnight, AC Perkins. A method of source-depth estimation using a Hybrid Gamma Camera. British Institute of Radiology (BIR) Annual Congress, London, UK, 2015. Abstract available in: http://www.eposters.net/poster/a-method-for-source-depth-estimation-using-a-hybrid-gamma-camera.

8. JE Lees, AC Perkins, SL Bugby, BS Bhatia, LK Jambi, MS Alqahtani, WR McKnight, **NS Dawood**, AH Ng. A high-resolution handheld hybrid camera for gamma and optical imaging. British Nuclear Medicine Society (BNMS) Autumn Meeting, London, UK, 2015.

Table of contents

Chapter 1: **Introduction**

Nuclear medicine plays an important role in diagnostic procedures of different disease. In cancer cases, nuclear medicine allows surgeons to determine the location and stage of cancer inside the body. It is also used to provide information about how the cancer responds to treatment. There are many types of cancers common in the world, for example, bone, breast, stomach and thyroid and lymphoma cancer. In the US, approximately 75000 people were diagnosed with lymphatic system cancer, lymphoma, in 2011, with 11% of cases Hodgkin's lymphoma (HL) and 89% of cases non- Hodgkin's lymphoma (NHL); actually, NHL is the seventh most common type of cancer in the US [1]. Breast cancer is the most widespread cancer type among women worldwide; the International Agency for Research on Cancer reported that more than 1.6 million new cases of breast cancer were registered in 2012 [2]. Cancer Research UK (CRUK) reported that breast, prostate and lung cancer account for more than half of the UK's new cancer cases each year. In 2015, CRUK had registered 359,734 new cases of cancer, where 182,749 cases were in males, and 176,985 cases were in females; also in 2015 there were 163,930 cancer deaths, where 87,138 were males and 76,792 were females [3].

In nuclear imaging, the function of the organ is one of the parameters that determines the type of pharmaceutical material used for targeting rather than the organ's shape, where a radiopharmaceutical represents a chemical carrier of radioactive material to the target. This substance is designed to be taken up in specific organs and radioisotopes such as Technetium-99m pertechnetate ($^{99m}TcO^{-4}$) are used for thyroid scintigraphy [4]. The maximum uptake of ^{99m}Tc-pertechnetate by the thyroid occurs at between 10 to 20 minutes after injection [5], therefore a SPECT scan can be used for thyroid scintigraphy 20 min after injection of 185 MBq (5 mCi) of ^{99m}Tc-pertechnetate [6]. Another example is that the skeleton uptake rate of ^{99m}Tc- bisphosphonates is from 50 to 60% of the total injected amount which ranges between 300 and 740 MBq after four hours of being injected [7].

Diagnosis in nuclear medicine depends on two main factors: gamma detection and radioactive material accumulated inside the target organ. Gamma rays emitted from the accumulated radioisotope region can be detected by an external detector such as a non-

imaging gamma probe (GP) [8] which is used to estimate the location of radioisotope distribution within the body during surgery, or by a gamma camera such as in SPECT or PET preoperatively. Also a hybrid imaging system such as single photon emission computed tomography/computed tomography (SPECT/CT) or Positron emission tomography/ computed tomography (PET/CT) can produce images of the gamma rays and provide combined information (functional and anatomical) about the target before surgery. However, because of their size such systems cannot be used inside the operating theatre.

Tsuchimochi and Hayama reported that many small gamma cameras (SGCs) are under development for surgical use. They also explained the characteristics, and performance of SGCs that are lightweight and small enough to be used during surgery [9], such as the Sentinella 102 small field of view (SFOV) gamma imaging system [10] and the Per-Operative Compact Imager (POCI) SFOV gamma camera [11].

The work presented in this thesis focusses on assessing the ability of the hybrid gamma camera (HGC) to estimate the depth of radioisotope sources within anatomical phantoms that are designed to simulate a tumour or sentinel lymph node at varying depths within the body.

1.1 Motivation and application

Locating the tumour before the operation procedure is important for complete removal without the destruction of the normal tissues which surround the tumour. There is a possibility that the surgeon will excise more than required or that parts of the tumour may remain inside the body, which were not identified previously. When the location of radiolabelled tissues are identified, the depth estimation of the radioisotope distribution during surgery would help the surgeons to minimize normal tissue damage and to aid the removal of the tumour. In general, this would lead to improved patient care.

The location of abnormal tissues within the body are determined using available techniques in nuclear medicine prior to surgery via such imaging systems as SPECT/CT or PET/CT [12, 13], where these instruments consist of several cameras that are moved around the patient to evaluate the functional status of the target organ from different angles.

A tumour inside the body can be localized during surgery using radiopharmaceuticals that deliver radioactive isotopes to the target, using a non-imaging system, such as a scintillator with a bismuth germanate crystal probe [14]. Surgeons determine the location of the accumulated radioactive material based on the intensity of sound, which depends on the number of photons detected and is shown on a screen to judge the amount of gamma photons emitted from the target within the FOV, which can help locate the tumour but without producing an image. This technology does not provide information on shape or depth of the targeted tissue. To utilise images during surgery, the surgeons must look to SFOV systems that have been designed to be near to the patient and work within the operating theatre. The Bioimaging Unit team in the Space Research Centre (SRC), University of Leicester, in collaboration with the University of Nottingham, have developed a novel high-resolution SFOV hybrid gamma camera (HGC) which has the capability to provide a hybrid optical-gamma imaging system in one setup.

The HGC was assessed as a new imaging technique to address both diagnostic and surgical needs, especially intraoperative imaging due to its potential advantages such as its small size portability, light weight and high spatial resolution gamma imaging combined with optical imaging system [15-17]. In addition, the hybrid gamma/optical camera concept may be extended to estimate the position (or depth) of radioisotope accumulations inside the body [18].

1.2 **Objective**

In medical imaging, the development of gamma cameras is intended to provide a good spatial resolution to allow two nodes within a surgical field to be distinguished with an extended field of view (FOV), increased sensitivity for better signal-to-noise ratios, to reduce acquisition times, give better energy resolution with the multi-radioisotopes used for imaging such as ^{99m}Tc and ^{123}I, and to improve the ability to localise radioisotope distributions.

The spatial resolution and the sensitivity represent the most important characteristics to play a role in medical diagnosis using SPECT and PET scans. Clinically, SPECT scans can provide a spatial resolution of about 1 cm, whereas some preclinical SPECT scans can provide sub-millimetre spatial resolutions using a multi-pinhole geometry [19].The

spatial resolution of clinical PET scans are about 4-6 mm but can achieve a spatial resolution of approximately 2.5 mm in the centre of the FOV during a brain scan [20]. The sensitivity of a gamma camera must be sufficient to provide a good image within the acquisition time, such as 120 seconds, and a standard dose of radioisotopes, which depends on the type of scan [21].

During the last decade, a number of companies, researchers and academic laboratories have attempted to develop small-scale detectors for clinical cases, where the diagnostics are focussed on the detection of radioisotope accumulations within the small organs or tissues within targeted area.

The pinhole collimator provides a valuable FOV with imaging distance and is therefore can be used for small organ imaging, such as a thyroid, whereas a parallel hole collimator provides one field of view at all imaging distances [22].

A portable gamma camera is used to image small organs in order to localise the radionuclide within the surgical field. Actually, gamma probes see widespread use in determining the locations of sentinel lymph nodes (SLNs), the first lymph node encountered in the lymphatic system by lymphatic vessels draining a tumour [23], where this node will be subject to histological examination. The use of a mobile gamma camera offers a high resolution, high sensitivity system which would aid the localisation of SLNs and potentially reduce the time required for the surgical process.

For intraoperative SLNs scintigraphy, ^{99m}Tc is one of the radioisotope used in medical imaging, the SLN's absorption of radioisotopes ranges between 1 kBq and 1 MBq, which depends on a number of parameters [24]. To detect the SLNs during surgery, the minimum sensitivity required is between 1 cps/kBq and 2.2 cps/kBq, such as, for the ^{99m}Tc 140-keV γ-ray [25, 26] within an acquisition time of around 20-120 seconds [11, 25], with a desired spatial resolution of a 2 mm [27]. The emphasis is more on the sensitivity of the gamma camera in order to accelerate the acquisition of gamma rays than on spatial resolution in the operating theatre [28].

The main objective of this thesis is the development and assessment of a depth-estimation technique for targeted tissues during intraoperative imaging procedures using a portable hybrid gamma camera which combines gamma and optical imaging. To achieve this aim, three camera arrangements were examined to select the best configuration for depth

estimation of a radioisotope source, using three phantoms to simulate a number of clinically relevant scenarios, and to study the effects on depth estimation of the normal motion of organs under different types of patient breathing patterns.

1.3 Thesis Organisation

The overall structure of the thesis takes the form of seven chapters, including this introductory chapter. Chapter 2 begins by laying out the background to nuclear medicine imaging, the limitations of the technologies currently available in nuclear medicine departments, and an explanation of the concept and principles of 3D imaging.

The third chapter is concerned with the concept of the hybrid gamma camera design through describing the camera's components and the role of each component in the imaging procedures used for this study. The fourth chapter presents the proposed configuration of the HGC for depth estimation through the study of three camera arrangements, focussing on selecting the best configuration in order to allow the best depth estimation of the radioisotope source within a phantom. Chapter 5 investigates the ability of the hybrid gamma camera (HGC) to estimate the depth of radioisotope sources using different anatomical phantoms, while Chapter 6 investigates the effect of source movement on depth estimation.

In Chapter 7, the conclusions of this thesis are presented, and an outline of possible future work to be undertaken for the HGC is discussed.

1.4 Personal contribution

Chapter 3

In this thesis, the calculation of the collimator spatial resolution and the collimator sensitivity of the HGC were made using different pinhole diameters; 0.25, 0.5 and 1 mm. These calculated values were compared with the measured (theoretical) values [29, 30].

A cross phantom that was previously designed and manufactured by the Space Research Centre (SRC), University of Leicester [18] and V-shaped phantom that was designed and

manufactured during the current study by the Space Research Centre, University of Leicester are described. These two phantoms were used to evaluate the efficiency of the HGC imaging in terms of the localisation of an accumulated radioisotope; the effect of different distances between two point sources was investigated to simulate the detection of the nodes close to each other from a predefined imaging distance and to estimate the required separation between the two cameras.

Chapter 4

A previous study was carried out to create stereoscopic images of a radioisotope source, using the HGC perpendicular to the source [17]. The current study expands this concept to calculate the depth of a source within an object. Three possible arrangements of two hybrid gamma cameras (HGCs) were considered and evaluated for their suitability to estimate the depth of a radioisotope source inside different phantoms. The effect of each arrangement on the depth estimation of the radioisotope source inside the phantom was examined. The arrangements considered were perpendicular, divergent and convergent. The aim was to select the best arrangement depending on the results of the theoretical and practical analysis for each arrangement.

Chapter 5

The sensitivity of the HGC, fitted with a 0.5 mm diameter pinhole collimator, was calculated with a number of layers of Perspex to simulate the effect of soft tissues, and an aluminium bar to simulate the effect of bone on sensitivity.

A previous study focused on the localisation of radionuclides in the environment including calculating the distance using a single HGC [18]. This study was expanded to calculate the depth of the radioisotope source within phantoms using one HGC that is displaced a specific distance to simulate two cameras, which were perpendicular to source. A study was carried out using three phantoms; a breast phantom [31], a head and neck phantom [32], and the chest phantom that were designed and manufactured by the Space Research Centre, University of Leicester. The depth of the source inside the phantom was calculated depending on varying distances from collimator to the source/surface of the phantom. The objective of this chapter was to assess the ability of HGC to estimate the depth that could be used for targeted tissues during surgery.

Chapter 6

Because there is the potential to use the HGC to image radiolabelled tissue inside the chest or abdomen areas, the study of the effect of respiratory motion on the location and depth of tumour within these areas is important. In this investigation, a simulation of the tumour motion within the body and the ability of the HGC to estimate the depth of the moving source was conducted using phantoms and a laboratory jack, with two different movement patterns. These simulations were for perpendicular and diagonal source movements toward the camera.

Chapter 2: **Current technologies available in nuclear medicine departments**

2.1 **Introduction**

Medical imaging is one of the areas of nuclear medicine that can be used to diagnose the type and stage of cancer. Nuclear medicine is minimally-invasive and able to identify anatomical (morphology of the target) and functional (physiological processes) information of a targeted organ and to identify sentinel lymph nodes (SLNs) inside the body, which are the first nodes to receive activity from a primary tumour, thereby offering the possibility of determining disease in its earliest stages.

The type of nuclear medicine examination determines the method of delivering the radioisotope; it can be either injected or swallowed as a liquid or inhaled as a gas. After a specific time, it will accumulate within the target for subsequent examination. Gamma rays emitted from the radiotracer are detected by a gamma camera that can consequently produce images of the radioisotope distribution inside the human body and provide functional information about the targeted tissues.

Lymphoscintigraphy is an essential part of lymphatic mapping that provides crucial information about the localisation, and the number, of sentinel lymph nodes, and further allows for differentiation between these nodes [33]. A number of authors have debated the lymphoscintigraphy plan in patients with non-detection, and have examined ways to detect such 'invisible' sentinel lymph nodes [34-36]. Therefore, many researchers have focussed on developing the efficiency of the lymphoscintigraphy procedures in terms of the localisation of an accumulated radioisotope and a number of SLNs within body [37, 38].

For surgical use, a hybrid system is required for use during an operation which is portable; indeed, a number of research groups and manufactures have been working towards this goal. For example, the hybrid gamma camera (HGC), which combines optical and gamma imaging with hand-held and portable operation, has been developed by the Space Research Centre, University of Leicester, to address this challenge. One of the considerable advantages of this system is the removal of any parallax error, when imaging

from different views, as the acquisition of gamma and optical images are acquired simultaneously and in co-alignment [17]. This new system has been evaluated in a number of applications including clinical studies involving patients [15, 39-41].

2.2 Concept sentinel lymph node (SLN)

The concept of the sentinel lymph nodes follows from the lymphatic mapping in abnormal tissues, which are dependent on the drain lymph flow from a primary tumour site to a specific located lymph node (Figure 2.1) [42]. The term sentinel node is defined as the first lymph node, which is encountered in the lymphatic network by lymphatic vessels draining a tumour [23]. Lymph fluid moves from the primary tumour to the first SLN through lymph channels. Second level lymphocytes (and perhaps cancer cells) received from the first level of the lymph node, then drains through the lymph nodes towards the lymph nodes of the third level, etc.

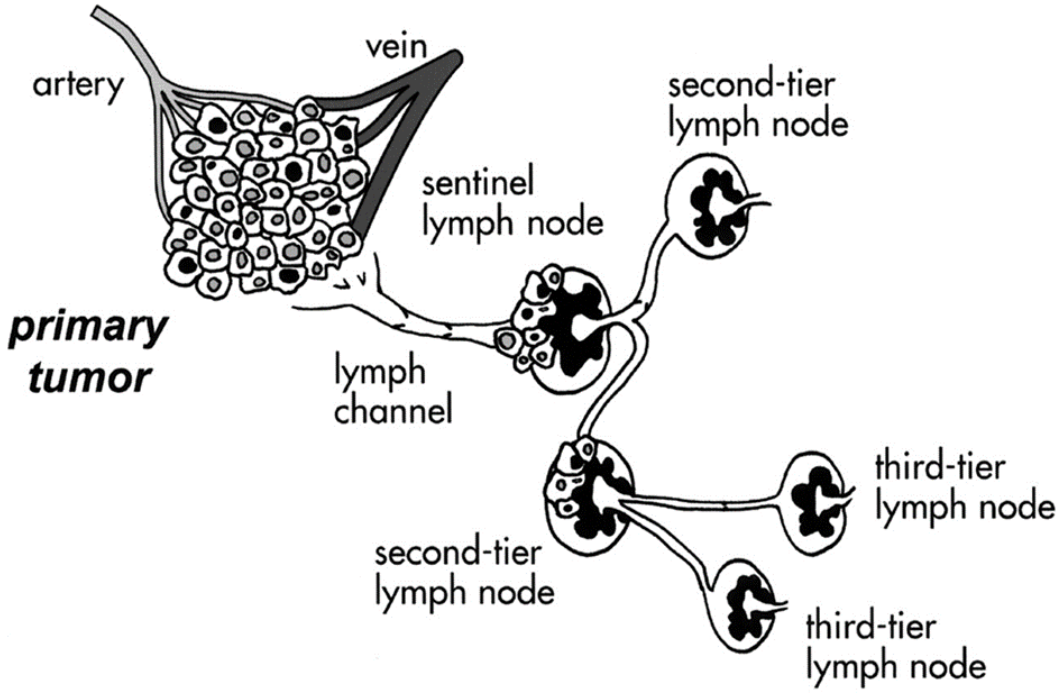

Figure 2.1: Schematic concept of sentinel lymph node. Being the first node encountered by lymph draining from the primary tumour, the sentinel lymph node should be the site where clusters of tumour cells migrating through lymphatic channels are most likely to be entrapped and possibly proliferate before widespread tumour dissemination in body. Second-tier (or second-echelon) lymph nodes receive lymph (and possibly tumour cells) from sentinel lymph node and in turn drain lymph toward third-tier lymph nodes, reproduced with permission [42].

There are many researchers and manufacturers interested in improving sentinel lymph node (SLN) detection procedures as well as obtaining better radiolabelled tissue detection techniques [43, 44]. For example, Figure 2.2 shows four SLN detecting methods; the first two, (A) and (B), are the current standard for SLN detection, which are the blue dye and the radioisotope method. The second two, (C) and (D), are considered novel methods for SLN detection, which involve optical imaging and magnetic tracer guidance [38]. Lymph nodes could be identified using a combination of radiopharmaceutical and blue-dye injection preoperative lymphoscintigraphy, and using gamma ray probes intraoperatively; this combination has led to an increase in the detection rate of SLNs [45, 46]. One of the crucial points in the development of the detection technique of SLNs is to ensure that they are detected preoperatively in order to be removed intraoperatively. The normal size of the sentinel lymph nodes ranges from a few millimetres to 2.0 cm but this size changes depending on the location of the lymph node, which are spread throughout the body [47]. An example of SLNs for head and neck is shown in Figure 2.3.

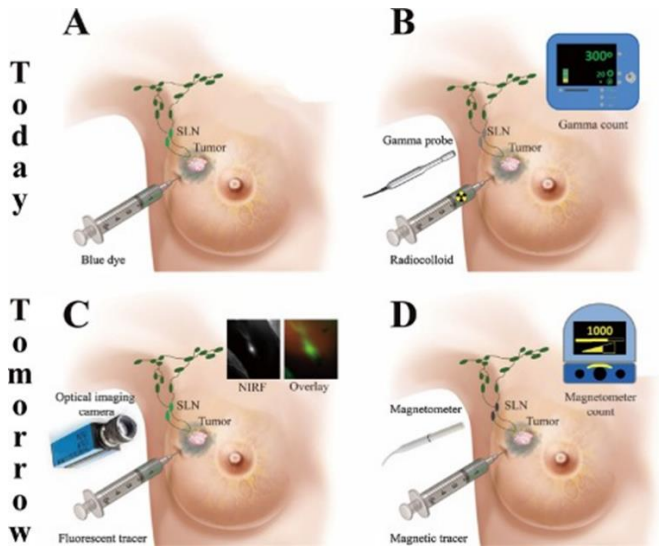

Figure 2.2: Four sentinel lymph node (SLN) detecting methods. (A & B) current standard of care for SLN detection: A) the blue dye method relies on the visual detection of the blue stained SLNs; B) the radioisotope method locates the SLNs by using a gamma probe for detecting the radiation emitted from the radioactive tracer accumulated in the SLNs. (C & D) novel methods for SLN detection: C) optical imaging guided SLN detection provides a real-time map for locating the SLNs; D) magnetic tracer guided SLN detection locates the SLNs by using a hand-held magnetometer to magnetize the magnetic tracer and detect the particles' magnetic response, reproduced with permission [38].

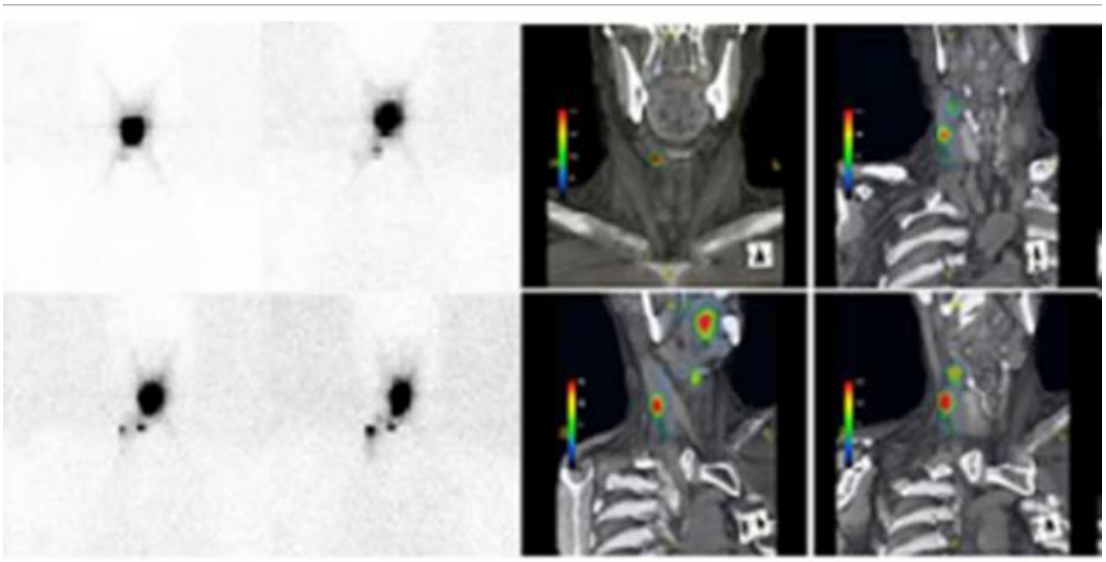

Figure 2.3: 2-D conventional planar lymphoscintigraphy and fused SPECT/CT in evaluation of a patient with floor-of-mouth carcinoma and the relationship of sentinel lymph node location to anatomic landmarks, reproduced with permission [37].

2.3 Radiopharmaceuticals

Radiopharmaceutical materials are designed as molecules that carry the radioisotopes to the target tissue to determine the localization and the distribution of accumulated radioisotope within the body (for example, ^{99m}Tc-methylene diphosphonate for bone scintigraphy, ^{99m}Tc - tetrofosmin for brain cancer) [7]. These materials are absorbed in targeted tissues at greater and faster than the surrounding tissue because the cancer cells have a hyperactive rate of metabolism greater than normal cells [48], therefore they absorb radioactive material faster than healthy cells. The selection of radiopharmaceutical and radioactive material for a specific scan depends on the metabolism process of the target within the body, the physical half-life of the radionuclide, the size of the molecule, compounds of targeted tissues, the purpose of the examination, and weight and size of patient, where the target tissue absorbs a certain amount of isotopes and the excess material is eliminated by the kidneys [49, 50]. For example, Phosphate analogues are mixed with a ^{99m}Tc radioisotope (500 MBq as average) and can be used for bone scans due to high absorption by bone and rapid clearance from the body by kidneys [7]. Table 2.1 and Table 2.2 show some of the radiopharmaceuticals that are used in particular with SPECT scans [51] and PET scans [52].

Table 2.1: Commonly used radiopharmaceuticals in SPECT imaging, reproduced with permission.

Chemical form	**Clinical Use**
^{99m}Tc-nanocolloid human serum albumin	Lymphatic imaging
^{99m}Tc-Mercaptoacetyltriglycine	Renography
^{99m}Tc-Macroaggregated Albumin (MAA)	Pulmonary blood flow (lung scan)
^{99m}Tc-Diethylene Triamino Penta Acetic Acid (DTPA)	Renal blood flow, function and excretion (Renogram)
^{99m}Tc-Methylene DiPhosphonate (MDP)	Skeletal studies (bone scan)
^{99m}Tc-Sodium Pertechnetate	Thyroid, salivary gland, brain and nasolacrimal drainage imaging
123I-Sodium Iodide	Thyroid scan

Table 2.2: Several imaging agents used in PET in some central nervous system (CNS) disorders, reproduced with permission from [52].

Radiopharmaceutical	**CNS disorder**
^{18}F-FDDNP	AD
^{18}F-FDOPA	PD
^{11}C-PIB	AD
^{11}C-raclopride	PD, schizophrenia, depression
^{11}C-PK11195	AD, MS, Huntington's disease
^{11}C-flumazenil	Epilepsy
^{11}C-nicotine	AD

Note: AD, Alzheimer's disease; PD, Parkinson's disease; MS, multiple sclerosis.

For SLN biopsy mapping of breast cancer, the radiopharmaceutical is injected under the skin or near to the tumour site, the location of the tumour being identified previously. Therefore the sentinel lymph nodes (SLNs) will receive the activity after drainage from the primary tumour [24]. For example, a 40MBq ^{99m}Tc solution was suspended with sulfur colloid for SLNs biopsy mapping of the breast tumour [53]. Because the radioactive colloids drain from primary tumour to the regional lymph nodes, biopsy of lymph nodes is useful to predict cancer spread [24]. The SLNs uptake activities range between 1 kBq and 1 MBq, depending on the number and size of lymph nodes in the same region of the tumour, the distance between the site of injection and the tumour (drainage distance), time between injection of the radiopharmaceutical substance and surgery, and the anatomical location of the tumour [24]. Table 2.3 shows some standard amounts of radioisotope used in nuclear medicine [54].

Table 2.3: Standard amounts of radioisotope used in nuclear medicine, reproduced with permission [54].

Type of procedures	Radionuclide	Administrated activity (MBq
Bone scintigraphy	^{99m}Tc	600–627
DaTscan (Brain scan)	123I	185
Lacrimal drainage scintigraphy	^{99m}Tc	1 per in each eye
Leukocyte scintigraphy	^{99m}Tc	100–225
Thyroid scintigraphy	^{99m}Tc, 123I	75–78, 18.5–20
Lymphoscintigraphy	^{99m}Tc	10–20 per injection site
Sentinel lymph node biopsy (SLNB)	^{99m}Tc	20.5

2.4 **Principles of imaging**

The basic principles of nuclear medicine imaging are as follows: the radiopharmaceutical is an emitter of gamma-rays which are detected by an external detector; the gamma camera detects the radioactivity from the target and from specified angles of view. The images are acquired at various viewing angles giving 2-dimensional (2D) images,

software is used to reconstruct into the 3-dimensional (3D) distribution of a radioisotope within the human body.

2.4.1 **SPECT imaging**

Single-photon emission computed tomography (SPECT) (Figure 2.4) is a functional imaging technique based on the emission of individual gamma photons from the target [55]. A SPECT system can be composed of one camera or a group of gamma cameras installed on a gantry and therefore the detectors can record images from several viewing angles and similar time intervals around the body. Gamma camera heads move around the patient to assess the functional status of the targeted organ at different angles. For example, the use of two cameras that cover 180^{o} angles leads to two gamma images being obtained simultaneously [56], or triple head cameras with 120^{o} coverage can be used [57], whereas 90° coverage is needed for a four-headed system [58]. The benefit of multiple heads is to improve the sensitivity that is provided by increased coverage of the solid angle for the targeted tissue, reducing the gamma-ray attenuation and minimizing the angular range of motion to obtain complete data about the target [58]. The images can be shown as thin slices along any imaging axis of the target, which are providing information about the radioisotopes distribution within the target.

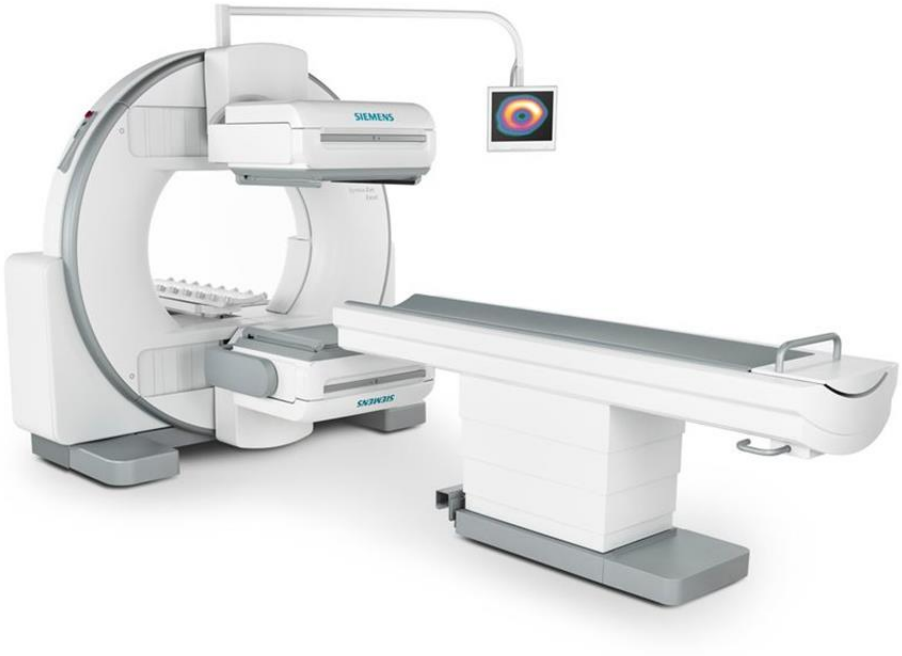

Figure 2.4: Example of SPECT imaging system from Siemens Medical Solutions USA, reproduced with permission [59].

Single photon emission computed tomography images are gained after administering a radiopharmaceutical that is used for nuclear medicine imaging, see Table 2.1. The standard amounts of radioactive material and radioisotope that are injected are shown in Table 2.3. The injected radioisotope accumulates in specific areas within human body, according to the type of exam being performed; for instance, it will show gall bladder and bile ducts for a hepatobiliary scan, and bone for a bone scan. In most situations, a full 360^0 rotation is used to acquire full images about targeted tissues. The acquisition time to acquire each image is variable, but 15–20 seconds is normal, the total scan time therefore ranging between 15 and 30 minutes [58]. Table 2.4 shows some radioisotope used with SPECT scan [52].

Table 2.4: Most common used SPECT radioisotopes, reproduced with permission from [52].

Radionuclides	^{67}Ga	^{67}Cu	^{99m}Tc	^{111}In	^{123}I	^{153}Sm	^{159}Gd	^{166}Ho	^{177}Ln
Energy (KeV)	93	185	140	245	159	103	363	80	208
$T_{1/2}$	3.26 d	3 d	6.06 h	2.38 d	13.2 h	47 h	20 h	26 h	7 d

Note: d, days; h, hours.

2.4.2 **PET imaging**

Positron emission tomography (PET) (Figure 2.5) system is a functional imaging technique based on the emission of two gamma photons (pair production) from a radioisotope that is accumulated in the organ of interest [60]. It is used to monitor metabolic procedures inside the human body. PET systems consist of multi detectors in a ring around the patient to capture gamma photons emitted from the target to create 2-D images with software used to reconstruct these images to create 3-D images of the radiopharmaceutical concentrations within the target [61].

Figure 2.5: Example of PET scan from Siemens Medical Solutions USA, reproduced with permission [62].

A PET system detects pairs of gamma photons that are created when a positron interacts with an electron, the interaction resulting in the complete annihilation of both particles to produce two gamma photons that travel in opposite directions (back to back annihilation process). The annihilation of an electron-positron produces two 511 keV gamma photons emitted at opposite direction (180 degrees between them), therefore, there is the potential to determine the location of a source along a straight line of response (LOR). Radionuclides used with PET scans are shown in Table 2.5.

Table 2.5: Most common used PET radioisotopes, reproduced with permission from [52].

Radionuclides	^{11}C	^{13}N	^{15}O	^{18}F	^{64}Cu	^{68}Ga	^{82}Rb	^{166}Ho
Energy (KeV)	511	511	511	511	511	511	511	511
$T_{1/2}$	20.39 m	9.97 m	2.04 m	109.77 m	13 h	67/63 m	1.27 m	27 h

Note: m, minutes; h, hours.

PET scanning has the ability to image certain diseases such as brain and heart disorders. Berti et al. reported that the PET scan with different radiopharmaceuticals offers reliable information about dementia, that can help the radiologist to diagnosis various dementia disorders [63]. Clinically, PET has ability to distinguish between malignant and benign solitary pulmonary nodules with a range of sizes from 0.6 to 3 cm when radiographic findings are indeterminate [64].

2.4.3 **CT- scan**

A computed tomography scanner (CT-scan) (Figure 2.6) is an anatomical imaging technique based on an X-ray passing through the body, then being detected by a detector which is placed behind the patient. A number of beams are sent simultaneously per unit time from various viewing angles instead of using a single X-ray angle to illuminate the human body as with ordinary X-ray machines. These beams have energy levels between 20 and 150 keV and are monochromatic. The beam passes through different thickness of tissues to provide the cross-sectional images ("slices") of the target.

The basic principle of CT is its dependence on the density of the tissue which the X-ray beams passed through, which may be measured by the calculation of an attenuation coefficient [65, 66]. Those beams that have passed through low density tissue such as the lungs will have a high intensity on the detector, whereas beams that have passed through high density tissue such as bone will have a low intensity on the detector. The overlap of the tissues in the human body appear in the image. The CT scan has overcome this problem by scanning thin slices of the target and using a narrow X-ray beam which is

rotated around the body. Software is used to process this information, that is, cross-sectional images (slices) of the target, and displays them as a 2-D image on a monitor of the computer and then reconstructs them into 3-D images, where the information about the anatomical target that can be provided, leading to better surgical outcomes that can aid surgeons when treating diseases.

Figure 2.6 : Example of CT scan from Siemens Medical Solutions USA, reproduced with permission [67].

2.4.4 **Hybrid Imaging Systems**

A combined anatomical / functional imaging technique allows for better identification of tumour location and SLNs (number and location) compared to using a single imaging system [68],where a SPECT scan, PET scan or CT scan separately would provide functional information or anatomical structural information about the targeted organ, with one of part of the information missing.

In many nuclear medicine centres, SPECT or PET images can be combined with computed tomography (CT) (Figure 2.7) to produce specific images of the target in a procedure known as image fusion or co-registration. These images combine the information from two different scans for interpretation as one image, leading to more accurate information and diagnosis, such as CT combined with SPECT (SPECT-CT), or with PET (PET-CT) [12, 13] and, recently, PET combined with MRI (PET-MRI) [69, 70]. Both SPECT/CT and PET/CT have enabled physicians to obtain a deeper, more comprehensive understanding of images created by nuclear medicine imaging and subsequently increased their utility. In addition, the integration of anatomical structural information with diagnosed functional abnormalities in a tumour can provide useful information for further treatment or external radiotherapy. Figure 2.7 shows examples of SPECT/CT and PET/CT, and Figure 2.8 shows example of SPECT/CT and PET/CT images.

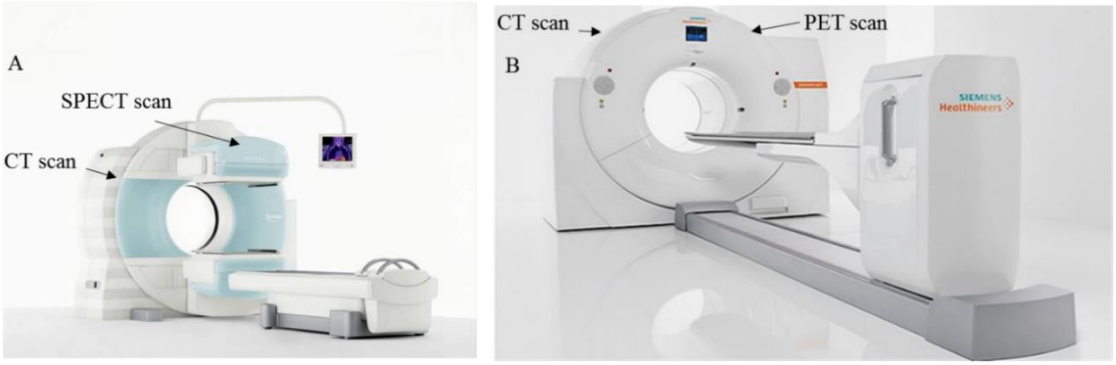

Figure 2.7: Siemens Medical Solutions USA. SPECT/CT Symbia T Series (A), reproduce with permission [71], and PET/CT Biograph Vision (B), reproduced with permission [72].

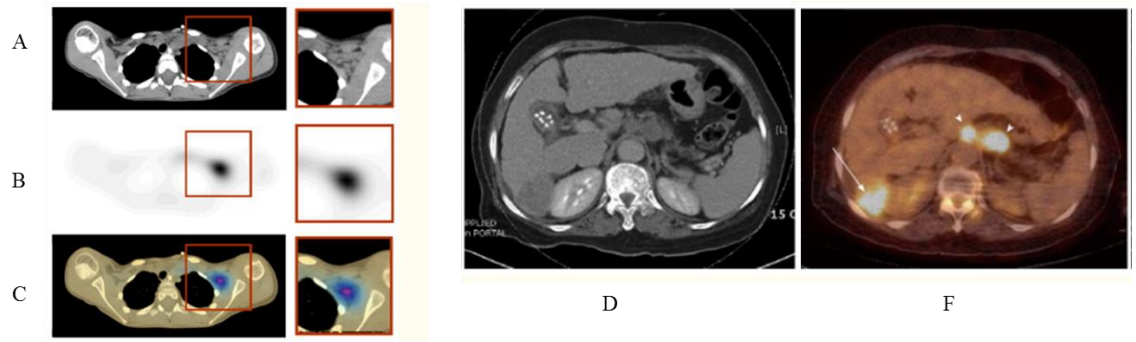

Figure 2.8: Example of fused image available from combined CT–scintillation camera imaging system. CT image (A) is shown along with spatially correlated SPECT image (B) indicating ^{131}I-MIBG uptake in lymph node in patient's left axilla and fused SPECT/CT image (C) [73], ^{18}F-fluorodeoxyglucose PET/ CT in hepatocellular carcinoma; CT image (D) and fused image PET/CT (F) show hot uptake in the primary lesion (arrow) in the right lobe of the liver and regional lymph node metastases (arrowhead), reproduced with permission [74].

There are a number of research groups that have manufactured and developed hybrid imaging systems for use in medical science applications. Olcott et al. reported a novel intraoperative handheld gamma camera (IHGC) combined with a gamma probe (GP) for determining the accumulation of radioactive SLNs in the head-and-neck region and other difficult cases within the human body [24]. Lees et al. designed a new hybrid gamma camera system (HGC) which combines gamma and optical cameras and produces multi format images output such as single image (gamma and optical) or fused images; the HGC imaging system provides visual identification of the sites of accumulation of radioisotopes within the body and offers high resolution that could play an important role during surgery [17]. These systems could aid surgeons and radiologists to achieve more accurate and comprehensive diagnosis than using one modality alone because more information will be available. Finally, the purpose of combining anatomical and functional information into SPECT/CT or PET/CT scans is to confirm the location of tumours inside the patient where the anatomical images will be background of functional target, CT scan was used to attenuation correction of gamma photons that absorbed by SPECT or PET scans because the resolution of the CT scan higher than SPECT scan [75].

2.5 Intraoperative radio-guidance surgery

A small field of view gamma camera system is used for imaging small targets within the body such as SLNs. For example, the hand-held gamma camera which consists of a hexagonal parallel-hole collimator coupled to NaI (Tl) scintillation crystal, has been developed specially in order to accelerate the determination of sentinel lymph nodes during surgery [76]. A second example of a SFOV gamma camera used during surgery is the CarolIReS camera, where the prototype of the CarolIReS camera consists of a parallel lead collimator thickness coupled to a 2 mm inorganic scintillating crystal. The sensitivity of this system is 2.2 cps/kBq with a spatial resolution of 1 cm for a point source placed at 50 mm distance from the collimator face, this camera was used in the localization of SLNs within the body during surgery [77].

A small field of view gamma camera is designed to be close to the patient, where the patient can be sitting opposite the camera or lying on the bed in an operating room. During imaging procedures, the position of the camera is kept stable for the entire acquisition time to avoid artefacts that are caused by camera movement.

A gamma detection probe system (GP) (Figure 2.9) consists of a solid-state detector coupled to a single scintillation crystal, and a collimator that allows gamma rays to pass through a small aperture [78]. The GP allows the estimation of the location of a radioisotope distribution uptake within the body based on the gammas detected, which are converted to count rates, displayed on the monitor, and an acoustic signal [8]. Therefore, surgeons and radiologists must move the GP around the surgical field to obtain the largest number of photons and highest audio signal [78].

Figure 2.9: Example of a gamma probe manufactured by Surgiceye Company, reproduced with permission [78].

2.6 Concept of SFOV gamma cameras usage in medical settings

Large field of view (LFOV) imaging systems are bulky, and were originally designed to provide gamma images of large target organs or even the whole body of the patient. However, there has been a focus on the development of integrated (SFOV) imaging systems because there is an increasing need for intraoperative imaging tools in the clinical theatre. Over the past few decades, a number of researchers and manufacturers have invested in the medical imaging field to develop portable gamma cameras [17, 79] because the routinely used imaging gamma cameras are bulky and show poor manoeuvrability during diagnosis such as SPECT/CT or PET/CT, or non-imaging such as GP.

In recent years, many researchers have focused on the development of high-resolution SFOV-type gamma camera detectors for imaging small organs to allow detection of tumours in the breast or thyroid, for instance [80]. The main feature of the SFOV gamma camera is that it is sufficient to allow the imaging of small organs inside the body and has intraoperative manoeuvrability, such as for detection of tumours in the breast or thyroid [80], where the advantages of the SFOV gamma camera are that they are smaller, lighter, more efficient and easier to use during surgery than the LFOV gamma camera.

The main parts of all the gamma cameras are the collimators (pinhole, parallel hole arrays or slats), the conversion medium (scintillator or a semiconductor), and a readout mechanism (Photomultiplier Tubes (PMTs) or semiconductor arrays) [18]. The gamma camera design depends on the parameters, which are driven by the required Field of View (FOV) (small or large field of views), sensitivity, spatial resolution and portability [81, 82].

The main parts of the SFOV gamma camera are the scintillator, detector and collimator. A scintillator such as caesium iodide scintillator doped with thallium CsI(Tl)converts high energy gamma-ray photons to lower energy optical photons. A detector such as an electron multiplying charge-coupled device (CCD) converts optical photons to electronic charge, where the electrical signal produced in each pixel is processed by integrated circuit within the readout electronics [83, 84]. Solid-state detectors are available as pixelated arrays, such as CdTe and CdZnTe, and have a better energy resolution compared to scintillation detectors. When gamma photons interact with the semiconductor material, they are directly converted into an electronic signal, without passing through a

scintillation counter to form an electronic signal followed by electronic signal amplification. All signals produced in pixels are processed by the Application Integrated circuit (AIC)-based readout electronics [85].

Collimator design plays an important role in detecting the gamma rays emitted from the source within the body, such as pinhole and parallel-hole collimators. Sensitivity and spatial resolution are the most important features for collimators when they are used in gamma cameras. For example, the sensitivity of a parallel-hole collimator is nearly constant as a function of collimator to source distance, whereas the sensitivity of a pinhole collimator changes with collimator to source distance depending on the inverse square of the distance, and the sensitivity of a pinhole collimator increases as the square of the diameter with simultaneous loss in spatial resolution [22]. The pinhole collimator provides a variable imaging FOV at different imaging distances, whereas the parallel hole collimator has a field of view that does not change with imaging distance [86]. Using a pinhole collimator, the image is magnified when the distance from the source to collimator is less than the distance from collimator to detector, whereas it is de-magnified when the source-to-collimator distance is greater than the collimator-to-detector distance. The sensitivity and spatial resolution of pinhole collimators depends critically on the source-to-collimator distance [9, 87]. The selection of an appropriate collimator for using with gamma camera depends on size of the target. A pinhole collimator is a suitable to image small organ such as thyroid but a parallel hole collimator will be appropriate to image the whole body. For example, the pinhole collimator was used with the Hybrid Gamma Camera (HGC) to image the thyroid [15] and a parallel hole collimator was used with a SPECT scan to image the whole body [88]. Indeed, the collimator plays a substantial role in determining the performance of SFOV gamma cameras and gamma cameras generally [85].

For surgical use, a gamma camera must be as small as possible to be close to the surgical field (short distance between the collimator to the source) and manoeuvrable during surgery. Proximity to the surgical field leads to improved sensitivity and resolution of the gamma image on the detector. The surgeons need these images to determine the radioisotope accumulation in a given area within the field of view of detector. In contrast, SPECT/CT or PET/CT cannot be used intraoperative because of their size and inability to move.

2.7 Limitations of technology current in nuclear medicine departments

One of the most important characteristics of a gamma camera that should be studied in nuclear medicine is its efficiency, which is the ability to detect the low levels of the radiation based on the type of collimators [89].

The spatial resolution is the one of the most important parameters in nuclear imaging. However, the resolution of the gamma camera is affected by the collimator diameter, the distance between source and detector and the photon interaction with tissue and the patient's movement [90]. The resolution of the modern gamma camera such as sodium iodide gamma camera (SIGC), can be expressed by the full width half maximum (FWHM) [91]. For instance, as Sorenson et al. reported that the FWHM for ^{99m}Tc deteriorates from 7.5 mm to 19.1 mm where the source's depth in water changes from 2 cm to 22 cm [92]. The lower spatial resolution of gamma camera images lead to blurry images, which are caused by loss of signal and shape distortion, and these affect the reconstruction of the image [93]. Although, gamma images from SPECT and PET scan provide functional information to distinguish between normal and abnormal tissues, which are based on the level of uptake of radioactivity in targeted tissues, the anatomical information provided by a gamma images is considered very poor compared to CT scan because the resolution of SPECT or PET is very low compared with CT [90].

One major limitation of technology current in nuclear medicine is the attenuation factor of the bone. For example, in the diagnosis of dementia by SPECT imaging, it may be difficult to differentiate artefacts, which are caused by SPECT, the instrument or photon attenuation by high density tissues, i.e. the skull of the patient. The contrast between the images which result from attenuation correction by SPECT software may lead to artefacts when using the SPECT scans for the diagnosis procedures [94].

The limitations of PET/CT examination are observation of the ^{18}F- fluorodeoxyglucose (FDG) activity in the associated structures of the head and neck after the surgery, which occur either as a result of radiation from the side or surgical removal of one side. This dissimilarity in FDG activity between two sides of head and neck may lead to misdiagnosis [95]. Therefore, the anatomical or functional changes that arise from radiation or surgery greatly limit the use of CT or PET separately.

Another limitation of a PET/CT scan is the difference in their field of views (FOVs), where the FOV of PET is greater than the FOV of CT [96]. The artifacts appear when adult patients are imaged or when the patients are placed away from centre of the PET/CT gantry. Because a part of the patient will be outside of the FOV of CT, so there are no attenuation values in the corresponding area of the PET data. This reduces the number of photons detected and affects the attenuation-corrected PET images, which may result in misinterpretation of the PET imaging [97].

The gamma probe that is used to detect radioisotope uptake in the targeted tissues during surgery is a non-imaging system. These non-imaging systems are dependent on the number of photons that are detected from the radioisotope distribution within a surgical area. These systems have the ability to detect a very low activity inside body, which is approximately less than10 kBq within a few seconds [56, 57]. However, the GP detection cannot provide detailed information about targeted tissues. These devices suffer from a deterioration in the sensitivity if the targeted tissues are under the bone or more than 20 mm below the skin, as this reduces the detected signals from the targeted tissues [56, 57]. The tip of the GP should be placed close to the targeted tissues during the surgery to ensure the precise determination of the location of the radiolabelled tissues within the body.

2.8 Concept of stereoscopic imaging in the medical field.

Stereoscopic imaging techniques relies on the same principle of human vision of an object. The human brain collects and process two dimensional (2D) images from the right and left eyes of the observer to create a 3D image of the same object [98]. For instance, when a person looks at a something with both eyes at the same time, this leads to the creation of two slightly different images. These two images are transferred by visual nerves to the visual cortex to combine and create a stereoscopic image (3D).

Many kinds of 3-D imaging processing such as SPECT/CT and PET/CT have been developed [99]. These systems have offered better perception of the depth of region of interest than conventional 2-D systems, enabling more precise diagnosis and analysis of a given object [100]. It is important to tackle the three problems connected with 3-D stereo-imaging technology to develop stereoscopic medical devices, namely the

difficulties of camera calibration, efficient computation, and reliable depth estimation [101]. The application of this technique in the medical field has enhanced patient management [99].

2.8.1 Principles of the stereoscopic system

The three-dimensional imaging technique consists of two separate optical inputs, whereby two separate cameras are used under the same imaging conditions but with different viewing angles [99]. There are different kinds of stereoscopic systems, including the parallel camera structure and the beam-splitter structure, which are the most commonly used. The parallel-camera design can be implemented by placing two cameras side-by-side in a set-up that mimics the human eye [102], as shown in Figure 2.10 A. Some of the advantages to this arrangement are that 1) it is easy to set up and align in a suitable position and 2) there is no contrast in terms of colour degree and light exposure between the two images [99]. However, the possibility of obtaining close-up images is limited because modification of the distance between two axes of the cameras depends on the sizes of the lenses. The parallel camera arrangement is more convenient for imaging over longer distances [103]. In the beam-splitter arrangement, two cameras are positioned at a mutual right angle and a half-silvered mirror is set at 45^0 in the plane between the cameras in order to transmit the object image to them. This arrangement makes it easier to capture images at smaller distances [104], see Figure 2.10 B.

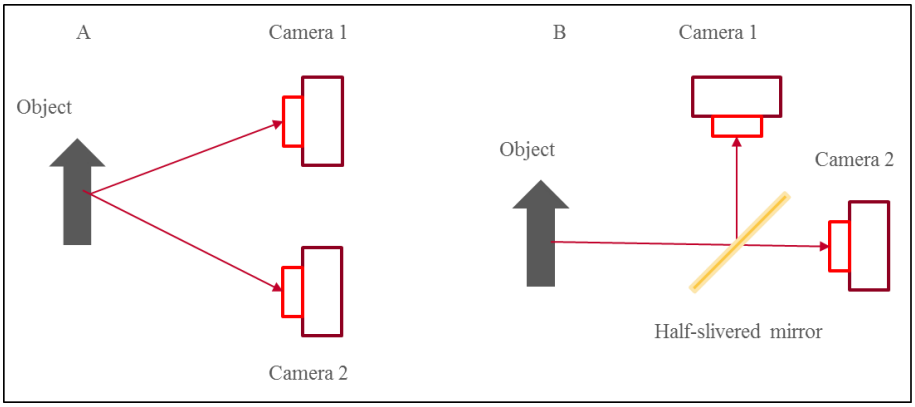

Figure 2.10: Basic arrangement of the 3-D technology. (A) Parallel-camera arrangement, (B) beam-splitter arrangement.

2.9 Summary

Diagnosis in nuclear medicine is undertaken using specific amounts of radioisotopes to diagnosis the type and stage of cancer. The examination determines the type of the radioisotope to be used. Two imaging systems are used to provide functional information about the target, namely SPECT and PET. In hybrid imaging systems, these are combined with CT to obtain integral information (anatomical and functional) with a 3D image of the target outside the operating theatre. Also, GP and SFOV gamma camera techniques have been used in intraoperative procedures to determine the radioisotope distribution within body, such as the intraoperative handheld gamma camera (IHGC) that was designed for imaging during surgery and to be positioned beside the patient. The limitations and the advantages of the imaging techniques in the field of nuclear medicine, as well as three-dimensional imaging, have been discussed.

Chapter 3: **The Hybrid Gamma Camera**

3.1 **Introduction**

Medical imaging diagnosis involves different ways to collect anatomical and functional information about a target organ. An anatomical image provides information about morphology and location of an organ within the body and a functional image provides information about physiological processes of organ. Functional and anatomic imaging information provide a beneficial tool for diagnosis without surgical intervention. There are three ways to collect functional and anatomical information together about a specific target organ [105]. The first approach is separate imaging modalities (such as CT, SPECT or PET), with the information from each combined after imaging. The second approach is by combining functional and anatomical imaging techniques within a single imaging system (e.g. PET-CT or SPECT-CT), where the first scan is SPECT followed by a CT scan on the same patient bed [12]. Finally, there is a fully integrated imaging system which images the targeted area using two systems simultaneously and the full anatomical and functional information about a targeted organ is obtained from the imaging area simultaneously, such as a combined PET-MRI technique [106, 107]. In the fully integrated imaging system, PET is inserted into the MRI scanner, the centre of field of view of the PET and MRI are identical, which improves the current techniques by providing full anatomical and functional information with a short acquisition time [107]; therefore this approach may be the preferred option among these imaging systems for the radiologist [105].

In a clinical setting, both anatomical and functional information is required to assess the condition of the patient. However, the techniques used to evaluate the anatomical structure of the organ (e.g., MRI and CT) are different than those used to evaluate function of cells (e.g., SPECT, PET) [108]. Hybrid imaging systems are being successfully used for nuclear medicine diagnosis, however, there is no single type of imaging that can provide all the information on the structure and function of an organ. The development of medical instruments has played a significant role in the improvement in accuracy of clinical diagnosis. After researchers were able to obtain functional and anatomical information about the targeted organ using PET- CT and SPECT- CT in a single scan

[109-111], there was a growing interest among researchers, clinicians, and manufacturers about combining two different imaging modalities into a single device. These hybrid cameras that combine functional and anatomical imaging have many benefits for patient management. However, SPECT/CT and PET/CT cannot be used during surgery because of their large size and immobility.

To be used in the operating theatre, a gamma camera needs to be small and light-weight to make its use effective within the limited operating space. A small gamma camera could be installed on an arm for acquiring different views (anterior, posterior and lateral), in contrast to the conventional non-portable cameras that are routinely used for clinical imaging [112-114]. However, the effectiveness of any camera depends on the spatial resolution and sensitivity, for example, the ability to distinguish between the normal and the abnormal sentinel lymph nodes (SLNs) (see chapter 2), which are located near to each other [17, 115].

3.2 Portable gamma camera systems

In nuclear medicine imaging, small single-headed cameras coupled to a mechanical trolley have been available over the last two decades. These cameras help the radiologists to perform imaging procedures of a specific organ within the patient, where the patient is lying on a standard bed beside the gamma camera. The initial examination by a "portable" scintillation camera in the theatre or other locations previously believed to be unreachable for diagnostic nuclear medicine was done by Hurwitz et al. [116] four decades ago. This camera was a modified standard Anger scintillation camera with a 12.7 mm thick NaI(Tl) crystal of 304.8 mm in diameter, coupled to a movable arm.

Figure 3.1 shows a portable digital gamma camera manufactured by Digirad Corporation (San Diego, CA, USA). This system has a 31.1 cm × 39.6 cm field of view produced by a segmented caesium iodide crystal doped with thallium CsI(Tl) coupled to silicon photodiodes and is suitable for detecting gamma energies from 50 keV to 350 keV with the aid of the interchangeable collimators. The camera has a weight of 305 kg but can be manoeuvred manually. This camera has been used in imaging the lung, liver, breast, sentinel lymph node and lymphoscintigraphy [10].

Figure 3.1: A solid-state mobile gamma camera-Digirad ergo™ Imaging System by Digirad, reproduced with permission from [117].

Figure 3.2 shows another example of commercially available mobile gamma camera manufactured by Mediso Medical Imaging (Budapest, Hungary), namely the Nucline^{TM}TH. The camera detector consists of a sodium iodide doped with thallium NaI(Tl) scintillation crystal, 6.5 mm thick backed by PMTs. The detector head is available in a different sizes; 230 mm × 210 mm, 260 mm × 246 mm and 300 mm × 300 mm. The system has a weight of 180 kg and the gantry is equipped with motorised height adjustment and interchangeable collimators. A separate computer unit is used for image acquisition.

Figure 3.2: A mobile gamma camera-Mediso 'Nucline^{TM} TH, reproduced with permission from [118].

Several small gamma camera systems have been developed for imaging during surgical procedures in order to localize abnormal tissues. An example of a SFOV gamma camera that is currently available for intraoperative imaging, the Sentinella 102 (Oncovision, Valencia, Spain) (Figure 3.3 A), consists of a compact scintillation camera with a 50 mm × 50 mm × 4 mm CsI(Na) crystal coupled to a pinhole collimator. This camera is connected to a computer with a touch-sensitive screen. It has three interchangeable pinhole collimators with different diameters; 1 mm, 2.5 mm and 4 mm. The camera is mounted on an adjustable arm and a cart with integrated mains isolation to facilitate movement during surgery; the weight of the camera is 1.2 kg [119].

An intraoperative hand held gamma camera (IHGC) that has been developed for clinical application, such as Sentinella [10] and Crystal Photonics-Germany [120] SFOV gamma cameras are shown in Figure 3.3. The IHGC has constant sensitivity as a function of imaging distance. The sensitivity of the Sentinella SFOV gamma camera is higher than conventional gamma camera as a function of imaging distance, and has a spatial resolution that decreases with increased imaging distance to the target [121]. It is

preferable to have the handheld gamma camera close to the targeted tissues because the spatial resolution of the camera will supply more information about the radioisotope distribution within the body than is acquired with the GP. The camera has the ability to image the larger area in a single acquisition, so IHGC will be a useful supplement to GP procedures when there is difficulty to determine the location of the SLNs with GP alone [24].

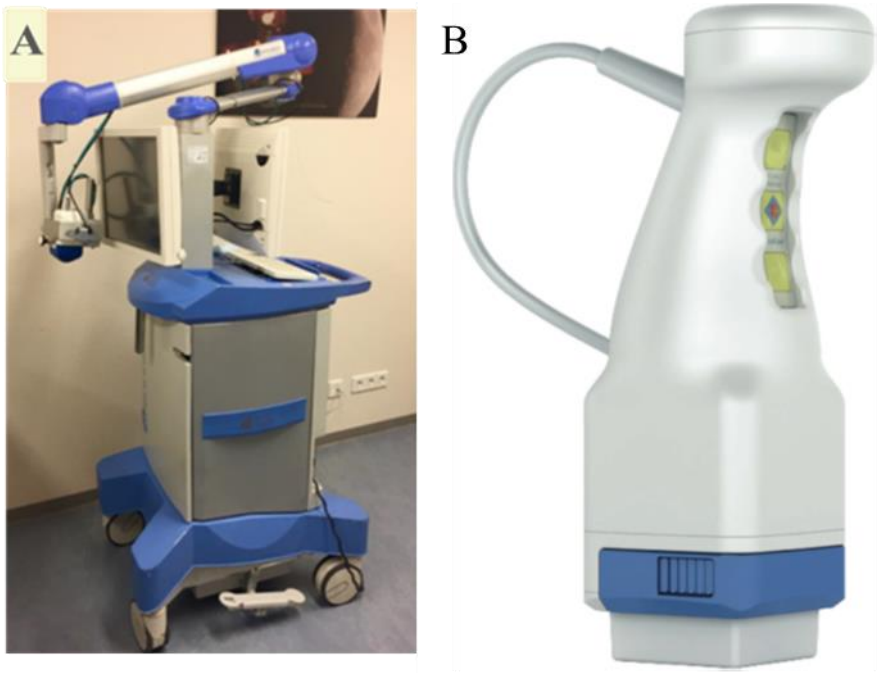

Figure 3.3: Photographs of intraoperative hand-held gamma camera; (A) the Sentinella 102 SFOV gamma imaging system [10], (B) the Crystal Photonics-Germany.

Accurate estimation of the location of the radioisotope accumulation within body would aid the surgeon to completely remove cancer [8, 122]. These technologies support surgeons in the localisation of SLNs in many types of cancer in the operating theatre [11].

The purpose of this chapter is to describe the hybrid gamma camera's (HGC's) design and the role of the diameter of the pinhole collimator in the imaging procedures in terms of resolution and sensitivity.

3.3 Hybrid Gamma Camera Design

In nuclear medicine, all gamma imaging systems consist of the following major components: collimator (pinhole, parallel hole arrays or slats), a conversion medium (scintillator or a semiconductor), and a readout mechanism (Photomultiplier Tubes (PMTs) or semiconductor arrays). In addition, gamma camera designs depend on the parameters that are important in the medical field such as the required Field of View (FOV), sensitivity, spatial resolution, portability, and cost [81, 82].

The hybrid gamma camera (HGC) was developed by the Space Research Centre (SRC), University of Leicester in collaboration with Radiological and Imaging Sciences at the University of Nottingham and was used for all the investigations in the current study. The HGC consists of an electron multiplying - charge coupled device (EM-CCD), which is the back-illuminated CCD97 produced by e2v technologies [123]. Itis coupled to a 1500 µm thick columnar caesium iodide scintillator doped with thallium CsI(Tl) and a 6 mm thick tungsten pinhole collimator. The pinhole collimator has a 60^0 acceptance angle, the diameter of collimator is 45 mm. The pinhole collimator provides a variable FOV at different imaging distances. The scintillator converts high energy gamma - ray photons to lower energy optical photons which are subsequently detected by the CCD; the number of incident photons depends on the incident photon energy [86]. The CsI(TI) has characteristics that make it an excellent material for gamma-ray detection such as a light output of 54 photons/keV and is one of the brightest scintillators known, with a high effective-Z of 54 and a high density approximately 4.5 g cm^{-3}. The peak wavelength of the scintillation photons is 565 nm which corresponds well with the spectral response of the CCD (e2v), which has an efficiency greater than 90% at this wavelength [86]. The CCD converts the optical photons to charge in the imaging area during the acquisition time. This charge is multiplied in the gain register before reaching read out. The read out provides information about energy and position for each of the incident gamma photons. The distance between the CCD and the pinhole collimator is fixed at 10mm and the distance from the pinhole collimator to the target being imaged determines the magnification on the CCD [18]. The HGC head is surrounded by a 3mm thick tungsten shield to protect it from scattered gamma rays and it is placed in a non-toxic plastic case for electrical and thermal isolation [17]. Figure 3.4 shows a schematic of the prototype hybrid gamma camera.

Optical components (optical camera and mirror) are co-aligned with the gamma camera using the aluminium base that is installed above the collimator. They are manually mounted on the HGC head in a specific position in order to ensure the position of mirror is at a 45^0 angle above the centre of collimator, and to ensure that the FOV for the gamma and optical cameras are identical and independent of the distance between the two cameras and the radioisotope source.

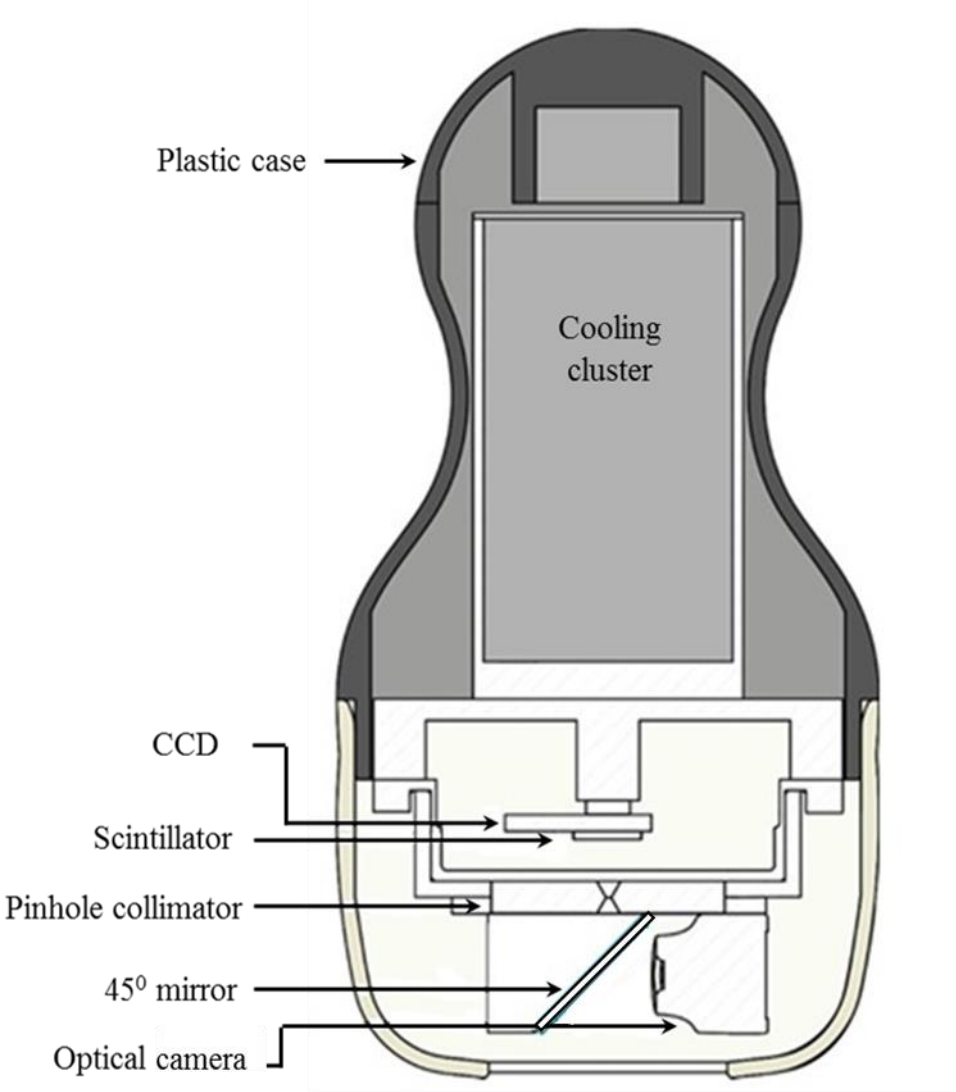

Figure 3.4: A schematic of the prototype hybrid gamma camera. The optical camera is placed in front of a 1 mm thick first surface mirror at 45 degrees centred above the window of the pinhole collimator [31].

There are many factors affecting the sensitivity of gamma cameras when using a pinhole collimator such photon energy, collimator material, pinhole diameter, acceptance angle and imaging distance. For example, at a 25 mm imaging distance (collimator to source distance) and for 140 keV gamma-ray photons, the geometric sensitivity, which is defined as the fraction of emitted photons from radioisotope source that pass through the aperture of the pinhole collimator, is predicted to be 1.4×10^{-4} and 4.3×10^{-5} with 1.0 mm and 0.5 mm diameter pinholes, respectively [86]. The hybrid gamma camera (HGC) was designed to be sensitive to photon energies in the range 30-140 keV. Further details about the HGC characterisation and basic design have been reported previously [124].

Gamma-ray photons emitted from radioisotopes pass through the mirror with minimal absorption (<1 %) and minimal scatter to the pinhole collimator. These photons are absorbed by the CsI(Tl) and are converted to optical photons which are then detected by the CCD to create the gamma image. The optical camera receives the source image which is reflected by the mirror directly. The gamma and optical images from both cameras can be displayed simultaneously or individually using bespoke imaging software. The optical image shows the surface of the area that has a similar region of interest (ROI) as the gamma camera [17].

The hybrid gamma / optical camera (HGC) represents a new imaging system, that could provide information about the radiolabelled tissues during surgery such as location of the radioisotope distribution in the targeted and surround areas [17]. In addition, the features of the camera design could help surgeons to enhance their confidence in diagnosis and entire tumour removal.

3.4 Imaging software

The imaging system has been designed to be carried out in single or dual modality mode. The gamma and optical images can be presented separately or in a combined image with adjustable colour tables to aid analysis. The gamma camera can deal with different exposure times and activity. The optical image is obtained directly from the optical camera. Further details about the imaging software have been reported elsewhere [124].

When a combined image is acquired, the optical image will form the background to the gamma image via overlaying the latter on the former. Each pixel of the optical image is compared to the corresponding pixel of the gamma image. Each single image (gamma or optical) or fused (gamma and optical) can be saved in different formats, such as JPEG or TIFF.

3.5 Pinhole collimator

The pinhole collimator was made from tungsten which has a high atomic number (74) and a high level of attenuation at the standard gamma photon energies to be imaged. Therefore the gamma rays will pass only from the single hole that is in the collimator to the detector. The pinhole collimator was used to determine the direction of the gamma ray photons reaching the detector, allowing an image to be created [125]. A circular knife-edge pinhole collimator design was used (Figure 3.5). Pinhole collimators have the ability to magnify and minimize image size; depending on the detector to collimator distance, *t*, and the collimator to source distance, *h*, the magnification factor of the image *M* is:

$$M = \frac{t}{h} \tag{3.1}$$

There are two main benefits of using pinhole collimators in the HGC. The first benefit is simplifying the manufacture and the second is a variable imaging field of view at different distances (a parallel hole collimator would have a field of view limited to the imaging area of the CCD ~ 8 mm x 8 mm [86]). The pinhole collimator, 6mm thick and 45mm diameter, has an acceptance angle of 60° [126]. Taking into consideration the requirements for sensitivity and spatial resolution in a range of applications, either a 1.0mm or 0.5mm diameter pinhole can be used with the HGC; however the basic design of the camera remains constant. Although many kinds of collimator may be utilised in gamma cameras, a pinhole collimator could be better than other types of collimator for SFOV in the medical imaging field because there is the potential to monitor large areas and display the same angular resolution [127]. However, the pinhole collimator's sensitivity reduces rapidly with increase in the distance from the camera to the source, because it is inversely proportional to the imaging distance (decrease in the number of

photons detected), and can have an effect on the spatial resolution across the field of view [128].

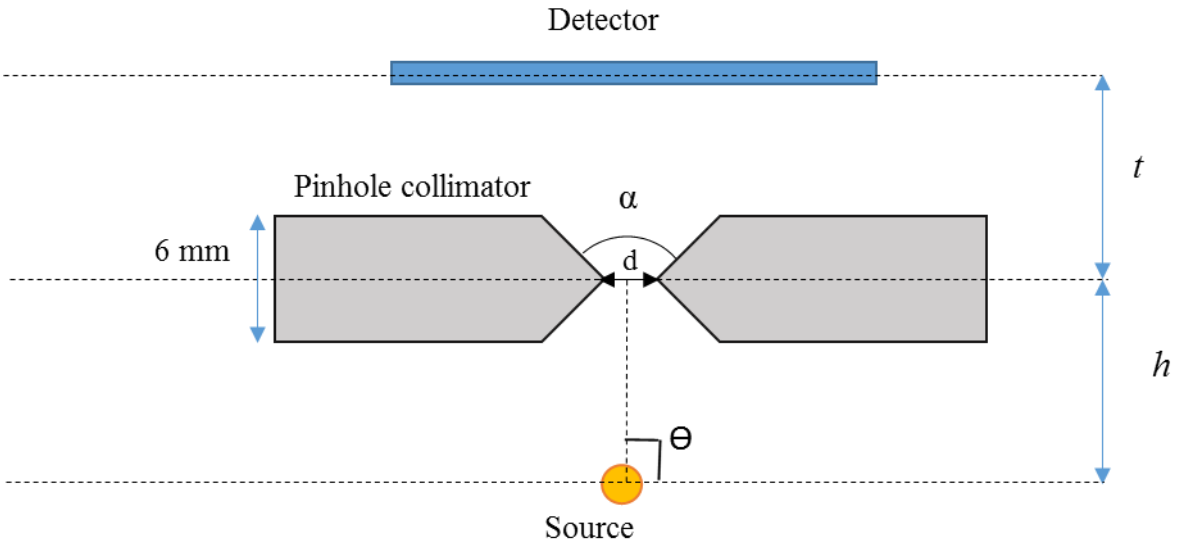

Figure 3.5: A diagram showing a cross-sectional view of the knife-edge pinhole collimator and detector-to-collimator and collimator-to-source geometry. The figure defines the detector to collimator distance *t*, collimator to source distance, *h*, acceptance angle, α, pinhole diameter, *d*, and source to collimator angle, *Θ* [129].

3.5.1 **Collimator Resolution**

For gamma cameras, the collimator spatial resolution is a critical performance parameter. The collimator spatial resolution of a gamma camera is indicative of the ability of the camera to distinguish two sources. It can be defined as the full width at half maximum (FWHM) of the image profile from a point source; this is also called the point spread function (PSF) [92, 130].

The measured resolution of the source image on the detector depends on the imaging distance (source to collimator distance) and diameter of the pinhole collimator, where the object size will be smaller with increasing distance when *M* is not equal to one. The spatial resolution of a point source positioned beneath the centre of the pinhole is given by:

$$R_{geom} = d\left(\frac{1}{M} + 1\right) \tag{3.2}$$

where d is the pinhole collimator diameter [131]. R_{geom} decreases with increasing imaging distance. Equation (3.2) does not take into account the possibility gamma photon penetration through the collimator material (tungsten). An effective pinhole diameter, $d_{eff,}$ can be used which is the diameter of the pinhole collimator d corrected for penetration at the edge of the pinhole. Therefore, equation (3.2) can be modified so as to account for the effect of the acceptance angle of the pinhole collimator and penetration, α, as per the Metzler resolution in Equation (3.3) [29, 132].

$$d_{eff}^2 = d\left(d + \frac{2tan\frac{\alpha}{2}}{\mu}\right) + \frac{2tan^2\frac{\alpha}{2}}{\mu^2} \tag{3.3}$$

Here, μ is the linear attenuation coefficient of the collimator material.

The effective resolution of the pinhole collimator diameter is based on the imaging angle θ. When the collimator is perpendicular to source ($d_{re\text{-}perpendicular}$), the effective resolution is described by an equation given in [30]. Actually, there are two effective resolution equations of the collimator diameter based on the imaging angle; perpendicular and parallel. When θ is 90^0, there is no difference between the results of the two equations [30].

$$d_{re-perpendicular} = \left(\left(d + \frac{ln2}{\mu}\, tan\frac{\alpha}{2} sin\theta\right)^2 - \left(\frac{ln2}{\mu}\right)^2 cos^2\theta\right)^{0.5} \tag{3.4}$$

where $d_{re\text{-}prependicular}$ is the effective diameter in the perpendicular direction to the pinhole collimator and source in one plane (along x-axis). The parameter ln2/μ is the path length through attenuating collimator material that gives attenuation by a factor of ln2, θ is the polar angle of the source (imaging angle). There is an effective diameter in the parallel direction to this plane [30] but has not been used in the current study for a comparison because θ is equal to 90^0.

In the perpendicular case, the effective pinhole collimator d_{eff}, as per the Accorsi resolution from Equation (3.5) and with θ equal to 90^0 [29] is

$$d_{eff} = d + \frac{ln2}{\mu}\left(tan\frac{\alpha}{2}\right) \quad (3.5)$$

For tungsten, μ is 3.64 mm^{-1} for 141keV energy [133]; therefore ln2/μ equates to 0.190 mm.

The factors that have an effect on the spatial resolution of a gamma camera are the pinhole diameter, magnification factor (detector-to-collimator distance *t* and collimator-to-source distance *h*), dimensions and materials of the detector, and energy of the radioactive source.

Figure 3.6 shows the comparison between theoretical spatial resolutions for three pinhole collimator diameters at different imaging distances. The spatial resolution improves with a decrease in diameter of the pinhole collimator while it deteriorates with increased imaging distance. The Accorsi resolution from the equation (3.5) is smaller (better) than the Metzler resolution from the equation (3.3) because the effective diameter from equation (3.3) depends on the imaging angle θ. Also the Accorsi resolution is better with small acceptance angle α, where the collimator with small α has a better (smaller) resolution than the collimator with large α.

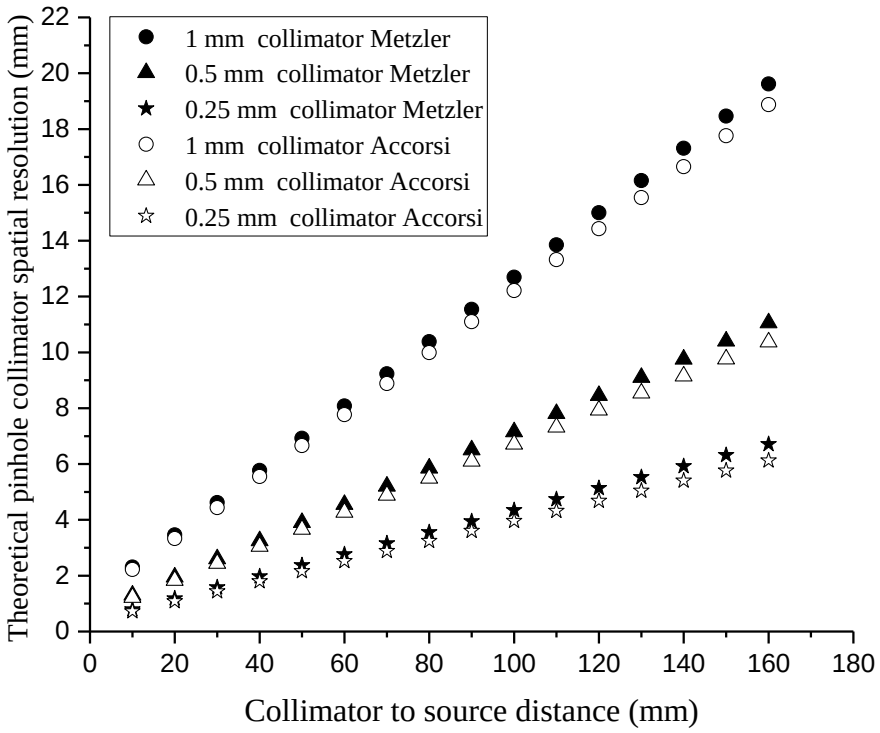

Figure 3.6: Comparison of the relationship between the theoretical collimator spatial resolution and distance from the centre of the pinhole collimator to source. The pinhole collimator diameters were 0.25 mm (star), 0.5 mm (triangle) and 1 mm (circle) diameter collimator. The black circle, triangle and star represent theoretical collimator spatial resolution using the Metzler resolution Equation (3.3). The white circle, triangle and star represent theoretical collimator spatial resolution using the theoretical Accorsi resolution Equation (3.5). Acceptance angle α is 60^0 and $\Theta = 90^0$.

3.5.2 **Collimator Sensitivity**

The sensitivity of the camera collimator is the number of photons that reach the detector per unit emission from a point source [134]. The count rate is basically dependent on the source-to-collimator distance, dimensions of the source, activity of the source and the detector material.

One of the most important contributions to overall sensitivity is the collimator sensitivity. Collimator sensitivity is the fraction of gamma rays emitted from the source which pass through the collimator to the detector. The collimator sensitivity is directly proportional to the square of the diameter of the pinhole collimator, whereas it is inversely proportional

to the square of the source-to-detector distance, h (equation (3.6). The theoretical collimator sensitivity, S, is given by [132].

$$S_{geom}(h,\theta) = \frac{d_{eff}^2 \sin^3\theta}{16h^2} \tag{3.6}$$

Effective pinhole diameter d_{eff} is defined by equation (3.3), θ is imaging angle.

Figure 3.7 shows the comparison between theoretical sensitivity for three diameter pinhole collimator diameters at different imaging distance. The sensitivity improves with an increase in the diameter of the pinhole collimator while it deteriorates with increased imaging distance. The sensitivity decreases to a quarter value when the distance from the camera is doubled. The acceptance angle α affects the collimator sensitivity, where the sensitivity of collimator with large α is a greater than the sensitivity of collimator with small α due to the higher number photons allowed to pass through it, as predicted by the Metzler sensitivity equation (3.3).

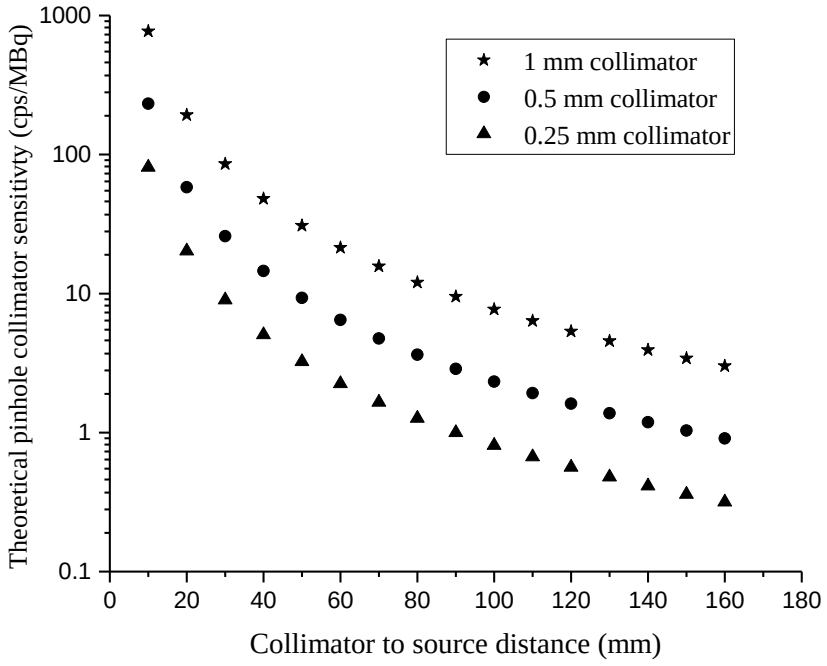

Figure 3.7: Relationship between the collimator sensitivity and the distance from the centre of the pinhole collimator to source, using Metzler sensitivity equation (3.5). The diameter of pinhole collimator was a 0.25 mm (triangle), 0.5 mm (circle) and 1 mm (star). Acceptance angle α is 60^0 and $\Theta = 90^0$.

3.6 Material and methods

The characteristics of the hybrid gamma camera detector were studied by Bugby et al. [124], and this study has proven useful in describing and comparing the HGC to other systems [39, 124].

There is a paper that describes detailed protocols for the evaluation of the performance parameters of the HGC [135]. However, in the current study, different diameters of pinhole collimator were used to investigate the sensitivity and spatial resolution, as they are important parameters in medical applications.

3.6.1 Experimental setup

The hybrid gamma camera (HGC) was fitted with a 0.25 mm, 0.5 mm or 1.0 mm diameter pinhole collimator to image a source containing ^{99m}Tc radioisotope solution ranging from 1.2 to 5 MBq, which was 5 mm in height and 2 mm in diameter. The source was positioned at various distances from the collimator face (*h)*, which varied between 40 mm and 180 mm in 10 mm increments. Images were produced from 3000 frames and the acquisition time was ~ 360 s. This experiment was designed to study the effect of pinhole collimator diameter on the spatial resolution and sensitivity of the gamma camera. Figure 3.8 shows a diagram of the experimental setup of this experiment.

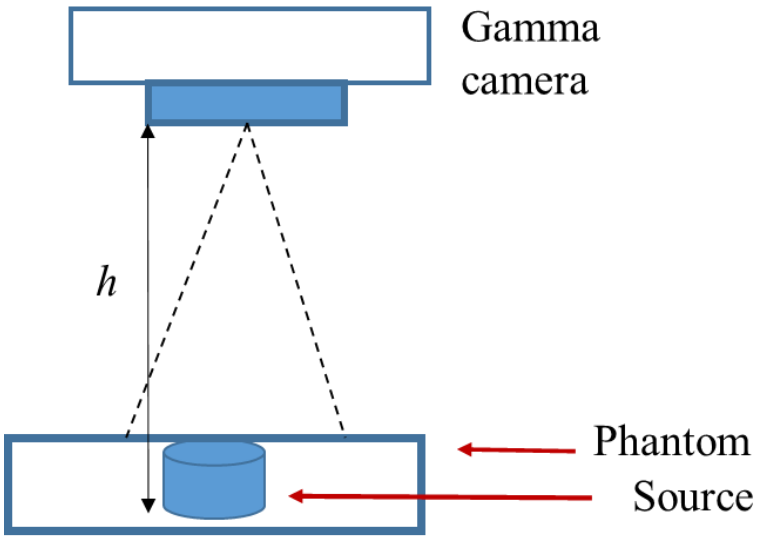

Figure 3.8: A diagram showing the experimental setup used to calculate the collimator spatial resolution and collimator sensitivity of the gamma camera.

3.6.1.1 **Collimator spatial resolution**

In this study, the collimator spatial resolution was calculated as the FWHM of a point source (2 mm in diameter) using the different pinhole collimator diameters fitted to the gamma camera. The images have been fitted with a Gaussian distribution [91].

The collimator spatial resolution represents the FWHM divided by magnification factor of each imaging distance. If the distance between the two images of the objects is less than the FWHM, the two images cannot distinguished on the detector, but if the distance was larger than the FWHM, there will be two clear images on the detector. Figure 3.9 demonstrates the collimator spatial resolution calculation process.

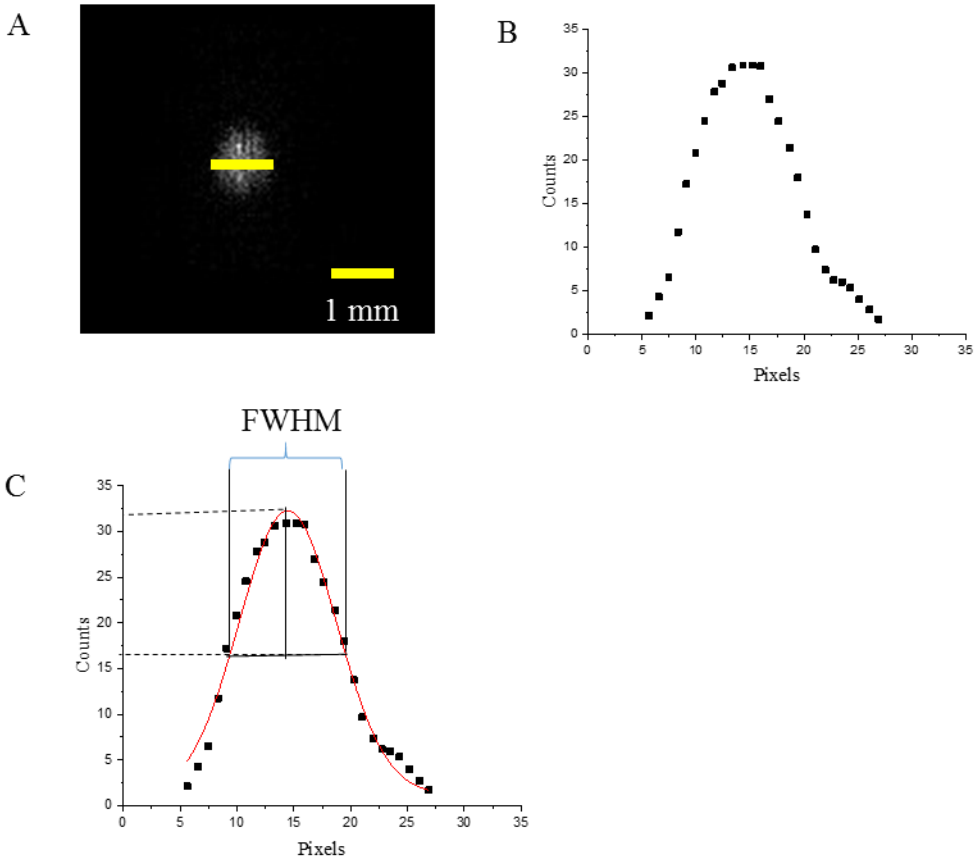

Figure 3.9: Graphs showing the collimator spatial resolution calculation process for a 1.2 MBq ^{99m}Tc source and a 1 mm diameter pinhole collimator. A) Final image of a ^{99m}Tc source at 60 mm distance. Total no. of frames was 3000 frames and the acquisition time was ~ 306 s. Yellow line indicates the profile taken that is displayed in (B). C) Fit of a Gaussian profile to the data in B, showing FWHM.

3.6.1.2 **Collimator sensitivity**

The sensitivity is the ratio of the recorded count rate (recorded counts divided by acquisition time) of the photons that were detected by detector to the activity of the radioisotope source. The recorded counts were calculated using equation (3.7) and by using the ImageJ software [136] locating a circle around the photon spot accumulated on the gamma image. The sensitivity was calculated using equation (3.8). Figure 3.10 demonstrates the collimator sensitivity calculation process using the ImageJ software [136].

$$Recorded\ counts\ = Area \times Mean \tag{3.7}$$

$$Sensitivity\ (\frac{cps}{MBq}) = \frac{recorded\ counts}{time\ (sec)} \times \frac{1}{source\ activity\ (MBq)} \tag{3.8}$$

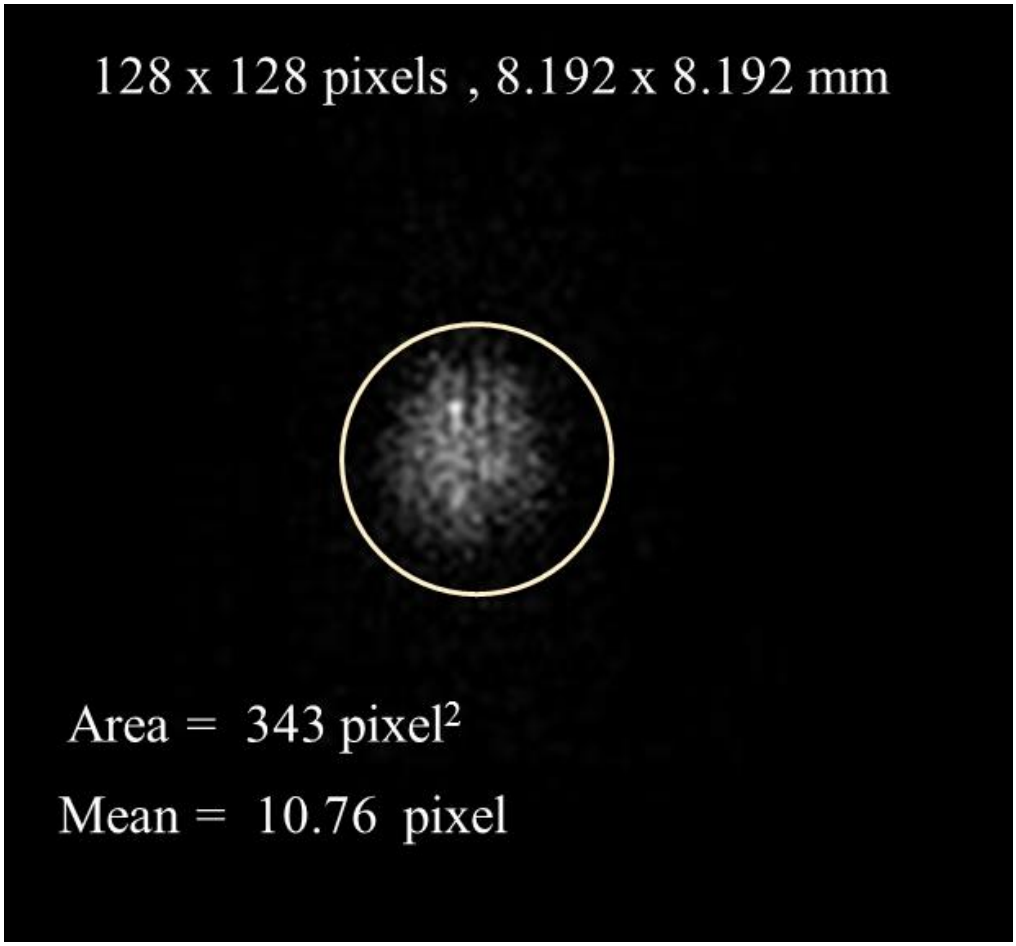

Figure 3.10: Graphs showing the gamma image for a 1.2 MBq ^{99m}Tc source and a 1 mm diameter pinhole collimator at a 60 mm distance from the 2 mm diameter source; total no. of frames was 3000 and the acquisition time was ~ 306 s. Area of the circle (Area of selection) and Mean (Number of photons detected within the selection area divided by the number of pixels) indicated in image.

3.7 Results

3.7.1 Collimator spatial resolution

Figure 3.11 shows the results obtained from the analysis of the relationship between collimator spatial resolutions (mm) versus the camera-to-source distance (mm) for different pinhole collimator diameters (0.25, 0.5 and 1 mm). The results indicate that the spatial resolution theoretical results were better than the experimental ones although they have the same trend. This is because of the error in the distance from collimator to source (± 2 mm), diameter of the pinhole collimator, and the profile taken, experimental. The fitting line equation for each the diameter of the pinhole collimator helps to determine collimator spatial resolution at any imaging distance.

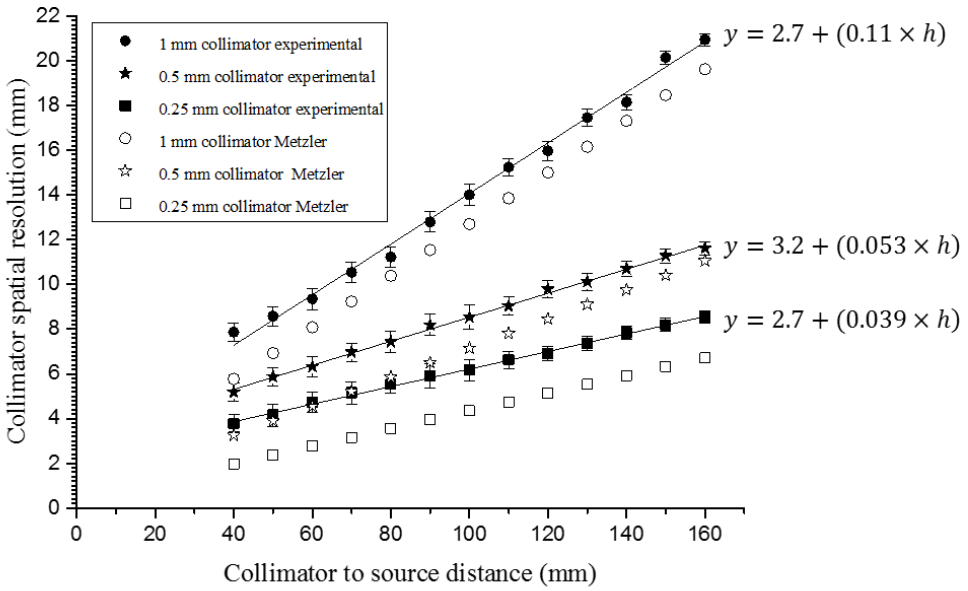

Figure 3.11: Comparison between theoretical and experimental results from the relationship between collimator spatial resolution and distance from the collimator face and source for different pinhole collimator diameters. Black circle, star and square represent a 1 mm, 0.5 and 0.25 mm pinhole collimator diameter experimentally. White circle, star and square represent a 1 mm, 0.5 and 0.25 mm pinhole collimator diameter theoretically from Equation (3.3).The experiment was conducted using a ^{99m}Tc source (2 mm diameter, and 1.2 and 5 MBq activity, and the acquisition time was ~ 306 s. The R^2 for all fitting lines of the experiment was equal 0.99.

3.7.2 **Collimator sensitivity**

Figure 3.12 shows the results acquired from the analysis of the relationship between collimator sensitivity and the camera-to-source distance (mm) for three pinhole collimator diameters (0.25, 0.5 and 1 mm), and the equations of fitted lines for each pinhole collimator. The results indicate that the theoretical results were better than the experimental ones although they have the same trend. This because of the error in circle area, diameter of the pinhole collimator and distance from collimator to source (±2 mm), experimental. The fitting line equation for each the diameter of the pinhole collimator could help to estimate collimator sensitivity at any imaging distance.

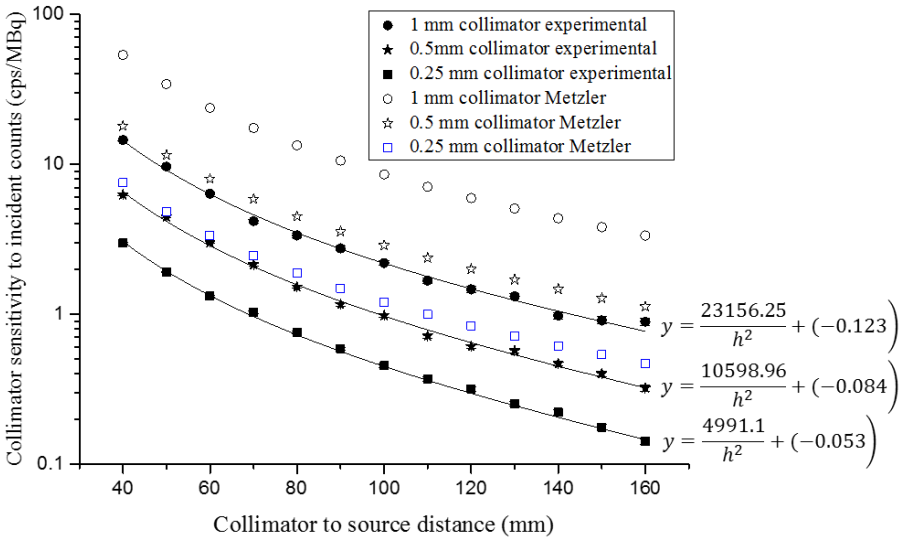

Figure 3.12: Graphs showing a comparison between theoretical and experimental results from the relationship between the collimator sensitivity to incident count (cps/MBq) and collimator to source distance (mm)) for three pinhole collimator. White circle, star and square represent a 1 mm, 0.5 and 0.25 mm pinhole collimator diameter (theoretical). Black circle, star and square represent a 1 mm, 0.5 and 0.25 mm pinhole collimator diameter (experimental).A ^{99m}Tc source (2 mm diameter and 1.2-5 MBq activity) and the acquisition time was ~ 360 s. Solid lines show the collimator sensitivity was used fit curves. The R^2 for all fitting lines of the experiment was equal to 0.995.

3.8 Scale factor

The HGC offers combined gamma and optical images. Because there is different between the dimensions of the gamma image and the optical image, the scale factor (*F*) can be applied to reduce the size of the optical image for matching with the gamma image. The combination of gamma and optical images depends on the arrangement of the optical component of the HGC (optical camera and mirror) in relation to the pinhole collimator [129]. This requires the mirror to put be below the aperture of the collimator at 45°.

In this work, the HGC is being used to determine the depth (in mm unit) of a source within the body.

3.8.1 Method

The hybrid gamma camera (HGC) was fitted with a 1mm diameter pinhole collimator (60^{o} acceptance angle) and used to image a ^{99m}Tc radioisotope solution (8 mm diameter, 6 mm thickness, 25 MBq activity). The camera-to-source distance was measured from the collimator face. This distance was varied from 80 mm to 240 mm in 20 mm increments. A single camera was used for imaging the two sources, the distance between them 20 mm, to obtain four images (two gamma and two optical). The acquisition time for each image was 240 seconds. An illustration of the experimental setup and the HGC is displayed in the Figure 3.13.

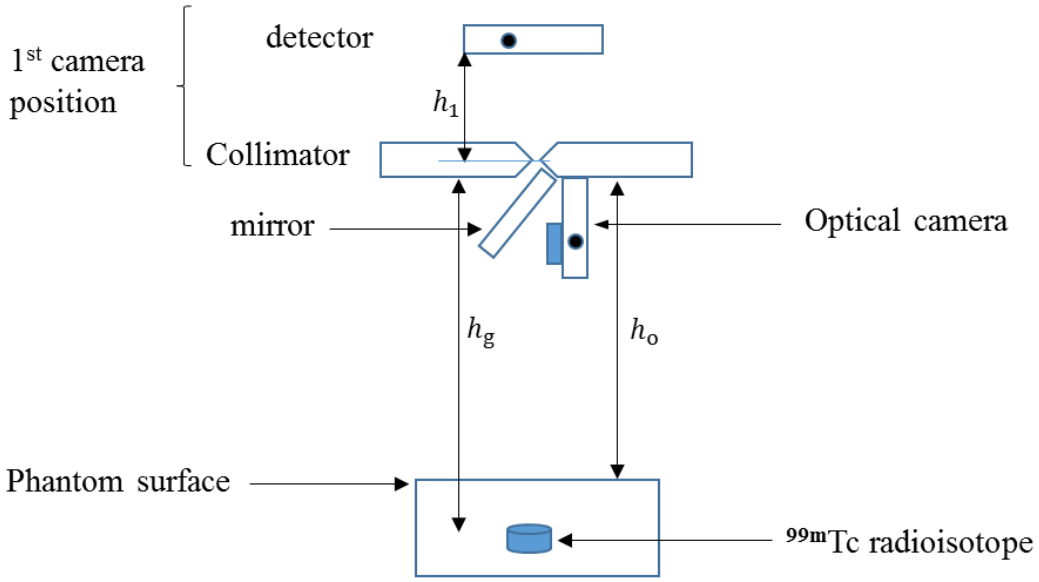

Figure 3.13: Schematic diagram showing the experimental setup used to calculate the scale factor.

A bespoke analysis program (written in IDL [137])[1] was used to image acquisition (gamma and optical), and a program written in IDL to determine the centre of the gamma and optical spots on the images, made by hand, at a number of imaging distances (see appendix B). The distance between the two centres of the optical / gamma images in pixel (*d*) was calculated and shown for reference in Figure 3.14.

[1] Previous work carried out by Oliver Blake, Adam Bark and others at the Bioimaging unit, University of Leicester.

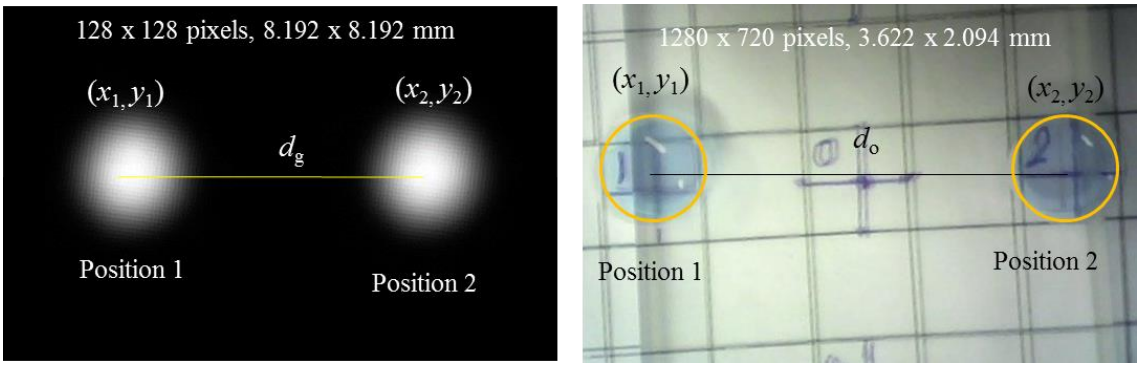

Figure 3.14: (A) Gamma image and (B) Optical image show two sites for radioactive sources below the hybrid gamma camera. The (X) represents physically the symbol on paper and the combined with source image optical images, and it was used to determine precisely the distance between two sources (two cameras).

The distance between the gamma spots is given by

$$d_g(\text{mm}) = d_g(\text{pixel}) \times 0.064 \tag{3.9}$$

where 0.064 mm is the pixel dimension of the gamma image from the charge-coupled device (CCD), and d_g (mm) and d_g (pixel) represent the distances between the two gamma images in millimetres and pixel units respectively. The distance from the collimator to the source is h_g (mm) and the distance between two positions of the source is D (mm).

$$\frac{d_g}{D} = \frac{t}{h_g}$$

$$h_g = \frac{t \times D}{d_g} \tag{3.10}$$

whereas for the optical images

$$d_o(\text{mm}) = d_o(\text{pixel}) \times 0.00283 \tag{3.11}$$

where 0.0028 mm is the pixel dimension of the optical detector, and do (mm) and d_o (pixel) represent the distance between the two optical images in millimetres and pixel units respectively. The distance from the collimator to the surface is h_o (mm).

$$\frac{d_o}{D} = \frac{t}{h_o} \tag{3.12}$$

$$h_o = \frac{t \times D}{d_o} \tag{3.13}$$

Therefore the scale factor is.

$$F = \frac{d_o\ (mm)}{d_g (mm)} \tag{3.14}$$

3.8.2 **Result**

F is a function of measured distance from the collimator of the gamma camera *h* (mm) as shown in Figure 3.15. The calculated distance from the collimator face to the radioactive source represents the largest source of error for the scaling factor, and is estimated to be less than 1.5% over 150 mm distance from collimator face. The results show that the mean of *F* for the HGC was 0.415 ± 0.004, which is used to make the correction when combining gamma and optical images. Figure 3.16 shows an example of a superimposed gamma and optical image

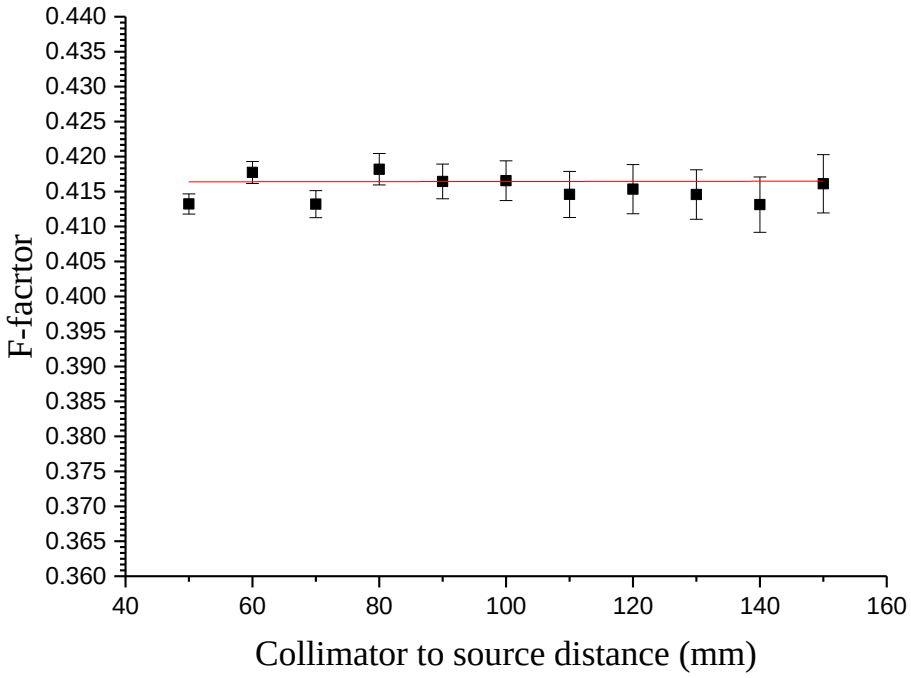

Figure 3.15: Scale factor as a function of the source distance from the pinhole collimator of the gamma camera *h*. The red line is a linear fit to the data with a *y*-intercept of 0.415.

Figure 3.16: Example of superimposed gamma and optical image from a ^{99m}Tc (25 MBq) source. Imaging distance from collimator face was 80 mm and the acquisition time was 204 second. Optical image (left), gamma image (middle) and combined gamma and optical image (right).

3.9 Detecting small distances between two sources

The HGC is being developed to support the estimation of the localization of radioisotope accumulation within the body and to distinguish between two nodes during surgery, such as lymph nodes (SLN). Therefore, two phantoms were used to simulate the medical scenario of nodes within the body at a small distance between them (the V-shaped phantom was designed during the study and the cross phantom was designed previously). These phantoms were used to evaluate the performance of the small field of view HGC imaging system in terms of the localisation of an accumulated radioisotope, to find the limit for resolving small distances between two point sources and to estimate the minimum separation between two cameras to detect nodes at one imaging distance.

3.9.1 Phantom manufacture

A V-shaped and cross phantom were designed and manufactured by the Space Research Centre, University of Leicester.

The phantoms have dimensions of 10 x10 cm with a thickness of 9 mm. The V-shape phantom has five pairs of holes in a V-shape, where the distances between pairs of holes from centre-to-centre horizontally were varied from 4 mm to 8 mm in 1 mm steps and the distance between each was 20 mm (Figure 3.17 A). The cross phantom has 21 holes in a cross shape, where the distance between each two holes was 5 mm, as shown in the Figure 3.17 B. Each hole has a diameter of 2 mm with a 3 mm depth. The phantoms have been manufactured from a Perspex plate (methyl methacrylate PMMA).

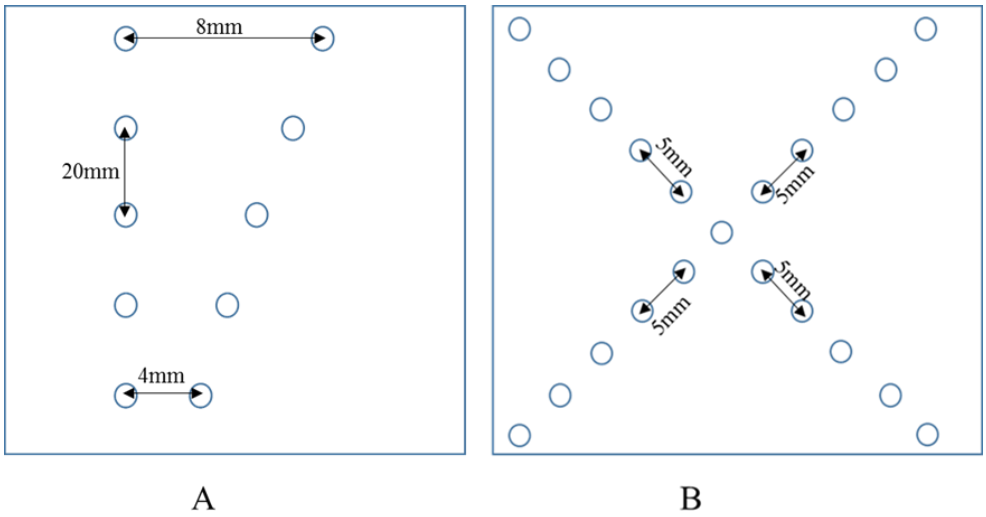

Figure 3.17: diagram of the V-Phantom showing 5 pairs of sources (A) and 21 sources in the cross phantom (B) with varying distances between the two sources.

3.9.2 Material and method

3.9.2.1 Experimental setup to distinguish between two sources using the V-phantom and the cross phantom

The hybrid gamma camera was fitted with either a 0.5 mm or 1 mm diameter pinhole collimator. About 5 MBq of ^{99m}Tc source solution was placed inside the holes of the phantoms. The distance between each pair was 4, 5, 6, 7 and 8 mm in the V-shape phantom and was 10, 15, 20, 25 and 30 mm from centre-to-centre in the cross phantom. The imaging distances from the camera to the source were measured from the collimator face, and ranged from 40 mm to 160 mm in 10 mm steps, with the acquisition time for each gamma image being four minutes. The HGC was held perpendicular to the phantom's surface. The imaging process was repeated for each distance.

3.9.2.2 Imaging procedures.

After the completion of the imaging procedures, ImageJ software [136] was used to process the gamma image in order to assess the ability of the HGC to detect the different distances between the two spots in images that were acquired from the HGC at the different imaging distances from the collimator face.

3.9.3 **Results**

The gamma images were acquired and analysed to show the ability of the HGC to distinguish between the two sources (gamma spots) when it was fitted with a 0.5 mm or a 1 mm diameter pinhole collimator at different imaging distances. As an example, Figure 3.18 demonstrates the two gamma spots from the four point sources, where the distances between the two sources were 7 mm or 8 mm at a 60 mm imaging distance.

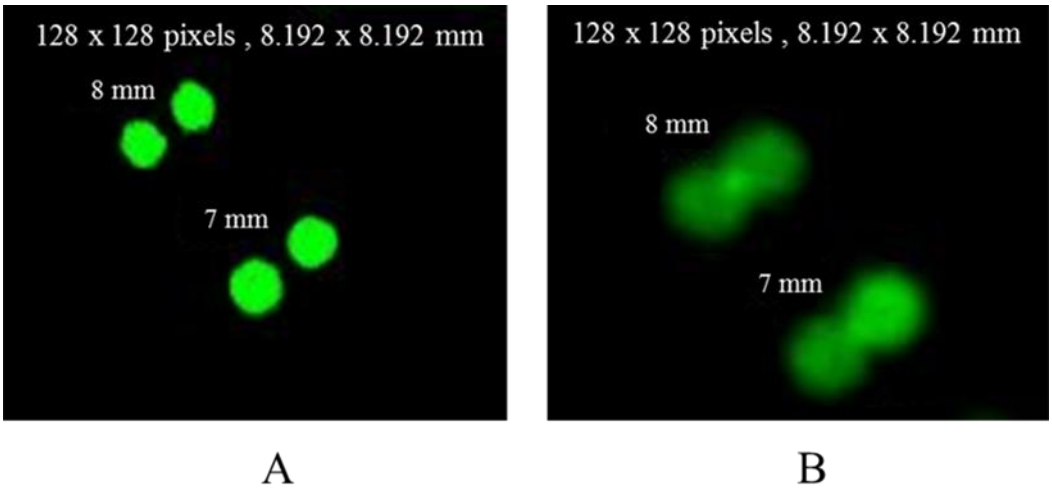

Figure 3.18: Gamma images showing two pairs of radioisotope sources in the V-phantom, where there were 8 mm and 7 mm distances between the first and second pairs, respectively. Gamma imaging used the (A) 0.5 mm and (B) 1 mm diameter pinhole collimator at a 60 mm collimator-to-source distance.

Table 3.1 shows the ability of the HGC to distinguish between two sources in V- shape phantom when the distances between them were 4, 5, 6, 7 and 8 mm over a range of the collimator-source distances conducted using a 0.5 mm or a 1 mm diameter pinhole collimator. The HGC fitted with 0.5 mm diameter pinhole collimator has the ability to detect the two sources when the distance between them is 4, 5 and 6 mm at 50 mm imaging distance, and has ability to distinguish between the two sources when the distance between them is 7 mm and 8 mm at 90 mm distance from collimator face. This is not true for the camera fitted with a 1 mm diameter

Table 3.1: Showing the distances between two sources (4, 5, 6, 7 and 8 mm) from the centre-to-centre in the V-phantom. The measured distances from the collimator to the source (mm) were from 40 mm to 160 mm. The symbol (||) represents clearly distinguished sources at a given distance from the source using HGC imaging with a 0.5 mm (A) and 1 mm (B) diameter pinhole collimator. The symbol (X) represents that the HGC was not able to distinguish between two nodes at a given distance (collimator-to-source).

	Distance between two nodes (mm)				
Imaging distance (mm)	4	5	6	7	8
40	||	||	||	||	||
50	||	||	||	||	||
60	X	||	||	||	||
70	X	||	||	||	||
80	X	||	||	||	||
90	X	X	X	||	||
100	X	X	X	X	X
110	X	X	X	X	X
120	X	X	X	X	X
130	X	X	X	X	X
140	X	X	X	X	X
150	X	X	X	X	X
160	X	X	X	X	X

A

	Distance between two nodes (mm)				
Imaging distance (mm)	4	5	6	7	8
40	X	X	||	||	||
50	X	X	X	||	||
60	X	X	X	X	X
70	X	X	X	X	X
80	X	X	X	X	X
90	X	X	X	X	X
100	X	X	X	X	X
110	X	X	X	X	X
120	X	X	X	X	X
130	X	X	X	X	X
140	X	X	X	X	X
150	X	X	X	X	X
160	X	X	X	X	X

B

From the distances between the two sources of 10, 15, 20, 25 and 30 mm in the cross phantom, the HGC fitted with a 0.5 mm or 1 mm diameter has the ability to distinguish between the two sources when the distances are 20 mm or more at all imaging distances from the collimator face, as detailed in Table 3.2. The results in this table relate to the results for collimator resolution that were shown in Figure 3.11.

Table 3.2: Illustration of the centre-to-centre distances between two sources (5, 10, 15, 20, 25 and 30 mm) in the cross phantom against distance measured from the collimator to the source (mm). The diameter of the source is 2 mm. The (II) represents clearly distinguished sources at a given distance from the source using HGC imaging with a 0.5 mm (A) and 1 mm (B) diameter pinhole collimator. The (X) represents that the HGC was not able to distinguish between two nodes at a given distance (collimator-to-source).

	Distance between two nodes (mm)				
Imaging distance (mm)	10	15	20	25	30
40	II	II	II	II	II
50	II	II	II	II	II
60	II	II	II	II	II
70	II	II	II	II	II
80	II	II	II	II	II
90	II	II	II	II	II
100	II	II	II	II	II
110	X	II	II	II	II
120	X	X	II	II	II
130	X	X	II	II	II
140	X	X	II	II	II
150	X	X	II	II	II
160	X	X	II	II	II

A

	Distance between two nodes (mm)				
Imaging distance (mm)	10	15	20	25	30
40	II	II	II	II	II
50	II	II	II	II	II
60	X	II	II	II	II
70	X	II	II	II	II
80	X	II	II	II	II
90	X	II	II	II	II
100	X	II	II	II	II
110	X	X	II	II	II
120	X	X	II	II	II
130	X	X	II	II	II
140	X	X	II	II	II
150	X	X	II	II	II
160	X	X	II	II	II

B

3.10 Discussion

This chapter described the HGC design and the effect of the pinhole collimator diameter on resolution and sensitivity of the camera.

Three pinhole collimator diameters (0.25 mm, 0.5 mm and 1 mm) were studied in terms of their collimator spatial resolution and collimator sensitivity. Although the behaviour of the experimental results of the spatial resolution and sensitivity are consistent with the expected theoretical results in terms of pinhole collimator diameter and imaging distances, the theoretical spatial resolution results were better than experimental results [29, 30]. The theoretical results represent collimator resolution and collimator sensitivity while the experimental results represent the resolution and sensitivity of both together collimator and detector.

The error sources in the calculation of the collimator spatial resolution and collimator sensitivity were the distance from collimator face, the determination of the gamma spot circle area and the activity of the source. For example, when the camera was fitted with a 1 mm diameter pinhole collimator and placed at 60 mm away from a source, the count per second (cps) was around 176 and 8 when the activity was 27 MBq and 1.2 MBq, respectively. But when the camera was placed at 120 mm from the source, the cps was approximately 41 and 2 when the activity was 27 MBq and 1.2 MBq respectively. So the activity of the radioisotope source and the imaging distance have an impact on the creation of the image on the detector, which affects the calculation of collimator spatial resolution. This affects the determination of the FWHM of the image, which leads to error in calculating the spatial resolution. The imaging distance effects on the number of photons detected by detector thus leads to error in calculation of the sensitivity.

The scale factor (F) was calculated and used to correct the difference in dimensions between the gamma and optical images before combining them. One of the main error sources was the determination of the centre of gamma and optical spots, which leads to error in the calculated distance between two images (gamma or optical) as well as the calculated distance from collimator to source/surface, and the distance between two cameras (see more details in an appendix A).

The distinction between two images on the detector depends on the spatial resolution of the collimator, which is dependent on the diameter of the pinhole collimator and distance

from collimator to source. The V-shape and cross phantoms were used to assess the ability of the HGC to distinguish between two sources. The HGC fitted with 0.5 mm or 1 mm collimator diameter has the ability to distinguish 20 mm or more distance between two sources all imaging distances investigated. This could explain how use of two cameras with a distance of 20 mm or more between them has the ability to detect the source at all imaging distances investigated, as explained in calculation of the scale factor.

3.11 **Conclusions**

In this chapter, the HGC has been described. Three pinhole collimators of 0.25 mm, 0.5 mm and 1.0 mm diameters were used to calculate the collimator spatial resolution and collimator sensitivity at different imaging distances from collimator face and the results were compared to theory. These are influenced by several parameters such as pinhole collimator diameter and magnification factor (detector-to-collimator distance t and collimator-to-source distance h) [138].

Collimator spatial resolution improves with a decrease in diameter of the pinhole collimator while collimator sensitivity improves with an increase in pinhole collimator diameter. They both deteriorate with increased imaging distance. The theoretical results were better than the experimentally, this being due to an errors in the distance from collimator (± 2 mm), diameter of the pinhole collimator, determination the circle around the gamma spot and profile taken of gamma spot.

The F factor was calculated to ensure the appropriate combination of gamma and optical images because there is a difference between the dimensions of gamma and optical images.

One of the more significant findings to emerge from the cross and V-shape phantoms study was the ability of the HGC to detect the small distance between two sources of 2 mm diameter, which was approximately 4 mm from centre to centre. The second finding was that 20 mm separation between two cameras could be the preferred distance between two cameras to detect nodes at all imaging distances and to obtain smallest and lighter house has two cameras. Finally, the hybrid gamma camera imaging system appears to represent a new imaging system with promising gamma detection. This technique could

help surgeons to determine the location of a number of radiopharmaceutical distributions of nodes during an operation.

Chapter 4: **Concept of two hybrid cameras for depth estimation**

4.1 **Introduction**

To enhance the localization of radiolabelled tissues or nodes for preoperative or intraoperative procedures, an estimation of the depth of the radioisotope source accumulated within the body would represent a useful addition to current clinical procedures. Lees et al. have described the HGC, which is a gamma and optical imaging method combined in a single system [17]. The hybrid gamma camera (HGC) can be adapted to estimate the depth of radioisotope uptake within a patient [18].

There are many approaches to estimating the depth of SLNs within the body preoperatively and intraoperatively, and each approach has different strengths and weaknesses. In all approaches, however, the skin is marked at the injection site(s) using conventional marking techniques. For example, a CT scan is an anatomical imaging technique and it can be used to determine the depth of a tumour within the body such as a stomach cancer [139], and PET and SPECT scans are suitable for the determination of the depth of a tumour due to their high sensitivity and good spatial resolution [52].

Intraoperative imaging using freehand SPECT, which consists of gamma probes coupled to surgical navigation systems, and emission tomography algorithms [140], provides a 3D anatomic and gamma image of the targeted lymph nodes in real-time and could facilitate sentinel lymph node biopsy (SLNB) [141]. The main advantage of this approach is to provide accurate information about the depth of the lymph node in real time, facilitating SLN detection [142]. The freehand SPECT technique is used to image SLN for head and neck cancers [143] and for breast cancer [144, 145]. Mathelin et al. reported that during surgery, SLNs could be localized using both the mini γ-camera and a γ-probe, and where a ruler (Aspen Surgical) was used to measure the depth of all SLNs before excision [25]. The localization of SLNs and a depth estimation were determined from the data using the width of the image of cumulative radioisotope source profiles within the breast, where the width is dependent on the distance between the SLN and the collimator face. The depth was estimated within an error of 5 mm [146]. The main limitation to this

approach was when the activity accumulated in the SLN was below 2 kBq, which led to difficulty in gaining a good depth estimation due to the poor signal-to-noise ratio [25].

In near-infrared fluorescence detection (NIR), fluorescent light has the ability to penetrate human tissue to a depth of 15–20 mm, indicating the maximum useful depth of this approach [147]. Although Fluorescence Detection (FLD) has a good ability to provide images showing the path of the contrast media and the location of associated accumulation, it is necessary to use a complementary tool to determine the depth profile because of the aforementioned depth limitation of FLD technology [148]. To overcome this limitation, NIR fluorescence combined with radioactive tracers are currently used for SLN mapping in head and neck melanoma [149, 150].

Lees et al. have reported that the use of two HGCs simultaneously can provide the ability to estimate the depth of the distribution of radioisotopes within the body [17]. Thus this chapter describes three models of the hybrid gamma camera (HGC) system that have been proposed for depth estimation. The performance of the HGC was investigated for three arrangements of the two cameras, which can be described as perpendicular, divergent and convergent. Each arrangement of the two cameras depends on a specific number of parameters, and the effects of these parameters on each of the arrangements has been investigated.

The aim of this chapter is to study these three camera arrangements and to select the best configuration for calculating the distance between the two spots produced by the gamma source on the detectors and to assess which arrangement, and under which conditions, lead to the most accurate estimation of depth.

4.2 Source image position on the detector

Figure 4.1 shows a schematic of a gamma camera whose pinhole collimator has a 60^0 acceptance angle; the source is placed at a distance, *x*, from the centreline of the pinhole collimator.

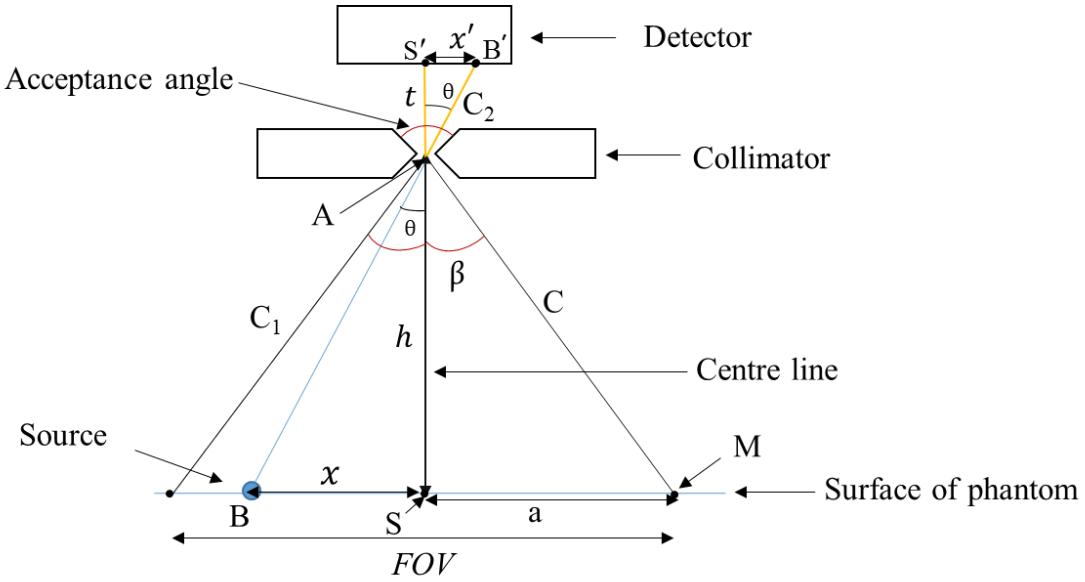

Figure 4.1: Schematic of the detector used to define the magnification and showing the acceptance angle (60^0) of the pinhole collimator and the source within the field of view (FOV) of a single camera.

When the radioisotope source is within the field of view (FOV) (see the next section), gamma-ray photons that pass through the pinhole collimator will be detected by the camera and create an image of the source on the detector.

The position of the image on the detector is defined as the position of the greatest accumulation of photons reaching the camera detector as emitted from radioisotope source. The position of the source image on the gamma camera detector, x', depends on the gamma camera's magnification factor, which is itself dependent on the distance between the pinhole collimator and detector, t, and the pinhole collimator to source distance, h, see Equation (4.1).

From the triangles *A B S* and *A B′ S′,* the position of the source image on the detector is given by:

$$x' = x\frac{t}{h} \tag{4.1}$$

where t and x are constant, and the source image on the detector depends on h; increasing h leads to a smaller value of x', while $\frac{t}{h}$ represents the magnification factor.

4.3 Calculating the distance between the two gamma spots on the detectors.

The calculation of the distance between the two gamma spots on the detectors requires a new arrangement. Therefore, the new arrangements are considering two cameras in a specific arrangement.

Equations to calculate the difference between the two positions of source images on the detector were derived, which are dependent on the three different arrangements of the cameras (perpendicular, divergence and convergence) and the position of the source.

4.3.1 Perpendicular arrangement.

A perpendicular camera arrangement is defined as the two cameras being placed side-by-side horizontally with a specific distance between them (Figure 4.2). In this arrangement, the source image position on the detector depends on the following parameters: the pinhole collimator to detector distance, *t*, the imaging distance (the distance from the pinhole collimator to the source), *h*, and the distance between the centres of the two pinhole collimators, *D*. Figure 4.2 shows two cameras perpendicular to the source, where the source distance from the centreline of the two cameras is *x*, and *D*/2 is the distance from the centre of the collimator to the centreline of the two cameras. The horizontal distances from the centre of the collimator to the source position are x_1 and x_2 for the first and second cameras respectively, and the position of the source images on the first and second detectors are x_1' and x_2' respectively. The acceptance angle (θ) of both pinhole collimators is 60^0.

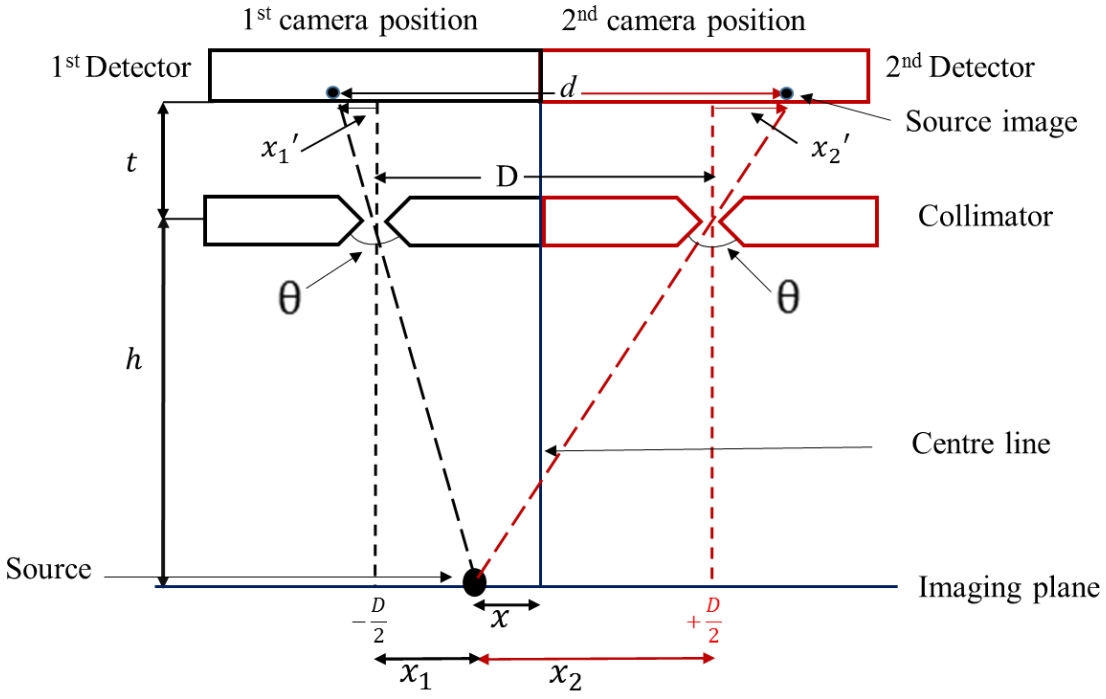

Figure 4.2: Schematic of two cameras in a perpendicular arrangement. This diagram was used to derive a generalised equation to calculate the difference between the positions of the source images on the two detectors.

4.3.1.1 **Position of the source image on the detectors**

Depending on equation (4.1), the position of the image on the first detector (x_1') is equal to:

$$x_1' = x_1 \times \frac{t}{h}$$

$$x_1 = -\frac{D}{2} - x \tag{4.2}$$

$$x_1' = \left(-\frac{D}{2} - x\right) \times \frac{t}{h} \tag{4.3}$$

Similarly, for the second detector:

$$x_2' = \left(\frac{D}{2} - x\right) \times \frac{t}{h} \tag{4.4}$$

4.3.1.2 **Calculating the separation between two source image positions**

The distance between two source image positions on the detectors, *d*, is:

$$d = x_2' - x_1' \tag{4.5}$$

$$d = \left(\left(-\frac{D}{2} - x\right) \times \frac{t}{h}\right) - \left(\left(\frac{D}{2} - x\right) \times \frac{t}{h}\right) \tag{4.6}$$

which simplifies to:

$$d = \frac{t}{h} \times D \tag{4.7}$$

As a result, *d* depends only on cameras' separation, *D*, and source distance from the collimator face, *h*.

When *t* is constant, the distance between two spots on the detectors, *d*, is inversely proportional to *h* and directly proportional to *D*.

For the HGC, the dimension of the CCD imaging area is 8 mm × 8 mm, therefore the maximum distance between two gamma spots on the detector is < 8 mm. If the distance is greater than 8 mm, at least one of the images will not be imaged on the CCD, see Figure 4.3.

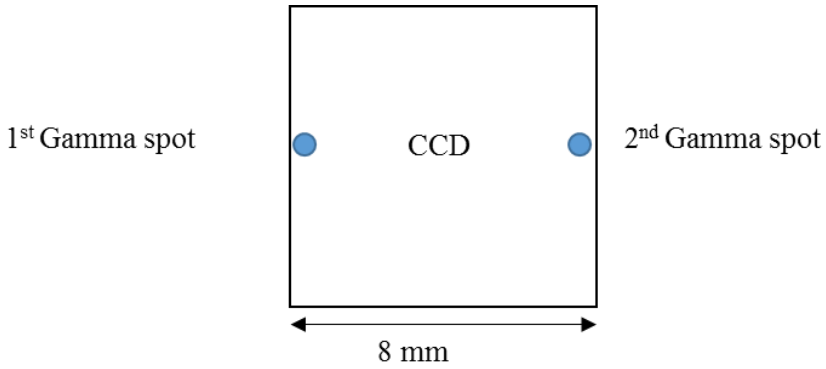

Figure 4.3: Relationship between the dimensions of the CCD and the maximum distance between the two positions of the gamma spots.

4.3.1.3 **Theoretical validation**

In a perpendicular camera arrangement, the distance between two gamma spots on the detectors depends on the imaging distance and the distance between the two cameras. Three distances between two cameras, *D*, of 20, 30, and 40 mm were studied with the distance between detector and collimator at 10 mm. The source was placed at three distances, *x*, of 0, 5 and 10 mm from the centreline of the two cameras for each distance between the two cameras. The results indicated that the distance between two images on the detectors, *d*, decreases with the imaging distance from the collimator, *h*, and the distance between two cameras, *D*, but there is no effect of the source position from the centreline, as shown in Figure 4.4. Due to the detector area (8 mm x 8 mm), one of the images or both images will be outside the detector area when the imaging distance is less than 26 mm, 38 mm and 50 mm from collimator face at 20, 30 and 40 mm distance between the two cameras, respectively.

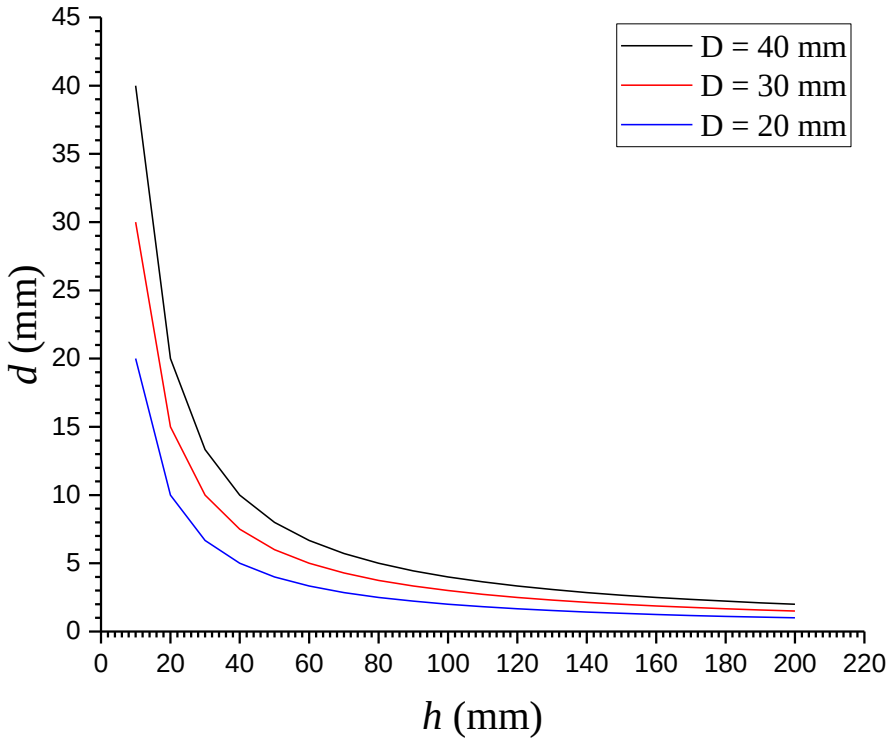

Figure 4.4: Theoretical relationship between the distance between two source images on the detector, *d*, and the imaging distance, *h* (mm) in a perpendicular arrangement. The distances between the two cameras were 20, 30 and 40 mm.

4.3.1.4 **Experimental validation**

Experimentally, the hybrid gamma cameras were each fitted with 0.5 mm diameter pinhole collimators (60^0 acceptance angle). A ^{57}Co radioisotope source (8 mm diameter and a height of 5 mm, 50 MBq activity) was positioned in the phantom, which has one hole. The acquisition time for each image was three minutes. A single camera was used for imaging the source, which was then displaced horizontally by D = 30 mm (the distance between the two centres of the pinhole collimators) to obtain a second set of images (both optical and gamma). The imaging distance, *h*, from the camera to the source was measured from the centre of the pinhole collimator face to the horizontal plane containing the source, which was adjusted between 80 mm and 240 mm in 20 mm steps. The HGC was perpendicular to the phantom's surface, as shown in Figure 4.5.

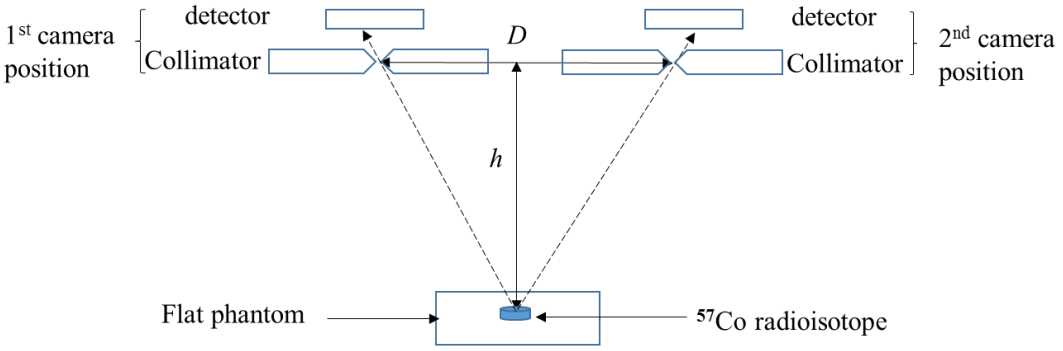

Figure 4.5: A schematic of the experiment to investigate the perpendicular camera arrangement.

Figure 4.6 shows the comparison between experimental and theoretical results for the separation between the two gamma spots on the detectors versus the imaging distance, *h*, in a perpendicular camera arrangement with a camera separation, *D*, of 30 mm. As an example, at 80 mm from the collimator face the distance between two images on the detector was 3.58 ± 0.01 mm experimentally and 3.75 mm theoretically, while the distance between two images was 1.246 ± 0.01 and 1.25 mm experimentally and theoretically, respectively, at a distance of 240 mm. The results demonstrate that the difference between theoretical and experimental results for the distance between two gamma spots on the detector were approximately 2%. The difference between experimental and theoretical results is related to the error in estimating the centre of the gamma spot, which was ± 0.1 pixels, the distance between two cameras, which was ± 2 mm, and the distance from the collimator face to the source, which was ± 2 mm.

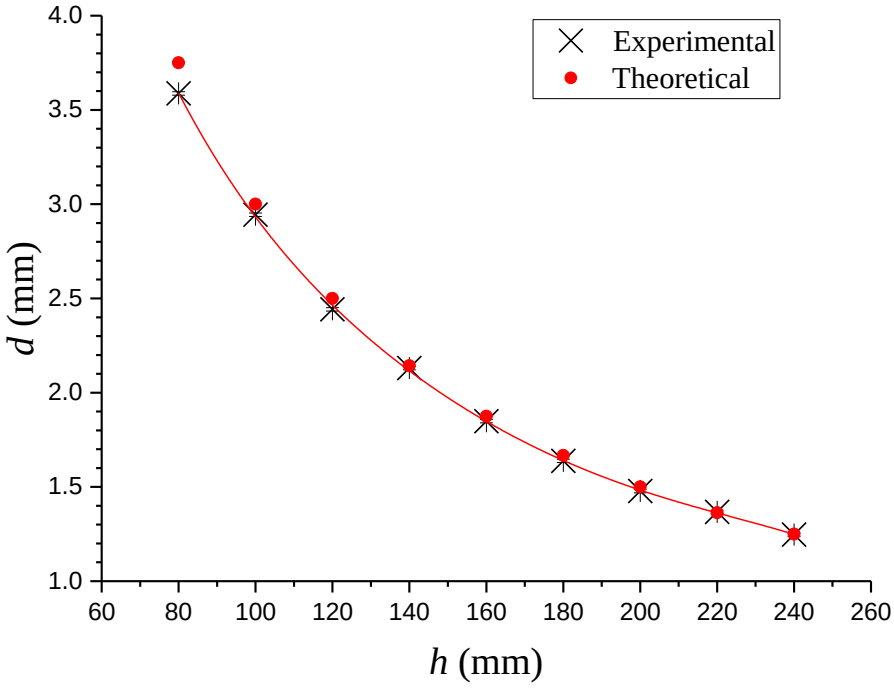

Figure 4.6: Comparison between the experimental and theoretical results for the separation between the two gamma spots from the source on the detector versus the imaging distances *h* in a perpendicular arrangement. The pinhole collimator-to-detector distance was t = 10 mm, and the distance between the two centres of the pinhole collimators was D = 30 mm. The fitted line to the experimental results was a polynomial of order 5, and R^2 was 0.999.

4.4 Calculating the distance between two spots on the detector using two cameras in an angled arrangement.

An angled camera arrangement (divergent or convergent) is defined as the two cameras being placed side-by-side horizontally with a specific distance between them and with both at a specific angle to the *y*-axis of each camera, where the two detectors are either angled inwards or outwards. In an angled camera arrangement, the position of the spots on the detector depends on the camera angle, θ, relative to the *y*-axis, the distance between the centres of the two pinhole collimators, D, the distance from the pinhole collimator to the source, h, the collimator-to-detector distance, t, and source displacement from the centreline of the cameras, f. An example of an angled camera arrangement is shown in Figure 4.7, which illustrates two cameras in an angled configuration where x_1 and

x_2 represent the positions of the source on the first and second camera planes, respectively, and x_1' and x_2' are the corresponding positions of the source image on the first and second camera detectors, respectively. The distances from the centre of the pinhole collimator to the imaging plane for the first and second cameras are L_1 and L_2, respectively.

In the divergent and convergent arrangements, the distance between the two images depends on their position relative to the centre of the detector; if the position is to the right of the centre of the detector, the value is considered positive, but if the position is to the left of the centre of the detector, the value is considered negative. Two angles control the positions of the images on the detectors; the first is the camera angle, θ, of the two cameras relative to the centreline, whilst the second is the angle of incidence of the radiation from the pinhole collimator to the detector, defined as ϕ and α in the first and second cameras, respectively. The positions of the spots relative to the centre of the detector changes when the imaging and incidence angles change.

4.4.1 Angled cameras (divergence arrangement)

A calculation of the distance between the two images on the detector when the cameras are in a divergent arrangement depends on an equation derived from the parameters described in the previous section, see Figure 4.7. This figure shows the normal line from the two cameras diverges from the centreline, which is between the two cameras, with increasing distance between the camera and the imaging plane that is itself dependent on the distance between the two cameras and the imaging angle.

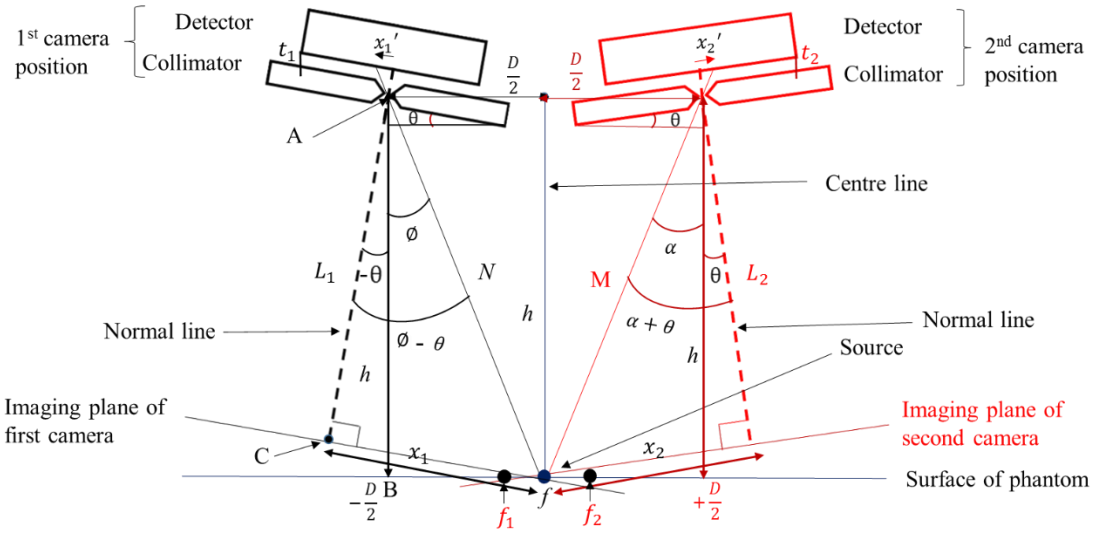

Figure 4.7: Schematic of two cameras (divergence arrangement) with imaging angles, θ, to y-axis. This schematic was used to derive an equation giving the distance between the two images on the detectors where the two image positions are on the opposite sides of the relevant detectors.

4.4.1.1 **Position of source image on the first detector**

From the triangle A B *f*,

$$\tan \emptyset = \frac{-\frac{D}{2} - f}{h} \tag{4.8}$$

From the triangle A C *f*,

$$x_1 = N \sin(\emptyset - \theta) \tag{4.9}$$

$$L_1 = N \cos(\emptyset - \theta) \tag{4.10}$$

According to equation (4.1), the position of the image on the first detector (x_1') is equal to:

$$x_1{}' = \frac{t_1}{L_1} \times x_1 \tag{4.11}$$

Therefore:

$$x_1{}' = t_1 \times \frac{N \times \sin(\emptyset - \theta)}{N \times \cos(\emptyset - \theta)} \tag{4.12}$$

$$x_1{}' = t_1 \times \tan(\emptyset - \theta) \tag{4.13}$$

$$x_1{}' = t_1 \times \frac{tan\emptyset - tan\theta}{1 + tan\theta\ tan\emptyset} \tag{4.14}$$

$$x_1{}' = t_1 \times \frac{-\frac{D}{2} - f}{1 + \frac{-\frac{D}{2} - f}{h} \times tan\theta} \tag{4.15}$$

Similarly, for the second detector:

$$x_2{}' = t_2 \times \frac{tan\theta + \frac{\frac{D}{2} - f}{h}}{1 - \frac{\frac{D}{2} - f}{h} \times tan\theta} \tag{4.16}$$

4.4.1.2 **Calculating the separation between two image positions**

Therefore, the distance between the two image positions on detector, *d*, in this arrangement is given by:

$$d = x_1' - x_2' \tag{4.17}$$

$$d = \left(t_1 \times \frac{-\frac{D}{2} - f}{\frac{h}{1 - \frac{-\frac{D}{2} - f}{h} \times tan\theta}} + tan\theta \right) - \left(t_2 \times \frac{tan\theta + \frac{\frac{D}{2} - f}{h}}{1 - \frac{\frac{D}{2} - f}{h} \times tan\theta} \right)$$

With $t = t_1 = t_2$:

$$d = t \times \left(\frac{-\frac{D}{2} - f}{\frac{h}{1 - \frac{-\frac{D}{2} - f}{h} \times tan\theta}} + tan\theta - \frac{tan\theta + \frac{\frac{D}{2} - f}{h}}{1 - \frac{\frac{D}{2} - f}{h} \times tan\theta} \right) \tag{4.18}$$

4.4.1.3 **Theoretical validation**

The distance between the two gamma images on the detector in a divergent camera arrangement depends on parameters, *D*, *f*, *h* and θ. The effect of these factors on the distance between the two images on the detector was studied. For example, the camera angles were varied from 8^0 to 20^0 in 2^0 steps (Figure 4.8). The separations between the two cameras, *D*, were varied from 26 to 32 mm in 2 mm steps (Figure 4.9), and the source positions from the centreline of the two cameras, *f*, were varied from 0 to 5 mm in 1 mm steps (Figure 4.10) for different imaging distances, *h*, while the pinhole collimator-to-detector distance *t* was 10 mm. The calculated distance between the two spots on the detector is *d*.

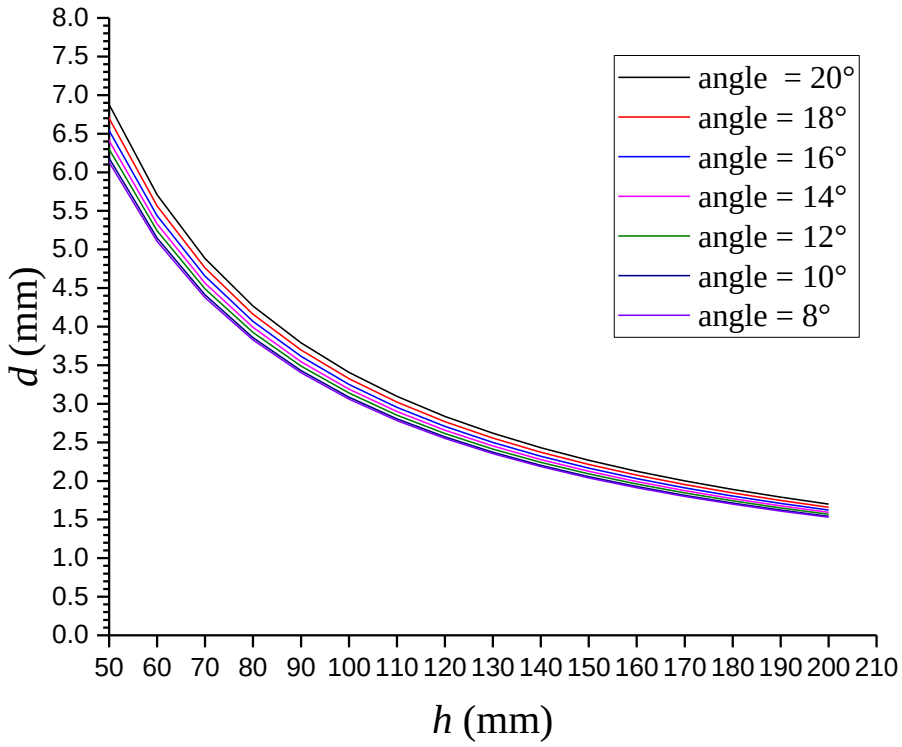

Figure 4.8: Theoretical relationship between the distance between the two gamma source images on the detector, *d*, and the imaging distance, *h*, at different camera angles in a divergent camera arrangement. The distance between the two cameras is 30 mm.

Figure 4.8 shows the relationship between *d* and *h* at different camera angles from 8^0 to 20^0, *D* was 30 mm. The results indicate that at 50 mm distance from the camera face, the distance between two images on the detector at 10^0 camera angle is less than the distance between two images at 16^0 and 20^0 by approximately 0.3 mm and 0.6 mm respectively. At 150 mm from the camera, the distance between the two images on the detector at 10^0 is less than the distance between two images at 16^0 and 20^0 by approximately 0.1 mm and 0.2 mm respectively.

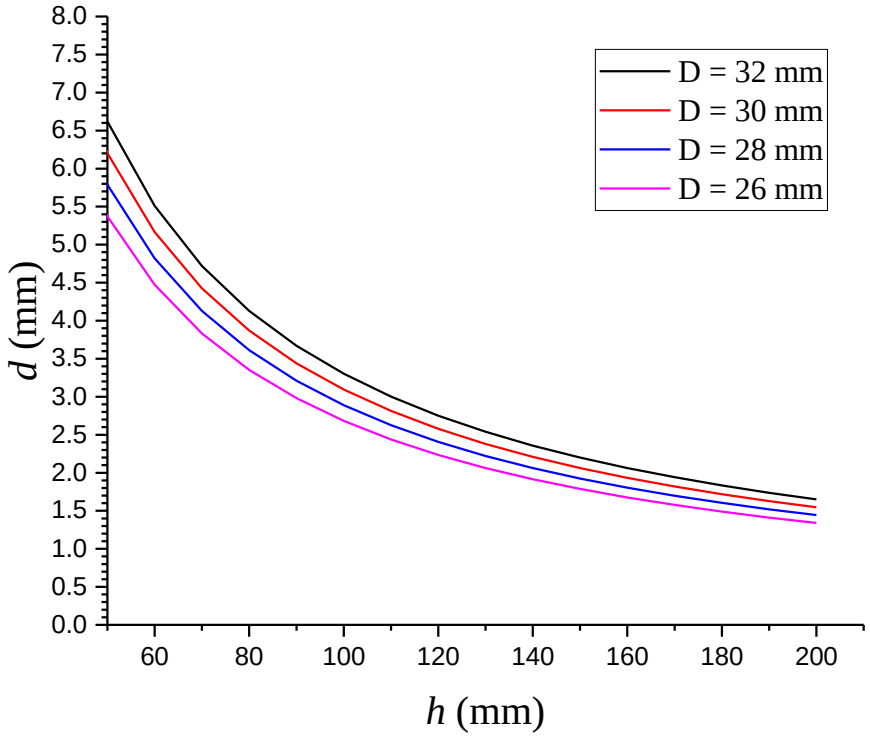

Figure 4.9: Theoretical relationship between the distance between the two gamma source images on the detector, *d*, and the imaging distance, *h*, at different distances between the two cameras. The camera angle is 10^{o} in a divergent camera arrangement.

Figure 4.9 shows the relationship between the distance between the two images on the detector and the distance from the collimator face at different distances between the two cameras. The camera angle is 10^{0}. At 30 mm distance between the two cameras, the results indicate that at 50 mm and 150 mm distance from the camera, the distance between the two images on the detector is greater by 13% and 6% when *D* is 26 and 28 mm, and less by 6% when *D* is 32 mm.

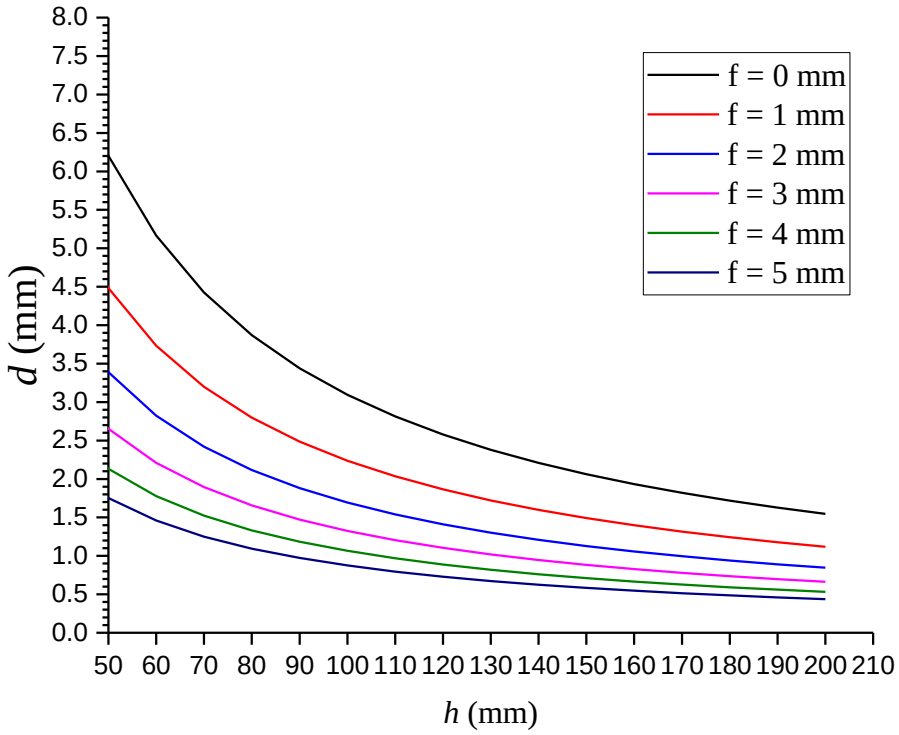

Figure 4.10: Theoretical relationship between the distance between the two gamma source images on the detector, *d*, and the imaging distance, *h*, at different distances from the centreline of the cameras. The camera angle is 10^{o} and the distance between the two cameras is 30 mm in a divergent camera arrangement.

Figure 4.10 shows the theoretical result of the relationship between *d* and *h* at different distances from the centreline of the two cameras. The camera angle is 10^{0} and there is 30 mm distance between the two cameras. At 0 mm from the centreline of the two cameras, the results indicate that at 50 mm and 150 mm from the camera face, the distance between the two images on the detector was greater by 45% and 71% when the source position is at 2 mm and 5 mm from the centreline of the two cameras respectively.

The theoretical validation of the divergent camera arrangement shows that the distance between the two images on the detector is increasing with the camera angle, θ, distance between two cameras, *D*, and distance from the centre line, *f*, and decreasing with the imaging distances, *h*.

4.4.1.4 **Experimental validation**

Experimentally, the hybrid gamma camera was fitted with a 0.5 mm diameter pinhole collimator (60^0 acceptance angle). A ^{57}Co radioisotope source (8 mm diameter and a height of 5 mm, 50 MBq activity) was positioned in the flat phantom. The acquisition time for each gamma image was three minutes. A single camera was used for imaging the source at a 10^o imaging angle, and was then was displaced horizontally by a distance, *D*, of 30 mm (the distance between the two centres of the pinhole collimators) and rotated to a -10^o imaging angle in a divergent camera arrangement to obtain a second set of images (both optical and gamma). The imaging distances, *h*, from the camera to the source were measured from the centre of the pinhole collimator face and ranged from 70 mm to 240 mm in 10 mm steps as shown Figure 4.11.

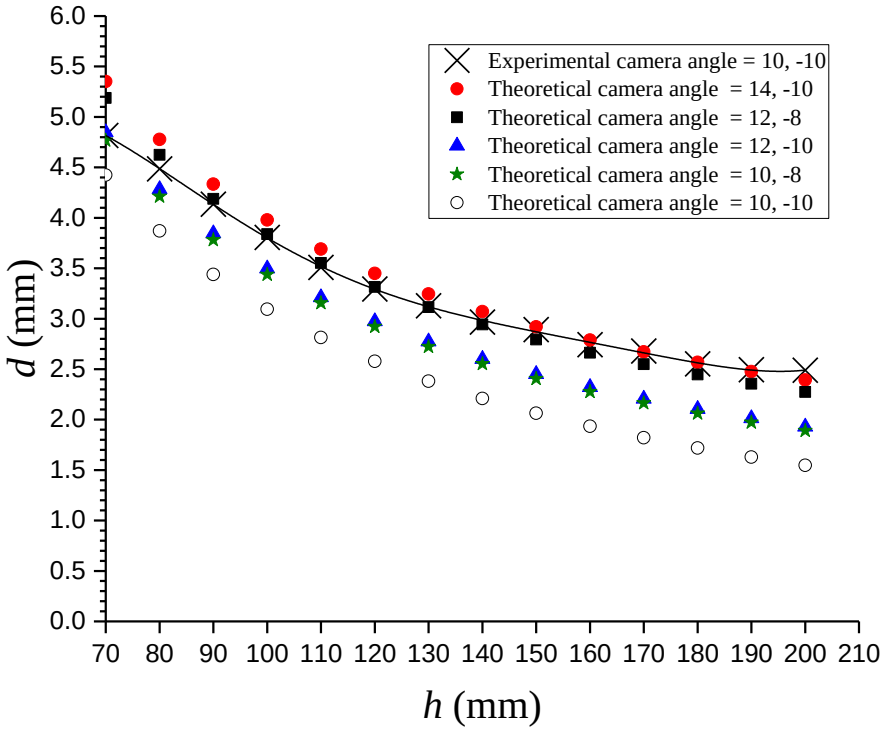

Figure 4.11: Comparison between the theoretically and experimentally determined distances between the two gamma source images on the detector versus the imaging distance, *h*, at a 10^0 camera angle in a divergent camera arrangement. The pinhole collimator-to-detector distance is t = 10 mm, whilst the distance between the two centres of the pinhole collimators is D = 30 mm. The fitted line to the experimental result was a polynomial of order 5, and R^2 was 0.999.

Figure 4.11 shows a comparison between experimentally and theoretically derived results for the separation between the two spots on the detector versus the imaging distances, *h*, at 10° camera angle experimentally and at different camera angles theoretically in a divergence camera arrangement. The theoretical and experimental results of the divergent camera arrangement have the same trend, as *d* decreases with increasing imaging distance, *h*. The best agreement between the theoretical and experimental results was for 12^0, -8^0 and 14^0,-10^0 camera angles. This shows the difficulty in setting the angles which can introduce an error in the experimental results. Also, this difference is a result of various error sources in the experiment, such as the error in determining each camera angle (± 2^0), distance between the two cameras (± 2 mm), imaging distance (± 2 mm), source position from the centreline of the two cameras ((± 1 mm) and estimation of the centre of the gamma spot (± 0.2 pixels).

4.4.2 Angled camera (convergent arrangement)

A calculation of the distance between the two gamma spots on the detector when the cameras are in a convergent arrangement depends on an equation which can be derived from the parameters described in section 4.4(see Figure 4.12). The normal lines of the two cameras will intersect at specific point, which is dependent on the distance between the two cameras, *D*, and the camera angle, θ. There is a convergence between the two lines before the intersection point (I.P.), and a spacing between the two lines after the intersection point.

Figure 4.13. These figures show the normal line from the two cameras intersecting at a specific imaging distance from the source that is dependent on the distance between the two cameras, *D*, and the camera angle, θ. There is a convergence between the two lines before the intersection point, and a divergence between the two lines after the intersection point.

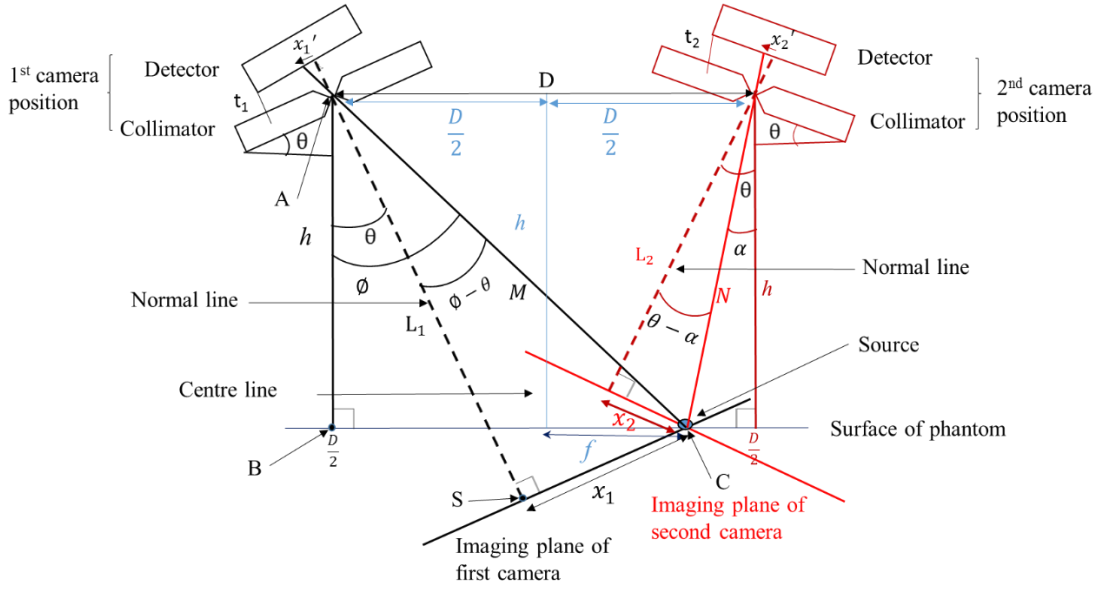

Figure 4.12: Schematic of two cameras (convergent arrangement) with camera angles of θ to the *y*-axis. This schematic was used to derive an equation for the distance between the two gamma images on the detectors where these are on opposite sides of the detectors.

Figure 4.13 shows two cameras in a convergent arrangement, with the distance (*D*) between them of 30 mm and camera angle (θ) of 10 degrees. The source is placed in the centre between the two cameras. At these parameters (*D* and θ), the normal lines from the two cameras intersect at a specific imaging distance (90 mm) from the collimator face. When one of these parameters (*D* or θ) is changed, the intersection point will change. The distance between the two images on the detectors will decrease before the I.P. then increase after I.P.; thus there are two imaging distances, *h*, that show the same distance between the two images, *d*, on the detector.

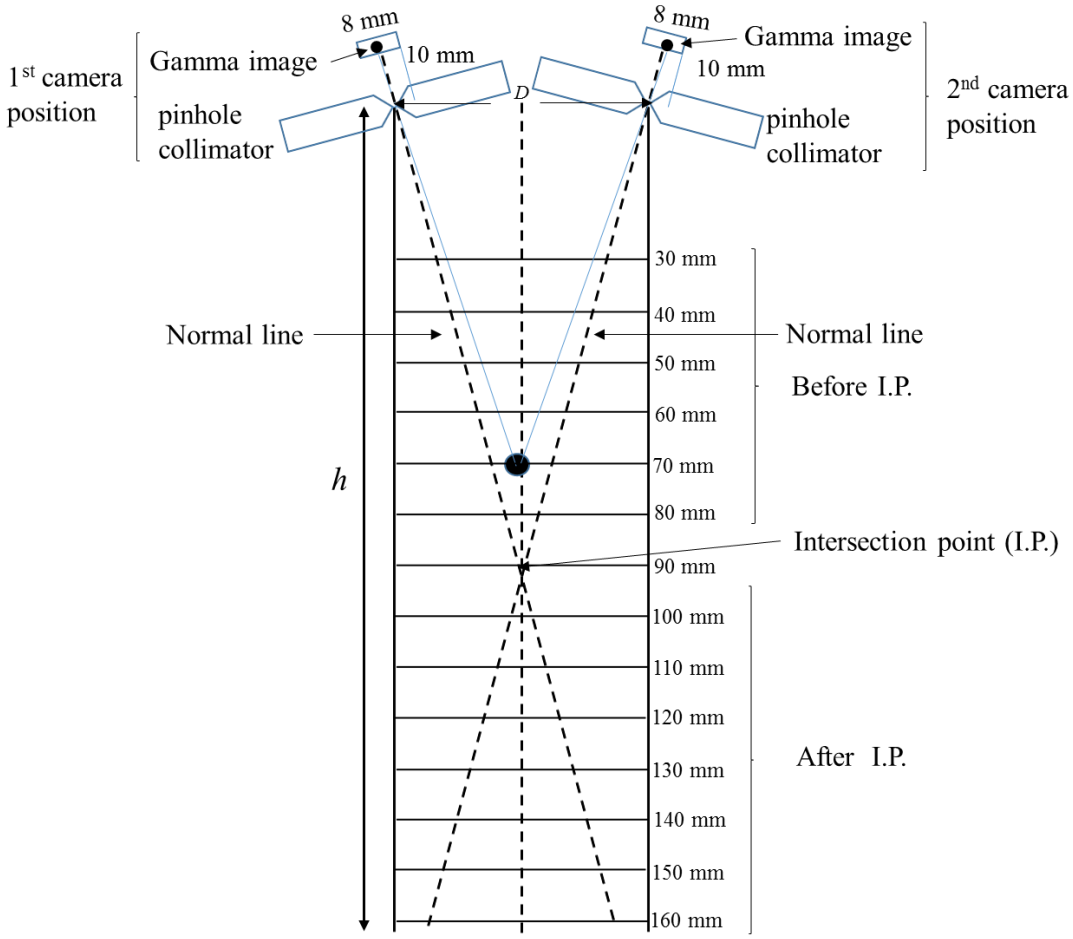

Figure 4.13: Diagram showing the positions of the two gamma cameras at a 10^0 camera angle in a convergent camera arrangement. The two normal lines intersect at 90 mm imaging distance. The distance between the two centres of the collimators, *D*, is 30 mm, and the gamma image on the detectors indicates the accumulated gamma rays emitted from a radioisotope source placed 70 mm from the camera.

For example, at a 30 mm distance between the two cameras and an imaging angle of 10^0, the intersection point is 90 mm from the collimator. Figure 4.14 shows that the two images on the detectors for this convergent arrangement for four imaging distances; two distances before I.P. and two distances after I.P. The separations between the two images were 5.96 mm and 1.1 mm at 30 mm and 65 mm imaging distances from collimator respectively, whereas after the intersection point the separations between the two images on the detectors were 1.1 mm and 1.83 mm at imaging distances of 125 mm and 180 mm respectively. The same separation (1.1 mm) between the two spots on the detectors is

observed at 65 mm (before intersection point) and 125 mm (after intersection point) from the collimator.

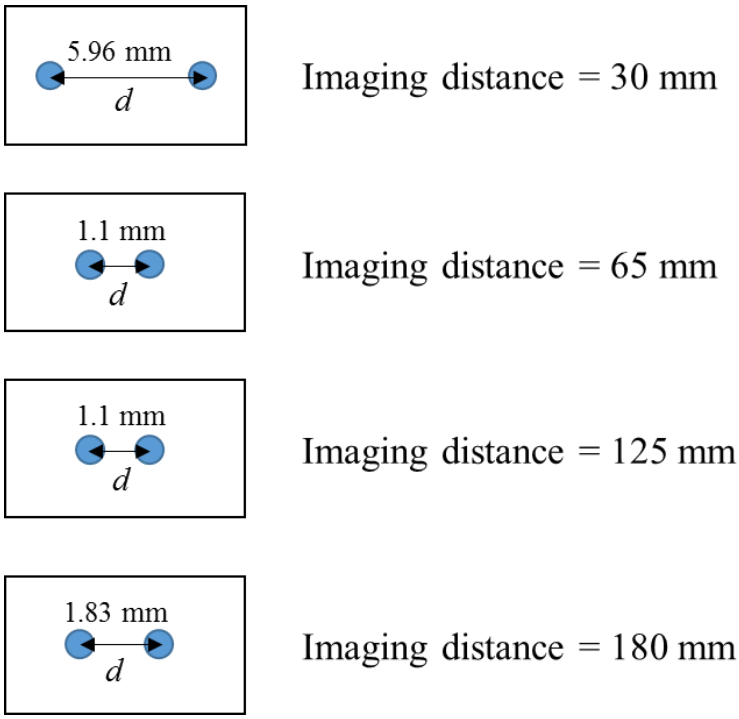

Figure 4.14: Relationship between the imaging distance and the distance between the two spots on the detectors in a convergent arrangement before the intersection point (5.96 and 1.1 mm) and after the intersection point (1.1 and 1.83 mm).

4.4.2.1 **Position of source image on the detectors (Figure 4.12)**

From the triangle A B C,

$$\tan \emptyset = \frac{\frac{D}{2} + f}{h} \tag{4.19}$$

From the triangle A C S,

$$x_1 = M \sin(\emptyset - \theta) \tag{4.20}$$

$$L_1 = M \cos(\emptyset - \theta) \tag{4.21}$$

Depending on equation (4.1), the position of the source image on the first detector (x_1') is given by:

$$x_1{}' = \frac{t_1}{L_1} \times x_1$$

Therefore:

$$x_1{}' = t_1 \times \frac{\frac{D}{2} + f}{\frac{h}{1 + \frac{\frac{D}{2} + f}{h} \times tan\theta}} - tan\theta \tag{4.22}$$

Similarly, for the second detector:

$$x_2{}' = t_2 \times \frac{tan\theta - \frac{\frac{D}{2} - f}{h}}{1 + \frac{\frac{D}{2} - f}{h} \times tan\theta} \tag{4.23}$$

4.4.2.2 **Calculating the separation between two source image positions**

The difference between the two gamma spots on the detector, *d*, can be defined as:

$$d = x_1{}' - x_2{}' \tag{4.24}$$

$$d = \left(t_1 \times \frac{\frac{D}{2} + f}{\frac{h}{1 + \frac{\frac{D}{2} + f}{h} \times tan\theta}} - tan\theta \right) - \left(t_2 \times \frac{tan\theta - \frac{\frac{D}{2} - f}{h}}{1 + \frac{\frac{D}{2} - f}{h} \times tan\theta} \right)$$

As $t = t_1 = t_2$

$$d = t \times \left(\frac{\frac{D}{2} + f}{h} - tan\theta \right) - \frac{tan\theta - \frac{\frac{D}{2} - f}{h}}{1 + \frac{\frac{D}{2} - f}{h} \times tan\theta} \qquad (4.25)$$

4.5 Effects of variables on the distance between the two gamma images on the detector in a convergent arrangement

In a convergent arrangement, the position of the gamma source images on the detector depends on θ, D, h, t and f, as shown in Figure 4.12 and Figure 4.13.

In the convergent arrangement, the normal lines (the line from the pinhole collimator to the imaging plane of the camera) of the two cameras will intersect at a specific imaging distance, which is represented by the Intersection Point (I.P). The I.P depends on the distance between the two cameras, D, and the camera angle, θ. Figure 4.15 shows the relationship between the I.P. and camera angle, θ, at different distances between the two cameras (20 mm, 30 mm and 40 mm). The I.P. is decreasing with the camera angle and increasing with the distance between the two cameras.

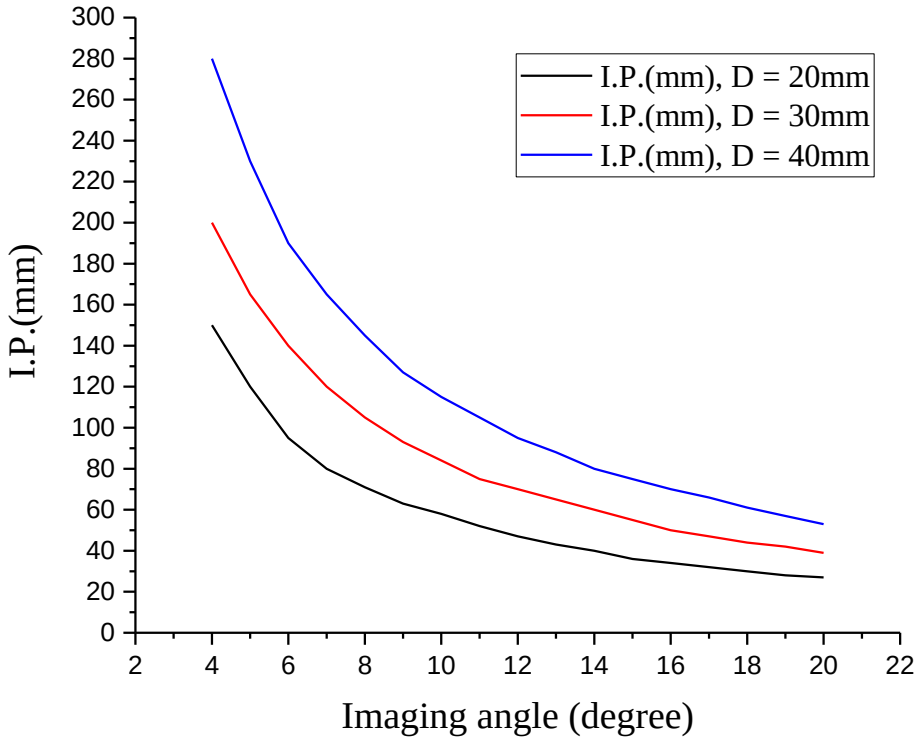

Figure 4.15: Relationship between the intersection point (I.P.) and camera angle, θ. The black, red and blue lines represent measurements taken with 20 mm, 30 mm and 40 mm separations between the two cameras respectively.

4.5.1 Effects on the distance between two gamma images on the detector as a function of off-axis source position, *f*

The effect of the off-axis source position, *f*, (from the centreline of the cameras) on the distance between the two images on the detector, *d*, has been studied to explain the behaviour of *d* before and after the intersection point with a change of source position from the centreline of the cameras of 0 mm to 20 mm. For example, consider 70 mm and 100 mm imaging distances before and after the intersection point respectively, with a 10^0 camera angle, θ, and the distance between the two cameras set at 30 mm. At 70 mm from the camera there was a convergence between the two images on the detector when *f* was moved away from the centreline of the two cameras, whereas at 100 mm from camera there was a divergence between the two images on the detector when *f* was moved away from the centreline of the two cameras (see Figure 4.16). Therefore, the behaviour of the

distance between two images on the detector is not affected by any change in distance between the centres of the two cameras.

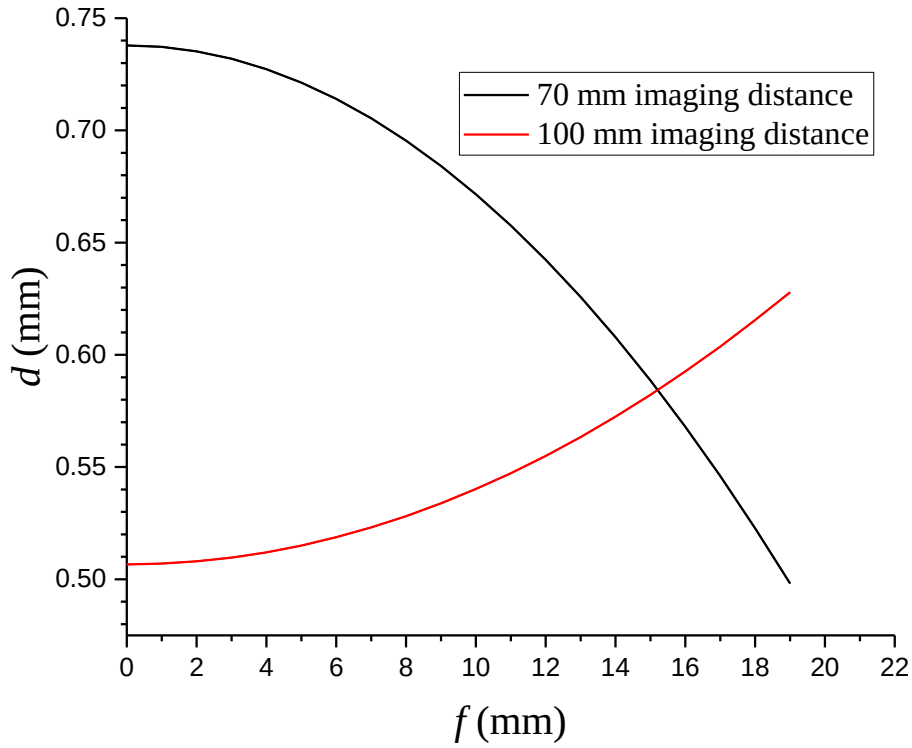

Figure 4.16: Relationship between the calculated distance between the two gamma source spots on the detector, *d*, and the distance from the centreline of the two cameras, *f*, in a convergent camera arrangement. The black line and red lines represent the calculated distance between the two images before and after the intersection point respectively.

4.5.2 Effect on distance between two gamma source images on the detector as a function of the camera angle, θ.

The effect of the camera angle, θ, on the distance between the two gamma images on the detectors, *d*, has been studied to explain the behaviour of *d* with change of camera angle from 0^0 to 19^0. For example, consider a 30 mm distance between the two cameras and a source position in the centreline of the two cameras, *f*, of 0 mm. Figure 4.18 shows that when the imaging distances were 70 mm and 100 mm from the source, there was a convergence between the two images on the detector with increasing imaging angle (0^0 to 12^0) and (0^o to 9^o) respectively, whereas there was a divergence between the two

images on the detector up to a 19^0 camera angle with the both imaging distances. The variation in and between 8^o and 9^o angle is small, as can be seen from Figure 4.17. The results indicate that the behaviour of the distance between the two gamma source images on the detector is affected by changes in the imaging angle.

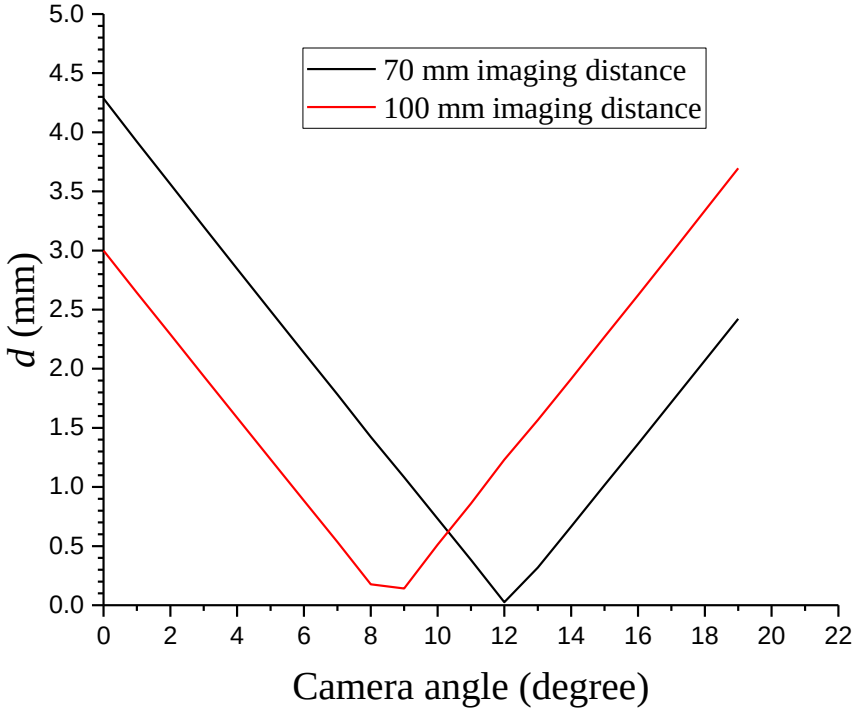

Figure 4.18: Relationship between calculated distances between the two gamma source images on the detectors and the imaging angle, θ, in a convergent camera arrangement. The black and red lines represent the calculated distance between the two images at 70 mm and 100 mm imaging distances respectively. The distance between the two cameras, D, was 30 mm.

4.5.3 Effect on distance between two gamma source images on the detector as a function of imaging distance, *h*.

The effect of the imaging distance on the distance between the two gamma source images on the camera detectors, d, has been studied to explain the behaviour of d before and after the intersection point with change of imaging distance, h, from 10 mm to 200 mm. For example, at a 10^0 imaging angle, a 30 mm distance between the two cameras and a source position in the centre of the two cameras f of 0 mm, there is a convergence between the

two images on the detector when increasing *h* to 80 mm (before I.P.) and then a divergence from the 100 mm imaging distance (after I.P.), where the I.P. was 90 mm from the collimator face (see Figure 4.19). Therefore, the behaviour of the distance between the two gamma source images on the detector is affected by any change in imaging distance.

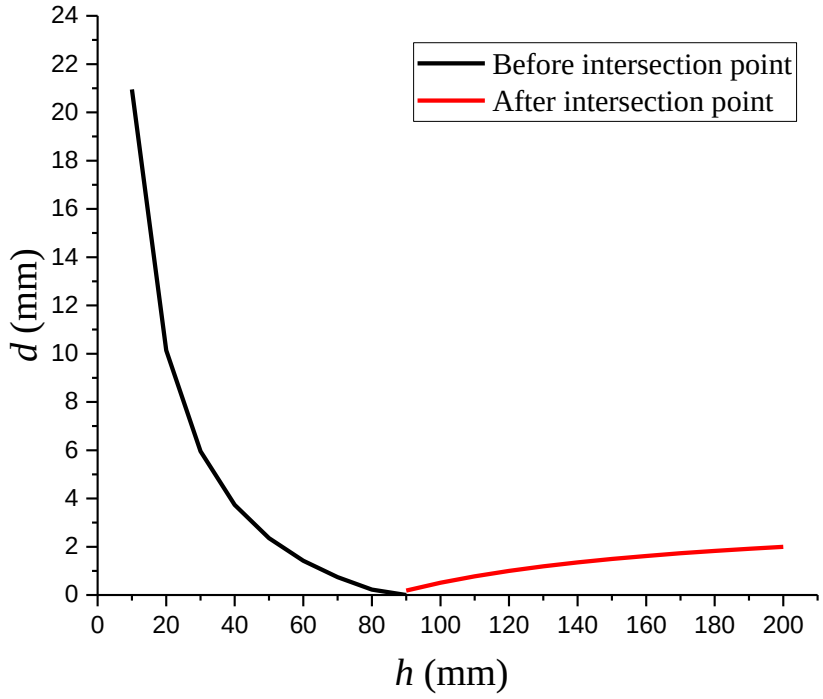

Figure 4.19: Relationship between the calculated distance between two images on the detector, *d*, and the imaging distance from the source, *h*, in a convergent camera arrangement. The black and red lines represent the calculated distance between the two images before and after the intersection point, respectively. The distance between the two cameras, *D*, was 30 mm.

4.5.4 Effect on distance between the two gamma images on the detector as a function of distance between the two cameras, *D*.

The effect of the distance between the two cameras on the distance between the two images on the camera detectors, *d*, has been studied to explain the behaviour of *d* with changes in the distances between the two cameras, *D*, of between 10 mm and 30 mm. For example, at a 10^0 camera angle and a source position in the centreline of the cameras, *f*,

of 0 mm, when using a 100 mm imaging distance the two images converge on the detector with increasing distance between the two cameras from 10 to 29 mm, but at a 70 mm imaging distance the two images converge on the detector when the distance between the two cameras increases from 10 mm to 25 mm, while there is divergence between the two images on the detector at a distance of greater than 25 mm between the cameras (as shown in Figure 4.20). Therefore, the behaviour of the distance between the two images on the detector is affected by changes in the distance between the two cameras.

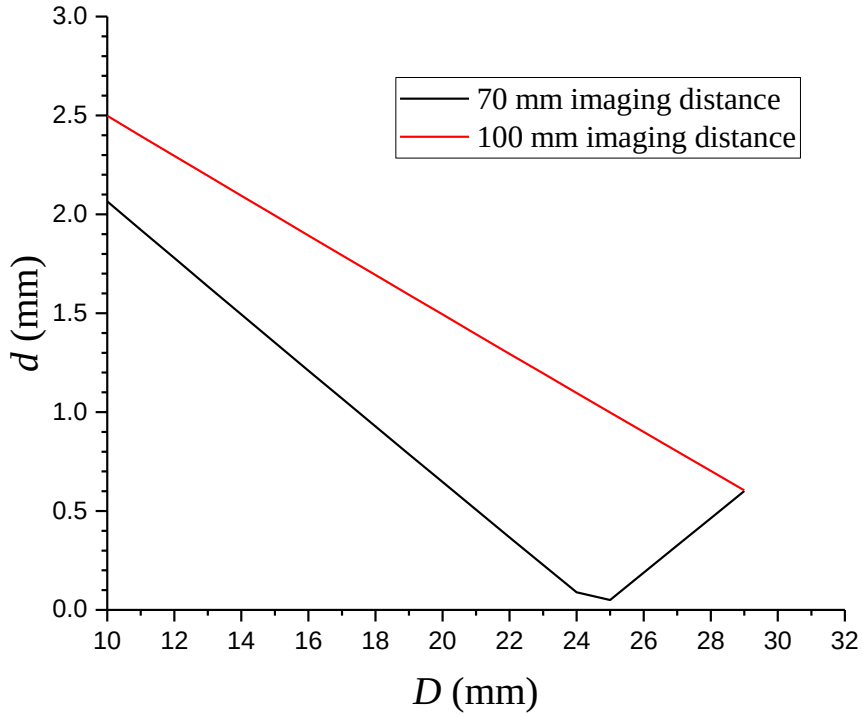

Figure 4.20: Theoretical relationship between the calculated distance between two images on the detector, *d*, and the distance between the two cameras, *D*, in a convergent camera arrangement. The black and red lines represent the calculated distance between the two images before and after the intersection point respectively.

4.5.5 Theoretical validation

The distance between the two gamma images on the detector in a convergent camera arrangement depends on parameters, *D*, *f*, *h* and θ. The effect of θ on the distance between the two images on the detector was studied in this section. Figure 4.21 shows the relationship between *d* and *h* at different camera angles, *θ*, between 8° and 14° in 2° steps.

The distance between two cameras, *D*, was 30 mm the pinhole collimator to detector distance *t* was 10 mm, and the source position *f* was in the centre of the two cameras, (0 mm distance from the centreline of the cameras on the surface of phantom).

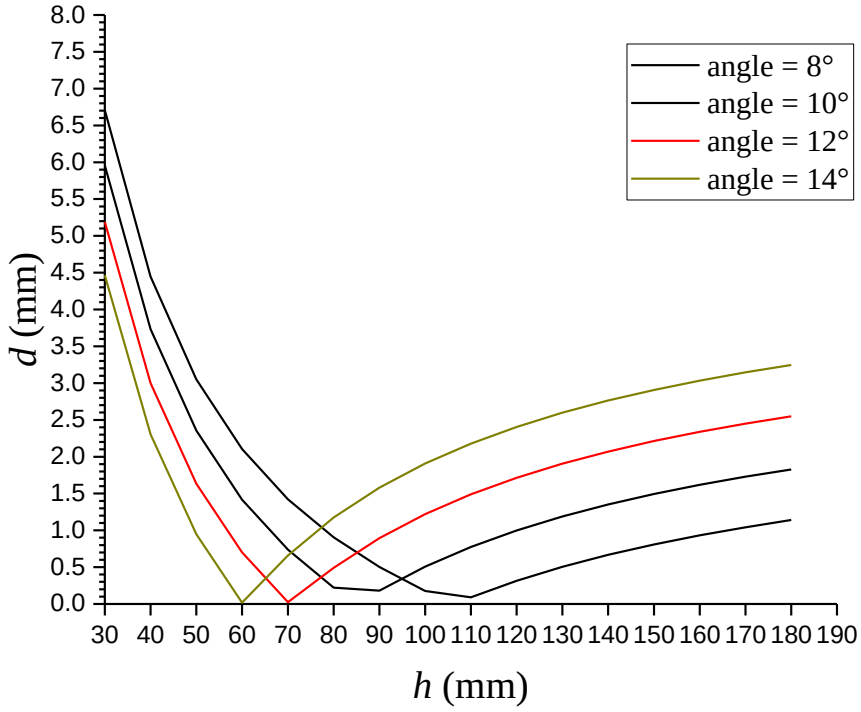

Figure 4.21: Theoretical relationship between the imaging distance, *h*, and the distance between two gamma source images on the detectors, *d*, at different camera angle in a convergent camera arrangement. *D* was 30 mm.

Figure 4.22 shows the relationship between *d* and *h* at different distances *D* between the two cameras between 26 mm and 32 mm in 2 mm steps. The camera angle, θ, was at 10^0, the pinhole collimator to detector distance *t* was 10 mm, and the source position *f* was in the centre of the two cameras (0 mm distance from the centreline of the cameras on the surface of phantom).

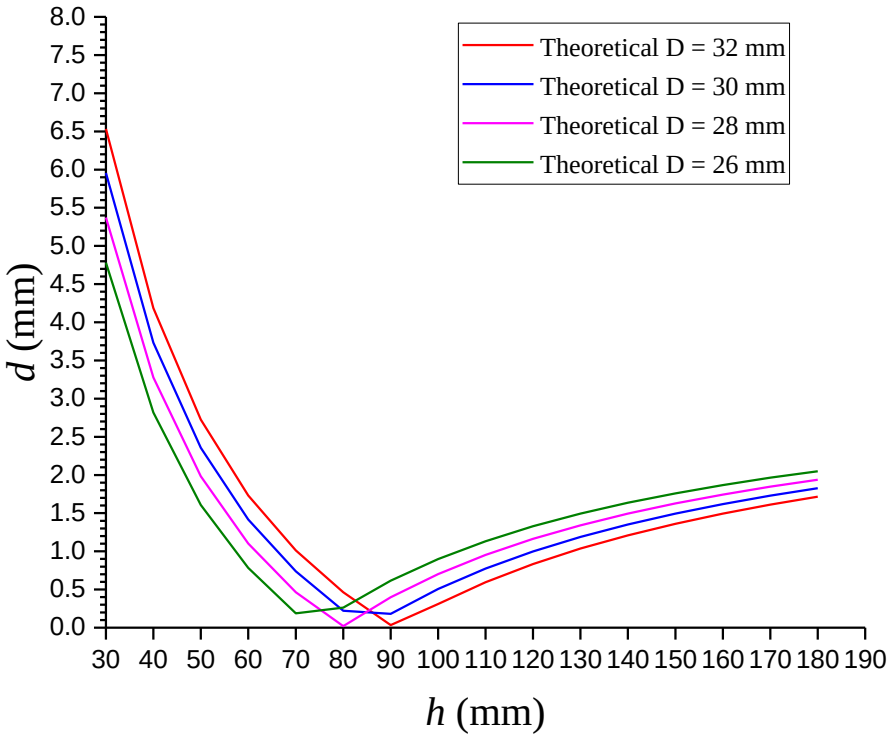

Figure 4.22: Theoretical relationship between the imaging distance, *h*, and the distance between the two spots on the detectors, *d*, at different distances between the two cameras in a convergent camera arrangement. The camera angle, θ, was 10^0.

Figure 4.21 and Figure 4.22 indicate that the distance between two spots on the detector decreases before the intersection point, whereas it increases after the intersection point. At 30 mm distance between two cameras, the intersection points were at 110 mm, 90 mm, 70 mm and 60 mm distances from the camera for 8^0, 10^0, 12^0 and 14^0 camera angles, respectively (see figure 4.20). At 10^o camera angle, the intersection points were at 70 mm, 80 mm, 90 mm and 90 mm distances from the camera for 26 mm, 28 mm, 30 mm and 32 mm distances between the two cameras respectively (see figure 4.21). At these intersection points, the distance between the two gamma spots on the detector was around 0.2 mm. Before the intersection point, the distance between two images on the detector *d* decreases with decreasing the distance between the two cameras, whereas it increases with increasing distance between the two cameras after the intersection point.

4.5.6 **Experimental validation**

Experimentally, the hybrid gamma camera was fitted with a 0.5 mm diameter pinhole collimator (60^0 acceptance angle). A ^{57}Co radioisotope source (8 mm diameter, 5 mm height, and 50 MBq activity) was positioned inside the hole in the flat phantom. The acquisition time for each gamma image was three minutes. A single camera was used for imaging the source at a 10^0 camera angle, after which it was then displaced horizontally by a distance, *D*, of 30 mm (the distance between two centres of the pinhole collimators) and rotated to a (10^0) camera angle in a convergent camera arrangement to obtain a second set of images (both optical and gamma). The imaging distance, *h*, from the camera to the source was measured from the centre of the pinhole collimator face, and ranged from 30 mm to 180 mm in 10 mm steps.

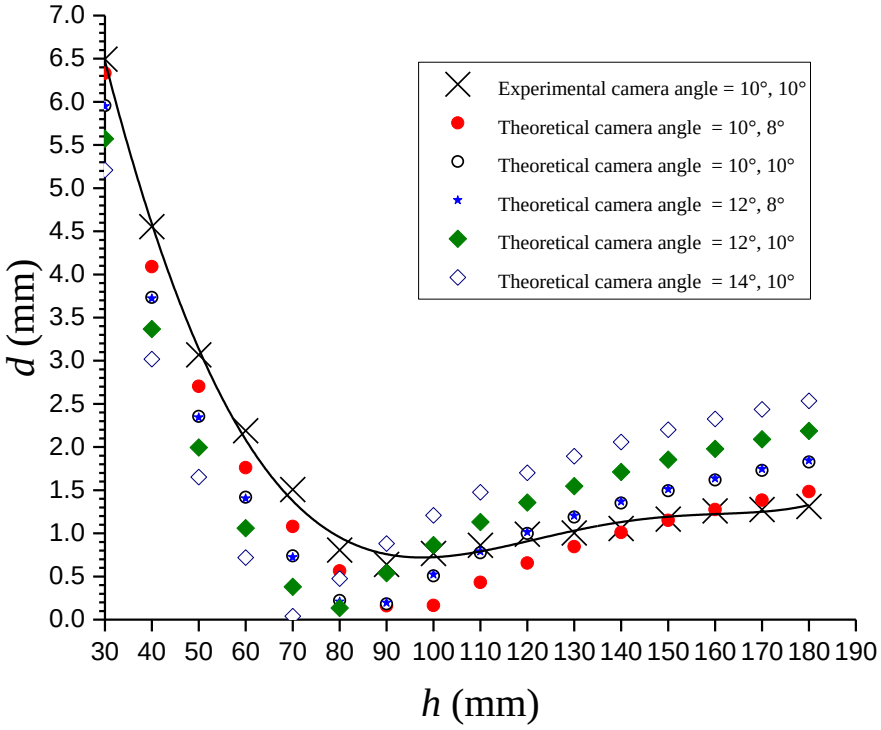

Figure 4.23: Comparison between the theoretically and experimentally derived distances between the two gamma source images on the detector versus the imaging distances, *h*, at a 10^0 camera angle in a convergent camera arrangement. The pinhole collimator to detector distance *t* was 10 mm, and the distance between the two centres of the pinhole collimators was *D* = 30 mm. The fitted line to the experimental results was a polynomial of order 5, and R^2 was 0.999.

Figure 4.23 shows a comparison between the experimentally and theoretically derived values for the distance between the images on the detector, *d*, and the imaging distance, *h*, in a convergent camera arrangement. The theoretical and experimental results for the convergent camera arrangement show the same behaviour with regards to *d* before and after the intersection point, namely that it decreases with all imaging distances, *h*, before the intersection point and it increases with all imaging distances, *h*, after the intersection point. The intersection point was at a 90 mm distance from the camera experimentally, and for camera angles 10^0-8^0, 10^o-10^o and 12^o-8^o, and it was 70 mm, and 80 mm for camera angles of 14^0-10^0 and 12^0-10^0 respectively. The distance between the two spots on the detector was 0.64 mm experimentally and it was around 2mm for 90 mm intersection point. At 70 mm and 80 mm intersection points *d* was 0.04 mm and 0.13 mm respectively. When camera angles (10^o -10^o) experimentally and theoretically, at a 30mm distance from collimator face *d* experimental was greater than *d* theoretical by approximately 8% , while after the intersection point, at 160 mm from the camera, *d* experimental less than *d* theoretical by approximately 28%. The best fitting of the theoretical camera angle with experimental result was for 10^o, 8^o camera angle where at 30 mm distance from the camera *d* experimental was greater than *d* theoretical by approximately 2%, while was less than 1% at 160 mm distance from camera. This shows the error in experiment may be because of the error in the determination of the camera angle, the distance between the two cameras, the distance from collimator to source and the determination of the centre of gamma spot.

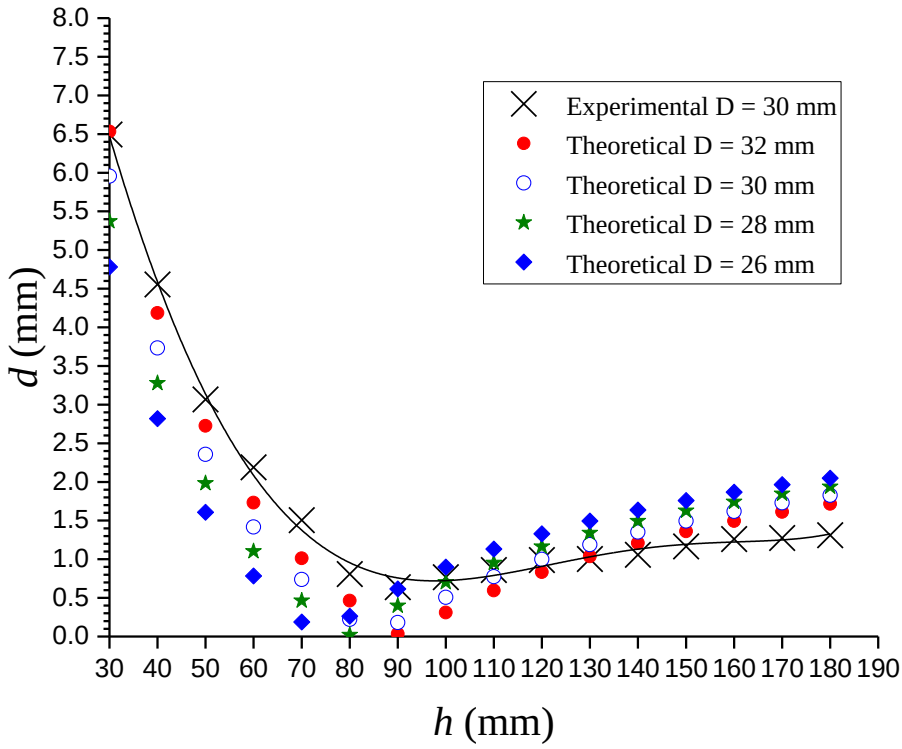

Figure 4.24: Comparison between the theoretically and experimentally derived distances between the two gamma spots on the detector versus the imaging distances, *h*, at a 10^0 camera angle in a convergent camera arrangement. The pinhole collimator to detector distance *t* was 10 mm, and the distance between the two centres of the pinhole collimators was *D* = 30 mm experimentally; and theoretically D was varied between 26 mm and 32 mm in 2 mm steps. The fitted line to the experimental result was a polynomial of order 5, and R^2 was 0.999.

Figure 4.24 shows a comparison between the experimentally and theoretically derived values for the calculated distance between the gamma images on the detector, *d*, and the imaging distance, *h*, in a convergent camera arrangement. The theoretical and experimental results for this arrangement show the same behaviour with regards to *d* before and after the intersection point. The I.P. changed depending on the distance between the cameras, where I.P. was at 90 mm for a 30 mm distance between two cameras, and it was 70 mm, 80 mm and 90 mm when the distance between the two cameras was 26 mm, 28 mm, and 32 mm respectively. At the intersection points, the distance between two gamma images on the detector was 0.639 mm experimentally, and it was 0.19 mm, 0.02 mm, 0.18 and 0.03 mm for the 26 mm, 28 mm, 30 mm and 32 mm

distance between two cameras respectively. Before the intersection point, at a 30 mm distance from collimator face *d* was approximately 6.5 mm experimentally and it was greater than theoretically predicted by 26%, 17%, 8% and 0% for 26 mm, 28 mm 30 mm and 32 mm distance between the two cameras respectively. After the I.P., at a 160 mm from the camera, *d* was around 1.26 mm experimentally and it was less than theoretically predicated by 33%, 28%, 22% and 15% for 26, 28, 30 and 32 mm distance between the two cameras respectively. The best fitting to the theoretical with experimental result was at 32 mm distance between two cameras. This shows that the error in experiment may be because of the error in the determination of the distance between two cameras, the determination of the camera angle, the distance from collimator to source and the determination of the centre of the gamma spot. The reasons for the difference between experimental and theoretical results were discussed in section 4.4.1.4.

4.6 Calculating overlapping FOV

4.6.1 Field of view

The field of view (FOV) of a single gamma camera will be a square shape, reflecting the shape of the CCD. When the source lies within the FOV, the camera will be able to detect the gamma source. The field of view of the camera depends on the acceptance angle of the pinhole collimator (60^0), which was chosen to utilise the entire detector area (8×8 mm), and is placed 10 mm from the detector face, with the distance from the centre of the pinhole to the source plane denoted by *h*, as shown in Figure 4.1.

From the triangle *A S M* in the Figure 4.1, the half-field of view (a) of the single camera is given by:

$$a = h\ tan\beta \tag{4.26}$$

Therefore the FOV = $2a$

where β is equal to 30° (half acceptance angle of collimator).

If $a > x$ (position of the source from the centre line of the pinhole collimator), then the FOV is, by definition, larger than *x*, and consequently the source will be within the field-

of-view of the pinhole collimator. However, if $a < x$, the source is out of the field-of-view and will not be detected by the camera.

Figure 4.25 shows the relationship between the FOV of the gamma camera and the distance from collimator face, *h*, with a 60^0 acceptance angle for the pinhole collimator.

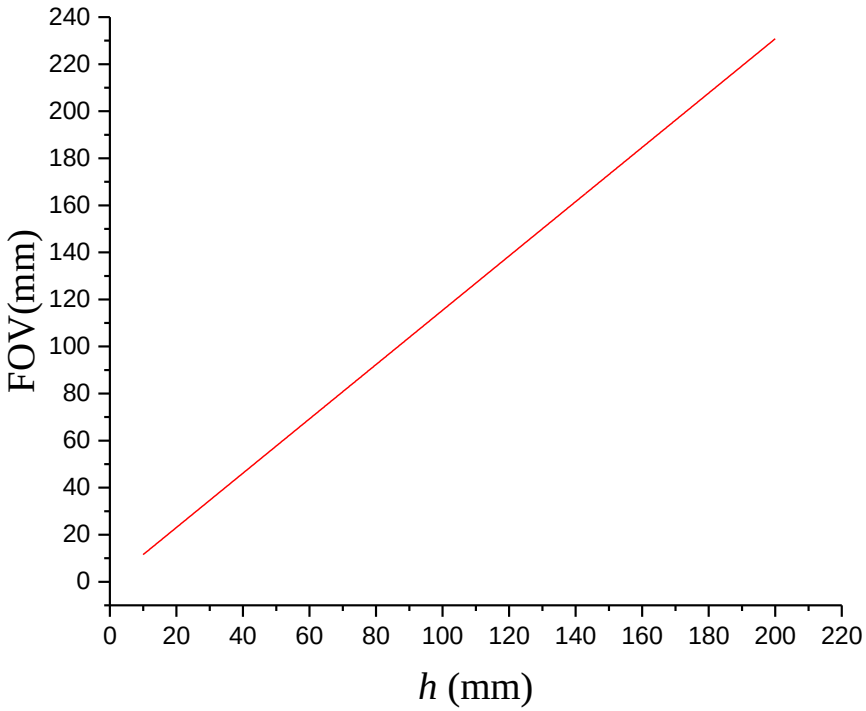

Figure 4.25: Relationship between the field-of-view (FOV) of the gamma camera and the distance from the source, *h* (mm), with a 60^0 acceptance angle for the pinhole collimator.

The overlapping FOV of the two cameras is the intersection between the individual fields of view of the cameras in which both cameras can detect the radioisotope source, as shown schematically in Figure 4.26.

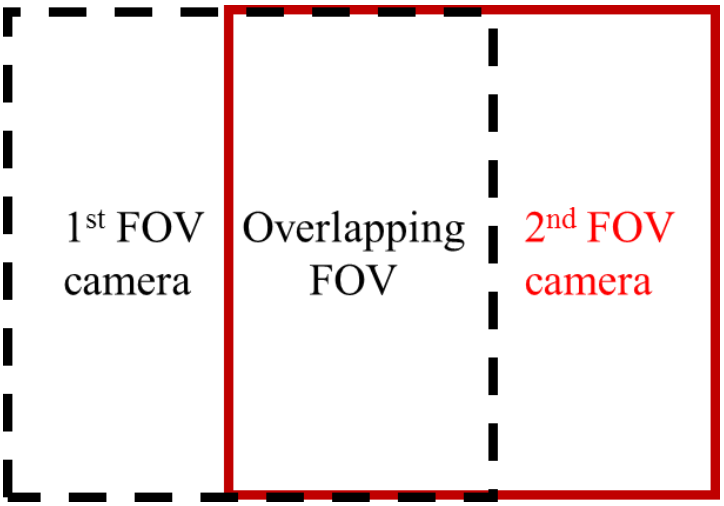

Figure 4.26: Schematic of the overlapping FOVs of the two cameras.

4.6.2 **Overlapping FOV in a perpendicular arrangement**

In a perpendicular arrangement, the overlapping FOV depends on the distance between the two cameras, *D*, and the distance from the centre of the pinhole collimator, *h*. Figure 4.27 shows a schematic of the overlapping FOV of the two cameras in a perpendicular arrangement, where *d* represents the distance from the middle point of *D* to the intersection point of the FOVs of the two cameras. The distance from the intersection point of the FOVs to the middle of the overlapping FOVs on the imaging plane is *a*, and *b* represents the half distance of the overlapping FOVs on the imaging plane. The acceptance angle of the pinhole collimator ϕ is 60^0, while α is 30^0.

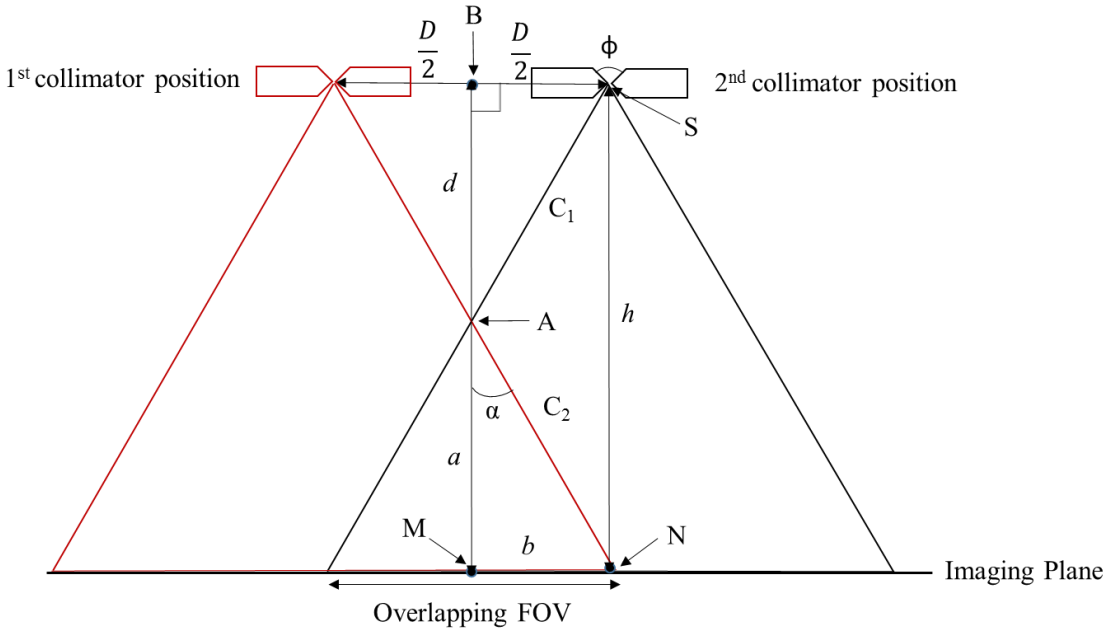

Figure 4.27: Schematic of the overlapping FOV in a perpendicular arrangement.

To calculate the overlapping FOV:

From the triangle A B S,

$$d = \frac{D}{2} \tan \phi \tag{4.27}$$

$$a = h - d \tag{4.28}$$

From the triangle *A M N*,

$$\tan \alpha = \frac{b}{a} \tag{4.29}$$

$$b = a \tan \alpha \tag{4.30}$$

$$\text{Overlapping FOV} = 2\left(h - \frac{D}{2}\tan\phi\right)\tan\alpha \tag{4.31}$$

The relationship between the overlapping FOV in a perpendicular arrangement and imaging distance, *h*, with a distance between the two cameras, *D*, of 30 mm, is shown in Figure 4.28.

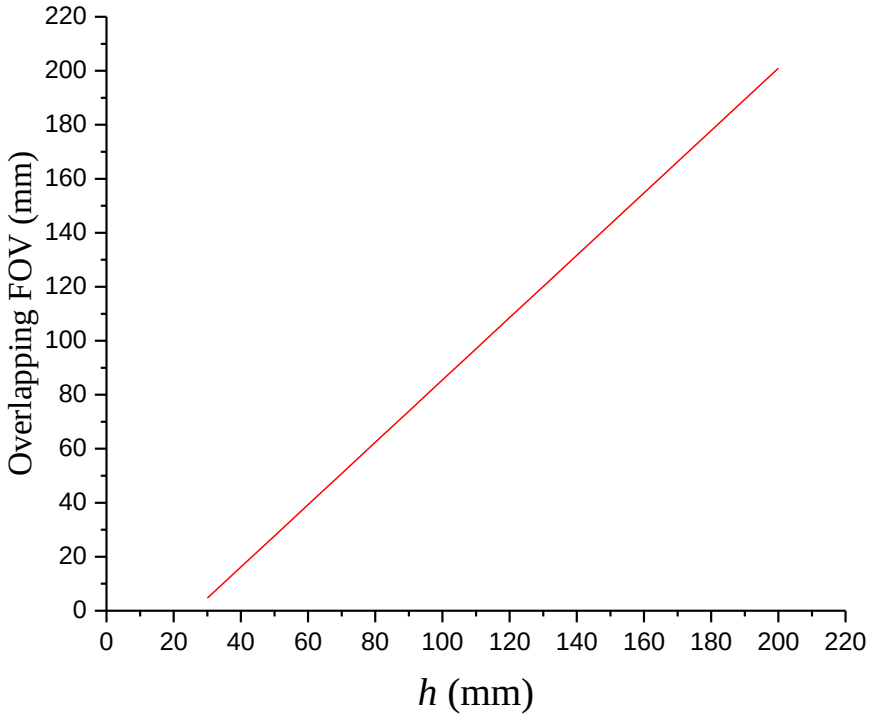

Figure 4.28: Relationship between the overlap of the FOV in a perpendicular arrangement and imaging distance, *h*. The distance between the two cameras is 30 mm.

4.6.3 Overlap of the FOVs in a divergent arrangement

The overlap of the FOVs in a divergent camera arrangement depends on the distance between the two cameras, *D*, the distance from the pinhole collimator to imaging plane, *h*, and camera angle, *θ*. Figure 4.29 shows a schematic of the overlapping FOV of the two cameras in a divergent arrangement, where *d* represents the distance from the midpoint of the cameras to the intersection point (A) of their FOVs The distance from the

intersection point of the FOVs to the middle of the overlapping FOV on the imaging plane is given by *a*, *b* is half the distance of the overlap of the FOVs in the imaging plane, and ϕ is the 60^0 acceptance angle of the pinhole collimator.

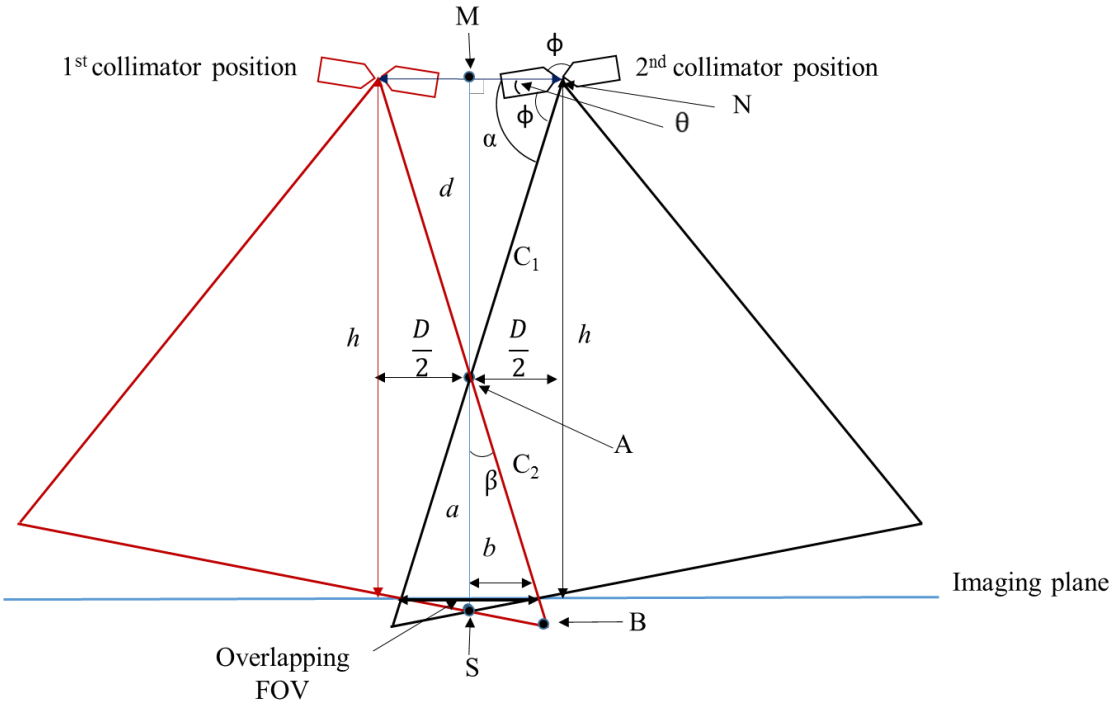

Figure 4.29: Schematic of the overlap of the FOVs in a divergent camera arrangement.

To calculate overlap of the FOVs:

$$\alpha = \phi + \theta \tag{4.32}$$

From triangle *A B S*,

$$\beta = \frac{\phi}{2} - \theta \tag{4.33}$$

From triangle *A M N*,

$$d = \frac{D}{2} \tan \alpha \tag{4.34}$$

$$a = h - d \tag{4.35}$$

$$b = a \tan \beta \tag{4.36}$$

$$\text{Overlapping FOV} = 2(h - \frac{D}{2} \tan(\phi + \theta)) \tan(\frac{\phi}{2} - \theta) \tag{4.37}$$

Figure 4.30 illustrates the relationship between the overlapping FOV of the two cameras in a divergent arrangement and imaging distance, *h*, with a distance between the two cameras, *D*, of 30 mm.

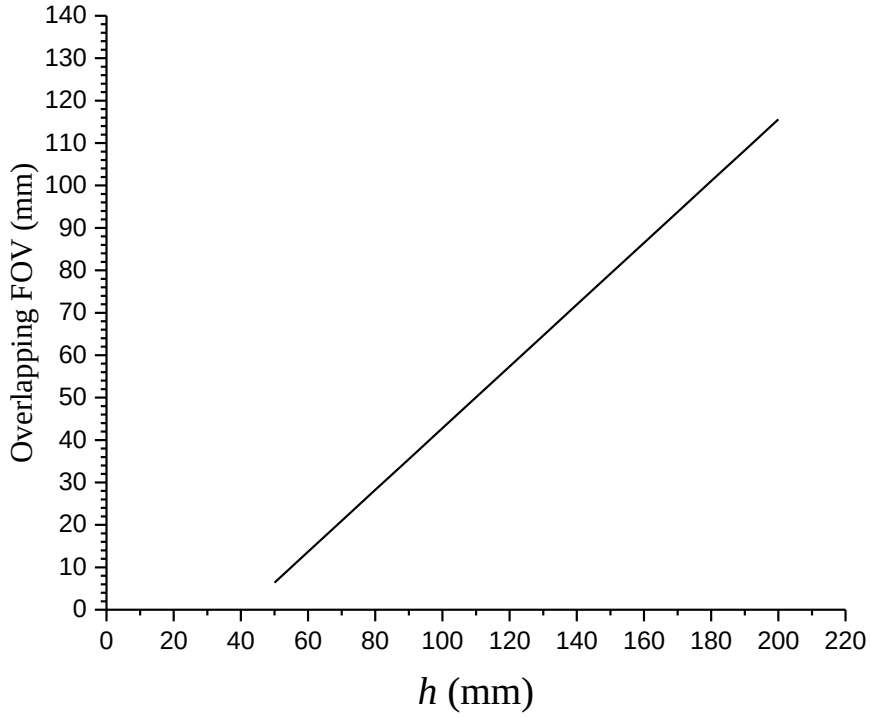

Figure 4.30: Relationship between the overlapping FOV of a divergent camera arrangement and imaging distance, *h* (mm), at a camera angle of 10^0 to the *y*-axis with a 30 mm distance between the two cameras.

4.6.4 Overlapping FOV in a convergence arrangement

In a convergent camera arrangement, the overlapping FOV depends on the distance between the two cameras, *D*, the imaging distance from the centre of the pinhole collimator, *h*, and camera angle, θ. Figure 4.31 shows a schematic of the overlap of the FOVs of the two cameras in a convergent arrangement, where $\emptyset$ is the 60^0 acceptance angle of the pinhole collimator, α and β represent angles less than and greater than the half acceptance angle of the pinhole collimator by the imaging angle θ respectively. x_1, x_2, x_3 and x_4 represent the distances between the intersection point of the edge of FOV and point of the imaging distance (h) on the horizontal plane. x_1', x_2', x_3' and x_4' represent the distances between the intersection of the edge of the FOV and the centreline of the cameras.

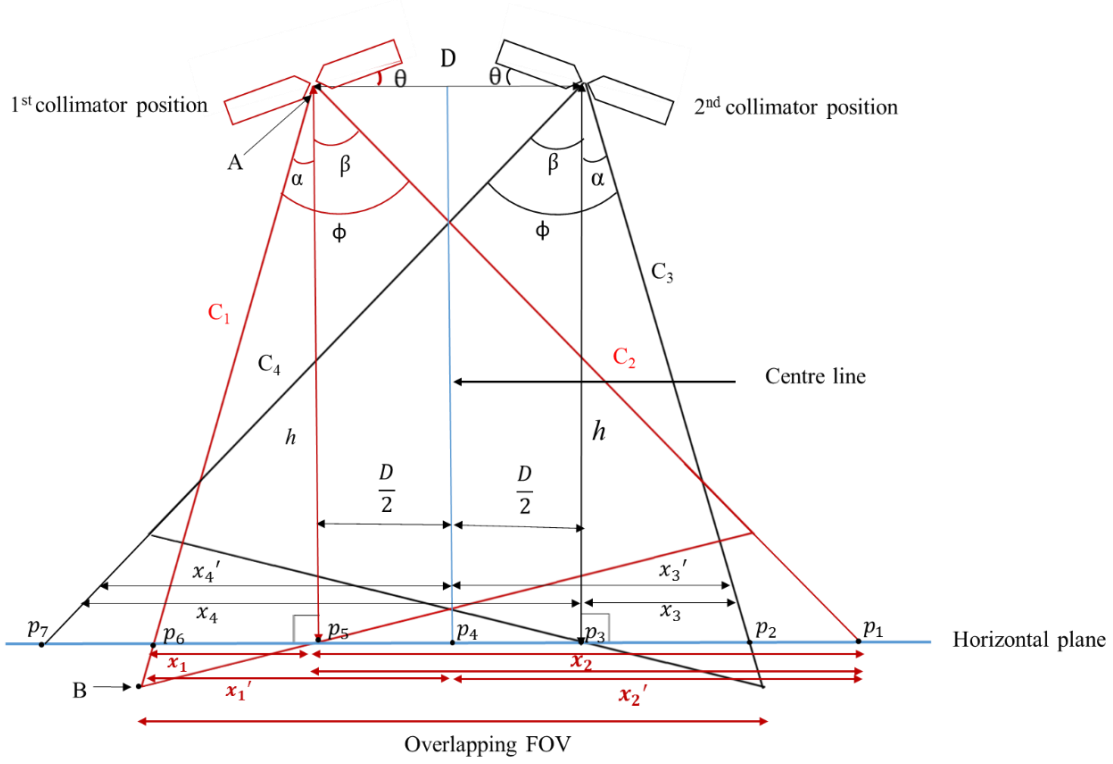

Figure 4.31: Schematic of the overlap of the FOVs in a convergent camera arrangement.

To calculate the overlap of the FOVs:

$$\alpha = \frac{\Phi}{2} - \theta \tag{4.38}$$

$$\beta = \frac{\Phi}{2} + \theta \tag{4.39}$$

From the first camera:

From the triangle *A B P₅*,

$$x_1 = p_6 - p_5 = h \tan \alpha \tag{4.40}$$

From the triangle *A P₁ P₅*,

$$x_2 = p_5 - p_1 = h \tan \beta \tag{4.41}$$

$$x_1' = p_6 - p_4 = x_1 + \frac{D}{2} \tag{4.42}$$

$$x_2' = p_4 - p_1 = x_2 - \frac{D}{2} \tag{4.43}$$

Similarly, for the second camera:

$$x_3 = p_3 - p_2$$
$$x_4 = p_7 - p_3$$

$$x_3' = p_4 - p_2 = x_3 + \frac{D}{2} \tag{4.44}$$

$$x_4' = p_7 - p_4 = x_4 - \frac{D}{2} \tag{4.45}$$

$$\text{Overlapping FOV} = x_1' + x_3' \tag{4.46}$$

Figure 4.32 illustrates the relationship between the overlapping FOV in a convergent arrangement and imaging distance, *h*, where the distance between the two cameras is 30 mm.

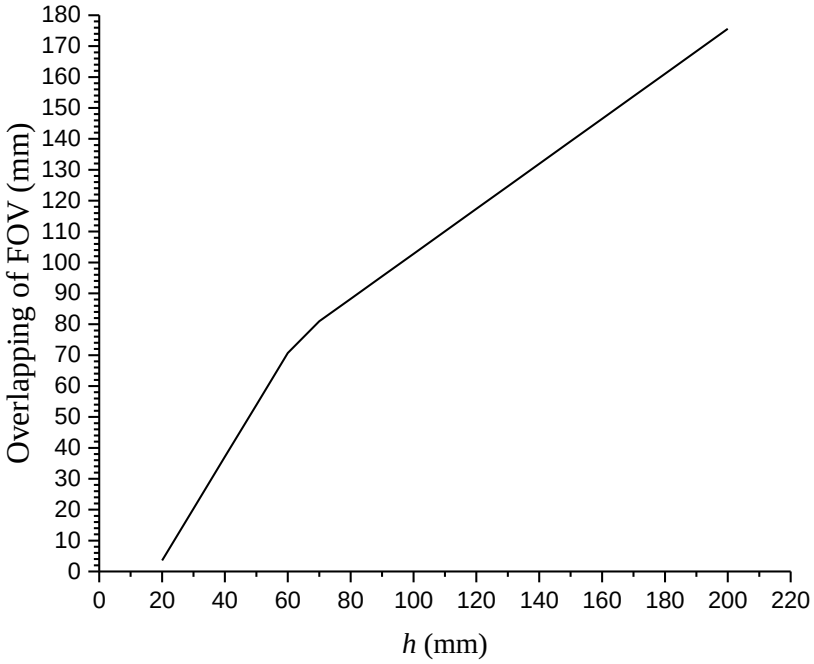

Figure 4.32: Relationship between the overlap of the FOVs in a convergent camera arrangement and imaging distance, *h* (mm), at a camera angle of 10^0 and a 30 mm imaging distance between the two cameras.

4.6.5 Theoretical comparison between the overlap of the FOVs

The overlap of the FOVs of the two cameras depends on the camera arrangements (perpendicular, divergent and convergent). Figure 4.33 shows the FOV of the single camera and a comparison between the overlap of the FOVs of the two gamma cameras in the three different arrangements, assuming D = 30 mm and with a 10^{o} camera angle for the divergence and convergence configurations. The overlap of the FOV in a perpendicular arrangement was approximately 5 mm at a 30 mm imaging distance, which then increased by 12 mm for each 10 mm increase in imaging distance. In a convergent

arrangement, the overlap of the FOV was approximately 4 mm at a 20 mm imaging distance, after which it increased by 17 mm for a 10 mm increase in source distance to 60 mm from the collimator; after the intersection point, the increase was 7 mm per 10 mm increase in source distance. By contrast, the overlap of the FOVs in a divergence arrangement was nearly 6 mm at a 50 mm distance from the source, increasing by approximately 7 mm when the camera-to-source distance increased by 10 mm. As can be seen, at 70 mm from the source, the overlap of the FOV in a perpendicular arrangement was 30 mm less than the convergent arrangement and 30 mm greater than the divergent arrangement; at a 140 mm distance from the collimator face, the overlap in the perpendicular and convergent arrangements was greater than the overlap in the divergence arrangement by approximately 60 mm, whereas the overlap in the perpendicular arrangement was approximately 25 mm and 85 mm greater than the convergent and divergent arrangements respectively at 200 mm from the camera.

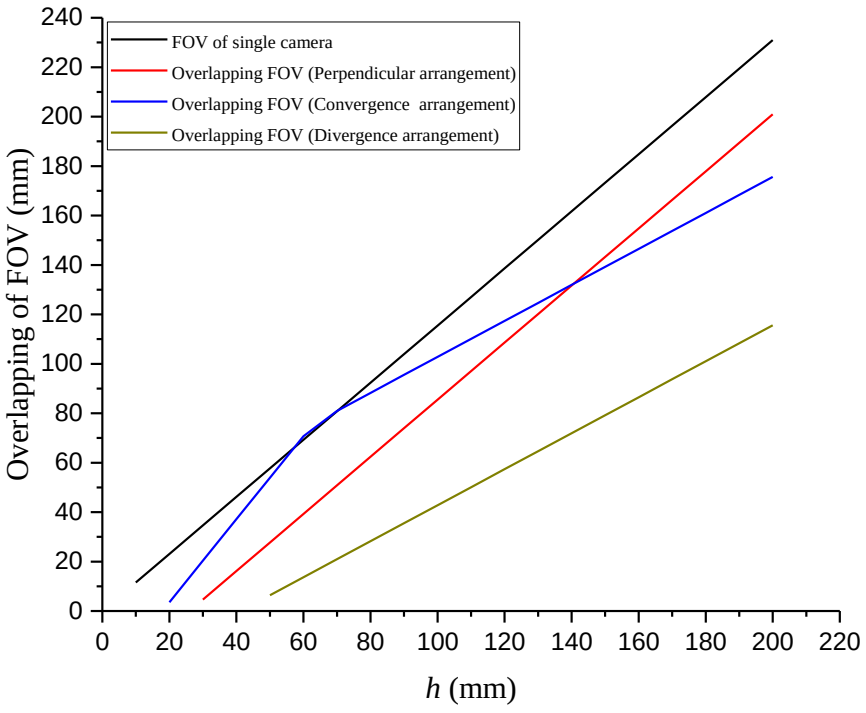

Figure 4.33: Schematic showing a theoretical comparison between the FOV of a single camera and the overlap of the FOVs in the perpendicular, convergent and divergent arrangements using a 10^0 camera angle and D = 30 mm.

4.7 Basic principle of depth estimation

The depth of the radioisotope source below the anatomical surface can be calculated using two hybrid systems positioned in a well-defined geometry, resulting in four images - two gamma and two optical. Using the known camera separation, the relationship between the imaging distance (from the source and from the surface) and the magnification factor (4.1) allows the distance from the camera to the gamma source / the surface of the object to be calculated. Combining these calculations provides an estimate of the depth of the gamma source below the surface of the phantom.

Depth calculations were based on the distance from the collimator to the source/surface. As the University of Leicester currently only has one imaging system, a single camera was used to image the source and phantom which was then displaced by 20 mm to obtain two images for each position (optical and gamma), as shown in Figure 4.34. A 20 mm distance between two cameras represents the preferable distance to detect the source and to estimate the depth within body, and to build the smallest structure that has two HGCs in future (see chapter 3).

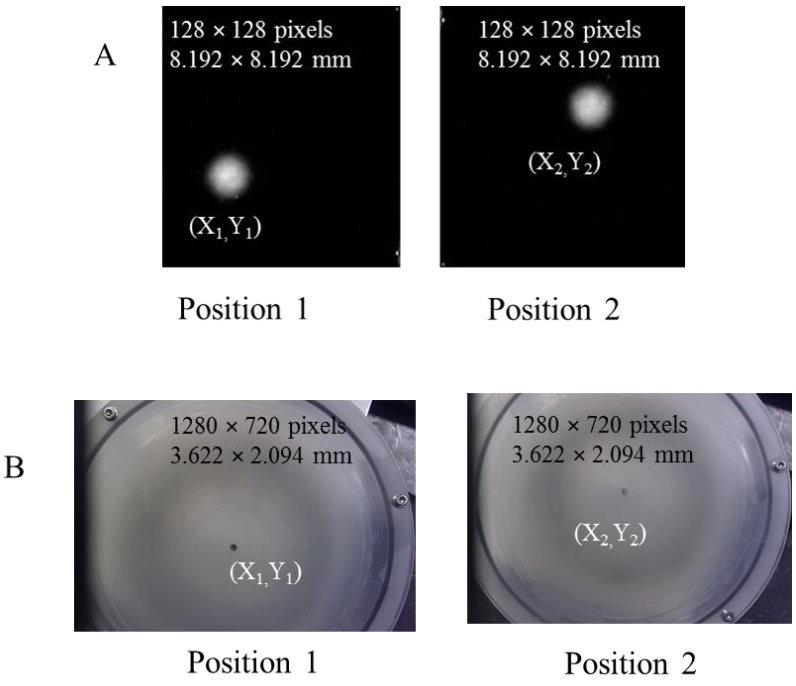

Figure 4.34: Gamma image (A) and optical image (B) show two locations for the radioactive sources within the phantom using the HGC. Position 1 denotes the first camera position, whereas position 2 denotes the second camera position; the distance between the two sources (cameras) was 20 mm, and 100 mm was the distance from the collimator.

A single HGC was used to image the source. The HGC was then moved 20 mm to obtain a second set of images (gamma and optical), as shown in figure (4.34). The distance between the two source positions (the two camera positions) is denoted by d_1, and two images (optical and gamma) are acquired from each camera position. Thereafter, the centre positions of the gamma spots (see Figure 4.34 A) and optical spots (see Figure 4.34 B) are determined. For example, in clinical applications, there is mark placed on the skin of the patient; this indicates that the accumulated radioisotope is below this mark, and it can be used as a reference for the optical image during depth estimation. In this study, the optical spot was used to simulate the mark on the skin of the patient. The gamma and optical image acquisition was by a bespoke analysis program (written in IDL [137]), and the gamma and optical spot centres in the images obtained from the HGC were determined by a cursor procedure using a program written in IDL. The distance between the two centres of the gamma spots, D_g (pixel), and the distance between the two centres of the optical spots, D_o (pixel), are then calculated in pixels using a simple Pythagorean relationship, as shown in equation (4.47). These distances are converted to millimetre units, D_g (mm) and D_o (mm), according to equations (4.48) and (4.50) respectively. The distances from the pinhole collimator to the source ($D_{c\text{-}source}$) and the surface ($D_{c\text{-}surface}$) are then calculated according to equations (4.52) and (4.53) respectively. Finally, the depth of the source beneath the surface of the phantom can be calculated according to equation (4.54).

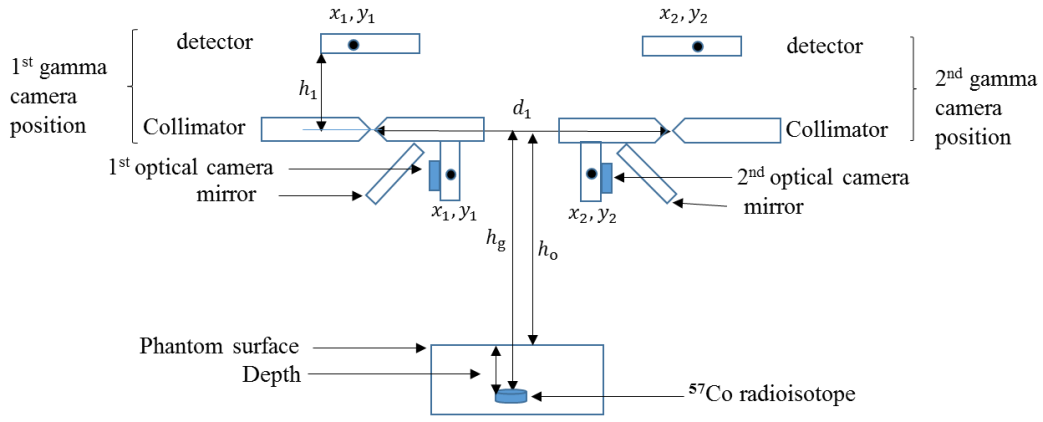

Figure 4.35: A schematic of the calculated distance from the collimator to the source/surface, where h1 is the detector-to-pinhole collimator distance (10mm), *h*o and *h*g are the calculated distances from the collimator to the surface and source respectively. d_1 is the distance between the two camera (gamma or optical) positions. The centre of the first gamma and optical images is (X_1, Y_1), and the centre of the second gamma and optical images is (Y_2, Y_2).

$$D = \sqrt[2]{(X_1 - X_2)^2 + (Y_1 - Y_2)^2} \tag{4.47}$$

where D is the distance between the two centres of the source points (images), and (X_1, Y_1) and (X_2, Y_2) represent the centres (in pixels) of the first and second spots, respectively.

$$D_g(mm) = D_g(pixel) \times 0.064 \tag{4.48}$$

where 0.064 is the pixel dimension of the gamma image (CCD), and D_g (mm) represents the distance between the two gamma spots on the detector, represented by d_2 in Equation 4.49;

$$D_o(mm) = D_0(pixel) \times 0.0034 \tag{4.50}$$

where 0.0034 is the pixel dimension of the optical image, and D_o (mm) represents the distance between the two optical spots, represented by d_2 in Equation 4.51;

To calculate the distance from the collimator face to the source within the phantom, $D_{c\text{-}source}$ (mm), which is represented by h_g in Figure 4.35.

$$h_g = \frac{h_1 \times d_1}{d_2} \tag{4.52}$$

where h_1 is the distance between the detector and pinhole collimator, which is equal to 10 mm. d_1 is the distance between two source (camera) positions, as shown in Figure 4.35

To calculate the distance between the collimator to the surface of the phantom, $D_{c\text{-}surface}$ (mm), which is represented by h_o

$$h_o = \frac{h_1 \times d_1}{D_o(mm)} \times scale\ factor \tag{4.53}$$

In this instance, to calculate the distance between the collimator and the surface of the phantom at the point of superimposition between the gamma and optical images, the magnification factor of the optical camera to the magnification factor of the gamma camera is equal to the scale factor (see chapter 3), so the distance ($D_{c\text{-surface}}$) is then multiplied by this scale factor.

Therefore, the depth estimation of the radioisotope source inside the phantom can be represented by the difference between $D_{\text{c-source}}$ and $D_{\text{c-surface}}$:

$$\text{Depth} = D_{c-source} - D_{c-surface} \tag{4.54}$$

4.8 Discussion

In this chapter, three camera arrangements were studied (perpendicular, divergent and convergent) to select the best configuration with which to calculate the distance between two gamma spots produced on the detector and to evaluate the most accurate depth estimation.

In the perpendicular camera arrangement, the distance between the two gamma spots on the detector is affected by the distance between the two cameras and the imaging distance. The difference between experimental and theoretical results was approximately 2%. The error is due to the error in determining the distance between the two cameras, the distance from the camera to the source, and in estimating the centres of the gamma spots. Experimentally, all of these can clearly affect the calculation of the distance between the two images. The results indicate that the errors could be reduced by fixing the distance between two cameras (building two cameras into one structure). This arrangement could be used to calculate the depth within the phantom with a smaller error. Thus, a perpendicular camera arrangement could be used to estimate depth in operating room.

In angled cameras (convergent and divergent arrangements), the effect of f, θ, h and D on the distance between the two images on the detector, d, were investigated.

In the divergent arrangement, although the relationship between d and h in experimental and theoretical results show the same trend (the distance between the two gamma spots on the detector decreased with imaging distance), there was a difference between the experimental and theoretical results. For example, with a 30 mm distance between the two cameras and at a 10° camera angle, the distance between two the spots on the detector experimentally was greater than the theoretical distances by approximately 19% at 90 mm, and by 39% at 200 mm distance from camera respectively. This difference was due to the various error sources in the experiment, such as the error in determining the camera angle, the distance from the camera, the distance between the two cameras and the error

in estimating the centre of the gamma spot. All of these affect the calculation of the distance between the two images. The results indicate that the error in calculated distance between the two spots on the detector will increase with imaging distance, which leads to an increase in the error of calculated depth within the phantom. This arrangement could not be used to calculate the depth within the body during surgery due to the large error.

In the convergent arrangement, because of the intersection of the normal lines of the cameras, the distance between the two spots on the detector was convergent before the I.P. and divergent after the I.P. For example, at a 30 mm distance between two the cameras and at a 10^{o} camera angle, the I.P. was at 90 mm distance from camera. The distance between the two spots on the detector experimentally was greater than theoretically by approximately 8 % at 30 mm distance from the camera, and less by 28% at 160 mm distance from camera. The difference between the experimental and theoretical results was due to the error in determining the centre of the gamma spot experimentally and the camera angle. In addition, there were additional errors in determining the distance between the two cameras and the distance from the collimator to the source, which affected the position of the images on the detector, and subsequently the calculated distance between the two spots on the detector. The changes in the behaviour of the distance between the two images on the detector, *d*, was evident in studying the effect of the distance between the gamma images on the detector as functions of *f*, θ, *h* and *D*, separately. The results indicate that the error in calculated distance between the two spots on the detector will decrease towards the I.P and increase after I.P. with imaging distances, which leads to the error in calculated depth within the phantom. This arrangement could not be used to calculate the depth within body during surgery due to the large error, In addition, the surgeon will be restricted to specific imaging distances due to the intersection point.

In general, the perpendicular arrangement showed the greatest overlap of field of view when compared to the divergent and convergent arrangements. In the perpendicular arrangement, the overlapping FOV was approximately 12% and 42% greater than in the convergent and divergent arrangements respectively at a 200 mm imaging distance. The overlap of the field of view was dependent on the distance between the two cameras and the imaging distance in the perpendicular arrangement, in addition to camera angle in the convergence and divergence arrangements. Clinically, the overlap of field of view of the

perpendicular camera arrangement would help the surgeons by covering the surgical area. For example, at 140 mm distance from the camera, the overlap of FOV was 131 mm, when imaging the thyroid, this overlap will cover the whole organ.

The depth estimation of the radioisotope within the phantom depends on the distance between the collimator and the surface of the phantom, and the distance between the collimator and source inside the phantom. These distances rely on the distances between the two gamma images, the two optical images, and between the two cameras. The error analysis of the depth estimation was also calculated, the details of which are given in the appendix.

4.9 Conclusions

Three camera arrangements; the perpendicular, divergent and convergent were investigated. The preferable configuration was then selected to calculate the distance between the two gamma images on the detector, thus allowing for a more accurate depth estimation.

The camera angle led to a minimization in the overlap of the field of view in the divergent arrangement compared to the perpendicular arrangement for all imaging distances, but by contrast led to an increase in the overlap of the field of view before the I.P and a decrease after the I.P, in the convergent arrangement (again, as compared to the perpendicular arrangement) with imaging distances. In convergent and divergent arrangements, there are many factors that affect the overlapping field of view of the two cameras. These are the same parameters that affect the calculation of the distance between the two images on the detector. In a perpendicular arrangement, the overlapping FOV is affected by the distance between two cameras only, which can be avoided when the two cameras are built with a specific distance between them. In a real-world scenario, a surgeon needs a camera to cover the largest field of the surgical area for all imaging distances. Therefore, a surgeon would be able to see a greater area of the surgical field with the perpendicular arrangement than with the other arrangements.

The convergent arrangement was excluded from consideration for use in the operating theatre to estimate the depth within the body because there were two imaging distances

that showed the same distance between the two gamma spots on the detector, before and after the I.P., which will require the HGC to be used at a specific imaging distance in the operating theatre; this would limit the use and the utility of this arrangement to the surgeon.

In the divergent arrangement, the overlap of the FOV is smaller than in the perpendicular arrangement. It is possible that the radioactive source may be out of the field-of-view of a camera, thus the surgeon would be unable to detect the depth of the accumulated radioisotope within the body in certain arrangements. Therefore, the divergent arrangement was also excluded from consideration for use in the operating theatre.

In the perpendicular arrangement, the small difference between the experimental and theoretical results indicated that the two images on the detector had a unique spacing at all imaging distances, and there was no effect of the distance from the centreline (off-axis) of the cameras on the behaviour of the distance between the two images on the detector at all imaging distances.

Based on the above, the perpendicular arrangement is thus considered the most suitable for use to calculate the distance between the two images on the detectors, and to subsequently estimate the depth of radioisotope sources accumulated within the body during surgery.

The overlap of FOV of the perpendicular camera arrangement could help to cover all of the required imaging area during surgery. For example, at a 150 mm distance from the collimator, the overlap was 155 mm; this overlap value could cover organs such as the thyroid, and tumours within breast and kidney.

The basic principle for the depth estimation of radioisotope sources using two HGC in a perpendicular arrangement was described in detail.

A distance between two cameras of 20 mm, as shown in chapter 3, has the ability to detect a gamma source at all imaging distances. To investigate the three camera arrangements, it is important to use the same value for the distance between the two cameras, both experimentally and theoretically. In the convergent camera arrangement, the intersection point will be at 60 mm from the camera for a 20 mm distance between the two cameras. To test this arrangement, various imaging distances were investigated to illustrate the

effect of the parameters on the distance between two images on the detector before and after the intersection point. So for a 30 mm distance between the cameras, it was important to investigate more imaging distances than when using a 20 mm distance. This distance (30 mm) between the two cameras was used to investigate these three arrangements.

Chapter 5: **Depth estimation of radioisotope sources using anatomical phantoms with a hybrid gamma optical camera**

5.1 **Introduction**

In many types of cancer, the evaluation of regional lymph nodes is important a determining the stage of cancer and planning subsequent treatment. During surgery, radioguided surgery provides information about the location of accumulated radioisotopes inside the body [8]. When the cancer is deeply in the body, this may lead to weakness or loss of the gamma ray detected, which may be due to attenuation by tissue or bone attenuation, thus leading to incomplete removal of the tumour [151]. For example, Hiroyuki Daiko et al. reported that of 41 patients suffering from lung tumours, the results of surgery led to incomplete resection in 6% of cases [152].

Currently, tumour detection procedure is based on the injection of radioisotopes such as ^{99m}Tc followed by the injection of a blue dye preoperatively, which are accumulated in the target organ. An intraoperative gamma camera can be used to localize the lesion while the blue dye provides for optical identification during surgery [153, 154]. The gamma probe technique is also commonly used to localize the accumulated activity within an organ [155]. Because it is difficult to prove that the tumour is completely resected, for example, when it is deeply within the body, there is a need for extra information on the localization of tumour such as a providing an accurate depth of target tissues within the patient's body [156].

The depth estimation for a tumour using an intraoperative gamma camera could provide a solution that allows for complete, accurate resection, allowing the surgeon to assess the problem before even picking up a scalpel. For example, Mathelin et al. reported the depth of the SLNs within the body with an estimated error of 5 mm [25].

The aim of this chapter is to develop a depth estimation technique for targeted tissues during intraoperative imaging procedures using the HGC. This was evaluated using different anthropomorphic phantoms in which radioisotope sources can be inserted. These

anthropomorphic phantoms (breast, head and neck, and chest) were used as medical phantoms to simulate parts of the human body.

5.2 Stereoscopic imaging

Stereoscopic imaging techniques create the optical illusion of three-dimensional (3-D) depth using separate two-dimensional (2-D) images from the right and left eyes of the observer. The human brain collects and processes these two-dimensional (2-D) images to produce a single 3-D image [98].

Development has been continuous in the field of 3-D medical imaging technology, where various stereoscopic imaging devices have been applied in the medical field. Physicians and radiologists are currently using 3-D imaging systems, which can supply more information than 2-D imaging systems, and which can lead to more accurate comprehension and analysis of a given target [100]. Many medical imaging instruments use stereoscopic imaging techniques, for example, stereo-microscopy [99] and stereo-endoscopy [157]. Stereoscopic technology has been developed and applied clinically to improve surgical accuracy and patient safety [99].

5.3 Phantoms

The radioisotope distribution within organs and tissues of the human body can be simulated using phantoms manufactured from tissue-equivalent materials [158]. During the development of the HGC, various types of phantoms have been designed and manufactured to assess the performance of this imaging system, starting from the simple multi-hole phantoms [40] to the more advanced phantoms that were used to simulate abnormal tissue, lymphatic vessels and the depths of the radiolabelled tissues with in the body [39, 41]. Phantoms can also be used to compare the performance of different imaging devices. A phantom could help to provide the evidence to support the use of the HGC in the operating theatre, for example in breast cancer diagnosis and for visualising other parts of the body [31].

In this chapter, radioisotopes were placed in three phantoms in order to simulate the accumulation of radioactive material inside the body. The source was positioned within a breast phantom to simulate a tumour inside soft tissue, or within the head and neck phantom to mimic abnormal tissues between soft tissue and bone where imaging can be controlled by manoeuvring the camera to avoid the effects of bones on the detection of the tumour. In the case of mimicking a tumour beneath a region of bone, the source was placed inside the chest phantom in such a position that the effects of bone on the detection of radiolabelled tissues were impossible to avoid.

5.3.1 Breast Phantom

The breast phantom was previously designed [31] to provide the shape and components necessary to simulate the equivalent part of the human anatomy. The breast phantom has a dome which is 160 mm diameter with a 3 mm wall thickness (base-to-dome apex height is 70 mm) and which sits on a base with a 160 mm inner diameter and 175 mm outer diameter that has a thickness of 35 mm. The dome is fixed to the base using metal screws [31].

Perspex (polymethyl methacrylate) is a material that is commonly used for building medical phantoms, due to its similarity to normal human tissue components in terms of the passage of gamma rays; the mean ratio of atomic number-to-mass, Z/A, is 0.54 for Perspex and 0.55 for soft tissue, while the density, ρ, is 1.19 gm/cm^3 for Perspex and 1.06 gm/cm^3 for soft tissue [133, 159]. To simplify the design, Perspex was used to fabricate the base and the plug.

The breast phantom design is sufficiently flexible that the radioisotope can be placed at different locations inside the dome. Figure 5.1 shows a number of views of the breast phantom.

Figure 5.1: Sketch of the breast phantom showing, left, an isometric view and, right, a plane and side view.

5.3.2 Head and Neck phantom

The detection procedures used to isolate SLNs in the head and neck region present a major surgical challenge because the SLNs are generally very close to either each other or to surrounding vital structures. The ability of a camera to image all of the surgical area is critical to the intraoperative determination of the location of such SLNs, and hence its utility during such procedures [32].

The head and neck phantom was previously designed by Alqahtani et al. [32] to imitate real parts of the head and neck, such as having a life-size thyroid and a simplified trachea and spine. This design also included a jig to hold simulated lymph nodes, injection sites and primary tumours. Figure 5.2 shows the final design of the head and neck phantom insert; this novel insert was used in conjunction with a commercial anthropomorphic head and neck phantom [160]. The phantom could be filled with water and was fabricated from cellulose acetate butyrate [32]. The head and neck phantom can provide different depths for simulated abnormal tissues, which can be positioned at any desired position within the phantom.

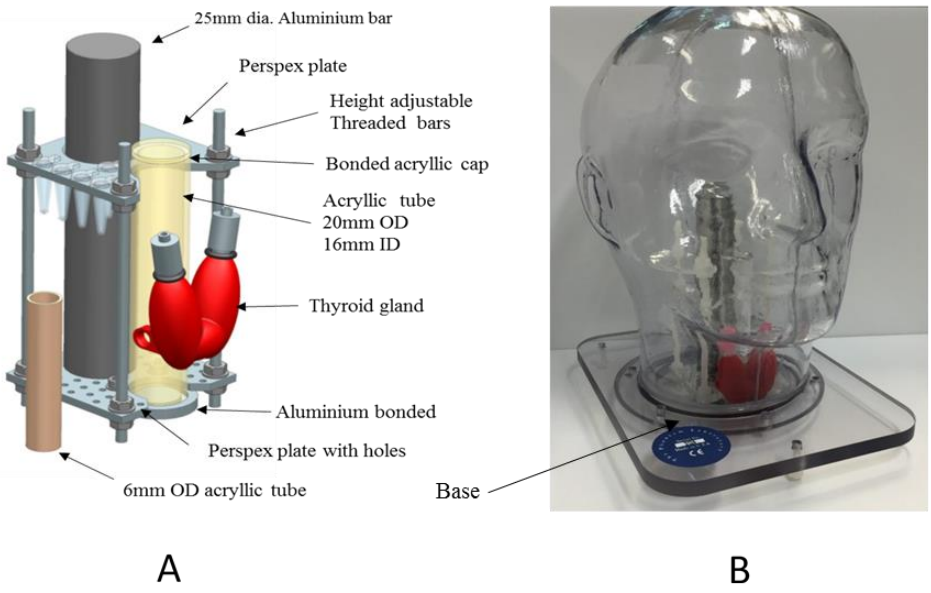

Figure 5.2: (A) Schematic of the insert for the head and neck phantom showing the thyroid, simplified trachea, and spinal parts; (B) photograph of the complete phantom with the insert in position inside the head. OD and ID indicate the outer and inner diameters respectively [32].

5.3.3 Chest Phantom

The chest phantom used during this study was designed and engineered by the Bioimaging Unit, Space Research Centre, University of Leicester, to provide a shape and internal components that can simulate the bone and soft tissue together in a manner representative of the human anatomy. The chest phantom was constructed from an aluminium bar and layers of Perspex with different thicknesses. These components were arranged to simulate the position of the bone (aluminium) and soft tissue (Perspex) of the human chest [161]. The source's position below the aluminium was used to simulate clinical cases such as ectopic tissues, e.g., an ectopic parathyroid gland predominantly located within the thymus, where the thymus is located between the heart and the sternum [162].

The design of the chest phantom consists of a 10 mm thick, 3 cm wide and 10 cm long aluminium bar and a number of Perspex layers with an area of 10 x 10 cm and different thicknesses, which are used to create the overall phantom.

5.3.3.1 **Qualification of Al-bone equivalent**

The atomic number of aluminium is 13, which is equivalent to the effective atomic number of bone at 13.8 [161]. A 10 mm thick aluminium bar was selected on the basis of having a high degree of equivalence to the radiation absorption of the maximum thickness of the ribs [161], where the absorption of the aluminium and the bone were approximately a 32% and 31% respectively of the source, as shown in Figure 5.3.

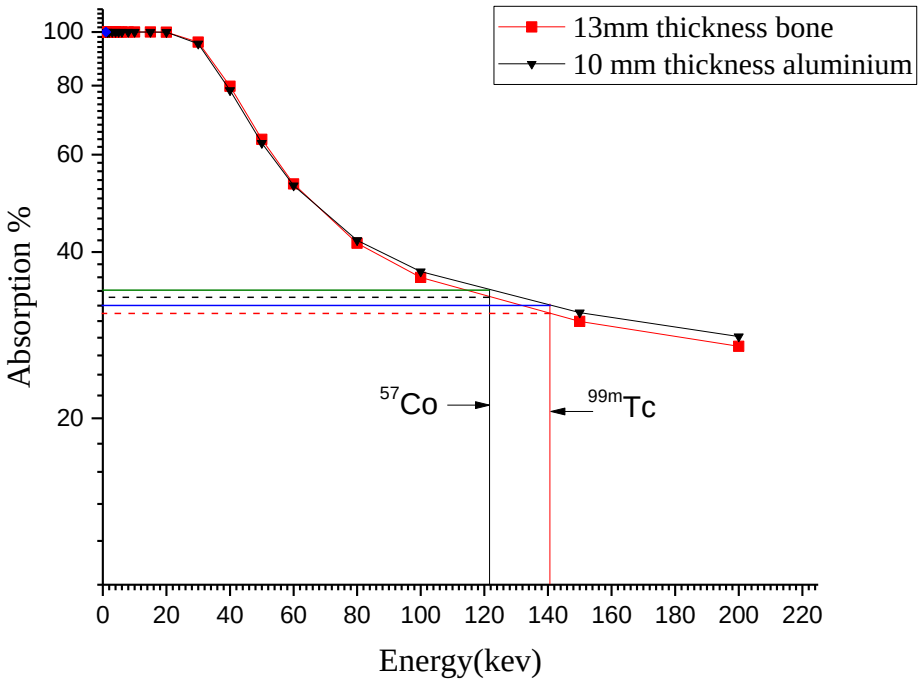

Figure 5.3: Comparison between the relationship between absorption and energy using a 13 mm thickness of bone and a 10 mm thickness of aluminium, based on the absorption and attenuation coefficient data from the National Institute of Standards and Technology (NIST) Standard reference database [133]. The red and black dashed lines represent the absorptions of ^{99m}Tc and ^{57}Co, respectively, for 13 mm thick bone. The blue and green solid lines represent the absorptions of ^{99m} Tc and ^{57}Co, respectively, for 10 mm thick aluminium.

The chest phantom design is sufficiently adaptable that the position of the aluminium can be changed to simulate different positions of the radioisotope source. The first position is where the aluminium is placed *above* the Perspex to simulate the bone being close to the skin, as might be expected with a slim patient; the second is where the aluminium is

placed *between* Perspex layers to simulate bone between soft tissues in an average-sized body; the third is where the aluminium is placed *below* the Perspex to simulate the bone within a larger, overweight patient. Figure 5.4 shows the chest phantom with the aluminium plate in each of these three positions.

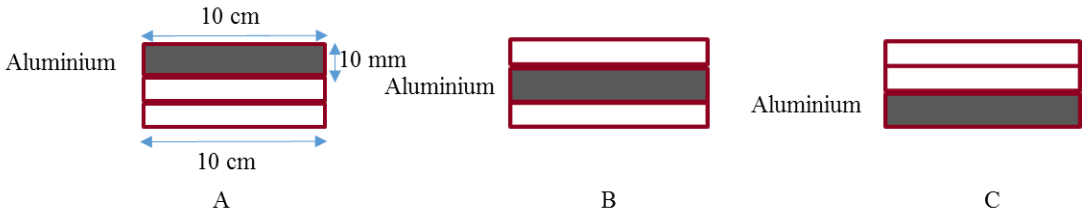

Figure 5.4: Sketch of the chest phantom showing the three positions in which the aluminium can be placed (A) above the Perspex, (B) between the Perspex and (C) below the Perspex.

To study the effect of bone on the detection of photons by the gamma camera (sensitivity of the HGC), see Figure 5.5. The camera was fitted with a 0.5 mm diameter pinhole collimator to image a ^{57}Co source (8 mm diameter, 5 mm thickness and 27 MBq activity). A ^{57}Co radioisotope source was used because of its availability in the Bioimaging laboratory and 122 keV photon energy, which is within the detection range of the HGC. The imaging distances were varied between 40 mm and 180 mm in 10 mm increments with an acquisition time of ~360 s. Gamma images were analysed using ImageJ software [136] and the collimator sensitivity was calculated.

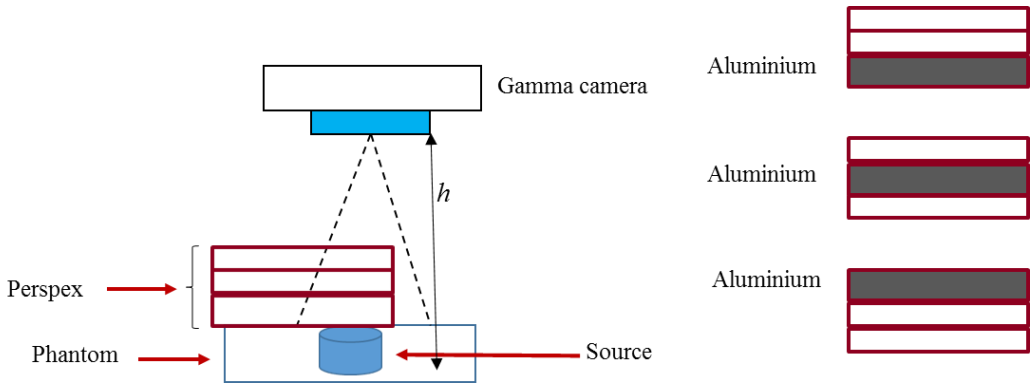

Figure 5.5: A diagram showing the experimental setup used to study the effects of the position of aluminium relative to the Perspex on the collimator sensitivity of the gamma camera.

The simulation of the effect of bone completely covering or partially covering the tumour on the detection of photons was conducted using an aluminium bar, which was placed above the source. The HGC was used to image a 27 MBq ^{99m}Tc radioisotope source in a hole (8 mm height, 10 mm diameter), which was covered with a 10 mm thick aluminium bar. This bar was displaced by 10 mm in 1 mm steps. The imaging distances were 50, 70 and 90 mm and the acquisition time was three minutes for each millimetre displacement step, as demonstrated in Figure 5.6.

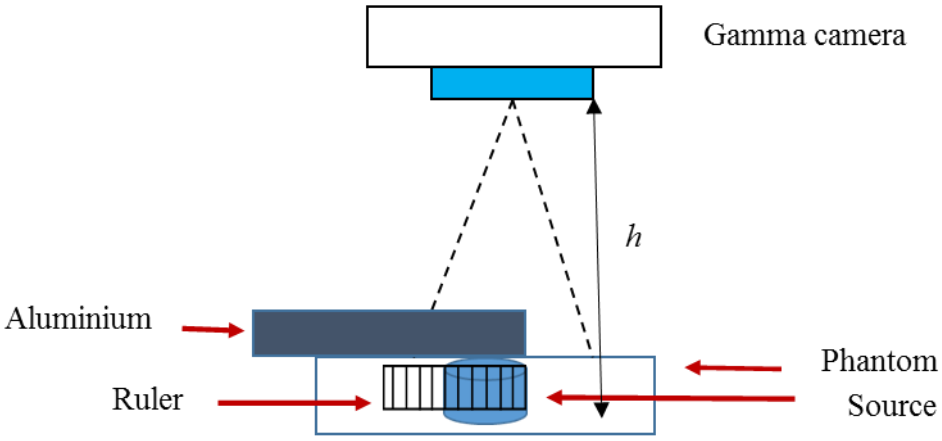

Figure 5.6: A diagram showing the experimental setup used to study the effects of aluminium on the collimator sensitivity of the gamma camera.

5.3.3.2 **Effect of Bone on collimator Sensitivity**

An aluminium bar was used to simulate the effect of the bone on the sensitivity of the gamma camera; the results of this simulation are shown in Figure 5.7. Figure 5.7 shows the results obtained from the analysis of the relationship between collimator sensitivity, as calculated with and without a 10 mm thick aluminium bar covering the ^{99m}Tc source, and the distance from the collimator face, with the equations fitted for both lines.

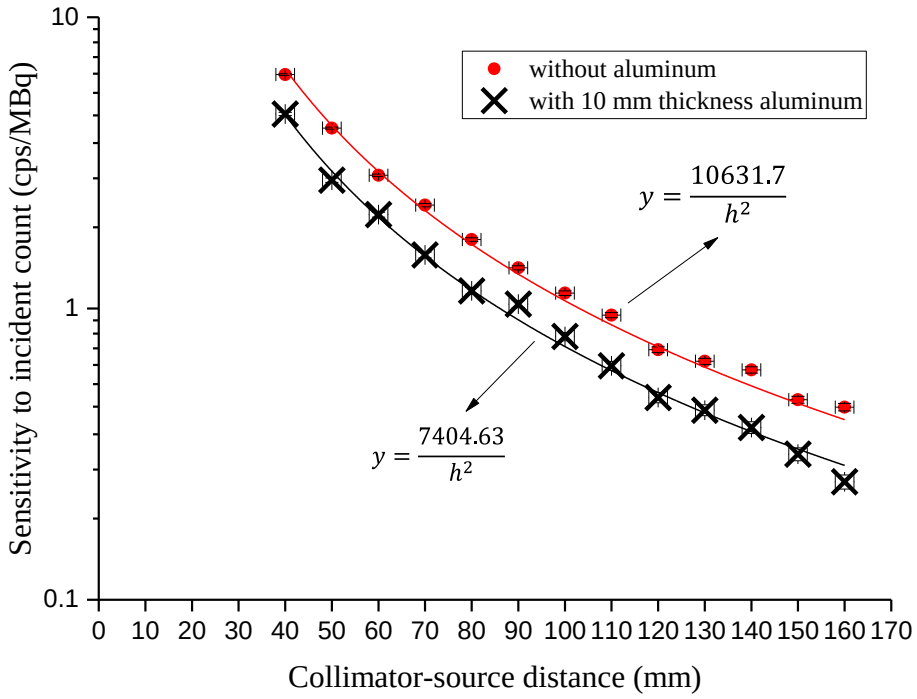

Figure 5.7: Graphs showing the relationship between the collimator sensitivity to incident count (cps/MBq) and collimator to source distance, *h*, using a 6 MBq ^{99m}Tc source solution with a 0.5 mm diameter pinhole collimator. The circles and crosses represent the collimator sensitivity without and with a 10 mm thickness aluminium bar, respectively. The acquisition time was ~306 s. R^2 for both lines was 0.99.

Figure 5.8 shows the results acquired from the analysis of the relationship between the collimator sensitivity, calculated with a 10 mm thick aluminium bar causing partial coverage of the ^{99m}Tc source at 50, 70 and 90 mm from the source, and the area of source uncovered (partially covering). As an example of the results, the sensitivity was reduced by 12%, 27% and 30 % at 50, 70 and 90 mm from the collimator respectively, when 50% of the source area was covered by the aluminium.

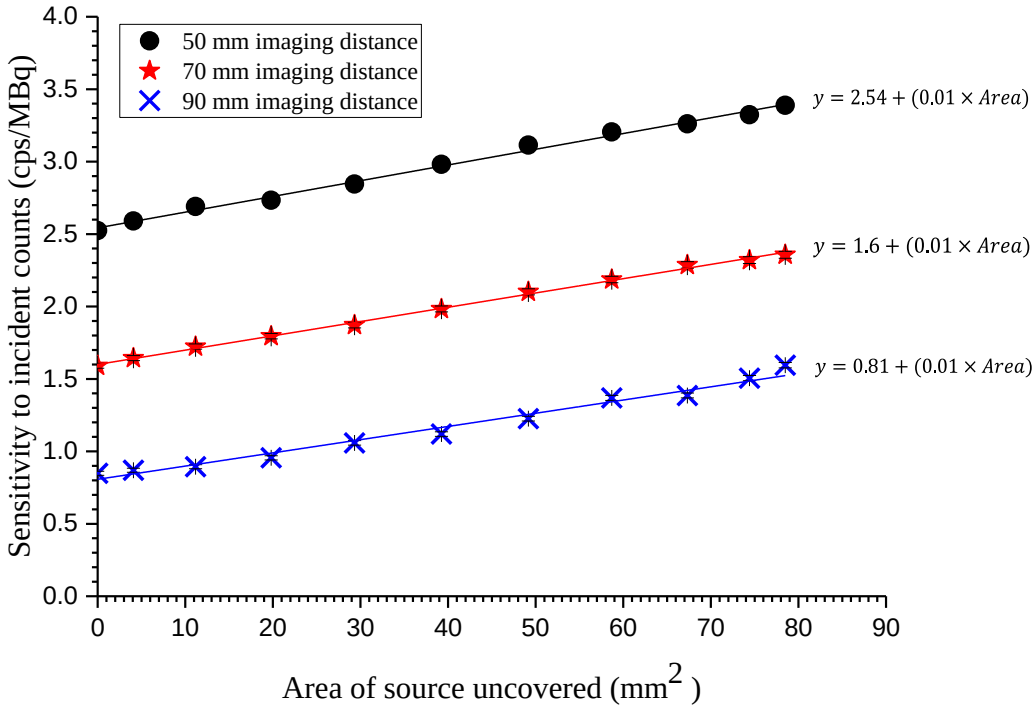

Figure 5.8: Graphs showing the relationship between the collimator sensitivity to incident count (cps/MBq) and the area of source left uncovered by a 10 mm thick aluminium bar, using a ^{99m}Tc radioisotope source in a hole (8 mm height, 10 mm diameter, 27 MBq activity). The HGC was fitted with a 0.5 mm diameter pinhole collimator. The circles, stars and crosses represent the 50 mm, 70 mm and 90 mm imaging distances from the source respectively. The acquisition time was ~306 s. R^2 for each of the three lines was 0.99.

Figure 5.9 shows the combination of gamma and optical images when the aluminium was used to partially cover the ^{99m}Tc source at 70 mm from the source. The partial coverage of the ^{99m}Tc source by the aluminium bar is evident in the Figure 5.9.

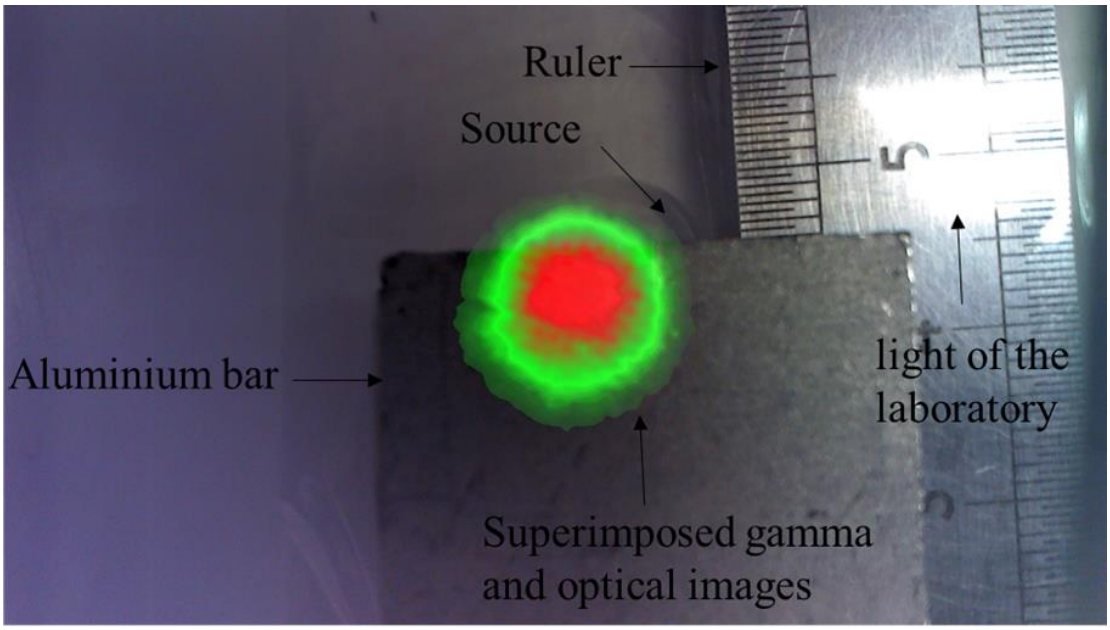

Figure 5.9: Superimposed gamma and optical images from a ^{99m}Tc source below the aluminium bar. Imaging distance was 70 mm from the source. The acquisition time was approximately 5 minutes.

5.3.3.3 Position of the Aluminium Relative to the Perspex (Position of the Bone Relative to the Soft Tissue)

To study the effects of bone relative to soft tissue on the detection of photons by the gamma camera, a 10 mm thick aluminium bar was placed in different positions with respect to the Perspex layers and the sensitivity of the gamma camera was measured. The result of the analysis of this simulation are shown in Figure 5.10. Figure 5.10 shows the relationship between the collimator sensitivity and incident count (cps/MBq) and the collimator to source distance (mm), using a ^{57}Co source with a 0.5 mm diameter collimator. As an example of the results, at a 40 mm distance from the collimator face the sensitivity was decreased by 42 ± 0.7%, 42 ± 0.7%, 39 ± 0.8% when the aluminium was *under*, *between* and *above* the Perspex respectively, while the sensitivity decreased by 41 ± 2.6%, 41 ± 2.4% and 40 ± 2.5% at a distance of 140 mm from the camera and at the same respective positions for the aluminium and Perspex. This represents a decrease compared to the calculated sensitivity when the source was directly beneath the pinhole collimator. When the source was under a 20 mm thick Perspex, at a 40 mm distance from the collimator face the sensitivity was decreased by 29 ± 0.5%, 29 ± 0.7%, 25 ± 0.4%

when the aluminium was *under*, *between* and *above* the Perspex respectively, while the sensitivity decreased by a 29 ± 1.3%, 28 ± 1.3% and 27 ± 1.2% at a distance of 140 mm from the camera and at the same respective positions for the aluminium and Perspex. In general, the maximum differences in the calculated sensitivity, depending on the position of the aluminium, were approximately ± 5%.

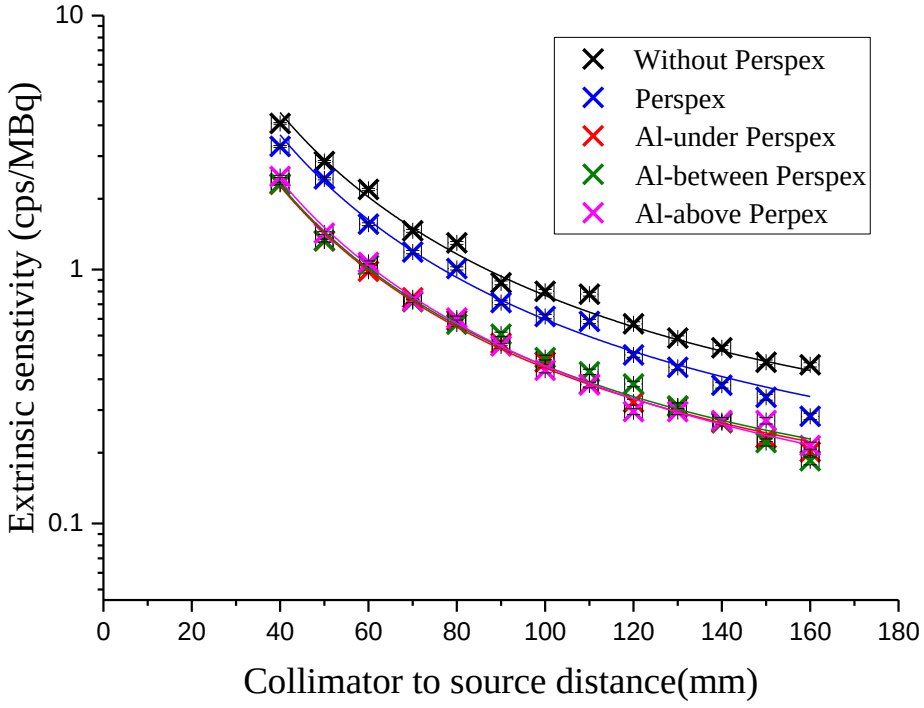

Figure 5.10: Graphs showing the relationship between the collimator sensitivity to incident count (cps/MBq) and collimator to source distance (mm), using a ^{57}Co source with a 0.5 mm diameter pinhole collimator. The black, blue, red, green and pink colours represent the collimator sensitivity without Perspex, with Perspex, aluminium under Perspex, aluminium between Perspex and aluminium above Perspex respectively. The acquisition time for each image was ~360 s.

5.4 Materials and Methods for depth estimation

Three phantoms (breast, head and neck, and chest) were used to simulate specific regions of the human body. The radioisotope source was placed in different positions inside these phantoms to simulate the different depths of the nodes within the body and to assess the performance of the HGC for abnormal tissue imaging and depth estimation [31].

5.4.1 Experimental setup

The hybrid gamma camera (HGC) was fitted with a 1 mm diameter pinhole collimator to image the phantom and to calculate the depths of the radioisotope sources inside the phantom at different distances from the collimator face, as described in chapter 4.

A radioactive ^{57}Co capsule source (8 mm diameter, 5 mm thickness and 40 MBq activity) was placed inside the phantom at different depths. A single camera was used to image the source, the camera was then displaced by 20 mm to obtain a second set of images (both optical and gamma), as seen in Figure 5.11. The various distances from the camera to the surface of the phantom were measured from the collimator face, and were varied between 60 mm to 160 mm in 20 mm steps.

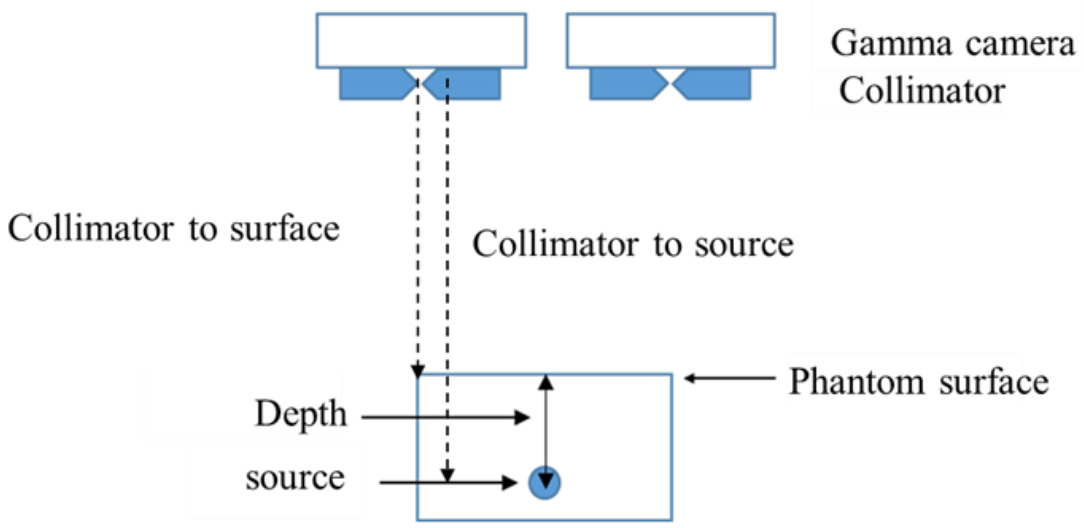

Figure 5.11: General schematic experimental setup for depth estimation.

The acquisition time for each gamma image was three minutes. The optical images were obtained from a single frame taken after the gamma image because the optical image is not dependent on acquisition time. This was repeated for each imaging distance in order to gain an estimate of the depth of the radioisotope over these distances. The actual (measured) depth of the radioisotope source was determined through direct measurement using a ruler.

The acquisition time of the gamma image was sufficient for the accumulated photon count on the detector to produce a clear gamma spot, which enabled the centre of the source to be easily localized. It was noticed that an increased acquisition time did not allow for a better localization, but only increased the accumulated photon count. Here, the acquisition time was increased to 4 and 5 minutes, but as mentioned this did not show any improvement in localizing the source centre. For example, when the camera was fitted with a 1 mm diameter collimator and the activity was approximately 22 MBq, for 153 second (1500 frame), 204 second (2000 frame) and 306 second (3000 frame) acquisition times, the recorded counts were 949, 1476 and 2150 photons respectively, at an imaging distance of 160 mm from the collimator source. Four hundred photons were found to create a gamma spot on the detector that was sufficient to allow the centre to be localized.

The imaging procedures were designed to allow imaging from several perspectives so as to simulate the location of tumour.

The depth of the radioisotope source inside the phantom was calculated for different perspectives (top, lateral, anterior and posterior) and different imaging angles, as dependent on the position of the camera. The measured (actual) depths were determined from the surface of the phantom using a ruler with ± 2 mm error, whilst the angles were measured using plastic goniometer with ± 2° accuracy.

In the investigation of the depths calculated for the source there were several potential sources of error. One of the major errors is in estimating the centre of gamma and optical spots, which led to an associated error in distance calculated between the two spots. This in turn affected the accuracy of the distance calculated between collimator and the source/surface, and thus the depth estimation of the radioisotope distribution.

5.5 **Breast Phantom**

Figure 5.12 shows a schematic of the experimental arrangement of the HGC and the breast phantom containing four radioactive source positions at different depths below the apex.

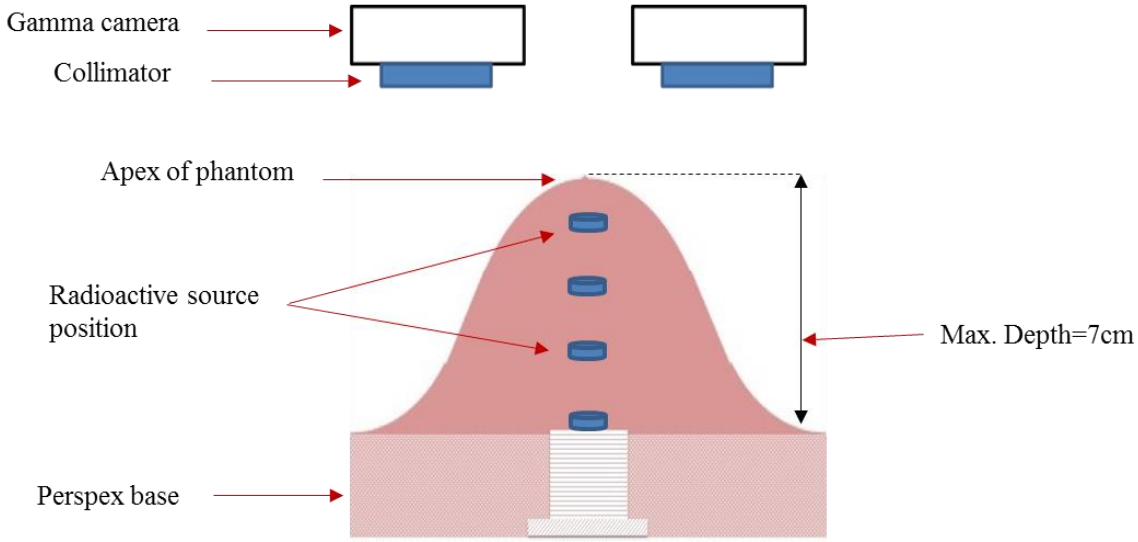

Figure 5.12: A schematic of the experimental arrangement of the HGC and the breast phantom, showing four source positions at different depths below the apex.

5.5.1 **Imaging procedures**

The breast phantom was imaged from above at angles of 10^0, 20^0 and 30^0 and perpendicular (0^0 to the *y*-axis), as shown in Figure 5.13, and from a lateral view (to the side of the breast phantom). The American Society of Breast Surgeons recommend a sensitivity of 95% and a false-negative rate of 5% for sentinel lymph node detection in breast tumours as being an acceptable rate; however, there is a strong need to improve detection preoperatively and intraoperatively [77]. This experiment was designed to simulate imaging procedures during surgery where the HGC could image from one angle and at different imaging distances, or image at one imaging distance with different imaging angles, in accordance with the patient's position on the bed inside the operating theatre. The experiments could also simulate different depths of accumulated radioisotope source within the body to allow simulation of the imaging process during surgery at different distances between the camera and the patient, in order to capture the largest number of the photons at the detector.

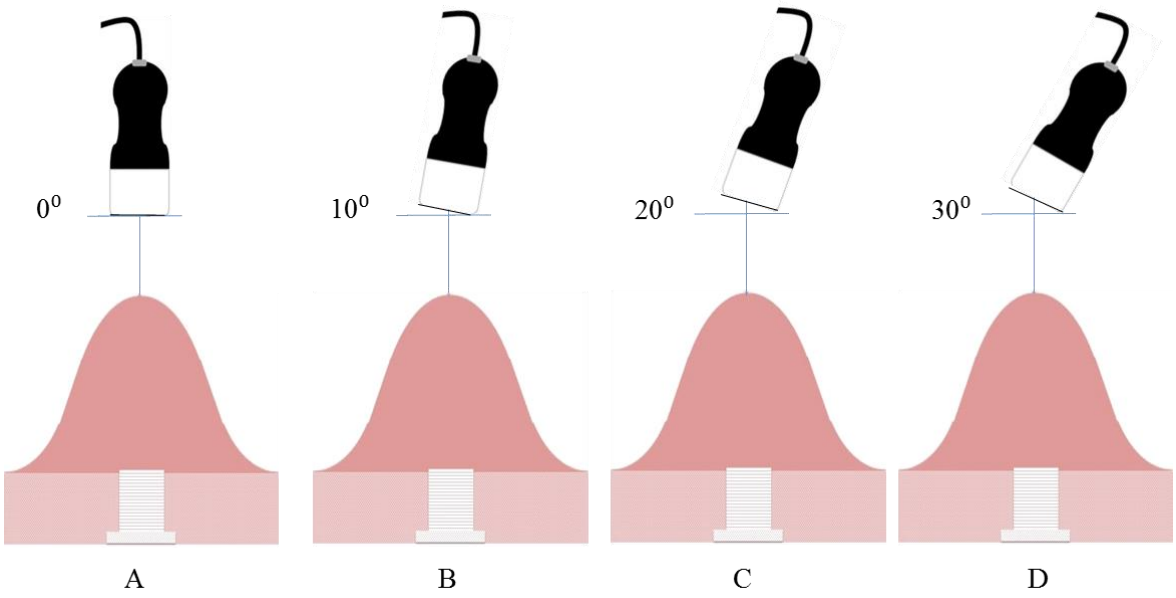

Figure 5.13: A schematic of the experimental arrangement of HGC and the breast phantom showing the different imaging angles; the imaging angles were 0^0 (A), 10^0 (B), 20^0 (C) and 30^0 (D).

5.5.1.1 **Top View**

For imaging from the top of the phantom, the camera was placed perpendicular above the phantom. A source was placed at depths of 20, 33, 50 and 70 mm from the apex of the dome, separately. The camera was initially positioned 60 mm above the apex of the phantom at a camera viewing angle of 0^o to the *y*-axis. The camera was then raised to a height of 160 mm in increments of 20 mm. A typical fused optical and gamma image, recorded at 120 mm above the apex (top view), is shown in Figure 5.14. This experiment was designed to simulate the imaging of a tumour and the surface of the body from above (perpendicular) during surgery.

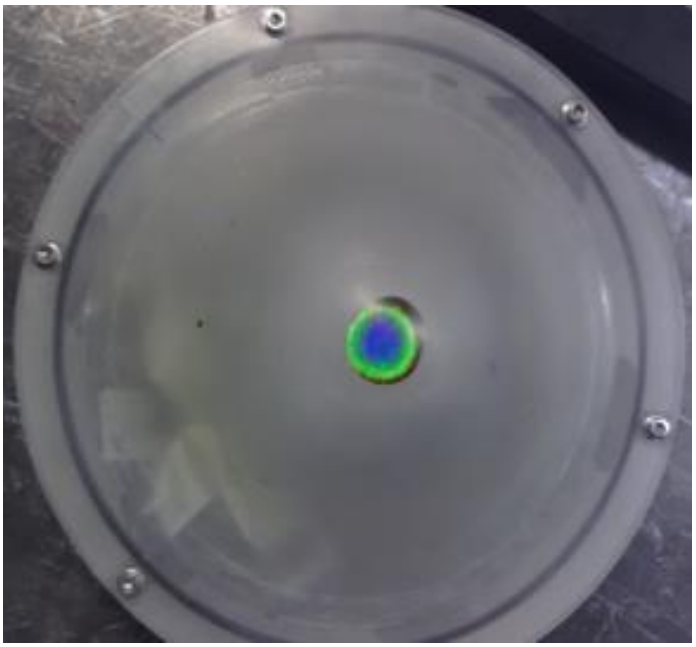

Figure 5.14: Superimposed gamma and optical images from a ^{57}Co source inside the breast phantom positioned at a distance of 50 mm below the apex (top view). The imaging distance was 120 mm above the apex (top view).

5.5.1.2 Lateral View

For lateral view imaging, a source was placed 33, 43 and 53 mm from the lateral side of the phantom, separately. The camera was initially placed 80 mm from the lateral surface of the phantom at a camera viewing angle of 0^{o} to the *y*-axis. The camera was then pulled back from the phantom to a maximum of 160 mm in increments of 20 mm (Figure 5.15). Figure 5.16 shows a typical fused optical and gamma image recorded at 100 mm from the side of the phantom (lateral view).

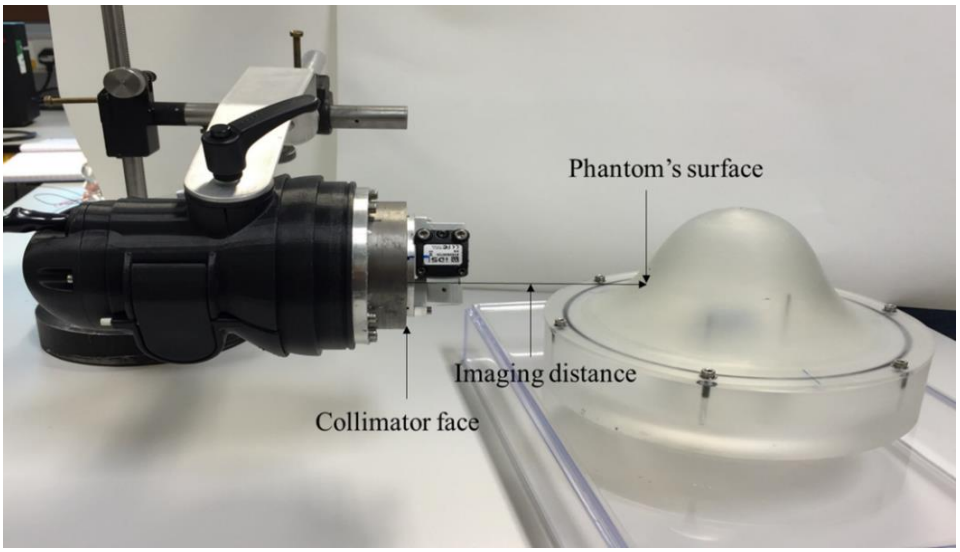

Figure 5.15: Photograph of the HGC positioned to take lateral images of the breast phantom.

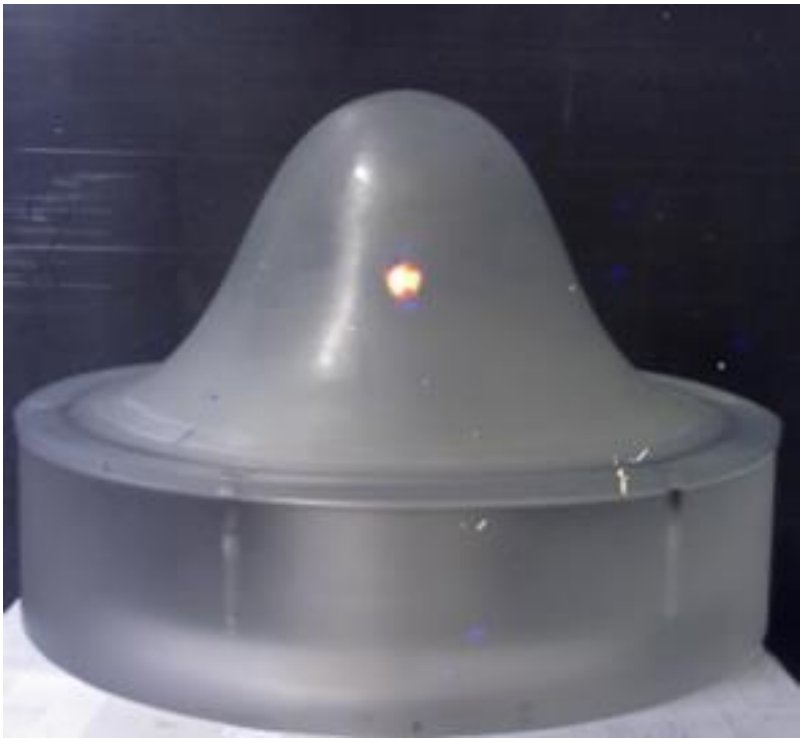

Figure 5.16: Superimposed gamma and optical images from a ^{57}Co source inside the breast phantom positioned at a distance of 43 mm beneath the surface (lateral view). The imaging distance was 100 mm to the side of the phantom (lateral view).

5.5.1.3 **Performance at different imaging angles**

The HGC was used to image the radioactive source (^{57}Co) and the breast phantom at different angles, θ (10°, 20° and 30°). A source was placed at distances of 20, 30, 53 and 70 mm below the apex of the dome. To simulate imaging by two cameras at a specific imaging angle, the first set of images (gamma and optical) were obtained at the first position of the phantom, which was then moved down by manually lowering a laboratory jack; the phantom was then displaced horizontally by 20 mm to obtain a second set of images (movement in the form of an 'L' shape). This is equivalent to using two cameras. An illustration of the experimental setup is shown in Figure 5.17.

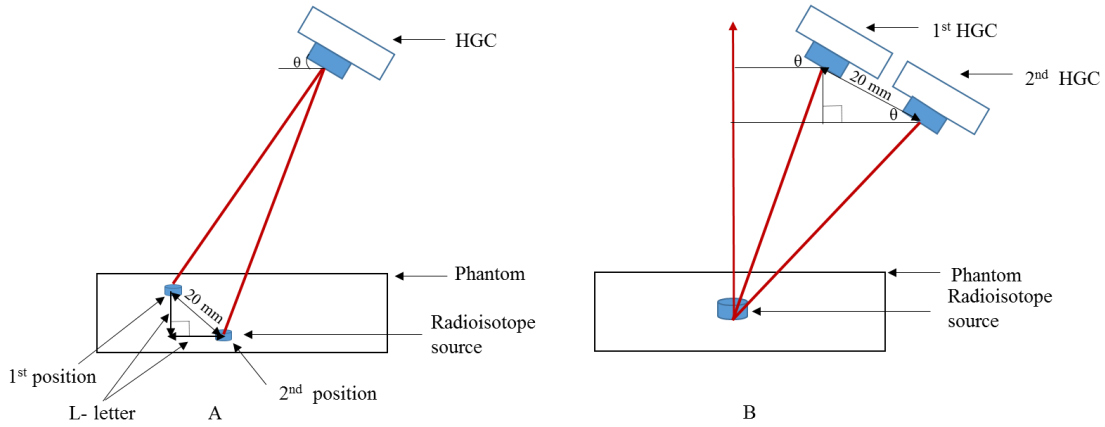

Figure 5.17: A schematic of the experimental setup at an arbitrary imaging angle; (A) using one camera to image one source at two different positions and (B) using a two-camera setup to represent the imaging procedures used during surgery.

5.5.2 **Results**

5.5.2.1 **Top and Lateral Views**

The measured depths were 20, 30, 53 and 70 mm below the apex, and were 33, 43, and 53 mm from the lateral side of the phantom, whereas the depths calculated for the source were determined experimentally. The results obtained from the analysis of the relationship between calculated depths (mm) and the camera-to-phantom distance (mm)

for sources positioned inside the breast phantom, as compared to the measured depths of the source over the same distances are summarised in Figure 5.18 (A) for the top view and (B) from the lateral view. In general, the differences between the calculated and actual values were no more than approximately 4% when the HGC axis was perpendicular to the source.

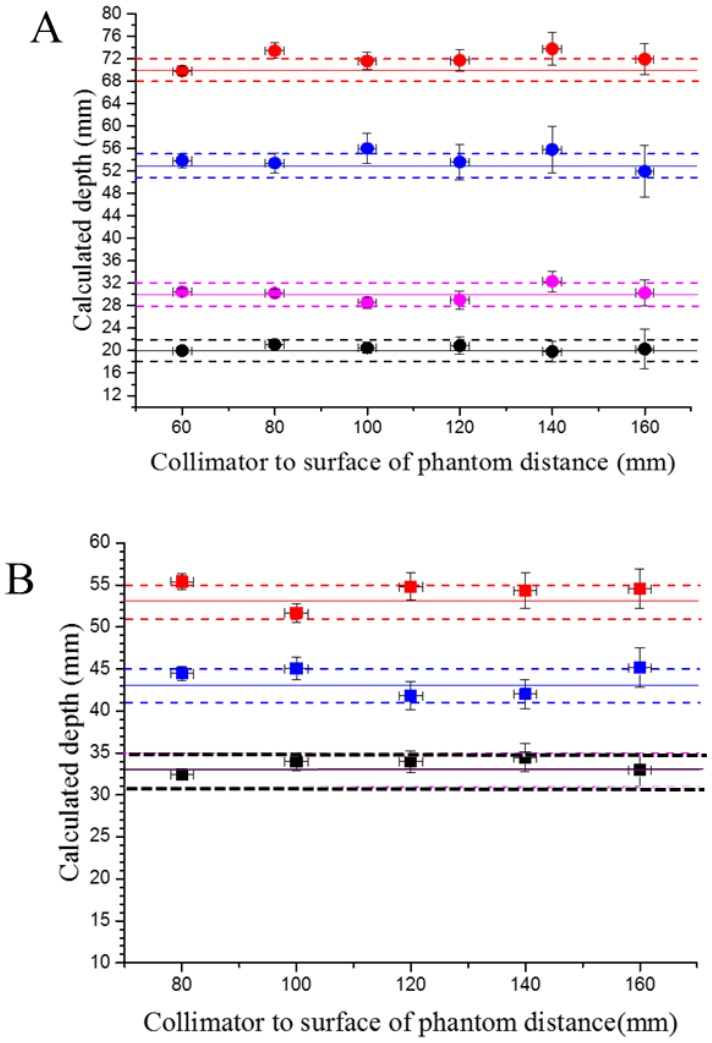

Figure 5.18: Relationship between calculated depths (mm) and the camera-to-phantom distance (mm) for a source at a different set positions (A) below the apex of the breast phantom and (B) from the lateral side of the phantom. The black, pink, blue and red colours indicate the calculated depths at set positions of 20, 30, 53 and 70 mm from the apex, and 33, 43 and 53 mm from the lateral perspective, respectively. The solid lines represent the measured depths of the source and the dashed lines the error in the measured depths of the source.

5.5.2.2 **Top View with Different Imaging Angles**

The measured depths from the apex of the phantom were 20, 30, 53 and 70 mm. Figure 5.19 shows a summary of the results acquired from the analysis of the relationship between the calculated depths and the distance from the collimator face for a source placed inside the phantom, as compared to the measured depths of the source over the same distances from the collimator. The imaging angles were at 10^0, 20^0 and $30^0 \pm 2^o$ to the *y*-axis, where the angles were taken at intervals of 10^o because the effect of an interval of 5^o on depth estimation was found to be small; the maximum selected angle was chosen as 30^o because this represented half the acceptance angle of the collimator, which cannot detect gamma photons at more than 30^0 imaging angle. Generally, the differences between the calculated and measured values were approximately 4% at the various imaging angles to the *y*-axis. The variation of calculated depth is small, for example, when the actual depth is 30 mm from the centre of the tumour, the error is 1.5 mm; this means the depth estimation is still within the source. This small difference in depth calculated shows there is small effect of imaging angle on depth estimation of the radioisotope within the body, and indicates the surgeons could use the HGC in the operating room at different imaging angles in order to obtain the best detection of gamma rays emitted from the source.

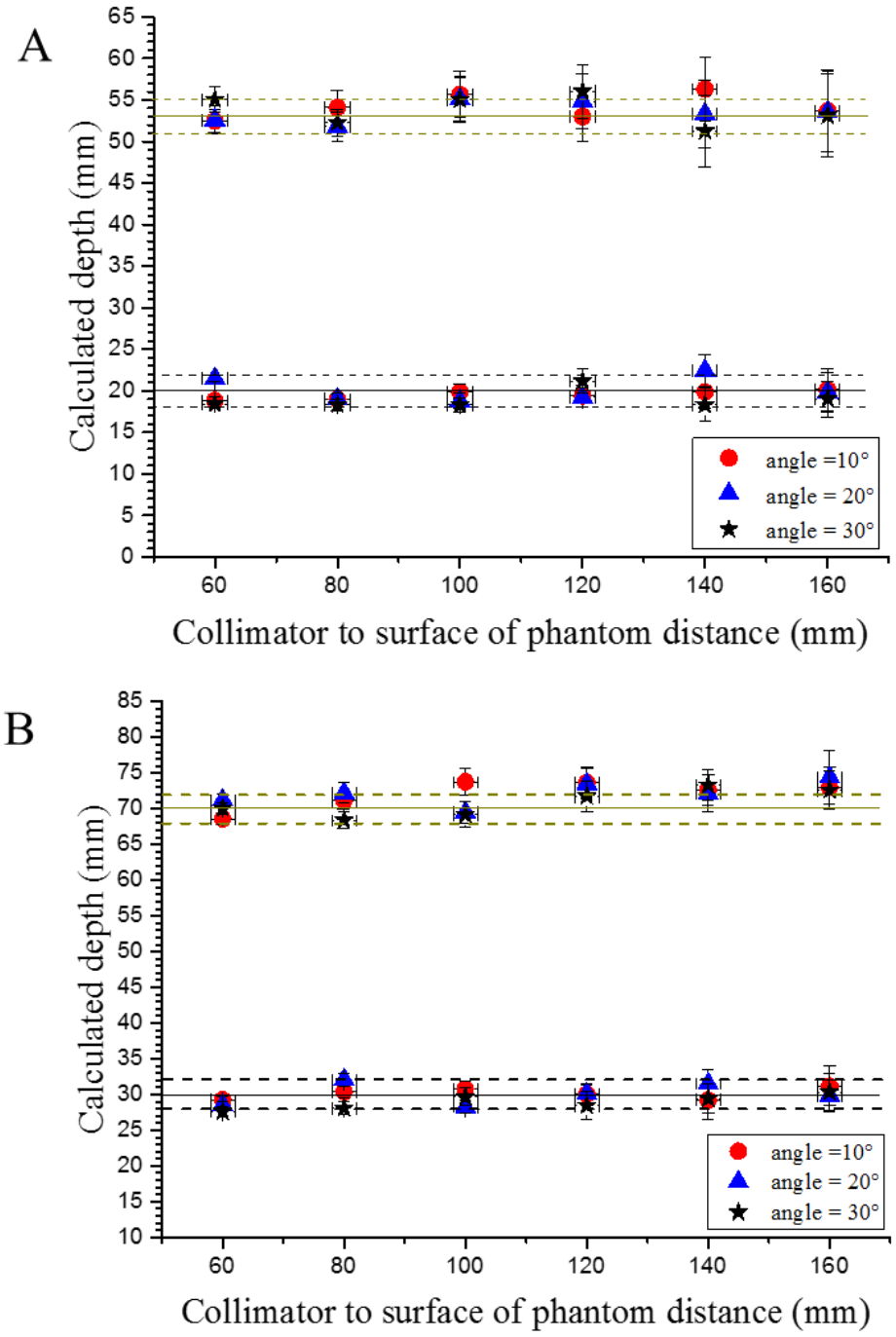

Figure 5.19: Relationship between the calculated depth (mm) and the camera-to-phantom apex distance (mm) for a source at the set positions below the apex of the breast phantom (A) 20 mm and 53 mm and (B) 30 mm and 70 mm with the hybrid camera at different imaging angles of 10^0, 20^0 and 30^0 to the *y*-axis. The red circles, blue triangles and black stars indicate the calculated depths at imaging angles of 10^0, 20^0 and 30^0, respectively. The solid lines represent the measured depths of the source, whereas the dashed lines represent the associated errors.

5.5.2.3 **Impact of imaging angle on depth estimation**

This study was designed to simulate the imaging process during operation at specific distance from the source, when surgeons need to move the camera to different angles in accordance with how the patient is positioned on the bed in the operating theatre. Actually, the result of this study depends on the previous figure (Figure 5.19), where the HGC imaged the source at distances of 60 mm and 160 mm from the top view with different imaging angles of 0°, 10°, 20°, and 30° to the *y*-axis. The results obtained from the analysis of the relationship between the calculated depths (mm) and imaging angle for a source positioned inside the breast phantom, and compared to the measured depths of the source over the same imaging angles, are shown in Figure 5.20. The maximum difference between the calculated and measured depths at each of the different imaging angles to the *y*-axis were consistent to within around 5%.

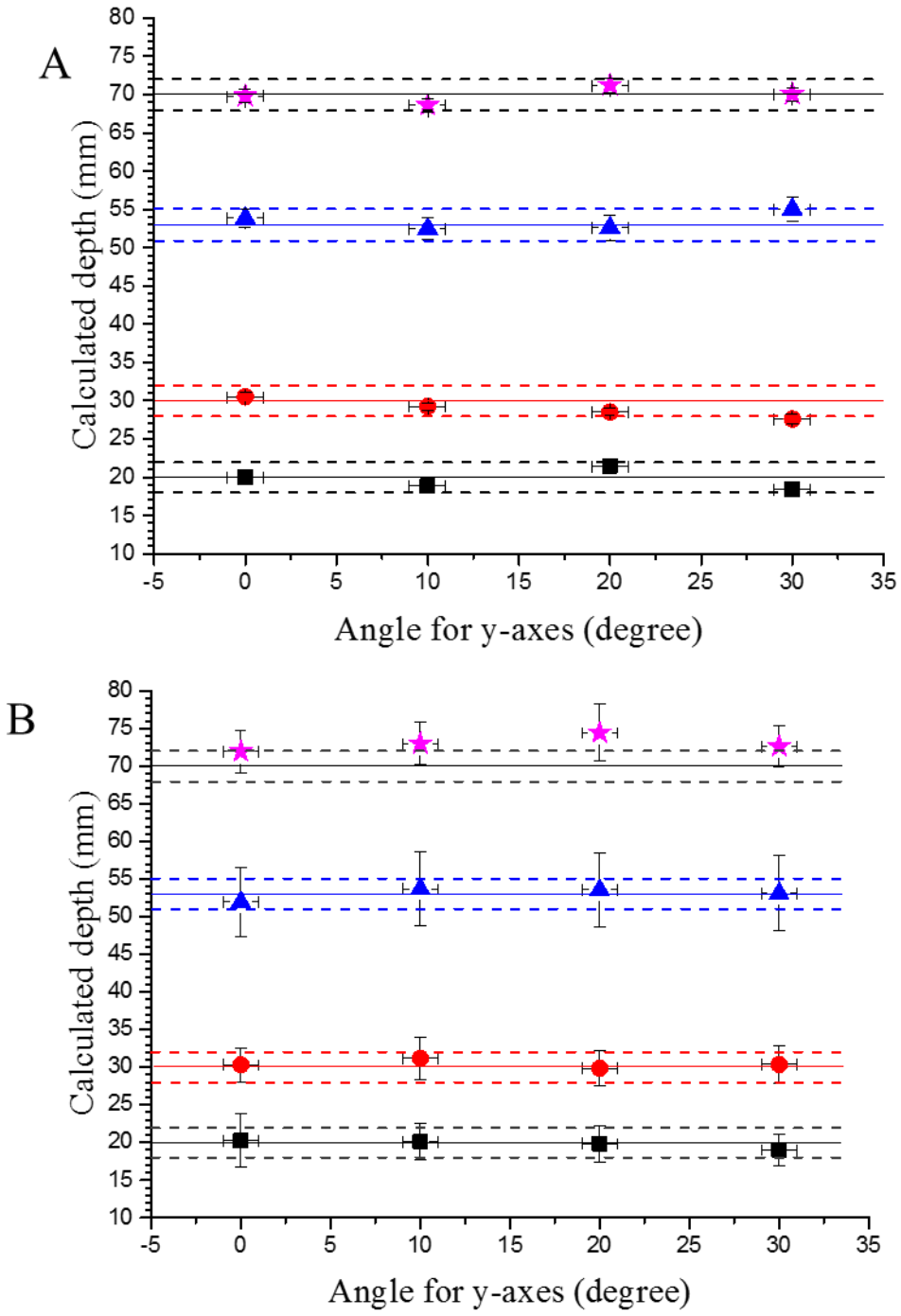

Figure 5.20: Relationship between the calculated depth (mm) and the different imaging angles (0^0, 10^0, 20^0 and 30^0) to the *y*-axis from the top view perspective at a 60 mm (A) and a 160 mm (B) imaging distance from the surface of the phantom. The black squares, red circles, blue triangles and pink stars indicate the calculated depths at set positions of 20, 30, 53 and 70 mm, respectively. The solid lines represent the measured depths of the source, whilst the dashed lines represent the associated error.

5.5.2.4 **Stereoscopic imaging**

To test the idea of stereoscopic (3-D) imaging, the HGC was used to image the breast phantom and sources, as described in section 5.5 for the top view. In this study, a single camera was used to image the phantom and source which was then moved horizontally by 20 mm to obtain a second set of images; this arrangement mimics the view of the human eyes. The source was placed in the centreline between the two cameras to ensure the same the distance and angle from the pinhole collimator to each of the cameras, and that the source would be within the field of view of the camera in each of these two positions.

The two HGC imaging systems (see Figure 5.12) offer the possibility of obtaining four separate images: two gamma ray, and two optical. These images could be offered as either 'fused' in optical and gamma pairs, or as individual images. In this stereoscopic imaging system, the combination of gamma and optical images was used to create a 3-D image. Adobe Photoshop CC 2015.5 software was used to generate 3-D images. Using two hybrid gamma and optical images, the first image was red filtered, whilst the second image was green filtered. Using cardboard Red Blue glasses, the image will have an apparent 3-D form, where the eyes will see the red and green colours which result from the red and the green filters with depth (see Figure 5.21). This figure illustrates the combined images from imaging the breast phantom with a single radioisotope source placed inside. This 'classic' 3-D image requires red/blue glasses to view the effect of the stereoscopic images.

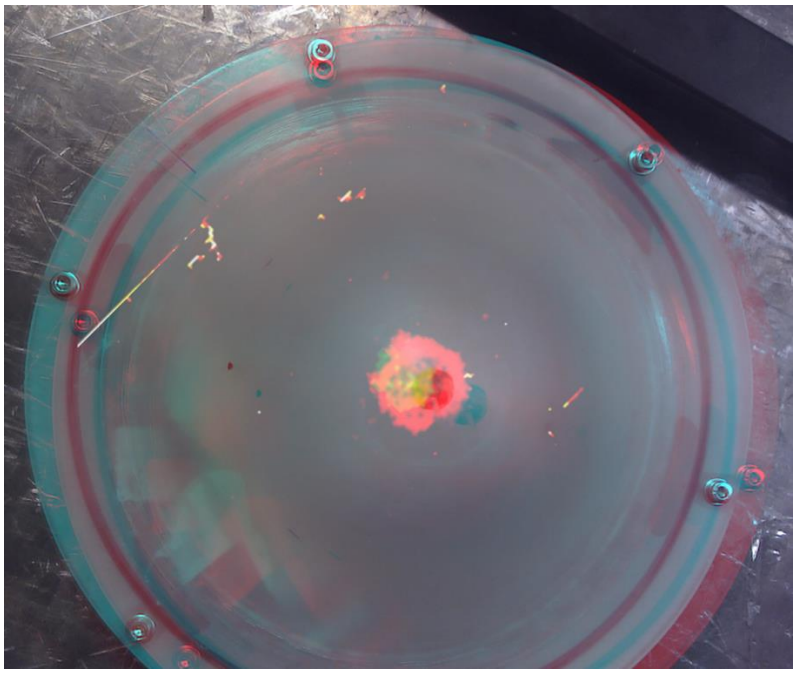

Figure 5.21: The stereoscopic image from the combined optical and gamma images of a single ^{57}Co radioactive source placed inside the breast phantom, with an imaging distance of 200 mm from the collimator face of the HGC.

5.6 Head and Neck phantom

Figure 5.22 shows the experimental layout for imaging the head and neck phantom using the HGC. The head and neck phantom contained a radioisotope source positioned at a specific depth beneath the surface for anterior imaging.

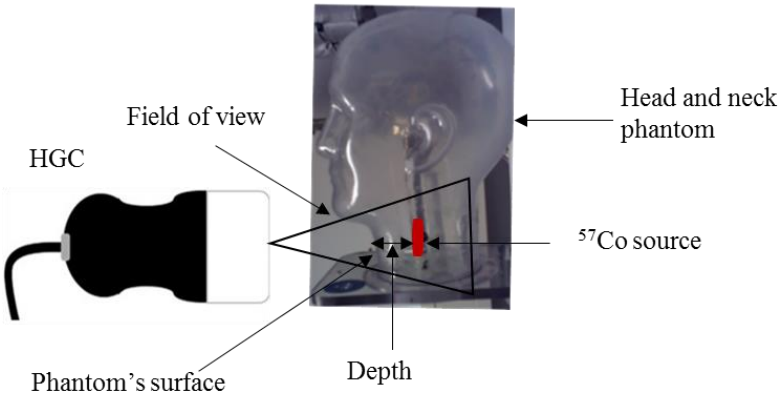

Figure 5.22: A schematic of the experimental arrangement of the HGC and the head and neck phantom showing a source positioned at a specific depth beneath the surface for anterior imaging.

5.6.1 Imaging procedures

5.6.1.1 Depth at different perspectives

While using the head and neck phantom, the camera-to-surface distance of the phantom was varied between 70 mm and 180 mm in 10 mm steps. A ^{99m}Tc radioisotope solution in a vial (5 mm height, 4 mm diameter and different activities between 10-14 MBq) was used to imitate the targeted nodes at various depths inside the head and neck of 10, 15, 20, 25, 30 and 35 mm, separately. The phantom's base was removed and the sources were fixed using blue tags at the different positions and depths, after which the base was replaced. The imaging was performed from different perspectives, i.e., lateral, posterior and anterior, in order to simulate the imaging process during surgery, including an attempt to avoid the effects of attenuation of the gamma radiation due to intervening bone (Figure 5.2).

Figure 5.23 provides an overview of the head and neck phantom imaging in different modes (the different orientations adopted) using the HGC. For example, the phantoms were placed on their sides to show the whole phantom with superimposed gamma and optical images. These experiments were designed to simulate SLNs located at certain depths under the skin of the head and neck region.

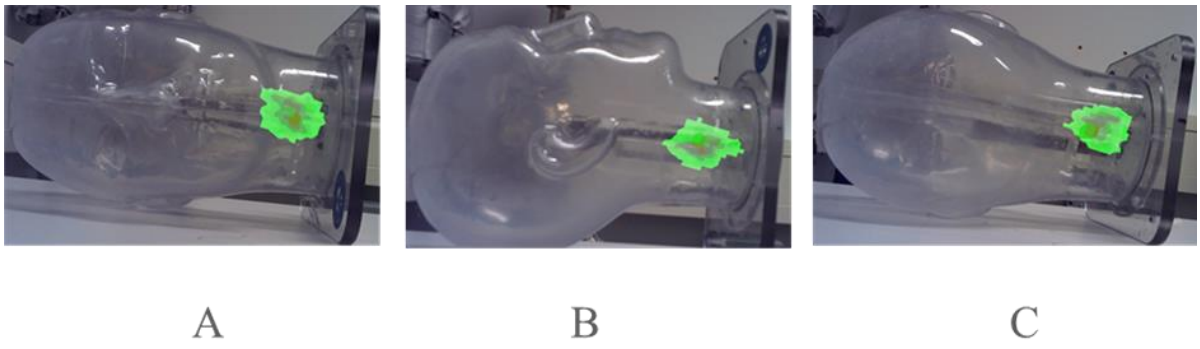

Figure 5.23: Superimposed gamma and optical images from a ^{57}Co source (40 MBq) inside the head and neck phantom positioned at a distance of 30 mm beneath the surface: (A) anterior view, (B) lateral view, and (C) posterior view. Imaging distance was 40 cm from the phantom surface.

5.6.1.2 **Multiple source in one setup**

Four vials containing ^{99m}Tc radioisotope solutions with low activities ranging from 0.75 to 0.94 MBq were placed at a number of different depths (15, 20, 30 and 40 mm) inside the phantom, whilst the imaging was performed from a posterior perspective. The acquisition time for each gamma image was four minutes. The imaging position was selected from the posterior side of the head and neck phantom because it is flat in shape, and the depth of the sources and the distance from the collimator to the surface can be measured in a straightforward manner. This experiment was designed to simulate a number of SLNs at different positions within the head and neck region in order to demonstrate the ability of the HGC to simultaneously detect positions and depths. Figure 5.24 shows a typical combined optical and gamma image with the HGC positioned 80 mm from the surface (posterior view).

Table 5.2: position, activity and depths of ^{99m}Tc liquid using in the Figure 5.24.

Position	1	2	3	4
Depth (mm)	15	20	30	40
Activity (MBq)	0.87	0.8	0.75	0.94

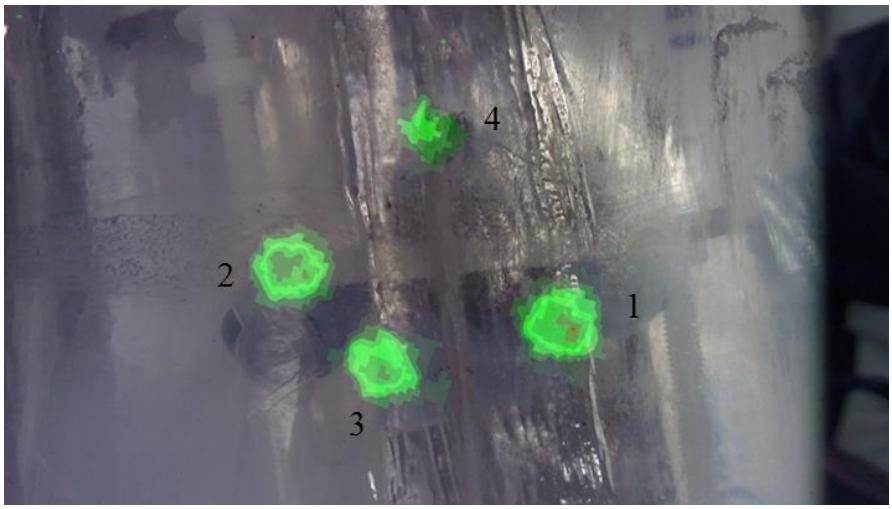

Figure 5.24: Superimposed gamma and optical images from a low activity ^{99m}Tc source inside the head and neck phantom positioned at distances of 15 (1), 20 (2), 30 (3) and 40 (4) mm below the surface (posterior view). The imaging distance was 80 mm from the phantom surface and the acquisition time was four minutes.

5.6.2 Result

5.6.2.1 Depth at different perspectives

The camera was positioned to image the source when placed at different positions inside the head and neck phantom, and from different perspectives.

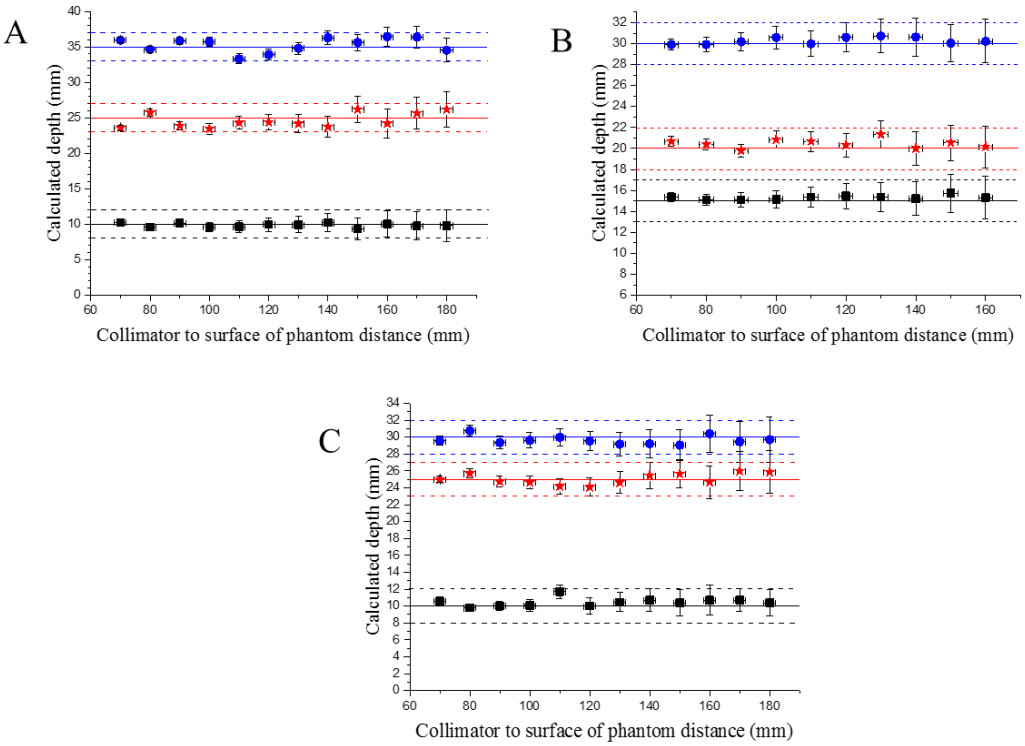

Figure 5.25: Comparison of the calculated depths (mm) and the camera-to-phantom surface distance (mm) for a source at a number of positions inside the phantom, from the anterior view (A), the lateral view (B), and from the posterior view (C). The black squares, red stars and blue circles are the calculated depths. The solid lines represent the measured depths of the source, whilst the dashed lines represent the associated error.

Figure 5.25 shows the results of the analysis of the relationship between the calculated depths (mm) and the distance from the collimator face (mm) for a source positioned inside the head and neck phantom compared to the measured depths of the source over the same of distances from the collimator (A) from the anterior view, (B) from the lateral view, and

(C) from the posterior perspective. In general, the differences between the calculated and measured depths were found to be no more than ± 5%.

5.6.2.2 **Different depths in one setup**

The camera was positioned to image four sources that were placed together of different positions and depths inside the head and neck phantom, 15, 20, 30 and 40 mm, and with activities ranging between 0.75 to 94 MBq, The results from the analysis of the relationship between the calculated depths (mm) and the distance from the camera (mm) for the sources placed inside the head and neck phantom compared to the measured depths of the sources over the same distances from the camera are summarised in Figure 5.26. The results show that the difference between the calculated and actual depths of the source were no more than ± 5%.

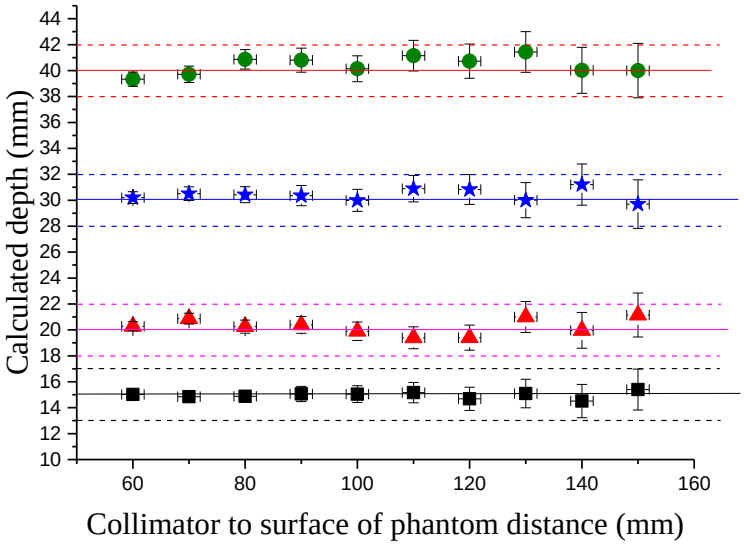

Figure 5.26: Comparison of the calculated depths and the camera-to-phantom depth with the camera in a posterior viewing position. The black squares, red triangles, blue stars and green circles are the calculated depths with the source positioned at depths of 15, 20, 30 and 40 mm, respectively. The solid lines represent the measured depths of the source, whereas the dashed lines represent the upper and lower limits of the measured depths of the source.

5.7 Chest Phantom

Figure 5.27 shows a schematic of the experimental arrangement of HGC and the chest phantom showing an aluminium plate between the Perspex layers and the source positioned below them at a specific depth inside the phantom.

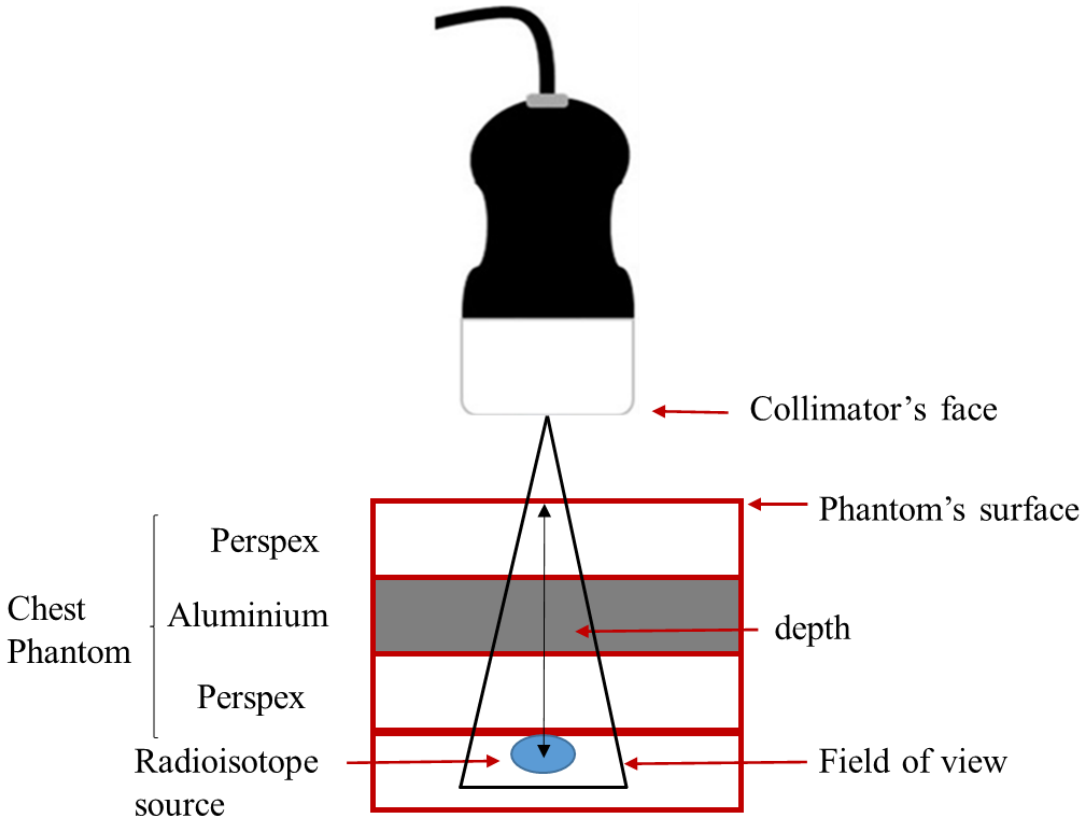

Figure 5.27: A schematic of the experimental arrangement of HGC and the chest phantom showing the source positioned at a specific depth inside the phantom with an aluminium plate between the Perspex layers.

5.7.1 Imaging procedures

The HGC was used to image the source at different imaging distances (collimator to phantom surface) that was varied between 40 mm and 160 mm in 10 mm steps. A ^{99m}Tc radioisotope source in a hole (6 mm height, 5 mm diameter and 8-12 MBq activity) was placed at varying depths (20, 30, and 50 mm) beneath the surface of the chest phantom, whilst the imaging was from a top perspective, as per Figure 5.4 B.

An example of the chest phantom imaged from above, is shown in Figure 5.28. The aluminium bar was placed above the source such that it was in the centre of the chest phantom. The light on the right side of the aluminium bar is due to one of the laboratory lights. In this experiment, the design of the chest phantom is equivalent to the design illustrated in Figure 5.4 B. This was a simulation of a tumour located at certain depths under the skin in the chest region.

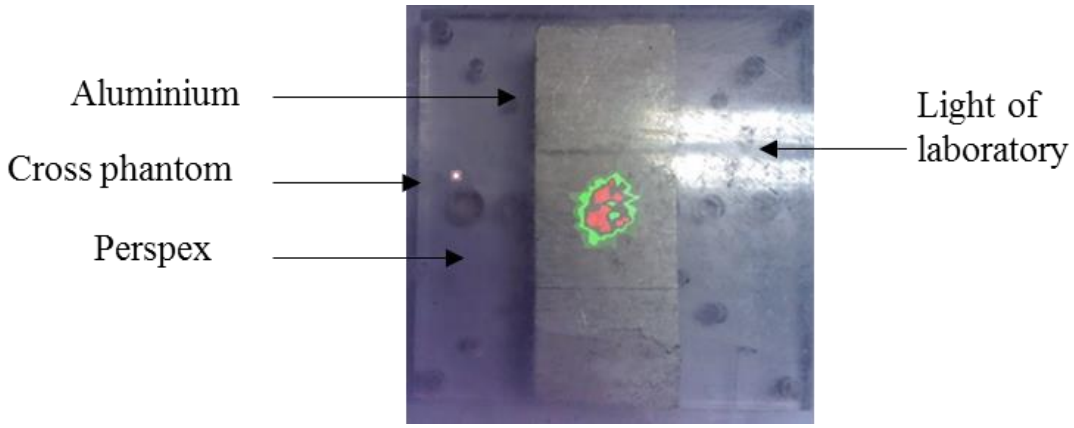

Figure 5.28: Superimposed gamma and optical images from a ^{57}Co source that was placed inside the chest phantom 50 mm below its surface. The imaging distance was 160 mm from the phantom's surface. The acquisition time was three minutes.

5.7.2 **Result**

The measured depths of the source were 20, 30 and 50 mm from the surface of the phantom, which were imaged from above. The results of the analysis of the relationship between the calculated depths (mm) and the camera-to-phantom distance for sources at three set positions inside the chest phantom compared to the measured depths of the source over the same distances from the collimator are shown in Figure 5.29. These results show that the differences between the measured and calculated depths of the source over a range of camera-to-phantom distances were approximately ± 5%.

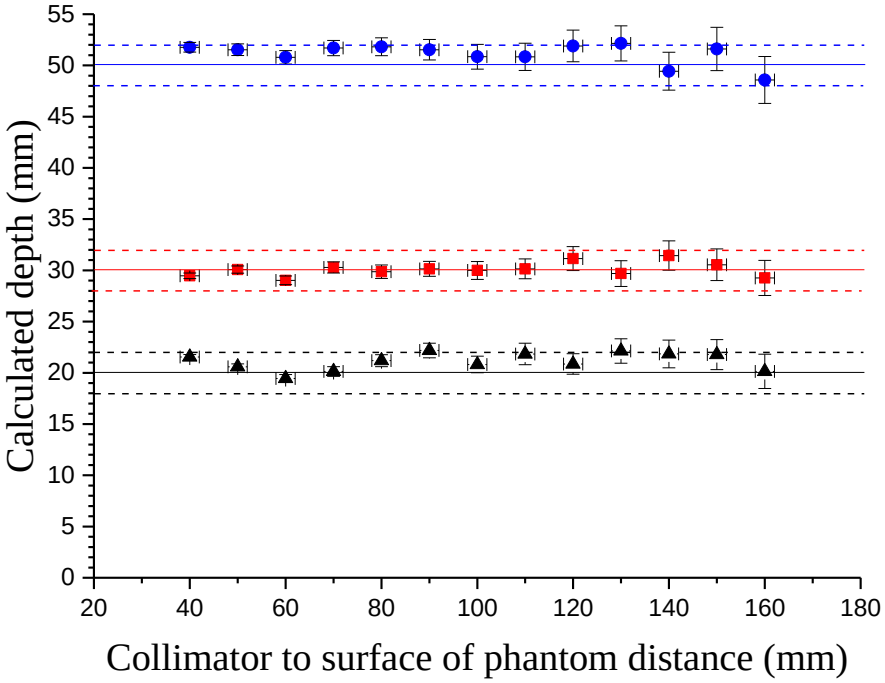

Figure 5.29: Comparison of the calculated depths (mm) and the camera-to-phantom surface depths (mm) for a source at a number of positions inside the phantom (anterior view). The black triangles, red squares and blue circles are the calculated depths at actual depths of 20, 30 and 50 mm respectively. The solid lines represent the measured depths of the source, whilst the dashed line represents the associated errors.

5.8 The performance of the hybrid gamma camera in estimating the depth of accumulated radioisotopes inside the body: clinical study

Melanoma is a serious health problem and is increasingly occurring around the world. Accurate identification of the sentinel lymph node (SLN) is the most important factor in diagnosing melanoma in the early stages [163]. The primary criteria to determine and evaluate melanoma patients are sentinel lymph node biopsy (SLNB) procedures[164]. Lymphoscintigraphy imaging to locate SLNs inside patients who suffer from melanomas requires the intradermal injection of a radioisotope source such as (^{99m}Tc- nanocolloids) surrounding the melanoma site[165].

The melanoma can spread to different parts of the body such as the leg and back, but the most dangerous is the spread in the head and neck area [166]. One of imaging systems

trialled for melanoma diagnosis is the Freehand SPECT system, which is a combined gamma probe or portable gamma camera and optical camera [167]. This system showed the ability to estimate the depth, which was found to be useful by surgeons [141]. The HGC, as previously shown, is a portable SFOV camera that has the ability to provide gamma and optical images simultaneously. This could help depth estimation of radioisotope accumulations within the surgical area [18].

The aim of the study was to evaluate the HGC performance for the depth estimation of the radioisotope accumulation within a small number of patients.

5.8.1 Patient Imaging

To clinically assess the performance of the HGC for estimating the depth of the radioisotope accumulation inside the body, two volunteer patients were studied, where the first was injected in the lower leg and the second in the back. To complete this assessment clinically, this work has received ethical approval from Research and Innovation, the University of Nottingham NHS Trust and the National Commission for Research Ethics in the United Kingdom (Reference no. 17/YH/0041).

5.8.2 Material and Method

The HGC was fitted with a 1 mm diameter pinhole collimator to image the two patients who suffered from leg and back melanoma, imaging was during pre-operative SLN detection procedures in order to localise SLNs and determine the area and depth of radioisotope accumulation. The imaging distance from the HGC to surface of the patient was 120 mm and 150 mm from a top view perspective for the first and second patient respectively. The acquisition time was 204 seconds for each gamma image. The first patient was injected in the region of the right ankle with a ^{99m}Tc- nanocolloid (20 MBq), and the camera was moved approximately 21 mm between each set of images (in total two gamma ray and two optical) (Figure 5.30 A). The second patient was injected in the back (near to the shoulder) with ^{99m}Tc- nanocolloids (20 MBq), and the camera was moved approximately 17 mm between each set of images, Figure 5.30 B.

The gamma spot created by the accumulated gamma photons on the detector were from photons emitted from the radioisotope source within the body. The optical spot was determined from the centre of combined gamma and optical images. The estimation of the gamma and optical centres lead to the determination of the distance between the two gamma spots / two optical spots. Then the distance from collimator to source/surface could be calculated. The depth estimation is the difference between these distances.

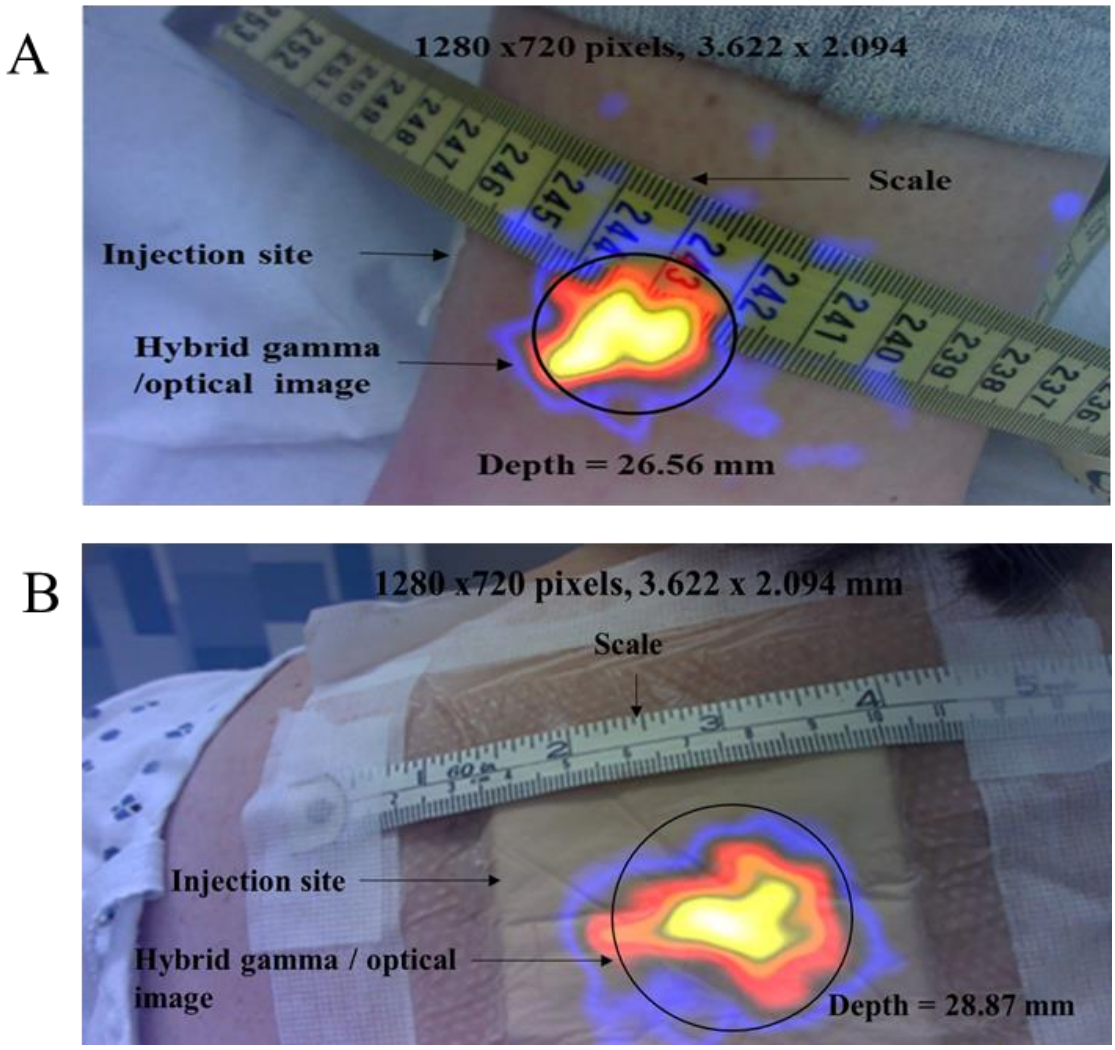

Figure 5.30: A combined gamma and optical image of radioisotope sources (20 MBq ^{99m}Tc) injected into the ankle of the right patient's leg (A) (first patient), and in the patient's back (B) (second patient). Imaging distances of 120 mm and 150 mm from the surface of the cover of the HGC were used for (A) and (B) respectively.

5.8.3 Results

5.8.3.1 First Patient

The depth of the accumulated source (^{99m}Tc) within the ankle of the right patient's leg could be estimated, which depends on the calculation of the distance from collimator to source/ surface. Figure 5.31 shows the optical images of the right patient's leg that was determined from the combined gamma and optical images. The depth in this instance was equal to 26.56 ± 0.92 mm. Because there is no measured depth (actual depth) inside ankle to compare with calculated depth, the calculated depth within the patient's leg may be reasonable when compared to the adult's leg that is around 70 ± 5 mm. The result in this instance shows that there is a possibility of being able to estimate the depth of abnormal tissue within the body using the HGC with top view imaging.

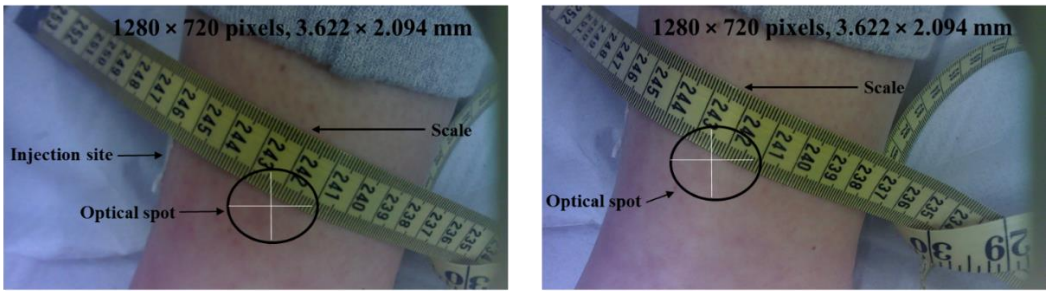

Site 1 Site 2

Figure 5.31: Two optical images (1280 × 720 pixels, 3.622 × 2.094 mm) show the injection site of the ^{99m}Tc source that was injected into the ankle of the right patient's leg, where the centres of the two optical spots were used to calculate the distance from the collimator to the skin of the patient. Site 1 was given by the first camera position, and site 2 is by the second camera position. The distance between the two camera positions is 20 mm.

5.8.3.2 Second patient

The depth estimation of accumulated radioisotope source within the back of the patient (near to the right shoulder) has been investigated. The distance from collimator to accumulated source and to surface (skin) was calculated. Figure 5.32 shows the optical images of the back of the patient depends on the combined gamma and optical images. The calculated depth of the accumulated source (^{99m}Tc) within the patient's back was

around 28.87 ± 1.69 mm. There is no actual depth (calculated depth) known inside the patient's back to compare with the calculated depth, so the calculated depth may be reasonable when compared to the same size of the adult that is around 140 mm ± 5 mm. The result indicates that there is a potential of being for estimation the depth of radiolabelled tissue within the body using the HCG with top view imaging.

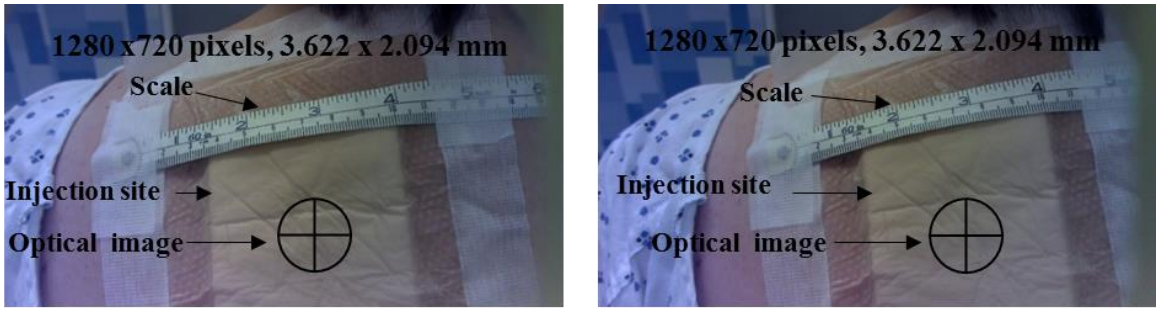

Site 1 Site 2

Figure 5.32: Two optical images (1280 × 720 pixels, 3.622 × 2.094 mm) show the injection site of the ^{99m}Tc source that was injected into the patient's back. The centre of the two optical spots was used to calculate the distance from the collimator to the surface of the skin. Site 1 was given by the first camera position, and site 2 by the second camera position. A 17 mm distance was found between the two camera positions.

5.9 Discussion

This work was carried out to assess the ability of the HGC to image sources within different phantoms. Phantoms were used to simulate parts of the human body and different sources used to simulate the different depths and positions inside the body (breast, head and neck, and chest).

In this study, various imaging procedures for the source within the phantom were used to simulate imaging procedures and tumour location during surgery. The source was imaged inside a breast phantom from the top and from a lateral view so as to simulate SLNs within soft tissues. Similarly, the source was imaged inside a head and neck phantom from different imaging perspectives; the anterior, lateral and posterior, to simulate tumours and SLNs located between bone and soft tissues and to study the possibility of

avoiding attenuation due to bone density. The source within the chest phantom was imaged to simulate a tumour or SLNs between a bone and soft tissue, in a scenario where it would otherwise be impossible to avoid attenuation due to bone, such as with an ectopic parathyroid gland in the thymus. Detection of various sources with low activity within the phantom in a single setup were used to simulate a number of tumours or SLNs with different positions within the body.

The imaging distances have an effect on the creation of the image (photon accumulation) on the detector. If the camera is near to the source, there is an increase in the number of photons detected which results in the creation of a spot, the centre of which, can be determined easily (see Figure 5.16), whereas if the camera is far from the source, there is a decrease in the number of photons detected and that leads to difficulty in estimation of the centre of the configured spot (see Figure 5.23). The sensitivity and resolution of the gamma camera deteriorates with increased distance, which affects the creation of the image on the detector. For example, the HGC was used to image a 2 mm diameter source when fitted with a 1 mm diameter pinhole collimator, whose sensitivity and resolution were 3.35 cps/MBq and 11.22 mm respectively, at an 80 mm imaging distance. At a 160 mm imaging distance, the sensitivity and resolution were 0.9 cps/MBq and 20.94 mm, respectively, as described in chapter 3. In this result, the effect was small on an estimation of the centre of the image, leading to a small error in the depth estimation of the radioisotope within the phantom. To avoid this problem during surgery, the position of the camera must be near to the source (near to the surface of the patient's skin).

The aluminium affected the sensitivity of the gamma camera due to absorption of gamma photons, thus decreasing the number of photons detected. The calculated sensitivity showed that there is a reduction in the sensitivity when the radioisotope source is beneath the aluminium bar, and with an increased imaging distance, because of the attenuation of the gamma photon by the aluminium. The reduction is approximately 10% greater than expected from theoretical considerations due to the aluminium not being pure. The effect on sensitivity of partially covering the source with aluminium is less than when the aluminium completely covers the source, as expected. Clinically, there is a possibility that the camera could not detect the target tissue when it is under the bone with a low level of activity (see chapter 3).

For a 10 mm thick aluminium with 20 mm thick Perspex, the sensitivity of the camera decrease by 42% from the sensitivity with the source only and decrease by 29% of the sensitivity with 20 mm Perspex only. This indicates the reduction effect of Perspex on the sensitivity is 13%. The effect of the position of a 10 mm thick aluminium in relation to the Perspex layers (under, between or above the layers of Perspex) on the collimator sensitivity of the camera is approximately 5%. This difference indicates that the position of the aluminium has approximately the same effect on the sensitivity of the gamma camera because the gamma photons pass through the same materials; therefore there is no difference in the percentage absorption expected for each. This means that when the source is under the bones and tissues together, the location of the bone (above, under or between the tissues) has the same effect on the number of photons detected.

One of the major sources of error in estimating the depth of the radioisotope can be attributed to difficulties in determining the exact centres of the gamma and optical spots, especially when the gamma spot contains few photons, which is, in part, related to the sensitivity of the camera and centroid method employed. Also, there are other sources of error such as the distance between the two cameras, and the distance from the collimator to the source and the surface of the phantom. For example, a one-pixel error in determining the centre of the optical spot leads to a 0.02 mm difference in the distance between the two optical images, or a ± 0.3% difference in the collimator-to-surface distance that can affect depth calculations by ± 1%. A 0.1 pixel error in determining the centre of the gamma spot will lead to a 0.002 mm difference in the distance between the two gamma images, and an approximate ± 3.3% difference in the collimator-to-source distance, which can affect the depth estimation by ± 6%. A 1 mm error in distance between the two cameras can lead to a ± 5% error in the distance from the collimator to the surface of phantom and an approximate ± 6% error in the collimator-to-source distance, and finally an error in depth calculation of ± 6% for the measured depth. This indicates that the error in determination of the centre of the optical spot may not affect the calculation of the distance between the camera and surface of phantom, therefore will have little impact on the depth estimate, whereas the error in estimation of the centre of the gamma spot has a significant impact on the depth estimate.

The error in the depth estimation of the source within the phantom can also be used to simulate the error in the depth of the tumour within the body during surgery, despite the

fact that the surface of the patient's body is not flat (as for the phantoms). The error in depth estimation could be reduced in two ways: the first is to build two cameras in one housing, therefore ensuring the distance between them will be constant, whilst the second would be to determine the centre of the gamma and optical spots in an automated manner. The accuracy of the depth estimation is higher when the imaging distance between the camera and the target is reduced.

In order to calculate the depth of the source within phantoms, the source within the breast phantom was imaged at different angles ranging between 10^0 and 30^0 to the *y*-axis, using the HGC. The range of imaging angles had little effect on the measured and calculated depths with the difference being approximately ± 5%.

Also, the HGC was used to image a radioisotope source that was positioned at different sites inside three phantoms (breast, head and neck, and chest). The imaging was from different perspectives (top, anterior, lateral and posterior) in order to calculate different depths of the source. At the different imaging distances, the maximum difference between the measured and calculated depths is around ± 5%. The imaging procedures were performed to assess the ability of the HGC to image the phantom from different perspectives and to estimate the depth of the source as suitable with the patient's position during surgery. The differences between depths (calculated and measured) was due to the errors identified in the preceding paragraph and/or experimental setup. A stereoscopic imaging concept was used to create a pseudo 3D image using two 2D images, which are obtained from two cameras at the same time.

Clinically, the depth of the accumulation of radiopharmaceuticals in the two melanoma patients was calculated, the first was in the right leg and the second was in the back. These have been estimated depending on the gamma and optical images that were obtained from imaging the injection site by the HGC. These depths were approximately 26.56 ± 1.69 mm and 28.87 ± 1.69 mm from the patient's skin (surface). Since there is not a known measured depth (actual depth) to the accumulated radioisotope within the patient's leg or back to compare with calculated depth, it can be seen that the calculated depth of the accumulated radioisotope source may be reasonable when compared to the same size of the adult that is around 70 mm ± 5 mm for the leg and around 140 mm ± 5 mm for the back for the two cases examined.

5.10 Conclusion

This chapter describes the estimate of different depths of source within a phantom with different perspectives as a simulation of the depth of radiolabelled tissue within a patient using a novel small field of view (SFOV) hybrid gamma camera (HGC) that combines optical and gamma imaging.

The simulation of the three phantoms (breast, head and neck, and chest) illustrates that it is possible to use the HGC in order to obtain the depth estimation for the radioisotopes within these phantoms. By moving the HGC, there is possibility to avoid any effect on the detection of the gamma rays emitted from the body, such as by obscuration by bone(s) and the patient's position on the bed. These advantages were supported by the small differences between calculated and actual values.

The simulation of the effect of bones on the sensitivity of the HGC was as expected. Therefore the effect of bone within the body should be taken into account during the diagnosis and localisation of the tumour because the sensitivity will be reduced when the source is beneath soft tissue alone, or beneath bone and soft tissue together.

At the different imaging angles, the small differences between depth estimation and actual depth inside the breast phantom at different imaging distances indicate that even if the HGC is not perpendicular to the source, the depth could still be estimated with small error, even when the imaging angle is as large as 30^0. The camera performance reduces the precision required for positioning the camera when used with angles ranging between 0^0 and 30^0 in the operating theatre.

Although the differences between the calculated and measured depths with imaging phantoms were approximately 5%, the results show that the dual HGC imaging system could offer an accurate means of determining the localisation and the different depths of radioisotope-labelled tissue targets, where the camera is used to image from top, lateral, posterior and anterior views. This error in calculated depth is small when it is compared with the error of the calculated depth in the previous study by Mathelin et al., which was 5 mm [25]. Therefore, the results of this work appear to suggest that HGC could be a promising technique in terms of providing support in the operating theatre.

Clinically, there was no measured depth to compare with the calculated depth of the radioisotope accumulations within the two melanoma patients; the size of the patient's leg was taken into account to estimate the validity of the calculated depth. Although further study is needed to give a more detailed understanding about the use of the HGC in estimating the depth of radiolabelled tissues within the operating theatre, the results here show that there is possibility to estimate the depth of accumulated radioactivity within the body.

Chapter 6: **The effect of source movement on depth estimation**

6.1 **Introduction**

Patient movement can include involuntary motions such as breathing, and there may also be voluntary movement of the legs, head and shoulders, etc. These kinds of motion may lead to image abnormalities during imaging [168].

Patient motion is one of the potential causes of deterioration in diagnostic image quality, which leads to difficulties in diagnosis, especially for SPECT and PET images where patients can be required to remain motionless for extended periods due to the long acquisition times required for these methods [169]. A reduction of acquisition times during imaging can lead to increased patient comfort and a consequent reduction in patient movement and reduction in the artefacts ultimately present in the target image [170]. If the image quality is not adequate for diagnosis, re-imaging will be required, resulting in an additional radiation dose for the patient.

The distortions in images caused by respiratory activity can be reduced and corrected. Chun reported that artefacts in an image can be corrected or reduced using various methods such as attenuation / scattering correction, which are dependent on the matrix of hybrid imaging scanners such as SPECT/CT and PET/CT [171], where this matrix is 512x512 for a CT scan and 128x128 for SPECT and PET [172]. The gating method can also be used to correct for image artefacts due to breathing motions, where the breathing cycle can be divided into a number of time gates (images) according to the stage of breathing, with the data for each gate then being stored [173, 174]. A number of factors can affect the formation and size of an artefact, which can be associated with patient respiratory movement or movement of other parts of the body, while other factors include the nuclear medicine apparatus and the technologist's actions [175].

There are many types of source movement that can occur during a patient's breathing cycle, such as vertical or diagonal movements relative to a fixed camera, as shown in Figure 6.1. The length of such a motion may change depending on the variations in patients' breathing cycles. The expansion and contraction of the lungs during normal

respiration causes the movement of the tumour inside the lung and diaphragm; a diaphragm motion averages about 15 mm in height (range 1-19 mm) [176], with a normal breathing rate of 12-20 times per minute [177].

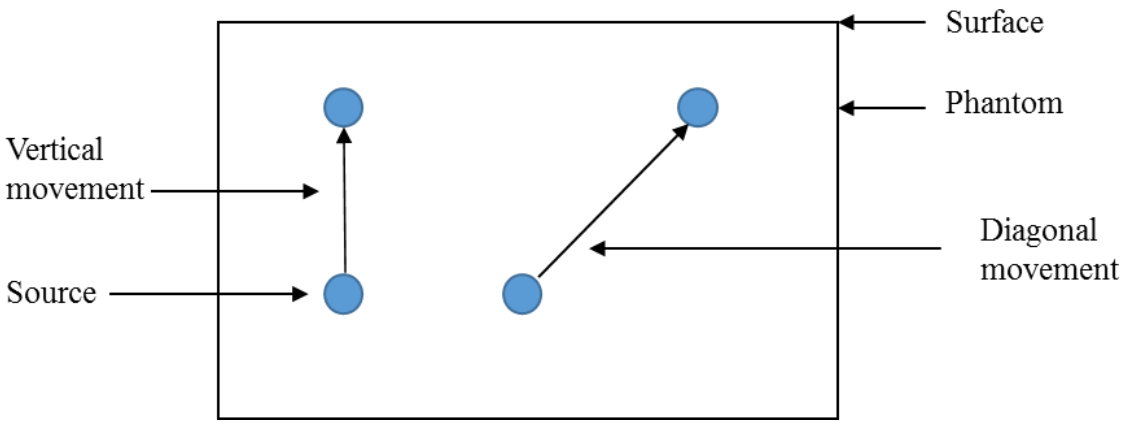

Figure 6.1: A diagram of the type of source movements within a body.

Although the type and degree of patient motion might affect the clinical diagnosis of abnormal tissue [178], Stevens et al. reported that the tumour motion distance does not depend on the location or size of the tumour, therefore suggesting that tumour motion should be evaluated individually [179]. Figure 6.2 shows the distance travelled by the tumour within a lung cancer patient during breathing; this image was obtained using a CT scan [180].

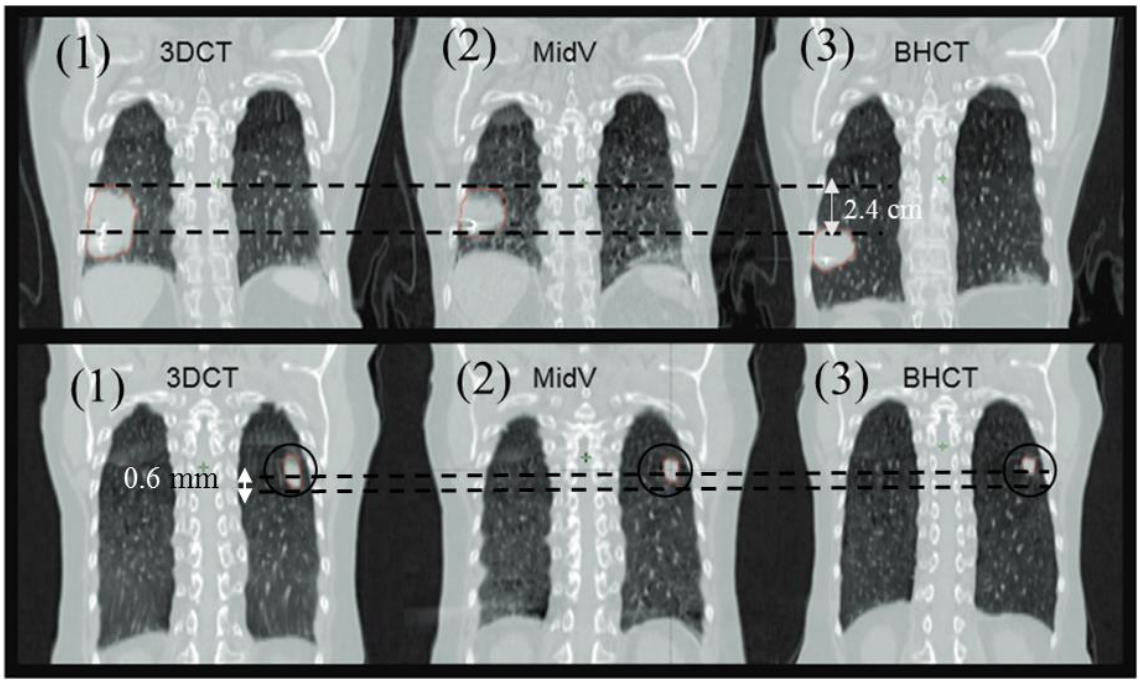

Figure 6.2: CT scans of two patients with large deviations in gross target volume (GTV) between lung scans: (1) conventional three-dimensional CT (3DCT), (2) four-dimensional CT (4DCT) mid-ventilation bin (MidV) and (3) breath-hold CT (BHCT). The upper row shows images from a patient with a tumour in the right lower lobe, the craniocaudal (CC) tumour motion was 2.4 cm. The lower row shows a patient with a tumour in the left lower lobe. The CC tumour motion was 0.6 cm, reproduced with permission from [180].

The objective of this chapter is to simulate tumour motion within the body and examine the ability of the HGC to estimate the depth of a moving radioisotope source.

6.2 Motion-induced artefacts

Hybrid imaging systems are an essential tool in nuclear medicine. For diagnosis, the most common are PET / CT and SPECT / CT. However, patient motion during hybrid imaging can create abnormalities in the image. These abnormalities may lead to clinical misinterpretation because of a mismatch between combined images, for instance due to the patient's breathing. Wen Yang et al. reported that the artefacts caused by the respiratory motion can cause two potential issues; the first of these aspects is that the SPECT data is obtained throughout the entire breathing period and this may result in blurring of the image; the second is that CT data obtained at a specific stage of the

respiratory cycle may not match the SPECT data, therefore will not reflect the real effect of attenuation of this data.

Patient motion also generates artefacts in reconstructed PET/CT images due to a difference in acquisition time between CT and PET. The long acquisition time for PET and SPECT scans (ranging from 15 to 30 minutes) means that respiratory movement causes blurring in the image that is attributable to the mean time of multiple breathing cycles (4 seconds is a normal breathing cycle) [181, 182]. In addition, the short acquisition time for CT scans (approximately 10 seconds) may result in a mismatch between the CT and PET images [183-185]. Hence, there are differences in the appearance and location of the diaphragm and base of the lungs, thus creating an artefact, mismatching and misdiagnosis [186]. For instance, many studies have demonstrated that the influence of respiratory motion in fluorodeoxyglucose (^{18}F FDG) PET imaging has resulted in blurring, which has affected the estimation of the liver target volume and reduced the standard PET absorption values [185, 187, 188]. Figure 6.3 shows such a mismatch in a simulated PET–CT image due to respiratory motion.

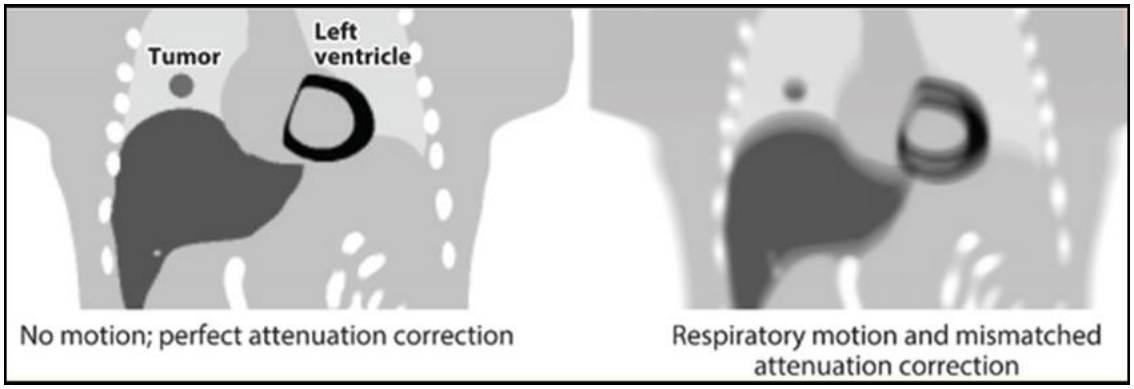

Figure 6.3: Simulated coronal slice of a human torso obtained by PET showing the effects of respiratory motion during combined acquisition of PET and CT data. In the left-hand image, there is no motion, so the lung tumour, liver boundaries, and the left ventricle of the heart are all well delineated. In right-hand image, respiratory motion is a present, so the blurring and mismatches in attenuation correction lead to artefacts and numerical errors, which introduce the potential for misdiagnosis (reproduce with permission from [93]).

6.3 Position of the radioactive source moving between two levels

6.3.1 Phantom study

A phantom was constructed to simulate the movement of the source (target) and surface (skin) during breathing. It consists of a Styrofoam layer of dimensions 8 cm x 8 cm x 8 cm that was used to fix the plastic vials, and Perspex plates (10 x 10 cm with different thickness) that were used to represent the surface of the phantom (Figure 6.4 A). The shape of the plastic vials was a combination of cylindrical and conical shapes, the former shape having a height of 5 mm, whilst the latter was 15 mm in height with a maximum diameter of 5 mm where it meets the cylinder (Figure 6.4 B).

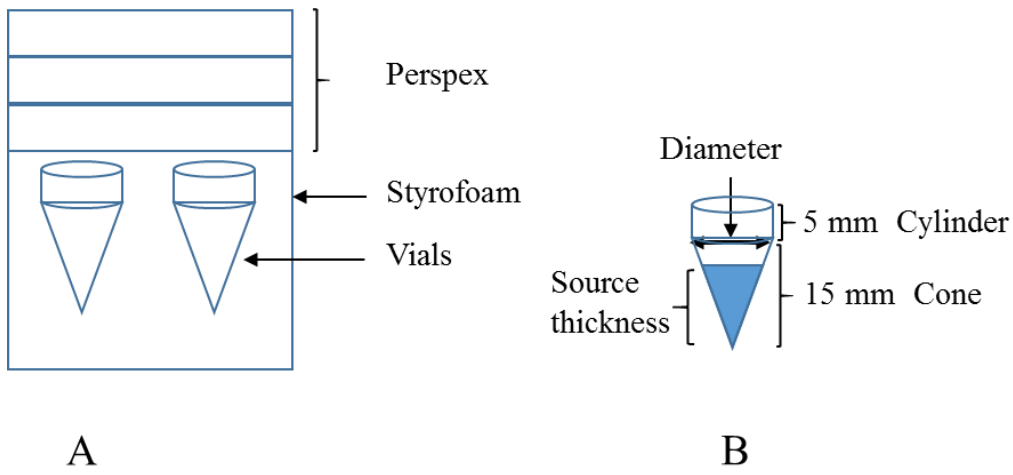

Figure 6.4: (A) A schematic of the phantom showing two vials and (B) the details of the vial.

6.3.2 Material and Method

One of the main problems in determining the position of an accumulated radioisotope source within the body is movement of the source during acquisition of an image, so this experiment was designed to investigate this effect. Two sources were used instead of two cameras, as explained in the chapter 4, section 4.8. The HGC was fitted with a 1 mm diameter pinhole collimator to image the two sources. Two vials were filled with 6 MBq ^{99m}Tc solution then placed in the phantom. Two ranges of imaging distance from centre of activity were assessed; the first was between 87 mm and 207 mm for the calculated distance from collimator to source, and the second was from 83 mm to 183 mm. The counts were recorded in 20 mm steps, with an acquisition time of three minutes for each

imaging distance. The calculated distance from the collimator to source was dependent on the distance between the two gamma images and the distance between the two cameras (two sources); see chapter 4 for further details. The source was at the maximum distance from the collimator face, then moved by 5, 10, 15 and 20 mm toward the collimator face, which was carried out by manually moving a laboratory jack. The number of movements of the laboratory jack from minimum to maximum distance from the collimator face were (18-20), (15-17), (11-13) and (8-10) times per minute for 5, 10, 15, 20 mm source movements respectively. The average collimator-to-source distance was used to represent an average distance between the minimum and maximum distances from the collimator.

The creation of the gamma image on the detector depends on the number of photons detected, where the average number of photons (recorded counts) detected from the source depends on the distance from the collimator face. All optical imaging was conducted at two distances; the first image was taken at the maximum distance to the camera whereas the second image was recorded at the minimum distance from the camera (Figure 6.5).

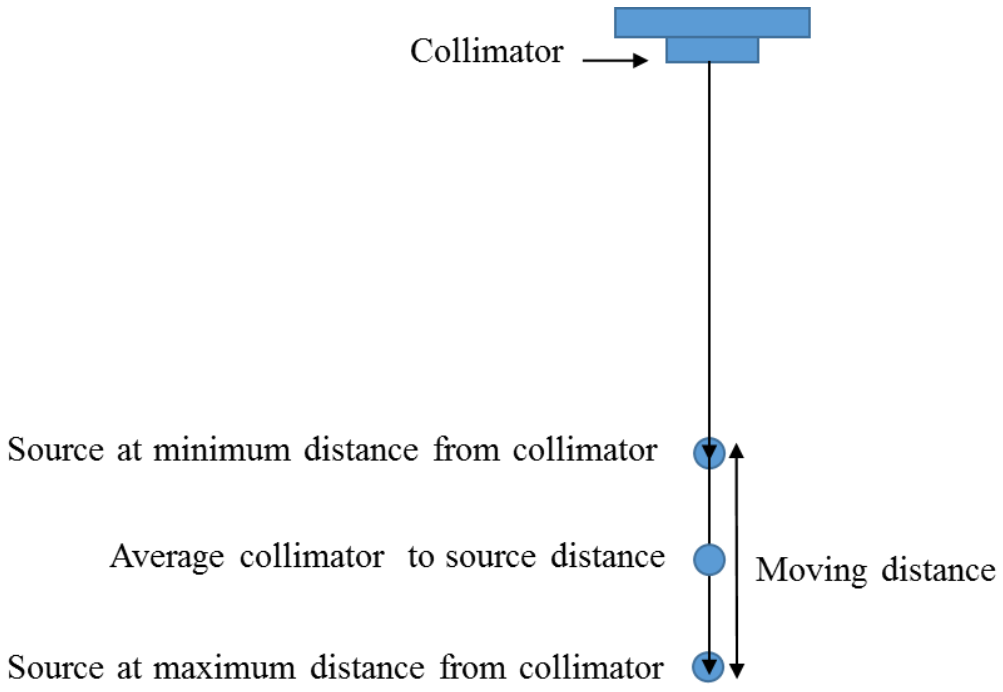

Figure 6.5: A schematic of the experiment used to image the source at the minimum and maximum distances from the collimator face.

6.3.3 **Results**

The distance from the collimator to the source was calculated when the source moved between the two levels over the range of imaging distances; see Figure 6.6.

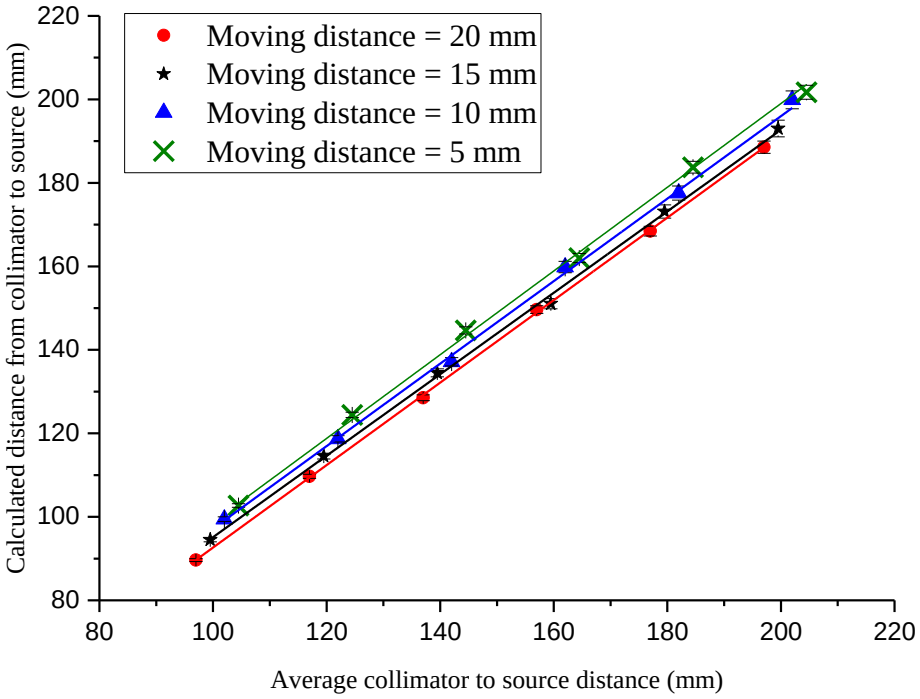

Figure 6.6: Relationship between the calculated distance from collimator to source and the average collimator-to-source distance at different moving distances. R^2 was 0.99 for the fitted line for all distances (5, 10, 15 and 20 mm).

The results obtained from the analysis of the linear relationship between calculated distances from the collimator face to the source (mm) versus average collimator-to-source distance (mm) for different imaging distances are summarised in Figure 6.6. As an example of the results, at an imaging distance of 127 mm from the collimator face the calculated distances were 124.4 ± 0.05 %, 118.7 ± 2.8%, 114.6 ± 4.3% and 109.7 ± 6.6% mm when the moving distances were 5, 10, 15 and 20 mm with a ± 2 mm error, respectively. The calculated distance from the collimator face was within the expected value because the number of photons detected at the minimum distance from collimator had a significant effect on creating the image on the detector. Also this distance was

between the average distance between the two levels and the minimum distance from the collimator.

The calculated distance from the collimator to the source for a 20 mm moving distance was less than the 5, 10 and 15 mm moving distances for each imaging distance, for example, as shown in Figure 6.7. This figure shows the effects of the moving distance of the source towards the collimator on calculated distance from the collimator face. The calculated distance from the collimator was less than measured distance (average distance) by approximately 1.74%, 2.6%, 5.3% and 8.2 % towards the collimator for the 5, 10, 15 and 20 mm moving distances respectively. This shows that the calculated distance when moving the source between two levels will always be near to the minimum distance from the collimator. The reason for the decreasing the calculated distance from collimator face with increasing moving distance is to adopt the maximum distance from the source. Whereas if the minimum distance from the source is adopted, the calculated distance from collimator face will increase with moving distance. This does not affect the determination of the distance from the collimator to the source at a single moving distance.

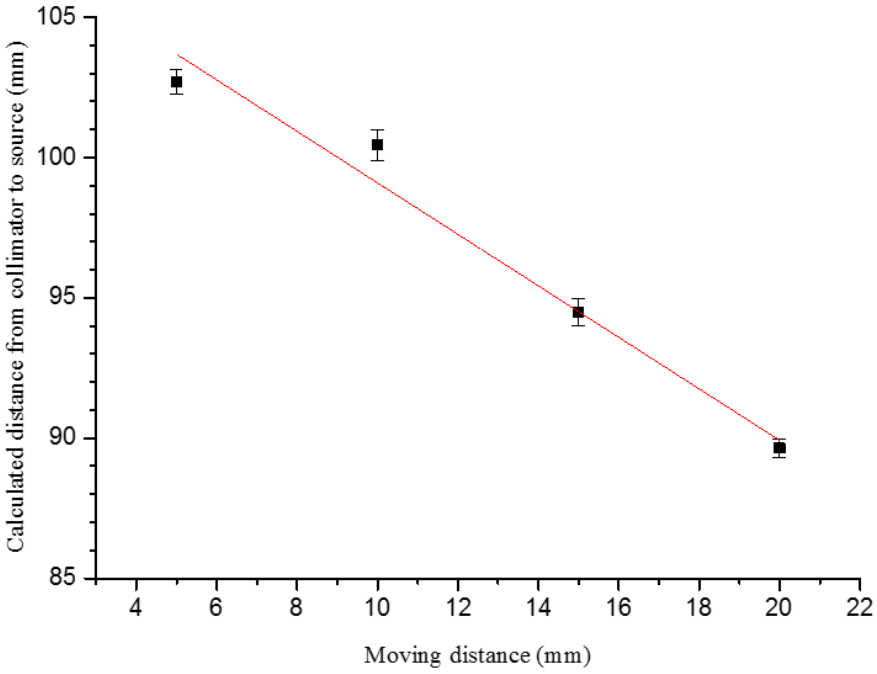

Figure 6.7: Relationship between calculated distance from the collimator to the source and the moving distance of the source. The maximum distance from the source was 107 mm, whilst the moving distances were 5, 10, 15 and 20 mm towards the collimator. R^2 was 0.95 for the fitted line, the intercept point was 108.3 mm and slope was -0.91.

Figure 6.8 shows the linear relationship between average difference errors (between calculated and average distance from the collimator to the source) and moving distance. The average difference increases with moving distance. The results show that the moving distance affects the calculated distance between the source and the camera, where the average difference increases with moving distance. This is influenced by the determination of the centre of the gamma image, which is related to the number of photons that are detected by the detector.

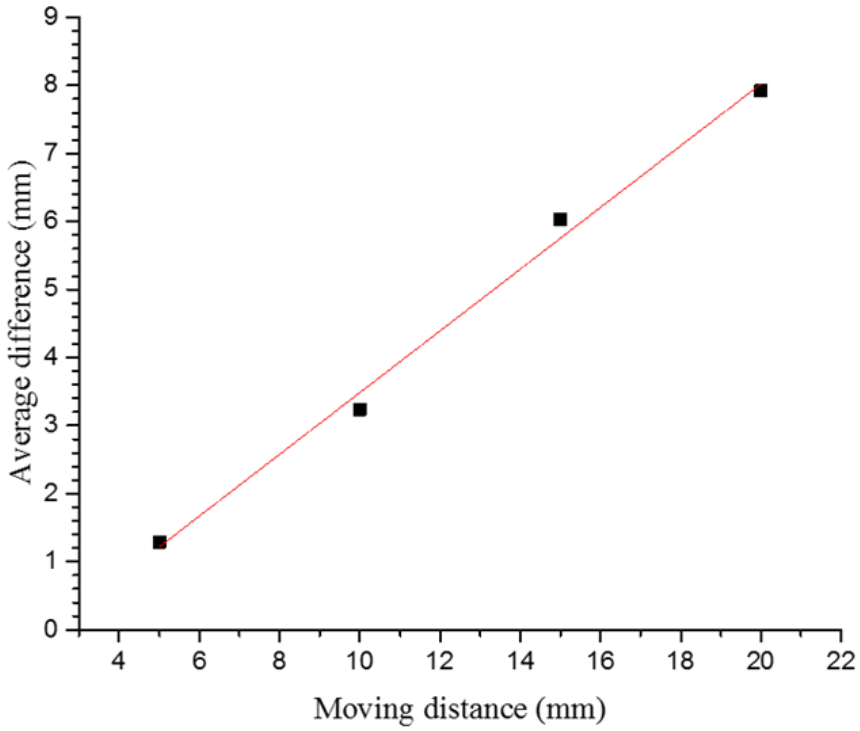

Figure 6.8: Relationship between average difference error (between the calculated and average collimator-to-source distances) and moving distance. R^2 was 0.99, the intercept point was -1.05 mm and the slope was 0.45. The error bar was very small compared with the scale of the *y*-axis; for example, at a 10 mm moving distance the maximum error was 0.009 mm, and therefore the error bar does not appear on the scale of the graph.

Figure 6.9 shows the effect of the distance from the collimator (h) on recorded counts, where the recorded counts decrease by $1/h^2$. The black circles and red stars of the same number represent the recorded counts at the minimum and maximum distances from the collimator face respectively. A single image was taken at each distance, so the numbers represent repeats at different maximum imaging distances. The minimum distance in one setup is equal to the maximum distance in the next. For example, black circle 1 and red star 1 represent the recorded counts at an 83 mm minimum distance and a 103 mm maximum distance of the source from the collimator for the same image respectively. Also, black circle 2 represents the recorded counts at a distance of 103 mm to the collimator at its maximum, whilst red star 1 is for the same image and distance but indicates the minimum distance for the next image in this case.

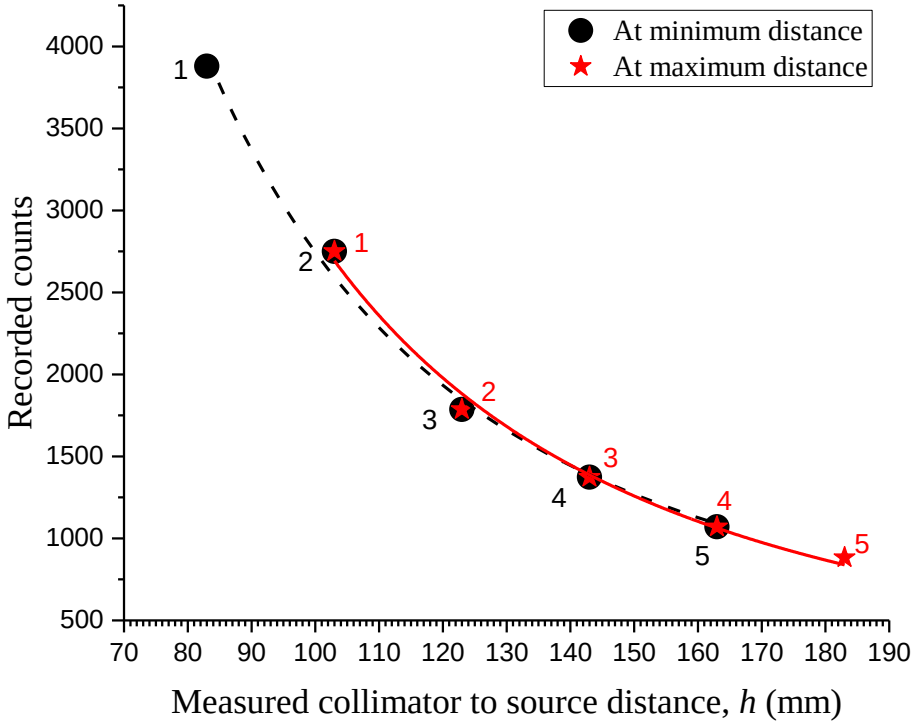

Figure 6.9: Relationship between recorded counts and measured distance from the collimator to the source at the minimum and maximum distances from the collimator. Black and red colours for the same number represent the minimum and maximum distance of the source from the collimator, where the source movement was 20 mm away from the camera at each imaging procedure. $R^2 = 0.99$ for the fitted $1/h^2$ curve at the minimum and maximum distance from camera.

6.4 Determining the effect of source distribution on the calculated depth

6.4.1 Material and Method

To study the effects of source distribution on the calculated position and depth of radioactivity, the centre of radioactivity within a homogeneous source must be determined, and accordingly two equations were used to obtain the centre of mass and the centre of detected activity, using a cylindrical source. The HGC was fitted with a 0.5 mm diameter pinhole collimator to image an extended cylindrical source. The source was

a tube with a 9 mm diameter that was filled with a ^{99m}Tc radioisotope solution to different heights, 20, 30, 40 and 50 mm, as measured from the bottom of tube, and with different activities (20 MBq – 60 MBq). The HGC was used to image the source and upper surface of the tube to obtain the first set of images (gamma and optical). Then the camera was displaced by 20 mm perpendicular to the source to obtain the second set of images (gamma and optical) at the same imaging distance. The acquisition time for the gamma images was three minutes at each imaging distance. The distances from the camera to the upper surface of the source were measured from the camera's collimator face, and were varied between 70 mm and 220 mm in 20 mm steps. A schematic of the experimental arrangement for determining the position of the centre of the detected activity is shown in Figure 6.10. The calculation of the distance from the camera to the source depends on the distance between the gamma spots and between the two cameras, as described in chapter 5. The source shape and the source height represented parameters that effect the determination of the position of the radioactivity within a source. The centre of mass of the cylinder was determined by Equation (6.1).

$$Centre\ of\ mass = \frac{source\ height}{2} \tag{6.1}$$

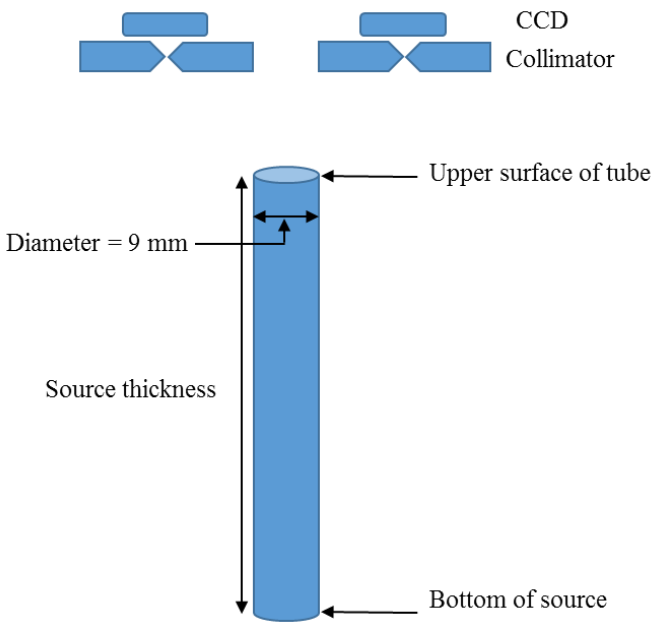

Figure 6.10: A schematic of the experimental arrangement of the tube source and the HGC used to determine the centre of detected activity within the source.

Theoretically, the calculated distance of a distributed source is dependent on the integral of the sensitivity equation (see chapter 3) which is dependent on the distance from the camera's collimator face *h*. That is, the areas of the source closest to the camera contribute the greatest number of photons to the resultant image.

$$\text{Centre of detected activity} = \frac{\int_{h1}^{h2} h \times p(h)dh}{\int_{h1}^{h2} p(h)dh} \tag{6.2}$$

where the numerator represents the sensitivity, and the denominator represents the sensitivity for the total distance. h_1 represents the camera-to-surface of the source distance and h_2 represents the camera-to-bottom of the source distance. $P(h)$ is the expression for sensitivity (see chapter 3). Therefore, the centre of detected activity would be expected to equal to:

$$\text{Centre of detected activity} = \frac{\ln h_1 - \ln h_2}{h_1^{-1} - h_2^{-1}} \tag{6.3}$$

The position of the radioactivity within the source was determined after the depth of the activity had been estimated (as described in chapter 5).

6.4.2 **Results**

The relationship between of the determination the centre of radioactivity and source thickness using the two equations (centre of mass and centre of detected activity equation) is illustrated in Figure 6.11. The values for the calculated centre of activity using Equation (6.1) were greater than the calculated values using Equation (6.3) for the cylinder source shape. The Equation (6.1) depends on the shape and height of source, whereas the Equation (6.3) depends on the height of source (source thickness).

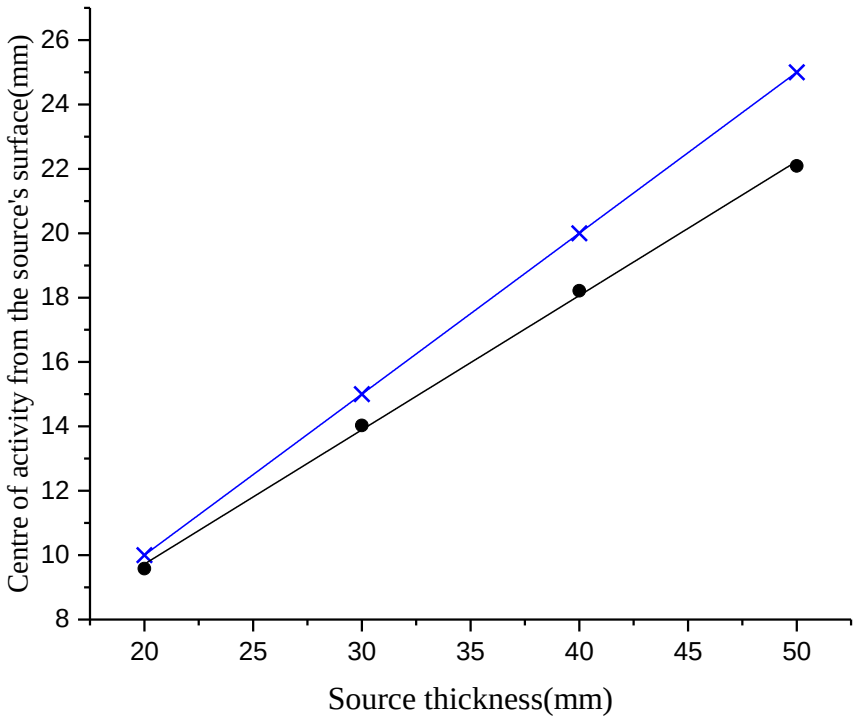

Figure 6.11: Relationship between the calculated centre of activity and source thickness. Source thicknesses were 20, 30, 40 and 50 mm. The crosses represent centres of activity from the centre of mass equation, while the circles represent data from the centre of detected activity equation. $R^2 = 0.99$ for both fitted lines.

Figure 6.12 shows the relationship between the calculated distance from the collimator to the position within source and the measured distance from the collimator to the surface of the source. The HGC axis was perpendicular to the source and the source thicknesses (height) were 20, 30, 40 and 50 mm with a ± 2 mm error (see Figure 6.10). The results indicate that the calculated distance from the collimator to the centre of activity increases with source thickness. This is because the centre of activity will be deeper with increased source thickness.

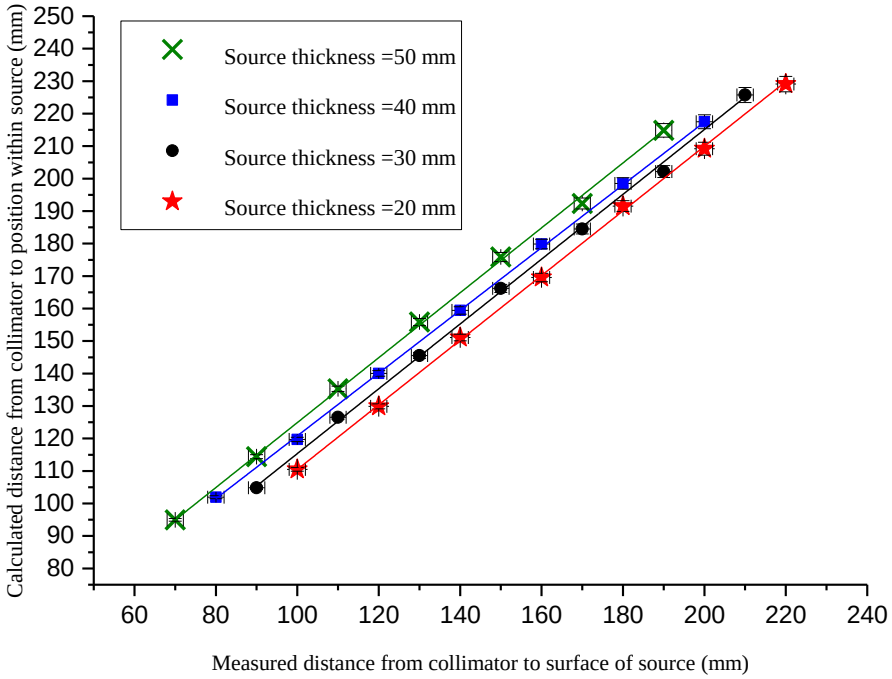

Figure 6.12: Relationship between calculated distances from the collimator to the position within the source versus measured distances from the collimator to the surface of the source. The source thicknesses were 50, 40, 30 and 20 mm. R^2 = 0.99 for the fitted line for all source thicknesses.

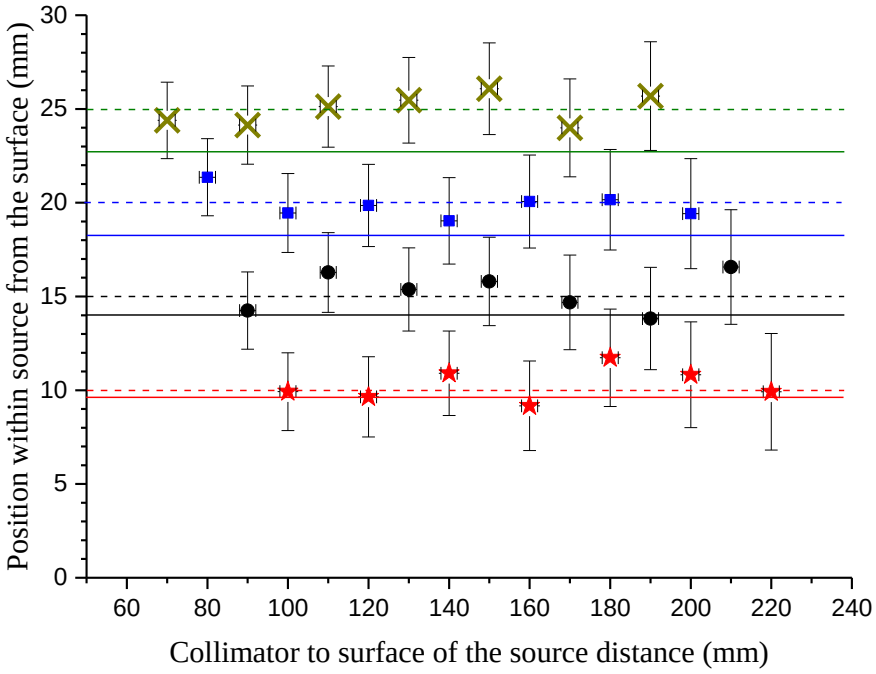

Figure 6.13: Relationship between the position within the source from the surface (mm) and collimator-to-surface distance. The HGC was perpendicular to source. The red stars, black circles, blue squares and green crosses indicate the experimental values of the position of the radioactivity within the source from the surface, whereas the red, black, blue and green solid and dashed lines represent the theoretical values of the centre of activity of the source that were calculated from the centre of detected activity and centre of mass's equations at 20, 30, 40 and 50 mm from the bottom of the tube (source thicknesses) respectively.

Figure 6.13 shows the relationship between the position within source from the surface (mm) and the collimator-to-surface of the source distance. The difference between the position of the activity within the source that was calculated experimentally and from the centre of mass equation was no more than ± 2% for the same source thicknesses. The results indicated that the position of the centre of the activity within source was almost identical to the position determined by the centre of mass equation. The results of calculating the centre of the source radioactivity based on the theoretical results from the centre of mass equation correspond to the calculation of the position of the radiation within the source experimentally. Therefore, this equation (centre of mass) can be applied to determine the centre of the homogeneous source that has accumulated within the phantom. Therefore, this equation could be applied clinically. For example, the centre of

a sentinel lymph node could be determined based on the assumption of a uniform radioisotope distribution, but it should be borne in mind that the organ itself will not necessarily be a regular shape; therefore further work on irregularly shaped organs is required in order to determine the centre of source activity. Therefore, the measured and calculated position and depth within the source will depend on the centre of mass equation. The adoption of the results on the shape and height of the source is consistent with the principle of determining the centre of accumulation of the radioisotope source within the body clinically.

6.5 Depth estimation

During the current study, it has been assumed that the surgeon (or radiologist) wants to examine the chest or abdomen area of the patient in order to determine the location and depth of the radiolabelled tissues during breathing. The source will move between the minimum distance from the camera (at the end of inhalation) and the maximum distance from camera (at the end of exhalation). This assumption has been used to design three models to simulate source motion during breathing and to study the effect this movement has on depth estimation.

The HGC was used to measure the effect of source movement on the depth estimation of the radioisotope source by simulating the various different types of patient movement. A phantom was employed to simulate the human body (this will be explained in section 6.5.1), and the movement of a laboratory jack was used to simulate patient motion during breathing.

6.5.1 Experimental setup

Two radioisotope sources were used to simulate the scenario of having two gamma imaging heads (see section 5.4.1.1). The HGC was fitted with a 0.5 mm diameter pinhole collimator. The activity of the 99mTc source solution used in these simulations was between 3 MBq and 11 MBq. Two vials were filled with a 99mTc radioisotope solution at a 15 mm source thickness (Figure 6.4 B) and were then placed inside the Styrofoam block to ensure an accurate distance between the two sources, see Figure 6.4 A. A three-minute acquisition time for the gamma images was used at each imaging distance, which

was sufficient to create a gamma image on the detector and to estimate the centre of the gamma spot (section 5.4.1.1). The distances from the camera to the surface of the phantom were measured from the collimator face, and were varied from 70 mm to 170 mm in 20 mm steps. The depth of the radioisotope source inside the phantom was measured from the phantom's surface to inside the source (dependent on the centre of mass), as shown in Figure 6.14.

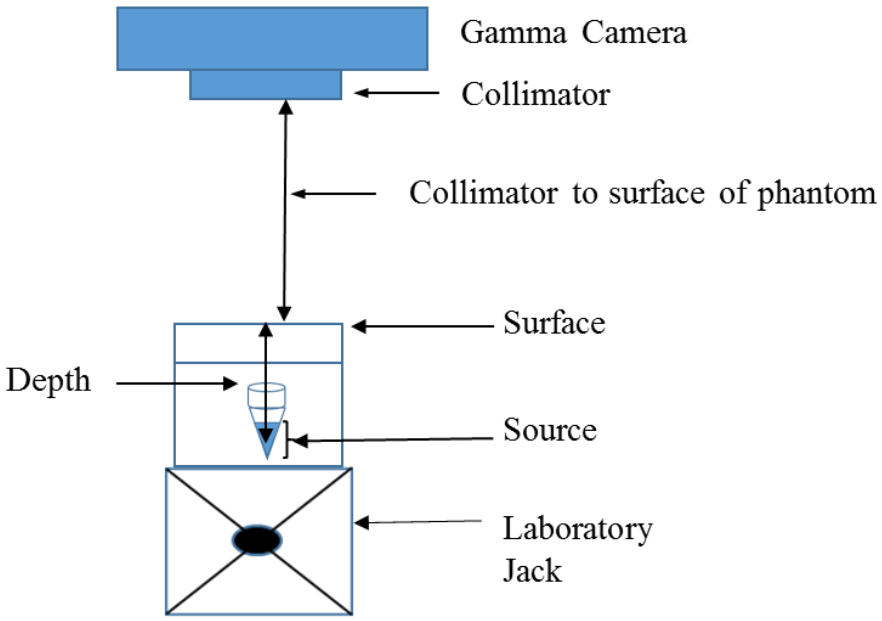

Figure 6.14: A schematic of the experimental arrangement showing the source within the phantom, the HGC, and the laboratory jack used to simulate breathing.

6.5.2 Depth and moving distance calculations

The calculation of the distances between the two optical images and between the two gamma images has been described in the Basic Principles for Depth Estimation section in chapter 4.

For each specific arrangement, the depth of the radioisotope source below the phantom surface, which was being moved between two levels, was calculated. This arrangement produced six images; four optical (two at the minimum distance and two at the maximum distance from the camera) and two gamma. The distance between two optical images at the minimum and maximum distances from camera, and the distance between the two

gamma images, were calculated. The minimum and maximum distances between the collimator face and the surface of the phantom/ source were also calculated. These calculations allowed the estimation of the depth of the gamma source below the surface of the phantom in positions 1 and 2. The moving distance (the movement of the source and phantom or surface of the phantom) represents the difference between the estimated depths in position 1 and 2.

6.5.3 Simulation methodology

In the simulation, two positions were used to simulate patient movement during breathing. Position 1 represented the minimum distance to the collimator face (simulating the inhalation level) whilst position 2 represented the maximum distance from the collimator face (simulating the exhalation level). The moving distances between position 1 and position 2 were 5, 10, 15 and 20 mm in order to simulate target and skin movement toward the camera during breathing, with the movement of the phantom and source continuously adjusted during the acquisition time of any given gamma image. This displacement was simulated by manually moving the laboratory jack to represent movement during breathing. Two sources were placed inside the phantom to simulate two HGCs during the imaging procedures, as described in chapter 5.

The gamma images were acquired when the phantom and sources were manually moved between position 1 and 2 using the laboratory jack, and where the acquisition time was three minutes for each imaging distance. One optical image was acquired in a single frame for the minimum and maximum position after the completion of the gamma image; the phantom was moved by manually adjusting the laboratory jack to position 1 (minimum distance to camera) in order to obtain the first optical image, after which it was returned to position 2 (maximum distance from camera) to acquire the second optical image

The movement of the phantom and source were used to simulate source motion during human respiration. Three situations were simulated with the camera position perpendicular to the patient. The first simulation was for tumour motion within soft tissues vertical to the camera, such as lung cancer and abdominal cancer, whilst the second simulation was for a static tumour, such as bone cancer, and the third simulation

was for a tumour moving diagonally with respect to the camera or position of the patient on the bed leading to diagonal motion relative to the camera, such as with lung cancer.

6.6 Simulation of target and surface moving perpendicularly

The first experiment simulated the target and skin moving in tandem, and was performed by moving the phantom and source together, perpendicular to the HGC. Figure 6.15 shows a schematic of the experimental arrangement of the source within the phantom, and with the HGC perpendicular to the source. The source and phantom were moved by manually adjusting the laboratory jack to simulate the source and phantom moving together between positions 1 and 2, as described in section 6.3.1.1. This experiment was designed to simulate, for example, lung cancers where the tumour is within the soft tissues and the surface (skin) that are moving together whilst breathing.

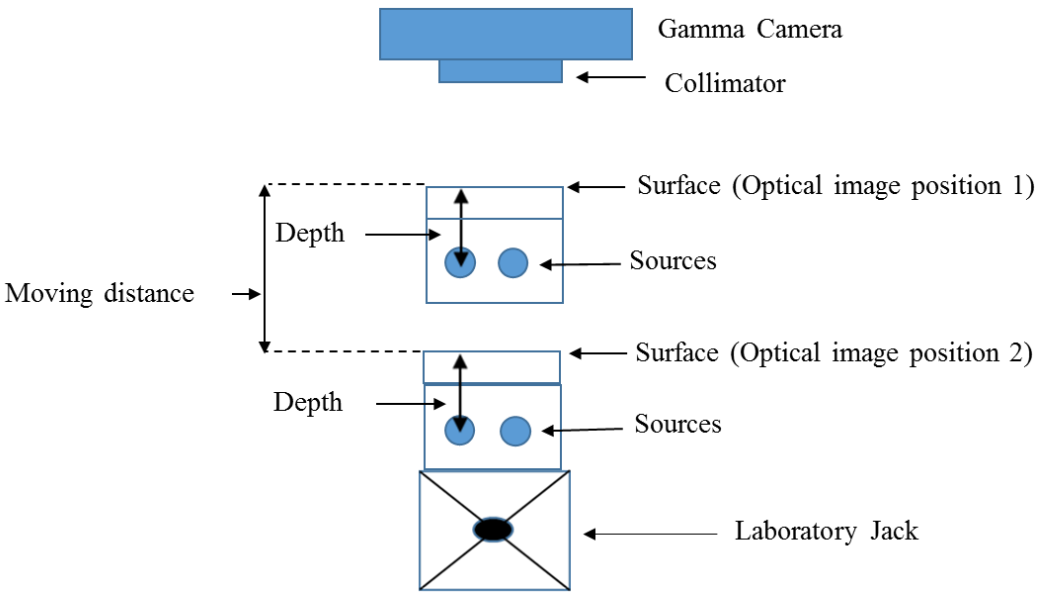

Figure 6.15: A schematic of the experimental arrangement of the source within the phantom and the HGC, showing the two positions of the phantom, position 1 and position 2.

6.6.1 **Result**

The measured depths were determined (below the surface of phantom) using a ruler. These depths were found as 13, 23 and 37 mm depending on the centre of mass of the cone shape source, which was equal to three-quarters of the source thickness, whereas the calculated depths from the surface to the source were determined experimentally. The results were obtained from the analysis of the relationship between the calculated depths and the camera-to-phantom distance for a source placed inside the phantom, which was moved between two levels. These calculated depths were compared to the measured depths of the source over the same distances from the collimator, as plotted in Figure 6.16. In general, the differences between the calculated and actual values at the minimum distance form camera, and between the calculated and measured moving distances, were approximately ± 5%. At the maximum distance from collimator, the differences between the calculated and actual values were around 10%, 35%, 50% and 75% when the moving distance was 5, 10, 15 and 20 mm. When the moving distance was a greater than actual depth, the estimated depth was negative because the distance from collimator to source was larger than the distance from collimator to surface. Therefore, The calculated depth at the minimum distance from the HGC will representative the depth of the source within the body during breathing, taking into account the moving distance.

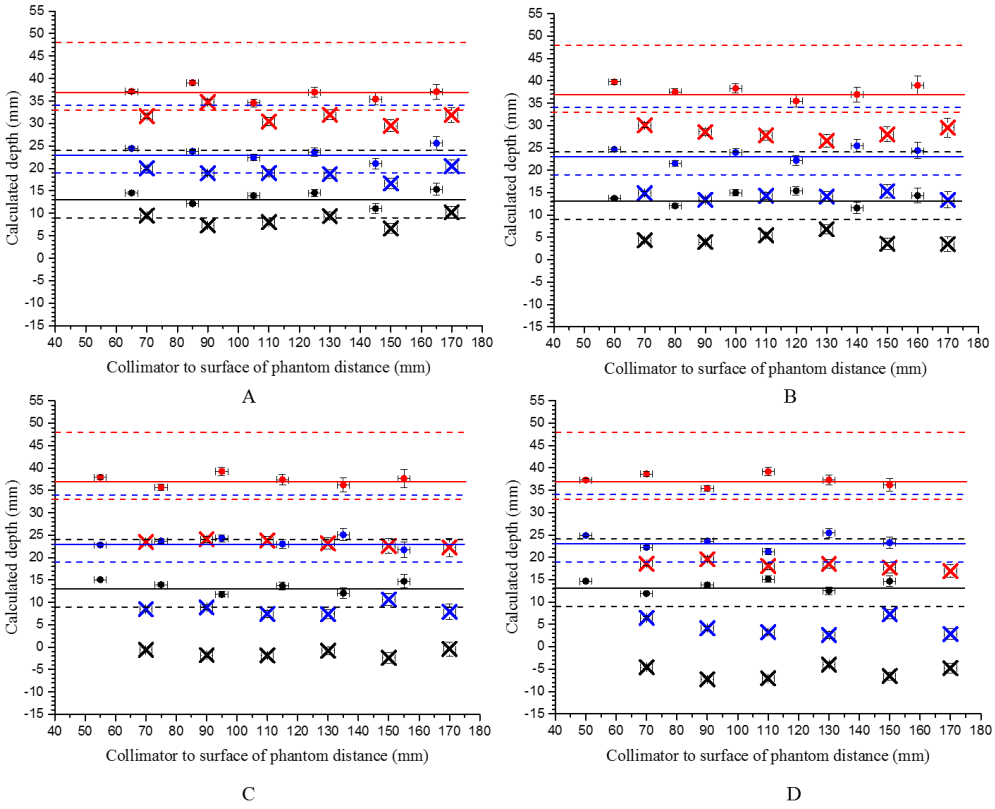

Figure 6.16: Relationship between calculated depths (mm) versus the collimator to the surface of the phantom distance (mm) for a 15 mm source thickness. The measured depths were 13, 23 and 37 mm. The circles and the crosses indicate the calculated depths using optical images taken at the minimum and maximum distances from the camera respectively. The difference between the two depths of the same colour represents the source and phantom movement, which are equivalent to 5 mm (A), 10 mm (B), 15 mm (C) and 20 mm (D). The solid lines represent the measured depths of the source while the distance between two dashed lines of the same colour represents the source thickness.

6.7 Simulation of a static target (surface moving perpendicularly)

The second experiment simulated a static target. Figure 6.17 shows a schematic of the experimental arrangement of the source within the phantom, with the HGC perpendicular to the source. The surface of the phantom was moved manually to simulate the surface, which was just moving between positions 1 and 2 during the experiment, but where the source itself was a static. The experiment was conducted to simulate a fixed target such as would be the case for bone cancer, and therefore just the surface (skin) of the patient was moving during breathing.

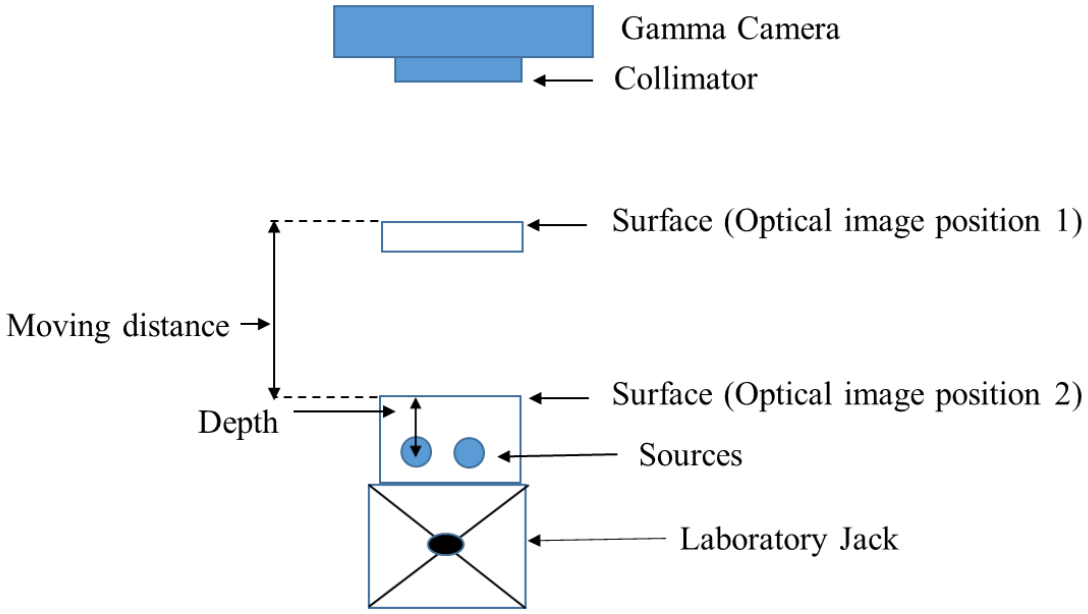

Figure 6.17: A schematic of the experimental arrangement of the source within the phantom and the HGC, showing two positions of surface movement, position 1 and position 2.

6.7.1 **Result**

The measured depths of the static source were 13, 23, and 37 mm and for the calculated depths, as described in section 6.5.2.

Figure 6.18 shows the results acquired from the analysis of the relationship of the calculated depths versus the camera-to-phantom distance for three static sources placed inside the phantom. These calculated depths were compared to the measured depths of the source over the same distances from the collimator. In general, the differences between the calculated and actual values at the minimum and maximum distance from camera, and between the calculated and measured moving distance were around ± 4%. Actually, for a static source, the two calculated depths at the minimum and maximum distances from the camera could dependably determine the depth of the source within body due to the source itself being static when the phantom surface was moving, such as might be the case with bone cancer

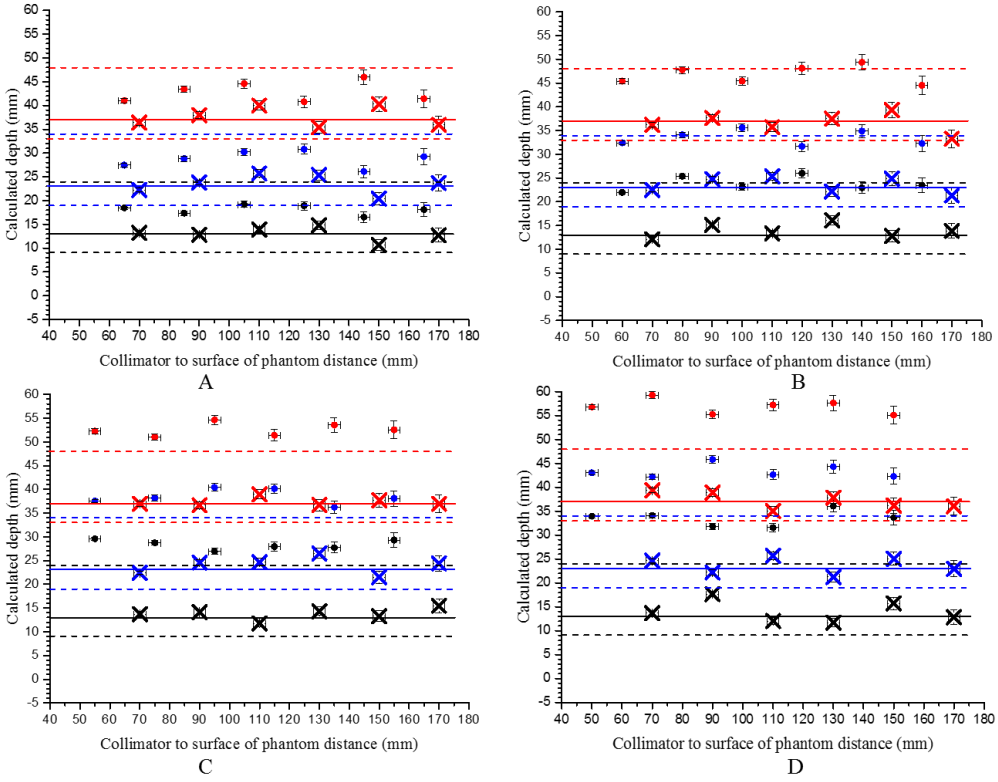

Figure 6.18: Relationship between calculated depths (mm) versus the collimator to the surface of the phantom distance (mm) for a 15 mm source thickness. The measured depths were 13, 23 and 37 mm. The circles and the crosses indicate the calculated depths at the minimum and the maximum distances from the camera respectively. The difference between the two depths of the same colour represents the surface of the phantom movement, which is equivalent to 5 mm (A), 10 mm (B), 15 mm (C) and 20 mm (D). The solid lines represent the measured depths of the source while the distance between two dashed lines of the same colour represents the source thickness.

6.8 Simulation of target moving diagonally

The third simulation was for diagonal source movement using two sources. Figure 6.19 shows a schematic of the experimental arrangement of the two sources, with the sources angled at 15^0 and 30^0 in the *x*-*z* plane, see section 5.5.1.3 in chapter 5. Two sources were placed in a specific position to simulate the source moving diagonally within the phantom with the HGC perpendicular to the sources. This experiment was performed to simulate a diagonal motion of the source within the body or when the patient is lying on the bed in the operating theatre. That is, the movement of the source within the body would be diagonally towards the camera, the latter being held perpendicular to the patient.

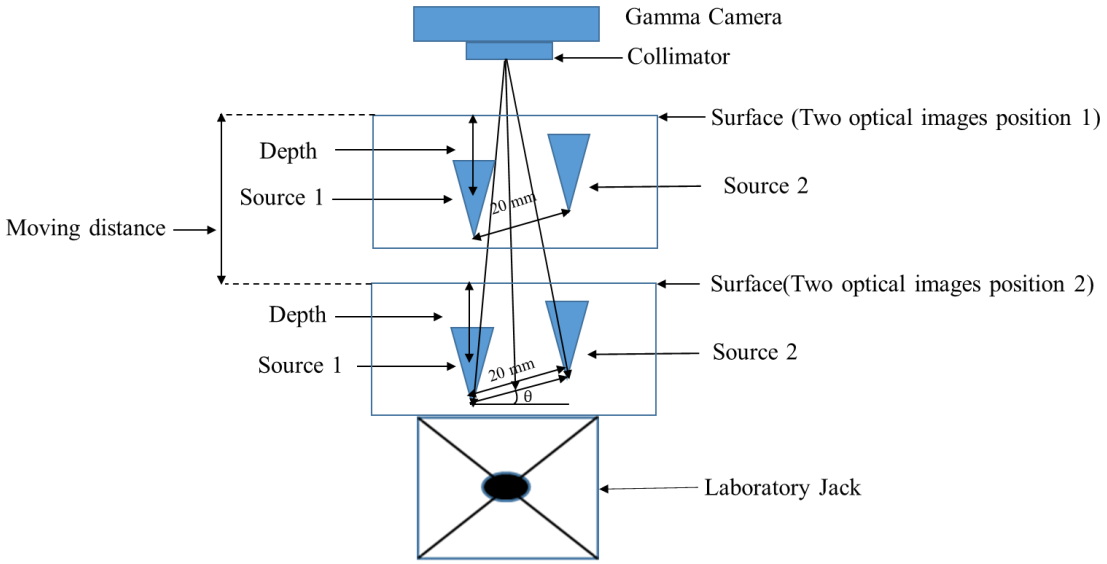

Figure 6.19: A schematic of the experimental arrangement of the two sources within the phantom, as arranged at 15^0 and 30^0 to the *x*-*z* plane with the HGC perpendicular to the sources. The two positions of the phantom and source movement, at position 1 and position 2, were achieved by manually moving the laboratory jack.

6.8.1 **Result**

The measured depth was 22 mm from the surface of the phantom, where the two sources were angled at 15° and 30° to the *x*-*z* plane, and for the calculated depth.

The results were acquired from the analysis of the relationship between the calculated depths and the camera-to-phantom distance for a source moving diagonally inside the phantom toward camera, which was moved between two levels. These calculated depths were compared to the measured depths of the source over the same distances from the collimator, as shown in Figure 6.20. Generally, at the minimum distance from camera angled (15°), the differences between the calculated and actual values (measured depth) were of the order of ± 4%. At the maximum distance from collimator, the differences between the calculated and actual values were around 15%, 40%, 55% and 75% when the moving distance was 5, 10, 15 and 20 mm. The number of photons detected at the minimum greatly affects the image creation on the detector. Therefore, the calculated depths at the minimum distance from the camera could be representative of the adopted depth of the source within the body, taking into account the moving distance.

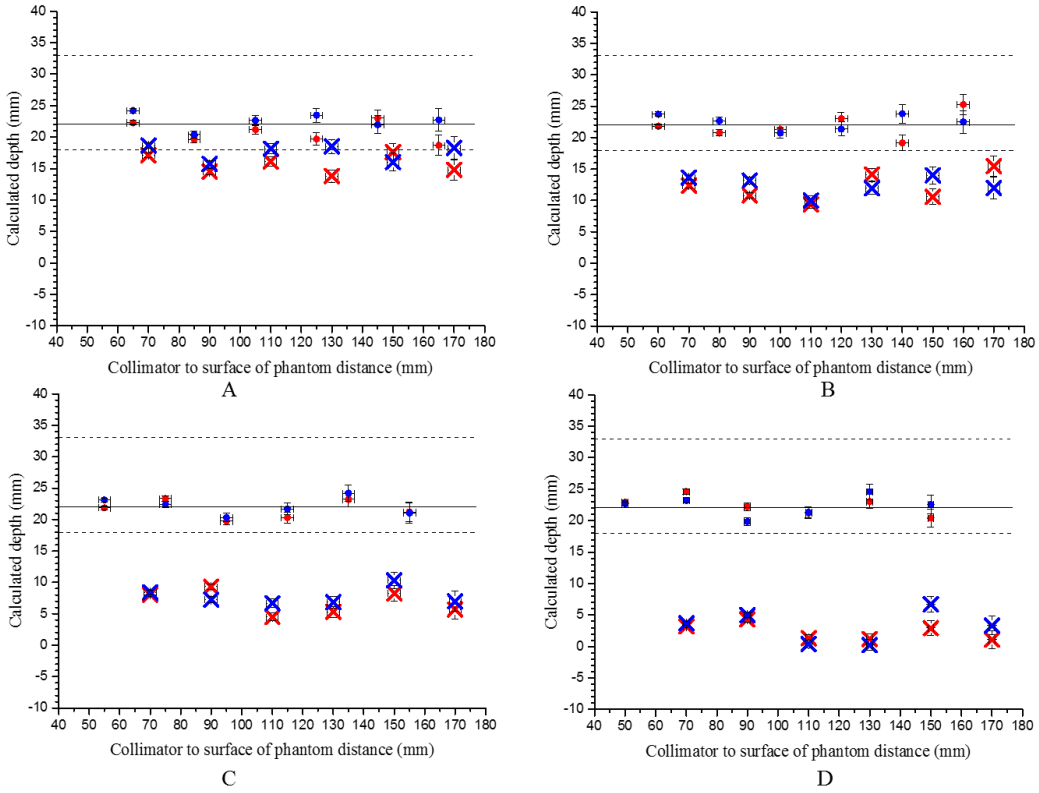

Figure 6.20: Relationship between calculated depth (mm) versus the collimator to the surface of the phantom distance (mm) for two source thicknesses (15 mm) which were at angles of 15^0 and 30^0 in the *x*-*z* plane. The measured depth was 22 mm. The circles and the crosses indicate the calculated depths at the minimum and maximum distances from the camera at the 30^0 (red) and 15^0 (Blue) angles respectively. The difference between the two depths of the same colour represents the moving distance, which is equivalent to 5 mm (A), 10 mm (B), 15 mm (C) and 20 mm (D). The solid lines represent the measured depths of the source, and the distance between the two dashed lines represents the source thickness.

6.9 Discussion

The HGC was used to evaluate the impact of source movement on the depth estimation of a radioisotope source inside a phantom. The study of the types and degrees of source movement represent the main goal in this chapter as a simulation of possible imaging procedure scenarios during surgery.

The number of photons detected by the detector is affected by the distance, and the results obtained are entirely consistent with the expectation, which is that the number of photons detected at the minimum distance will be greater than the number of photons detected at

the maximum distance from collimator. These recorded counts have a vital role in the creation of the gamma image on the detector, which will affect the estimation of the centre of the image and estimation of the depth of the source within the phantom. The source movement was between two levels, namely the minimum and maximum levels (distances) from the collimator face. Because the measured distance from the collimator face for a moving source could not be determined precisely, the average collimator-to-source distance was used instead when studying the relationship between the calculated and measured distances.

The difference between the calculated distance of the source moves between two levels and the average distance of the source was affected by the moving distance, which affects the number of photons detect by detector. The difference was around 1.74%, 2.6%, 5.3% and 8.2 % towards the collimator for the 5, 10, 15 and 20 mm moving distances respectively.

Two equations (the centre of mass and the centre of detected activity) were used to determine the centre of radioactivity within the cylindrical source. The centre of the source represents the centre of gamma ray emission from all of the source. The calculated results for the centre of the radioactive source as found experimentally were compatible with the results for the centre of mass equation. Therefore, the centre of mass equation was adopted to determine the centre of activity within the source when measuring the depth of the radioactive source within the phantom.

In the simulation of the moving source, the gamma and optical images acquired reflected the movement of the phantom that contained the source. In the simulation, the gamma image acquired was the average of the movement of the source between two levels. The depths at the minimum distance from the collimator were consistent with the measured depths as the recorded counts at the minimum distance from collimator were greater than at maximum distance from collimator. In the simulation of a static source (surface movement), the gamma image acquired was the result of a fixed source, where the photons detected were emitted from a single distance and only the phantom surface was moving during the experiment. The depths at the maximum distance from camera were consistent with the measured depths. These were themselves dependent on the maximum distance (exhalation phase) from the collimator, but actually, the two depths could be adopted to take into account the moving distance. Clinically, the surgeons can acquire

two optical images; one at the end of the inhalation phase and one at the end of the exhalation phase; after optical imaging, the surgeons can acquire a gamma image. Then they will have two depths that depend on the depths at the minimum distance from the camera (inhalation phase); they can avoid error if the tumour is moving or static, it taking into account the moving distance.

6.10 **Conclusion**

The ability of the HGC to detect the different depths of the radioisotope source, whether moving or static, during the movement of the phantom that contained the radioisotope source and the different moving distances during the imaging procedure have been investigated.

The calculated distance for the source that moves between two levels was within expected value because the number of photons detected at the minimum distance from collimator had a significant effect on creation of the image on the detector, which affects the estimation of the distance from collimator to source. Also, the calculated distance was between the average distance between the two levels and the minimum distance from the collimator.

The centre of mass equation was suitable to determine the centre of source activity, and is dependent on the shape and height of the source. This was supported by the calculated distances from the collimator face to the source indicated that the position of the radioactivity within the source was in good agreement with the determination of the centre of mass of the source. Therefore, this equation (centre of mass) was applied for all calculations of the centre of the source that was positioned within the phantom. This equation could be useful clinically, for example, the centres of SLNs could be estimated based on the assumption there is a uniform radioisotope distribution, though it should be noted that the organ is not necessarily going to be a regular shape. Therefore, further work on irregularly shaped organs is required to improve the estimate of the centre of the radioactive source.

The number of detected photons that creates the image is affected by the distance from the source and the moving distance between the two levels. This influences the estimation of the centre of the image and the calculation the distance from the camera to the source, and depth estimation of the source.

The calculated depths of the moving source were adopted as the minimum distance from the collimator (during exhalation) while the calculated depths of the static source could be adopted as the minimum and maximum distance from the collimator as compared with the measured depths. Clinically, to avoid a mistake during surgery, the calculated depths at the minimum distance from the camera could be a safe estimate in all cases within body when the source is static or moving, such as might be the case with bone cancer or lung cancer.

Although the difference between calculated and measured depths, and between the measured and calculated moving distances, was approximately ± 4%, there was still good agreement between the calculated and measured depths and the moving distances whether the source was static or moving (perpendicular or diagonal).

The results showed that the dual HGC offers an accurate means of determining the localisation and the depth of abnormal tissue within the body when 1: the target and surface move together, 2: there is only surface movement (static target), and 3: the source is moving diagonally at angles of 15^0 and 30^0 in the *x*-*z* plane. Here, one can determine the magnitude of the moving distances of the source and surface from the top view, with errors of approximately ± 4%.

The HGC could be used to determine the depths and the moving distance of the radiolabelled tissue that is moving inside body during breathing preoperatively and indeed could be used to reconfirm the specified depths of the tumour intraoperatively, taking into account the moving distance during respiratory motion. The results of this chapter suggest the HGC could offer a promising technique to aid the surgeons in estimating the depths of abnormal tissues during patient motion.

Chapter 7: **Summary, conclusions and future work**

7.1 **Summary**

The Hybrid Gamma Camera (HGC) has been designed, manufactured and developed by the Space Research Centre (SRC), University of Leicester in collaboration with the Department of Radiological and Imaging Sciences at the University of Nottingham to provide gamma and optical images with high spatial resolution in order to facilitate diagnostic procedures in the operating theatre.

In this thesis, the ability of the HGC to estimate the different depths of radioisotope accumulation (^{99m}Tc and ^{57}Co) inside three phantoms (breast, head and neck, chest) from different perspectives was examined. Also, three camera arrangements (perpendicular, convergent and divergent) were investigated to select the best arrangement to estimate the depth of radioisotope sources inside body. The perpendicular arrangement was found to be the preferred design.

A single camera was used for imaging the source and phantom, then it was displaced horizontally by 20 mm to obtain a second set of images (both optical and gamma) to simulate the two HGCs. The results of the imaging process were four images (two gamma and two optical), which were used to calculate the depth of the source within the phantom. The depth represents the difference between the distances from collimator to source /surface.

Six phantoms have been designed and manufactured by the Space Research Centre (SRC), University of Leicester; two phantoms (V-shape and cross) were used to assess the ability of camera to determine the localisation of accumulated radioactivity and to assess the effect of different distances between the two sources. To select the best separation between two cameras, three anthropomorphic phantoms (breast, head and neck, and chest) were used to simulate different parts of the human body, and one phantom was used to simulate the source movement during breathing.

In this thesis, three simulation methods of source movement during breathing (inhalation phase and exhalation phase) were performed to assess the ability of the HGC to estimate

the depth of a radiolabelled tissue within the body (moving or static), using a source inside the phantom and a laboratory jack.

Two clinical studies of depth estimation of accumulated radioisotopes were presented using the HGC, where two patients were imaged using a HGC while attending routine SPECT imaging appointments in a nuclear medicine department at Queen Medical Centre and Nottingham city hospital – Nottingham University Hospitals NHS Trust, Nottingham.

This chapter describes the comprehensive conclusions of this thesis, and their implications for evaluating the ability of the HGC to estimate the depth of radiolabelled tissues.

7.2 Conclusions

The small field of view (SFOV) hybrid gamma camera (HGC) has been described as a new imaging system that could be employed to estimate the depth of radiolabelled tissue within a patient through combined optical and gamma imaging during, just prior to surgery.

Three pinhole collimator diameters (0.25 mm, 0.5 mm and 1 mm) have been examined in terms of collimator spatial resolution and collimator sensitivity at different imaging distances. Collimator spatial resolution improves with a decrease in diameter of the pinhole collimator while collimator sensitivity improves with an increase in pinhole collimator diameter; they both deteriorate with increased imaging distance. The theoretical results were better than experimental as expected; the theoretical results represent collimator resolution and collimator sensitivity while the experimental results represent the resolution and sensitivity for both together collimator and detector, so the difference between them represent the sensitivity and resolution of the detector.

Three arrangements of two HGCs (perpendicular, divergent and convergent) were investigated to estimate the depth of radioisotope sources placed in a phantom. The convergent arrangement was excluded from use in the operating room because there were two imaging distances that showed the same distance between the two gamma spots on the detector: before and after the intersection point (I.P.). This would require the HGC to be used at a specific imaging distance in the operating theatre; this would limit the use and the utility of this arrangement to a surgeon. In the divergent arrangement, the overlap

of the FOVs was smaller than in the perpendicular arrangement by 50% at 100 mm from the camera. The difference between the experimental and theoretical results for the distance between two gamma spots on the detector was 13.5% at 70 mm from collimator while was 40.3% at 150 mm from the camera. This difference was due to the error in the determination of each camera angle (± 2^0), distance between the two cameras (± 2 mm), imaging distance (± 2 mm), source position from the centreline of the two cameras (± 1 mm) and estimation of the centre of the gamma spot (± 0.2 pixels). Thus the surgeon would be unable to detect the depth of the accumulated radioisotope within the body. The divergent arrangement was therefore also be excluded from consideration for use in the operating theatre.

In the perpendicular arrangement, the small difference between the experimental and theoretical results of around 2% indicated that the distance between the two gamma spots on the detector experimentally and theoretically was approximately the same at all imaging distances, and that the distance of the source from the centreline (off-axis) of the cameras had no effect on the distance between the two spots on the detector at all imaging distances. Therefore, the perpendicular camera arrangement was the most suitable for depth estimation of radioisotope distribution within the body of these three arrangements

The hybrid camera configuration allows four independent images to be obtained; two optical and two gamma, which can be displayed as individual images, combined optical-gamma images, or as a single combined stereoscopic image [18]. These images could be used to estimate the depth of source within the phantom. For source moves between the two levels, the determination of the depths and the moving distance were investigated. Furthermore, these images would help to study the effect of breathing motion on depth estimation of accumulated radioisotopes within the body during surgery.

Two phantoms (v- shape and cross) were used to assess the ability of the HGC to detect the different distances between the two sources and to evaluate the best distance between the two cameras. The result showed that at a distance of 20 mm or more between two sources, a single camera was able to resolve these distances over a range of 40 mm to 160 mm imaging distances. Therefore, a 20 mm distance between the two cameras is preferable to resolve the source and to estimate the depth within the body.

When calculating depth, the centre of detected activity varied from the measured depth by approximately 10%, while the centre of mass varied by 2%. Therefore, the determination of the centre of the radioactivity was dependent on the centre-of-mass. The depth is defined as the distance from the surface of the body to the position of the centre of the mass within the source. The basic principle behind estimating the depth of a radioisotope source using two HGCs in a perpendicular arrangement was described in detail.

Three phantoms (breast, and head and neck, and chest) were used to simulate a gamma source in a specific organ of the human body and to assess the ability of the HGC to estimate the depth of a radioisotope source within them. The breast phantom was used to simulate the source within soft tissues. The head and neck phantom was used to simulate a tumour between bone and soft tissues where there is the potential to avoid the effect of bone to detect by moving the camera. The chest phantom was used to simulate a tumour beneath bone and soft tissues. Use of the HGC to image these phantoms from the different perspectives has enhanced the depth estimation procedures for the location of the radioactive source within the phantom and has avoided affecting the detection of radiation emitted from the source as much as possible. These advantages were supported by the small differences between the calculated and actual values of depth. The differences between the calculated and measured depths when imaging a static phantom over a range of imaging distances were approximately 5%. The results show that the dual HGC imaging system could offer an accurate means of determining the localisation and the different depths of the radioisotope-labelled target tissue, where the camera was used to image from the top, lateral, posterior and anterior views. The error in calculated depth was found to be small. For example, when the depth was 53 mm inside the breast phantom, the error was 1.8 mm at 80 mm distance from the camera and 4 mm at 140 mm distance from the camera(compared with the error of the calculated depth in a similar, previous study by Mathelin et al., which was 5 mm [25]). Therefore, the results of this work appear to suggest that the HGC could represent a promising technique in terms of providing support in the operating theatre. These advantages were supported by the small differences between calculated and actual values.

A study of the effect of source movement on depth estimation shows the ability of the HGC to estimate the depth of source within phantom at the minimum and maximum

distance from camera. These calculations were performed through three simulations of the source movement within the body. As a result of the simulation, the HGC could be used to determine the depths and the moving distance of the radiolabelled tissue during breathing. The depth can be determined using SPECT/CT preoperatively, and the HGC could be used to reconfirm the specified depths of the accumulated radioisotopes intraoperatively, taking into account the moving distance during respiratory motion. The application of the HGC imaging systems during diagnosis and surgery could provide a sufficiently short acquisition time compared with the acquisition time of SPECT/CT scan, which is approximately 30-40 minutes [189] when sensitivity is taken into account and allows greater patient comfort, which would lead to reduced patient movement and any distortion associated with the target image, and which may be acceptable and practical compared to other imaging systems such as SPECT-CT or PET-CT.

There was good agreement at the minimum distance from the camera between the calculated and measured depths and the moving distances when the source was static or moving (perpendicular or diagonal), although the difference between calculated and measured depths, and between the measured and calculated moving distances were approximately ± 4%. At the maximum distance from the collimator when the source and surface were moving, the differences between the calculated and measured values were around 10%, 35%, 50% and 75% when the moving distance was 5, 10, 15 and 20 mm respectively. Therefore, the calculated depth at the minimum distance from the collimator could be adopted to represent the depth of source within body.

The ability of the HGC to detect the different depths of radioisotope sources within the static phantom and to detect a source, whether moving or static, inside the phantom for different moving distances during the imaging procedure have been investigated experimentally. It was shown that the combination of gamma and optical images could be used to estimate the depth of a source inside phantom over the specified imaging distances, and could further be used to determine the site and the number of sources in the phantom.

From two patients, further study may well be needed to give a more detailed understanding about the use of the HGC in estimating the depth of radiolabelled tissues within the operating theatre. Although there is no measured depth to compare with calculated depth, the calculated depths of 26.56 ± 0.92 mm and 28.87 ± 1.69 mm seem

reasonable compared to the size of the target organ .The results of the current study show that there is a *possibility* of being able to estimate the depth of radiolabelled tissue within the body using HGC with different views imaging.

Finally, the outcome of this study suggests that HGC could be a promising technique to give excellent support in the operating theatre.

7.3 Future work

In the field of medical imaging, all designers and manufacturers aim to improve their devices in terms of such properties as resolution, sensitivity and size in order to improve patient management and diagnosis in all medical cases. SFOV imaging systems could be the preferable solution among the various possible imaging systems, as they can provide beneficial information about the target area within the body during surgery and may be used in critical locations such as operations within the head or neck.

Therefore, there are many possible research areas to be studied to develop the ability of HGC imaging within the operating theatre, as well as the various aspects that can be developed in the current research work. In this section, there are two areas for potential further study, namely the experimental and clinical cases.

7.3.1 Experimental

During this study, there are several areas that have been identified to improve the accuracy of the experimental results in order to improve the use of the HGC intraoperatively.

1. Use soft tissue (i.e. beef) with different thicknesses and different shapes of bones instead of the phantoms and the aluminium to give a more realistic simulation of the human body, and to study the effect of attenuation by soft tissue and bone on the sensitivity of camera. The source should be positioned beneath the soft tissue at different depths (with different source activities) as a simulation of a source within the breast. The source could be inserted between soft tissue and bone at different depths and different positions (to completely or partially cover) as a

simulation of a tumour inside the head and neck. The source could be placed beneath the meat and bone together at different depths in order to simulate a tumour within the chest.

2. Two cameras should be built in to one structure and used simultaneously to avoid the error in determining the distance between the cameras and to increase accuracy in calculating the depth within the human body. This could be achieved using a collimator that has two holes with a specific distance between them and using a single CCD large enough to cover the two holes. This requires magnification in the external appearance and area of the head of the camera, and developments in acquisition software to deal with data from two cameras.
3. A laser pointer could be connected to the camera to determine and confirm the distance between the surface and the camera. This distance could be used to correct the distance that is calculated using the two optical images. However a problem is the deviation of the laser light at the phantom surface because the surface is not flat, such as in the breast and the head and neck phantoms, which leads to error in calculating the distance from the collimator to the surface and creates an error in depth estimation. Therefore, the laser pointer must be perpendicular to the selected point.

7.3.2 Clinical cases

Two cases have been imaged using HGC; one was in the right ankle and the second was in the back near to shoulder. Although there is no reference to compare with measured depth, the results were reasonable compared with the size of ankle and back. There is the possibility to ensure accurate depth estimation, for example, by using the HGC to image the patient from different sides; this would allow the calculation of the depths and comparison between them.

To further improve clinical data, the ability of the camera to estimate the depth of accumulated radioisotope within the body should be quantified by comparing with another imaging instruments such as SPECT and PET. This would require a number of patient populations to be examined in the future in order to gain a more accurate clinical

assessment of the advantages of the HGC, with both HGC and SPECT or PET images available for each.

There has already been a discussion with a surgical oncologist in the Baghdad Learning Hospital Centre. He has shown interest in using the HGC for SLN mapping of breast cancer patients due to it is small size that allows it to be used in the surgical theatre. He anticipates a better cancer treatment outcome as a result of using this new imaging technique.

We have discussed further the plan, and the obstacles that can be overcome such as training on using the HGC, radioactivity materials requirement, Licenses of IDL software, ethical approvals and patient requirements, and number and type of patients for imaging during training.

Our thoughts are to conduct with international cooperation, further investigations using the HGC on other cancer patients in other hospitals with other medical groups based on clear plans.

Patient requirement would be based on the surgical speciality, SLN mapping in breast conserving surgery (BCS) from drainage, head and neck Lesions, and prostate treatment. Resulting images will be compared with SPECT images for each patient in order to evaluate the HGC application to surgical procedures. Depth estimation evaluation of the HGC will be investigated by applying the same principles that have been used in my PhD studies.

Appendix A: Error analysis with real example from lab experimental

A. 1 Equations to calculate errors

There are three equations to calculate errors:-

1- The addition / subtraction equation

$$d = a + b + c \tag{A.1a}$$

$$\Delta d = \sqrt{(\Delta a)^2 + (\Delta b)^2 + (\Delta c)^2} \tag{A.2b}$$

2- The multiplication/division equation

If there are two different variables *a* and *b* (a ≠ b), and *c* is equal to multiplication of *a* and *b* ($a \times b$) the error of *c* is

$$\Delta c = c \times \sqrt{\left(\frac{\Delta a}{a}\right)^2 + \left(\frac{\Delta b}{b}\right)^2} \tag{A.2a}$$

Whereas, if there is one variable *a*, and c is equal a^2 the error of *c* is

$$\Delta c = c \times \frac{2 \times \Delta a}{a} \tag{A.2b}$$

C = a^2

3- For the square root of Z

$$\Delta c = c \times \frac{1}{2} \times \frac{\Delta a}{a} \tag{A.3}$$

A.2 Calculating the error in depth estimation

Depth estimation of the radioactive source within an object using the Hybrid Gamma Camera depends on two optical images and two gamma images. The difference between the distance from the collimator to the source and the distance from the collimator to the surface gives the depth of the source below the surface.

$$Depth = d_{cso} - d_{csu} \tag{A.4}$$

d_{cso} is the distance from the collimator to the source.

d_{csu} is the distance from the collimator to the surface.

The error on the calculation of the depth is

$$\Delta\text{Depth} = \sqrt{(\Delta d_{cso})^2 + (\Delta d_{csu})^2} \tag{A.5}$$

Where Δd_{cso} and Δd_{csu} is the respective error on the camera to source and surface measurements.

A.2.1 Optical image

There are two optical spots on the image, (x_1, y_1) and (x_2, y_2) are the centre of the first and second spot respectively (figure 1).

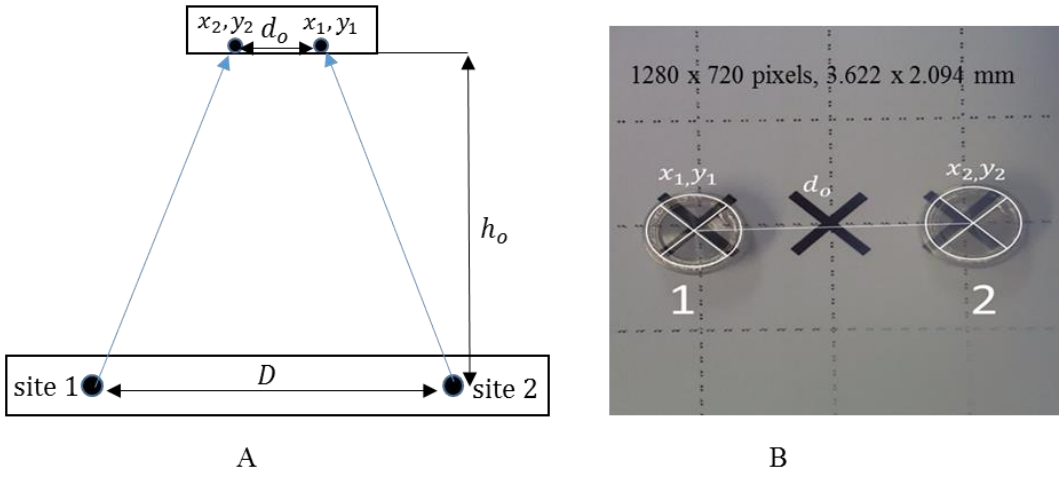

Figure 1: (A) Schematic diagram showing the experimental set up. (B) Optical image (1280×740 pixels, 3.622×2.094 mm) shows two sites for radioactive sources in the phantom. Site 1 is related to the first position of the source and the site 2 is related to the second position of the source. d_o and D represent the distance between two optical spots and the distance between two sources respectively.

X_1 = 882 pixel Y_1 = 592 pixel

X_2 = 562 pixel Y_2 = 284 pixel

When determining the centre of the spot, the measurements are repeated many times with each spot then the average of x and y-positions for each optical spot is calculated along with their errors.

$X_1 \pm \Delta X_1 = X1 \pm 1$ $Y_1 \pm \Delta Y_1 = Y1 \pm 1$

$X_2 \pm \Delta X_2 = X2 \pm 1$ $Y_2 \pm \Delta Y_2 = Y2 \pm 1$

ΔX_1, ΔX_2, ΔY_1 and ΔY_2 are ± 1 because one pixel is the limiting unit for the optical camera. The estimation of the centre of the image was carried out by repeating determine

the centre by 5 times by cursor procedure, then summation these values and divided by 5. The results were the centre value ± 1.

The distance between two optical spots is d_o

$$d_o = \sqrt{{d_x}^2 + {d_y}^2} \tag{A.6}$$

The difference between the positions of the two optical spots on the x-axes is d_x

$$d_x = |x_1 - x_2| \tag{A.7}$$

$d_x = 882 - 562 = 320$ pixel

The error in d_x is Δd_x (because calculating d_x is a subtraction operation the subtraction formula (eq.1) is needed to calculate the error).

$$\Delta d_x = \sqrt{(\Delta x_1)^2 + (\Delta x_2)^2} \tag{A.8}$$

$\Delta d_x = \sqrt{1^2 + 1^2}$ = 1.41 pixel

${d_x}^2 = d_x \times d_x$

${d_x}^2 = 320 \times 320 = 102400$ pixel^2

The error of ${d_x}^2$ is $\Delta({d_x}^2)$ (because the calculation of the ${d_x}^2$ is a a^2 operation the multiplication formula (eq.2b) is needed to calculate the error)

$$\frac{\Delta({d_x}^2)}{{d_x}^2} = 2 \times \frac{\Delta d_x}{d_x} \tag{A.9}$$

$$\frac{\Delta({d_x}^2)}{102400} = 2 \times \frac{\sqrt{2}}{320}$$

$\Delta({d_x}^2) = 905.1$ pixel^2

${d_x}^2 = 102400 \pm 905.1$ pixel^2

The difference between the positions of the two optical spots on the y-axes is d_y.

$$d_y = |y_2 - y_1|$$

$d_y = 592 - 284 = 308$ pixel

The error in d_y is Δd_y (because calculating d_y is a subtraction operation the subtraction formula (eq.1) is needed to calculate the error)

$$\Delta d_y = \sqrt{(\Delta y_1)^2 + (\Delta y_2)^2}$$

$\Delta d_y = \sqrt{1^2 + 1^2} = 1.41$

${d_y}^2 = d_y \times d_y$

${d_y}^2 = 308 \times 308 = 94864$ pixel^2

The error of ${d_y}^2$ is $\Delta({d_y}^2)$ (because the calculation of the ${d_y}^2$ is a a^2 operation the multiplication formula (eq. 2b) is needed to calculate the error)

$$\frac{\Delta({d_y}^2)}{{d_y}^2} = 2 \times \frac{\Delta d_y}{d_y}$$

$$\frac{\Delta({d_y}^2)}{94864} = 2 \times \frac{\sqrt{2}}{308}$$

$\Delta({d_y}^2) = 871.16$ pixel^2

${d_y}^2 = 94864 \pm 871.16$ pixel^2

Now we have

${d_x}^2 = 102400 \pm 905.1$ pixel^2

$d_y{}^2 = 94864 \pm 871.16$ pixel^2

To calculate the error in the distance between two optical spots (Δd_o):

$$d_o = \sqrt{d_x{}^2 + d_y{}^2}$$

$d_o = \sqrt{102400 + 94864}$

$d_o = 444.144$ pixel

$d_o{}^2 = d_x{}^2 + d_y{}^2$

$d_o{}^2 = (102400) + (94864)$

$d_o{}^2 = 197264$ pixel^2

The error of the $d_o{}^2$ is $\Delta(d_o{}^2)$

$$\Delta(d_o{}^2) = \sqrt{(\Delta(d_x{}^2))^2 + (\Delta(d_y{}^2))^2} \quad \text{(A.10)}$$

$\Delta(d_o{}^2) = \sqrt{(905.1)^2 + (871.16)^2}$

$\Delta(d_o{}^2) = 1256.23$ pixel^2

To calculate error Δd_o the square root equation must be used.

$$\Delta d_o = d_o \times \frac{1}{2} \times \frac{\Delta(d_o{}^2)}{d_o{}^2}$$

$\Delta d_o = 444.144 \times \frac{1}{2} \times \frac{1256.23}{197264}$

$\Delta d_o = 1.414$ pixel

The pixel size of optical camera is 0.00283 mm/pixel so Δd_o and d_o are

$\Delta d_o = 1.414 \times 0.00283 = 0.004$ mm

$d_o = 444.14 \times 0.00283 = 1.26$ mm

Distance from collimator to surface (d_{csu}) $= 10 \times \frac{20}{d_o} \times 0.415$

Where 10 mm represent the collimator to detector distance (*t)*, 20 mm is the distance between two cameras *D* with assuming there is no error, d_o is the distance between the two optical spots and the magnification factor of the system is 0.415

d_{csu} = 66.03 mm

The error of d_{csu} is Δd_{csu}

$$\Delta d_{csu} = (d_{csu}) \times \frac{\Delta d_o}{d_o} \quad \text{(A.11)}$$

$\Delta d_{csu} = 66.03 \times \frac{0.004}{1.26}$

$\Delta d_{csu} = 0.21$mm

$d_{csu} = 66.03 \pm 0.21$ mm

A.2.2 Gamma image

There are two gamma spots on the image, where (x_1, y_1) and (x_2, y_2) are the centre of the first and second spot respectively (figure 2).

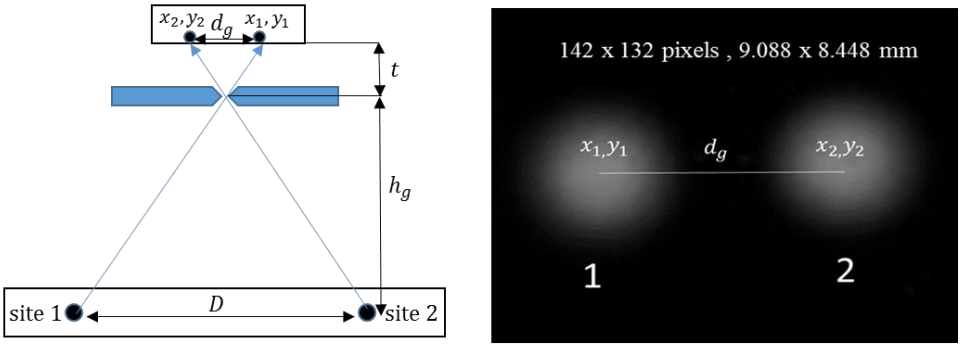

A B

Figure 2: (A) Schematic diagram showing the experimental set up. (B) Gamma image (128×128 pixels, 8.192 ×8.192 mm) shows two sites for radioactive sources in the phantom using the hybrid gamma camera. Site 1 is related to the first position of the source and the site 2 is related to the second position of the source. d_g and D represent distance between two gamma spots and distance between two cameras respectively.

X_1 = 54.24 pixel Y_1 = 73.68 pixel

X_2 = 77.13 pixel Y_2 = 75.96 pixel

When determining the centre of the spot, the measurements are repeated many times with each spot then the average of x and y positions for each gamma spot is calculated along with their errors.

$X_1 \pm \Delta X_1 = X_1 \pm 0.1$ $Y_1 \pm \Delta Y_1 = Y_1 \pm 0.1$

$X_2 \pm \Delta X_2 = X_2 \pm 0.1$ $Y_2 \pm \Delta Y_2 = Y_2 \pm 0.1$

$\Delta X_1, \Delta X_2, \Delta Y_1$ and ΔY_2 are ± 0.1 because 0.1 pixel is the estimate of the gamma camera system. The estimation of the centre of the image was carried out by repeating determine the centre by 5 times by cursor procedure, then summation these values and divided by 5. The results were the centre value ± 0.1.

Similarly, the procedure has been used for the optical images will be applied for the gamma images as follows:

The distance between two gamma spots is d_g

$$d_g = \sqrt{{d_x}^2 + {d_y}^2}$$

The difference between the positions of the two gamma spots on the x-axes is d_x

$d_x = 77.13 - 54.24 = 22.89$ pixel

The error in d_x is Δd_x (because the calculation of the d_x is a subtraction operation the subtraction formula (eq.1) is needed to calculate the error)

$\Delta d_x = \sqrt{0.1^2 + 0.1^2} = 0.141$ pixel

${d_x}^2 = d_x \times d_x$

${d_x}^2 = 22.89 \times 22.89 = 523.861$ pixel^2

The error of ${d_x}^2$ is $\Delta({d_x}^2)$ (because calculating ${d_x}^2$ is a a^2 operation the multiplication formula (eq. 2b) is needed to calculate error)

$$\frac{\Delta({d_x}^2)}{523.861} = 2 \times \frac{\sqrt{0.02}}{22.89}$$

$\Delta {d_x}^2 = 6.474$ pixel^2

${d_x}^2 = 523.861 \pm 6.474$ pixel^2

The difference between the positions of the two gamma spots on the y-axes is d_y

$d_y = 75.96 - 73.68 = 2.28$ pixel

The error in d_y is Δd_y (because calculating d_y is a subtraction operation the subtraction formula (eq.1) must be used)

$\Delta d_y = \sqrt{0.1^2 + 0.1^2} = 0.141$ pixel

$d_y{}^2 = d_y \times d_y$

$d_y{}^2 = 2.28 \times 2.28 = 5.18$ pixel^2

The error of $d_y{}^2$ is $\Delta(d_y{}^2)$ (because the calculation of the $d_y{}^2$ is a a^2 operation the multiplication formula (eq. 2b) is needed to calculate the error)

$$\frac{\Delta(d_y{}^2)}{5.18} = 2 \times \frac{\sqrt{0.02}}{2.28}$$

$\Delta(d_y{}^2) = 0.644$ pixel^2

$d_y{}^2 = 5.18 \pm 0.644$ pixel^2

$d_x{}^2 = 523.861 \pm 6.474$ pixel^2

To calculate the error in the distance between tow gamma spots (Δd_g)

$d_g = \sqrt{523.861 + 5.18}$

$d_g = 23.001$ pixels

$d_g{}^2 = d_x{}^2 + d_y{}^2$

$d_g{}^2 = (523.861) + (5.18)$

$d_g{}^2 = 529.04$ pixel^2

The error of $d_g{}^2$ is $\Delta d_g{}^2$(because calculating $d_g{}^2$ is an addition operation the addition formula (eq.1) must be used).

$\Delta d_g{}^2 = \sqrt{(6.474)^2 + (0.644)^2}$

$\Delta d_g{}^2 = 6.51$ pixel^2

To calculate error Δd_g the square root equation must be used.

$$\Delta d_g = 23.003 \times \frac{1}{2} \times \frac{6.51}{529.1504}$$

$\Delta d_g = 0.141$ Pixel

The pixel size of gamma camera is 0.064 mm/pixel so Δd_g and d_g are

$\Delta d_g = 0.141 \times 0.064 = 0.009$ mm

$d_g = 23.003 \times 0.064 = 1.47$ mm

Distance from collimator to source ($d_{collimator-source}$) $= 10 \times \frac{20}{d_g}$

Where 10 mm is the collimator to detector distance *t*, 20 mm is the distance between two cameras *D* and d_g is the distance between the two gamma spots.

d_{cso}= 135.86 mm

The error of d_{cso} is Δd_{cso}

$\Delta d_{cso} = 135.86 \times \frac{0.009}{1.47}$

$\Delta d_{cso} = 0.835$ mm

$d_{cso} = 135.86 \pm 0.835$ mm

To calculate error of the depth estimation

$d_{cso} = 135.86 \pm 0.835$ mm

$d_{csu} = 66.03 \pm 0.21$ mm

Depth = Distance from collimator to source - Distance from collimator to surface

Depth = $135.86 - 66.03$

Depth = 69.83 mm

The error of the Depth is $\Delta Depth$ (because the Depth is a subtraction operation the subtraction formula (eq.1) must be used)

$\Delta d = \sqrt[2]{(\Delta a)^2 + (\Delta b)^2 +}$

$$\Delta depth = \sqrt{(\Delta d_{cso})^2 + (d_{csu})^2}$$

$$\Delta depth = \sqrt{(0.835\ )^2 + (0.21)^2}$$

$$\Delta depth = 0.86 \text{ mm}$$

Depth = 69.83 $\pm$ 0.86 m

Appendix B: A program to determine the centre of spot (written in IDL)

B.1 Introduction:

A program has been written in an Interactive Data Language (IDL) software to estimate the centre of gamma and optical spot in images, which were presented in the results section. The determination the centroid (x, y) of gamma and optical spots were made by hand (cursor procedure). The cursor procedure is the process of moving the cursor (mouse) by hand on the spot in order to determine the centre of spot; this means it was used to read the position (centre) of the selected spot from the current image. This program has been built depending on the 2D image.

B.2 Estimate the centre of images by the cursor

The images were gamma or optical. This program determines the centre of the gamma spot or optical spot by a cursor procedure.

There are a number of steps required to explain how this program works. Firstly, a folder is opened in a specific path which contains a tiff file or jpg file only (this command is for calling the image from the folder in which it is saved). Then, the image (TIFF or JPEG) is read from the folder (as a two-dimensional image); this image has the same pixel dimensions as the original image obtained from the camera. The image can be displayed in specific size and specific location (window). The centre of the gamma spot or optical spot from the image was determined using the cursor procedure (Figure B. 1). The results can then be printed.

X_1= 54.53 Y_1= 73.97

X_2= 872.96 Y_2= 586.76

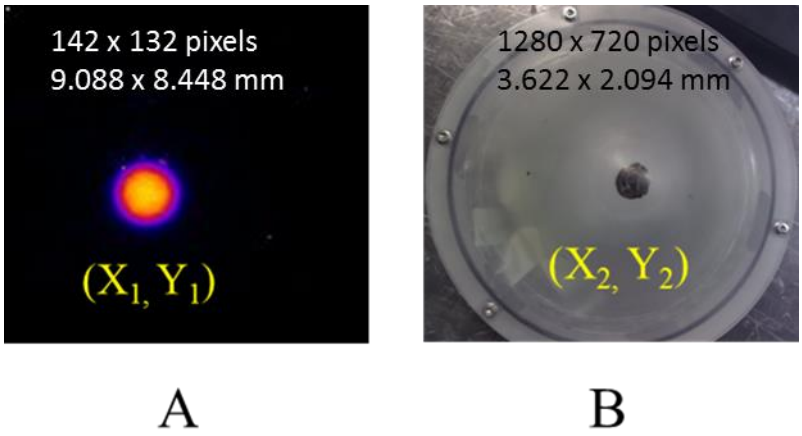

Figure B. 1: (A) Gamma image and (B) Optical image showing the location of a radioactive source within the phantom using a HGC.

Appendix C: Ethical Approval

NHS
Health Research Authority

Professor John E. Lees
BioImaging Unit
Space Research Centre
Dept. Physics and Astronomy
LE1 7RH

Email: hra.approval@nhs.net

03 May 2017

Dear Professor Lees

Letter of HRA Approval

Study title:	**Extended pilot evaluation of a prototype hand held hybrid gamma camera**
IRAS project ID:	**210776**
Protocol number:	**0591**
REC reference:	**17/YH/0041**
Sponsor	**University of Leicester**

I am pleased to confirm that **HRA Approval** has been given for the above referenced study, on the basis described in the application form, protocol, supporting documentation and any clarifications noted in this letter.

Participation of NHS Organisations in England

The sponsor should now provide a copy of this letter to all participating NHS organisations in England.

Appendix B provides important information for sponsors and participating NHS organisations in England for arranging and confirming capacity and capability. **Please read *Appendix B* carefully**, in particular the following sections:

- *Participating NHS organisations in England* – this clarifies the types of participating organisations in the study and whether or not all organisations will be undertaking the same activities
- *Confirmation of capacity and capability* - this confirms whether or not each type of participating NHS organisation in England is expected to give formal confirmation of capacity and capability. Where formal confirmation is not expected, the section also provides details on the time limit given to participating organisations to opt out of the study, or request additional time, before their participation is assumed.
- *Allocation of responsibilities and rights are agreed and documented (4.1 of HRA assessment criteria)* - this provides detail on the form of agreement to be used in the study to confirm capacity and capability, where applicable.

Further information on funding, HR processes, and compliance with HRA criteria and standards is also provided.

IRAS project ID	210776

It is critical that you involve both the research management function (e.g. R&D office) supporting each organisation and the local research team (where there is one) in setting up your study. Contact details and further information about working with the research management function for each organisation can be accessed from www.hra.nhs.uk/hra-approval.

Appendices

The HRA Approval letter contains the following appendices:

- A – List of documents reviewed during HRA assessment
- B – Summary of HRA assessment

After HRA Approval

The document *"After Ethical Review – guidance for sponsors and investigators"*, issued with your REC favourable opinion, gives detailed guidance on reporting expectations for studies, including:

- Registration of research
- Notifying amendments
- Notifying the end of the study

The HRA website also provides guidance on these topics, and is updated in the light of changes in reporting expectations or procedures.

In addition to the guidance in the above, please note the following:

- HRA Approval applies for the duration of your REC favourable opinion, unless otherwise notified in writing by the HRA.
- Substantial amendments should be submitted directly to the Research Ethics Committee, as detailed in the *After Ethical Review* document. Non-substantial amendments should be submitted for review by the HRA using the form provided on the HRA website, and emailed to hra.amendments@nhs.net.
- The HRA will categorise amendments (substantial and non-substantial) and issue confirmation of continued HRA Approval. Further details can be found on the HRA website.

Scope

HRA Approval provides an approval for research involving patients or staff in NHS organisations in England.

If your study involves NHS organisations in other countries in the UK, please contact the relevant national coordinating functions for support and advice. Further information can be found at http://www.hra.nhs.uk/resources/applying-for-reviews/nhs-hsc-rd-review/.

If there are participating non-NHS organisations, local agreement should be obtained in accordance with the procedures of the local participating non-NHS organisation.

User Feedback

The Health Research Authority is continually striving to provide a high quality service to all applicants and sponsors. You are invited to give your view of the service you have received and the application

IRAS project ID	210776

procedure. If you wish to make your views known please use the feedback form available on the HRA website: http://www.hra.nhs.uk/about-the-hra/governance/quality-assurance/.

HRA Training

We are pleased to welcome researchers and research management staff at our training days – see details at http://www.hra.nhs.uk/hra-training/

Your IRAS project ID is **210776**. Please quote this on all correspondence.

Yours sincerely

Maeve Ip Groot Bluemink
Assessor

Email: hra.approval@nhs.net

Copy to: *Dr.Diane Delahooke, University of Leicester – Sponsor Contact*
Ms Lauren Blackburn, Research & Innovation Nottingham University Hospitals NHS Trust – R&D Contact

IRAS project ID	210776

Appendix A - List of Documents

The final document set assessed and approved by HRA Approval is listed below.

Document	*Version*	*Date*
Contract/Study Agreement		14 January 2016
Covering letter on headed paper [Resp to HRA Initial Assessment Queries]		27 March 2017
Evidence of Sponsor insurance or indemnity (non NHS Sponsors only) [Insurance]		16 January 2017
Instructions for use of medical device [Technical guide]		12 January 2017
IRAS Application Form [IRAS_Form_26012017]		26 January 2017
Letter from funder		26 March 2015
MHRA Notice of No Objection Letter (Medical Devices) and relevant correspondence	1.0	01 December 2016
Other [Statement of Activities]	1	06 April 2017
Other [Schedule of Events]	1	06 April 2017
Other [Case report form]	final version 1.0	04 January 2017
Other [Bill CV]		
Other [SBugby CV]		
Other [PEB CV]		
Other [Feasibility assessment form]		
Participant consent form	1.2	27 March 2017
Participant information sheet (PIS)	1.2	27 March 2017
Referee's report or other scientific critique report		08 December 2016
Referee's report or other scientific critique report		13 December 2016
Research protocol or project proposal	final version 1.0	09 January 2017
Summary CV for Chief Investigator (CI)		15 August 2016
Summary CV for student [CV_Ng]		
Summary CV for student [CV Layal]		
Summary CV for student [CV Mohammed]		
Summary CV for student [CV Numan]		
Summary CV for supervisor (student research) [CV Alan]		
Summary, synopsis or diagram (flowchart) of protocol in non technical language	finalversion1.0	04 January 2017

IRAS project ID	210776

Appendix B - Summary of HRA Assessment

This appendix provides assurance to you, the sponsor and the NHS in England that the study, as reviewed for HRA Approval, is compliant with relevant standards. It also provides information and clarification, where appropriate, to participating NHS organisations in England to assist in assessing and arranging capacity and capability.

For information on how the sponsor should be working with participating NHS organisations in England, please refer to the, *participating NHS organisations*, *capacity and capability* and *Allocation of responsibilities and rights are agreed and documented (4.1 of HRA assessment criteria)* sections in this appendix.

The following person is the sponsor contact for the purpose of addressing participating organisation questions relating to the study:

Name: Dr Diane Delahook
Tel: 0116 252 5308
Email: uolsponsor@le.ac.uk

HRA assessment criteria

Section	HRA Assessment Criteria	Compliant with Standards	Comments
1.1	IRAS application completed correctly	Yes	No comments
2.1	Participant information/consent documents and consent process	Yes	No comments
3.1	Protocol assessment	Yes	No comments
4.1	Allocation of responsibilities and rights are agreed and documented	Yes	A Statement of Activities has been submitted and it is intended for this to be used as the contract between the NHS site and the Sponsor.
4.2	Insurance/indemnity arrangements assessed	Yes	Sponsor's insurance policy will cover the design and management of the study. NHS indemnity will apply for the conduct of the study while on NHS premises/under the duty of care of the

IRAS project ID	210776

Section	HRA Assessment Criteria	Compliant with Standards	Comments
			NHS. The applicant has confirmed that the Sponsor's insurance will cover the use of the study device. Where applicable, independent contractors (e.g. General Practitioners) should ensure that the professional indemnity provided by their medical defence organisation covers the activities expected of them for this research study
4.3	Financial arrangements assessed	Yes	Finance has been confirmed with the site and payments will be made to the participating NHS site by Nottingham University. The equipment will be made available to the site by the sponsor.
5.1	Compliance with the Data Protection Act and data security issues assessed	Yes	No comments
5.2	CTIMPS – Arrangements for compliance with the Clinical Trials Regulations assessed	Not Applicable	No comments
5.3	Compliance with any applicable laws or regulations	Yes	No comments
6.1	NHS Research Ethics Committee favourable opinion received for applicable studies	Yes	REC Favourable Opinion was issued by the Yorkshire and the Humber - Sheffield REC.
6.2	CTIMPS – Clinical Trials Authorisation (CTA) letter received	Not Applicable	No comments
6.3	Devices – MHRA notice of no objection received	Not Applicable	The Sponsor has stated that confirmation has been received from the MHRA that this study does not need to be registered with them as it is classed as an 'in house' device.

IRAS project ID	210776

Section	HRA Assessment Criteria	Compliant with Standards	Comments
6.4	Other regulatory approvals and authorisations received	Yes	An ARSAC PRA submission is not intended. Prof Alan Perkins (Key Investigator and Medical Physics Expert) and the Chief Investigator justified that this single-site study does not involve additional exposure to radiation and the administration of radioactive materials is part of standard NHS treatment care.

Participating NHS Organisations in England

This provides detail on the types of participating NHS organisations in the study and a statement as to whether the activities at all organisations are the same or different.
There is one type of participating NHS organisation in England; therefore, there is only one site type. The Chief Investigator or sponsor should share relevant study documents with participating NHS organisations in England in order to put arrangements in place to deliver the study. The documents should be sent to both the local study team, where applicable, and the office providing the research management function at the participating organisation. For NIHR CRN Portfolio studies, the Local LCRN contact should also be copied into this correspondence. For further guidance on working with participating NHS organisations please see the HRA website. If Chief Investigators, sponsors or Principal Investigators are asked to complete site level forms for participating NHS organisations in England which are not provided in IRAS or on the HRA website, the Chief Investigator, sponsor or Principal Investigator should notify the HRA immediately at hra.approval@nhs.net. The HRA will work with these organisations to achieve a consistent approach to information provision.

Confirmation of Capacity and Capability

This describes whether formal confirmation of capacity and capability is expected from participating NHS organisations in England.
Participating NHS organisations in England **will be expected to formally confirm their capacity and capability** to host this research. • The sponsor should ensure that participating NHS organisations are provided with a copy of this letter and all relevant study documentation, and work jointly with NHS organisations to arrange capacity and capability whilst the HRA assessment is ongoing. • Further detail on how capacity and capability will be confirmed by participating NHS organisations, following issue of the Letter of HRA Approval, is provided in the *Participating NHS Organisations* and *Allocation of responsibilities and rights are agreed and documented (4.1 of HRA assessment criteria)* sections of this appendix.

IRAS project ID	210776

The Assessing, Arranging, and Confirming document on the HRA website provides further information for the sponsor and NHS organisations on assessing, arranging and confirming capacity and capability.

Principal Investigator Suitability

This confirms whether the sponsor position on whether a PI, LC or neither should be in place is correct for each type of participating NHS organisation in England and the minimum expectations for education, training and experience that PIs should meet (where applicable).
A Principal Investigator (PI) is required for this type of study, and has been identified, as indicated in Part C of the IRAS form. The Sponsor's training expectations are detailed in the Statement of Activities and include GCP training to be undertaken by the local research team. GCP training is not a generic training expectation, in line with the HRA statement on training expectations.

HR Good Practice Resource Pack Expectations

This confirms the HR Good Practice Resource Pack expectations for the study and the pre-engagement checks that should and should not be undertaken
The activities at the participating NHS organisation will be undertaken by local staff therefore it is expected that adequate contractual relationship with the host organisation are already in place. Where contractual arrangements are not already in place, network staff (or similar) undertaking research activities would be expected to obtain Honorary Research Contracts on the basis of a Research Passport (if university employed) or a Letter of Access on the basis of an NHS to NHS confirmation of pre-engagement checks letter (if NHS employed). Standard DBS checks and occupational health clearance would be appropriate.

Other Information to Aid Study Set-up

This details any other information that may be helpful to sponsors and participating NHS organisations in England to aid study set-up.
The applicant has indicated that they intend to apply for inclusion on the NIHR CRN Portfolio.

References

1. *National Cancer Institute Surveillance, "E.a.E.R.S.P. SEER stat fact sheets: lymphoma," 2011* [(accessed on 07 July 2018)]; Available online: http://seer.cancer.gov/statfacts/html/lymph.html.
2. *Estimated Cancer Incidence, Mortality and Prevalence Worldwide in 2012.* [(accessed on 07 July 2018)]; Available online: http://globocan.iarc.fr/Pages/fact_sheets_population.aspx.
3. *Cancer Research UK. Statistics on preventable cancers CRUK, 2015. www.cancerresearchuk.org/health-professional/cancer-statistics/risk/preventable-cancers.*
4. Burke, G., et al., *Comparative thyroid uptake studies with 131I and 99mTcO4−.* The Journal of Clinical Endocrinology & Metabolism, 1972. **34**(4): p. 630-637.
5. Ramos, C.D., et al., *Thyroid uptake and scintigraphy using ^{99m}Tc pertechnetate: standardization in normal individuals.* Sao Paulo Medical Journal, 2002. **120**(2): p. 45-48.
6. Hou, H., et al., *Prognostic Value of-Pertechnetate Thyroid Scintigraphy in Radioiodine Therapy in a Cohort of Chinese Graves' Disease Patients: A Pilot Clinical Study.* BioMed research international, 2015. **2015**(Article ID 974689): p. 1-4.
7. Van den Wyngaert, T., et al., *The EANM practice guidelines for bone scintigraphy.* European journal of nuclear medicine and molecular imaging, 2016. **43**(9): p. 1723-1738.
8. Povoski, S.P., et al., *A comprehensive overview of radioguided surgery using gamma detection probe technology.* World J Surg Oncol, 2009. **7**(11): p. 1-63.
9. Tsuchimochi, M. and K. Hayama, *Intraoperative gamma cameras for radioguided surgery: technical characteristics, performance parameters, and clinical applications.* Phys Med, 2013. **29**(2): p. 126-38.
10. Perkins, A.C. and J.E. Lees, *Gamma cameras for interventional and intraoperative imaging*. 2016, CRC Press. London. p. 9: ISBN: 978-1-4987-2928-4.
11. Heller, S. and P. Zanzonico, *Nuclear probes and intraoperative gamma cameras.* Semin Nucl Med, 2011. **41**(3): p. 166-81.
12. Zaidi, H. and R. Prasad, *Advances in multimodality molecular imaging.* J. Med. Phy, 2009. **34**: p. 122-128.
13. Visioni, A. and J. Kim, *Positron emission tomography for benign and malignant disease.* Surg Clin North Am, 2011. **91**(1): p. 249-66.
14. Classe, J.M., et al., *Prospective comparison of 3 gamma-probes for sentinel lymph node detection in 200 breast cancer patients.* J Nucl Med, 2005. **46**(3): p. 395-9.
15. Bugby, S.L., et al., *Investigation of an SFOV hybrid gamma camera for thyroid imaging.* Phys Med, 2016. **32**(1): p. 290-6.
16. Lees, J.E., et al., *A small field of view camera for hybrid gamma and optical imaging.* Journal of Instrumentation, 2014. **9**(12): p. 1-10.
17. Lees, J.E., et al., *A Hybrid Camera for simultaneous imaging of gamma and optical photons.* Journal of Instrumentation, 2012. **7**(6): p. 1-11.

18. Lees, J.E., et al., *A hybrid camera for locating sources of gamma radiation in the environment.* Journal of Instrumentation, 2013. **8**(10): p. 1-11.
19. van der Have, F., et al., *U-SPECT-II: An Ultra-High-Resolution Device for Molecular Small-Animal Imaging.* J Nucl Med, 2009. **50**(4): p. 599-605.
20. Khalil, M.M., et al., *Molecular SPECT Imaging: An Overview.* Int J Mol Imaging, 2011. **2011**: p. 1-15, ID 796025.
21. Todd E. Peterson and L.R. Furenlid, *SPECT detectors: the Anger Camera and beyond.* Phys Med Biol, 2011. **56**(17): p. 145-182.
22. Islamian, J.P., et al., *Advances in pinhole and multi-pinhole collimators for single photon emission computed tomography imaging.* World journal of nuclear medicine, 2015. **14**(1): p. 3-9.
23. Gould, E.A., et al., *Observations on a "sentinel node" in cancer of the parotid.* Cancer, 1960. **13**(1): p. 77-78.
24. Olcott, P., et al., *Clinical evaluation of a novel intraoperative handheld gamma camera for sentinel lymph node biopsy.* Phys Med, 2014. **30**(3): p. 340-5.
25. Mathelin, C., et al., *Precise Localization of Sentinel Lymph Nodes and Estimation of Their Depth Using a Prototype Intraoperative Mini -Camera in Patients with Breast Cancer.* Journal of Nuclear Medicine, 2007. **48**(4): p. 623-629.
26. CAROLE MATHELIN, et al., *A New Intraoperative Gamma Camera for the Sentinel Lymph Node Procedure in Breast Cancer.* ANTICANCER RESEARCH 28: 2859-2864 (2008), 2008. **28**(5): p. 2859-2864.
27. Sergi Vidal-Sicart, et al., *Pre- and intra-operative imaging techniques for sentinel node localization in breast cancer* Imaging in Medicine 2013. **5**(3): p. 1-17.
28. Lynn T. Dengel, et al., *Intraoperative Imaging Guidance for Sentinel Node Biopsy in Melanoma Using a Mobile Gamma Camera.* Ann Surg, 2011. **253**(4): p. 774–778.
29. Metzler, S.D. and R. Accorsi, *Resolution- versus sensitivity-effective diameter in pinhole collimation: experimental verification.* Phys Med Biol, 2005. **50**(21): p. 5005-17.
30. Accorsi, R. and S.D. Metzler, *Analytic Determination of the Resolution-Equivalent Effective Diameter of a Pinhole Collimator.* IEEE TRANSACTIONS ON MEDICAL IMAGING,, 2004. **23**(6): p. 750-63.
31. Lees, J.E., et al., *A multimodality hybrid gamma-optical camera for intraoperative imaging.* Sensors, 2017. **17**(3): p. 554-66.
32. Alqahtani, M.S., et al., *Design and implementation of a prototype head and neck phantom for the performance evaluation of gamma imaging systems.* EJNMMI Phys, 2017. **4**(1): p. 19-36.
33. van der Ploeg, I.M., et al., *The hidden sentinel node and SPECT/CT in breast cancer patients.* Eur J Nucl Med Mol Imaging, 2009. **36**(1): p. 6-11.
34. Chakera, A.H., et al., *Factors of importance for scintigraphic non-visualisation of sentinel nodes in breast cancer.* Eur J Nucl Med Mol Imaging, 2005. **32**(3): p. 286-93.
35. Krausz, Y., et al., *Non-visualization of sentinel lymph node in patients with breast cancer.* Nuclear Medicine Communications, 2001. **22**(1): p. 25-32.
36. Kroon, B.K., et al., *Non-visualization of sentinel lymph nodes in penile carcinoma.* Eur J Nucl Med Mol Imaging, 2005. **32**(9): p. 1096-9.

37. Seim, N.B., C.L. Wright, and A. Agrawal, *Contemporary use of sentinel lymph node biopsy in the head and neck.* World journal of otorhinolaryngology-head and neck surgery, 2016. **2**(2): p. 117-125.

38. Qiu, S.-Q., et al., *Evolution in sentinel lymph node biopsy in breast cancer.* Critical reviews in oncology/hematology, 2018. **123**(1): p. 83-94.

39. Alqahtani, M.S., et al., *Lymphoscintigraphic imaging study for quantitative evaluation of a small field of view (SFOV) gamma camera.* Journal of Instrumentation, 2015. **10**(07): p. 1-17.

40. Lees, J.E., et al., *Design and use of mini-phantoms for high resolution planar gamma cameras.* Appl Radiat Isot, 2010. **68**(12): p. 2448-51.

41. Ng, A.H., et al, *Design and use of a sentinel node phantom for pre-surgical assessment of small field of view gamma cameras.* Nucl. Med. Commun, 2015. **36**(11): p. 1134-42.

42. Mariani, G., et al., *Radioguided sentinel lymph node biopsy in breast cancer surgery.* The journal of nuclear medicine, 2001. **42**(8): p. 1198-215.

43. Nieweg, O.E., et al., *Lymphatic mapping with tracer administration into the primary breast cancer.* EJSO, 2003. **29**(1): p. 95 - 97.

44. Eddy C. Hsueh and Aramndo E. Giuliano., *Sentinel Lymph Node Technique for Staging of Breast Cancer.* The Oncologist, 1998. **3**(3): p. 165-170.

45. d'Eredita, G., et al., *Effect of the use of vital dye, lymphoscintigraphy, or a combination for axillary lymphatic mapping and sentinel node biopsy in breast cancer.* World J Surg, 2002. **26**(5): p. 588-90.

46. Kelly M. McMasters, et al., *Sentinel Lymph Node Biopsy for Breast Cancer: A Suitable Alternative to Routine Axillary Dissection in Multi- Institutional Practice When Optimal Technique Is Used.* Journal of Clinical Oncology, 2000. **18**(13): p. 2560-2566.

47. Baldazzi, V., et al., *Modeling lymphocyte homing and encounters in lymph nodes.* BMC bioinformatics, 2009. **10**(1): p. 387-398.

48. Frei, E., *Albumin binding ligands and albumin conjugate uptake by cancer cells.* Diabetology & metabolic syndrome, 2011. **3**(1): p. 11-14.

49. van Dijk, J.D., et al., *Patient-specific tracer activity in MPI SPECT: A hands-on approach.* Journal of nuclear cardiology, 2016. **23**(1): p. 145-148.

50. Lee, Y.-S., *Radiopharmaceuticals for molecular imaging.* Open Nucl Med J, 2010. **2**: p. 178-85.

51. Ng, A.H., *Hybrid Gamma Camera Imaging: Translation from Bench to Bedside*, in *Radiological Sciences, Division of Clinical Neuroscience, School of Medicine*. 2018, University of Nottingham: Nottingham, UK.

52. Lu, F.-M. and Z. Yuan, *PET/SPECT molecular imaging in clinical neuroscience: recent advances in the investigation of CNS diseases.* Quantitative imaging in medicine and surgery, 2015. **5**(3): p. 433.

53. Thompson, M., et al., *Intraoperative radioisotope injection for sentinel lymph node biopsy.* Ann Surg Oncol, 2008. **15**(11): p. 3216-21.

54. Alqahtani, M.S.M., *Assessment of a novel small field of view medical hybrid gamma camera* in *Space Research Centre Department of Physics and Astronomy* 2018, University of Leicester: Leicester, UK.

55. Seo, Y., C. Mari, and B.H. Hasegawa, *Technological development and advances in single-photon emission computed tomography/computed tomography.* Seminars in nuclear medicine, 2008. **38**(3): p. 177-198.

56. Moshe Bocher, et al., *A fast cardiac gamma camera with dynamic SPECT capabilities: design, system validation and future potential.* Eur J Nucl Med Mol Imaging, 2010. **37**(10): p. 1887–1902.

57. Vanzi, E., et al., *Kinetic parameter estimation from renal measurements with a three-headed SPECT system: a simulation study.* IEEE Trans Med Imaging, 2004. **23**(3): p. 363-73.

58. Gullberg, G.T., et al., *Dynamic single photon emission computed tomography--basic principles and cardiac applications.* Phys Med Biol, 2010. **55**(20): p. 111-191.

59. *Siemens Medical Solutions USA. SPECT Imaging Systems. [Accessed on 9 September 2018]. Available from: https://www.healthcare.siemens.co.uk/molecularimaging/ spect-Imaging system.*

60. Phelps, M.E., *PET: The Merging of Biology and Imaging into Molecular Imaging.* J NuclMed, 2000. **41**(4): p. 661-668.

61. Cherry, S.R., *The 2006 Henry N. Wagner Lecture: Of Mice and Men (and Positrons)—Advances in PET Imaging Technology.* J Nucl Med November 2006. **42**(11): p. 1735-1745

62. *Siemens Medical Solutions USA. Biograph True Point 16-slice PET-CT. [Accessed on 9 September 2018]. Available from: https://www.medgadget.com/2009/03/new_16_slice_petct_from_siemens.html.*

63. Berti, V., A. Pupi, and L. Mosconi, *PET/CT in diagnosis of dementia.* Annals of the New York Academy of Sciences, 2011. **1228**(1): p. 81-92.

64. Steinert, H.C., *PET and PET-CT of lung cancer.* Methods Mol Biol, 2011. **727**: p. 33-51.

65. Chye Hwang Yan, et al., *Reconstruction Algorithm for Polychromatic CT Imaging: Application to Beam Hardening Correction.* IEEE TRANSACTIONS ON MEDICAL IMAGING, 2000. **19**(1): p. 1-11.

66. Wang, M., et al., *An adaptive reconstruction algorithm for spectral CT regularized by a reference image.* Phys Med Biol, 2016. **61**(24): p. 8699-8719.

67. *Siemens Medical Solutions USA. CT-SOMATOM. [Accessed on 9 September 2018]. Available from: https://www.healthcare.siemens.co.uk/molecularimaging/ CT-Somatom*

68. Uren, R.F., *SPECT/CT Lymphoscintigraphy to locate the sentinel lymph node in patients with melanoma.* Annals of surgical oncology, 2009. **16**(6): p. 1459-1460.

69. Cherry, S.R., *Multimodality imaging: beyond PET/CT and SPECT/CT.* Semin Nucl Med, 2009. **39**(5): p. 348-53.

70. Beyer, T., et al., *The future of hybrid imaging-part 3: PET/MR, small-animal imaging and beyond.* Insights Imaging, 2011. **2**(3): p. 235-246.

71. *Siemens Medical Solutions USA. SPECT/CT Symbia T Series [Accessed on 9 September 2018]. Available from: https://www.healthcare.siemens.co.uk/molecularimaging/ SPECT-CT.*

72. *Siemens Medical Solutions USA. PET/CT Biograph Vision [Accessed on 9 September 2018]. Available from: https://www.healthcare.siemens.co.uk/molecularimaging/ PET-CT.*

73. Tang, H.R., et al., *Neuroblastoma imaging using a combined CT scanner-scintillation camer and (131) I-MIBG.* The Journal of Nuclear Medicine, 2001. **42**(2): p. 237-47

74. Eo, J.S., J.C. Paeng, and D.S. Lee, *Nuclear imaging for functional evaluation and theragnosis in liver malignancy and transplantation.* World Journal of Gastroenterology: WJG, 2014. **20**(18): p. 5375–5388.

75. von Schulthess, G.K., *Integrated modality imaging with PET-CT and SPECT-CT: CT issues.* European Radiology Supplements, 2005. **15**(4): p. d121-d126.

76. Olcott, P.D., et al., *Performance Characterization of a Miniature, High Sensitivity Gamma Ray Camera.* IEEE Trans. Nucl. Sci., 2007. **54**(5): p. 1492 - 1497.

77. Tafra L, et al., *Credentialing issues with sentinel lymph node staging for breast cancer.* American journal of surgery, 2000. **180**(4): p. 268-73.

78. *Surgiceye. Declipse ® SPECT Open Surgery [Accessed on 9 September 2018]. Available from: https://www.surgiceye.com/?portfolio=declipsespect .*

79. Kaviani, S., et al., *Design and development of a dedicated portable gamma camera system for intra-operative imaging.* Physica Medica: European Journal of Medical Physics, 2016. **32**(7): p. 889-897.

80. Hung, N.M., et al., *Development of correction schemes for a small field of view gamma camera.* Biomedical Engineering Letters, 2013. **2**(4): p. 215-222.

81. Krings, T., et al., *A numerical method to improve the reconstruction of the activity content in homogeneous radioactive waste drums.* Nuclear Instruments and Methods in Physics Research Section A: Accelerators, Spectrometers, Detectors and Associated Equipment, 2013. **701**: p. 262-267.

82. *ANTECH Corporation, 9050 Marshall Court, Westminster, Colorado, 80031, U.S.A.*

83. Kim, H.-I., et al., *Gamma camera with a two-layer diverging-slat collimator for radioisotope monitoring.* Nuclear Instruments and Methods in Physics Research Section A: Accelerators, Spectrometers, Detectors and Associated Equipment, 2013. **698**(11): p. 90-93.

84. Olivier Gal, B.D., Franck Jean, Frédéric Lainé , and Christophe Lévêque, *Operation of the CARTOGAM Portable Gamma Camera in a Photon-Counting Mode.* IEEE T. Nucl Sci, , 2001. **48**(4): p. 1198 - 1204

85. Tsuchimochi, M., et al., *A prototype small CdTe gamma camera for radioguided surgery and other imaging applications.* Eur J Nucl Med Mol Imaging, 2003. **30**(12): p. 1605-14.

86. Lees, J.E., et al., *A high resolution Small Field Of View (SFOV) gamma camera: a columnar scintillator coated CCD imager for medical applications.* Journal of Instrumentation, 2011. **6**(12): p. 1-12.

87. Oda T, Hayama K, and T. M., *Evaluation of small semiconductor gamma camera--simulation of sentinel lymph node biopsy by using a trial product of clinical type gamma camera.* The Japanese journal of nuclear medicine, 2009. **46**(1): p. 1-12.

88. Pato, L.R., et al., *Parallel-hole collimator concept for stationary SPECT imaging.* Physics in Medicine & Biology, 2015. **60**(22): p. 8791.

89. Moore, S.C., K. Kouris, and I. Cullum, *Collimator design for single photon emission tomography.* Eur. J. Nucl. Med, 1992. **19**(2): p. 138-150.

90. Erdi, Y.E., *Limits of Tumor Detectability in Nuclear Medicine and PET.* Mol Imaging Radionucl Ther, 2012. **21**(1): p. 23-28.

91. Cecchin, D., et al., *Analytical and experimental FWHM of a gamma camera: theoretical and practical issues.* PeerJ, 2015. **3**(3): p. 722-35.

92. Sorenson, J.A. and M.E. Phelps, *Physics in Nuclear Medicine*. 2nd ed. 1987, PA, USA,: Elsevier.

93. Vaquero, J.J. and P. Kinahan, *Positron emission tomography: current challenges and opportunities for technological advances in clinical and preclinical imaging systems.* Annual review of biomedical engineering, 2015. **17**: p. 385-414.

94. Bohdan Bybel, et al., *SPECT/CT Imaging: Clinical Utility of an Emerging Technology.* RSNA RadioGraphics, 2008. **28**(4): p. 1079-1113.

95. Al-Ibraheem, A., et al., *Clinical Applications of FDG PET and PET/CT in Head and Neck Cancer.* J Oncol, 2009 (article ID 208725): p. 1-13.

96. Beyer, T., et al., *Dual-modality PET/CT imaging: the effect of respiratory motion on combined image quality in clinical oncology.* Eur J Nucl Med Mol Imaging, 2003. **30**: p. 588–96.

97. van Dalen, J.A., et al., *Multi-modality nuclear medicine imaging: artefacts, pitfalls and recommendations.* Cancer Imaging, 2007. **7**: p. 77-83.

98. Welchman, A.E., *The Human Brain in Depth: How We See in 3D.* Annu Rev Vis Sci, 2016. **2**: p. 345-376.

99. Nam, K.W., et al., *Application of stereo-imaging technology to medical field.* Healthc Inform Res, 2012. **18**(3): p. 158-63.

100. Howard IP and Rogers BJ, *Seeing in depth*. Vol. 1: Basic mechanisms. 2002, I Porteous, Toronto (printed at the University of Toronto Press): American Psychological Association. 650, ISBN 0 9730873 0 7.

101. Aung, S., *Computing the Three Dimensional Depth Measurement by the Multi Stereo Images.* International Journal of e-Education, e-Business, e-Management and e-Learning, 2013.

102. Brady, D.J., et al., *Parallel cameras.* Optica, 2018. **5**(2): p. 127-38.

103. Kavehvash, Z., K. Mehrany, and S. Bagheri, *Optimization of the lens-array structure for performance improvement of integral imaging* Optics Letters, 2011. **36**(20): p. 3993-3995.

104. CHOI, S. and S. MIN, *Depth estimation method using depth-of-field imaging with a retroreflector.* OPTICS EXPRESS 2018. **26**(5): p. 5655-5664.

105. Bindseil, G.A., et al., *First image from a combined positron emission tomography and field-cycled MRI system.* Magn Reson Med, 2011. **66**(1): p. 301-5.

106. Chun, S.Y., et al., *MRI-based nonrigid motion correction in simultaneous PET/MRI.* J Nucl Med, 2012. **53**(8): p. 1284-91.

107. Judenhofer, M.S., et al., *Simultaneous PET-MRI: a new approach for functional and morphological imaging.* Nat Med, 2008. **14**(4): p. 459-65.

108. Hasegawa, B.H., et al., *Dual-modality imaging of cancer with SPECT/CT.* Technol Cancer Res Treat, 2002. **1**(6): p. 449-58.

109. Townsend, D.W., *Multimodality imaging of structure and function.* Phys Med Biol, 2008. **53**(4): p. 1-39.

110. Walrand, S., M. Hesse, and F. Jamar, *Update on novel trends in PET/CT technology and its clinical applications.* The British journal of radiology, 2017. **91**(1081): p. 1-10.

111. Cal-Gonzalez, J., et al., *Hybrid imaging: Instrumentation and Data Processing.* Frontiers in Physics, 2018. **6**(3): p. 1-30.

112. Patt BE, e.a., *Development of an intraoperative gamma camera based on a 256-pixel mercuric iodine detector array.* IEEE Trans Nucl Sci 1997. **44**(3): p. 1242-1248.

113. Menard L, C.Y., Solal M, Laniece P, Mastrippolito R, Pinot L, et al. , *A compact high resolution gamma camera for intra-operative surgical use.* IEEE Trans Nucl Sci, 1998. **45**(3): p. 1293 - 1297

114. MacDonald LR, P.B., Iwanczyk JS, Yamaguchi Y, McElroy DP, Hoffman EJ, et al., *High-resolution hand-held gamma camera (proceedings paper).* editors. Penetrating radiation systems and applications II. San Diego, CA. Bellingham, WA: SPIE, 2000. **4142**(4): p. 242-253.

115. Stoffels, I., et al., *Evaluation of a radioactive and fluorescent hybrid tracer for sentinel lymph node biopsy in head and neck malignancies: prospective randomized clinical trial to compare ICG-(99m)Tc-nanocolloid hybrid tracer versus (99m)Tc-nanocolloid.* Eur J Nucl Med Mol Imaging, 2015. **42**(11): p. 1631-8.

116. Hurwitz, S.R., et al., *Clinical applications of a "portable" scintillation camera.* J Nucl Med, 1973. **14**(8): p. 585-7.

117. *Digirad Corporation. ergo™. [Accessed on 1 September 2018]. Available from: http://www.digirad.com/cameras/ergo/.*

118. *Mediso Medical Imaging System. Nucline™ TH. [Accessed on 1 September 2018]. Available from: http://www.mediso.com/.*

119. Vidal-Sicart, S., et al., *The use of a portable gamma camera for preoperative lymphatic mapping: a comparison with a conventional gamma camera.* European journal of nuclear medicine and molecular imaging, 2011. **38**(4): p. 636-641.

120. Ozkan, E. and A. Eroglu, *The utility of intraoperative handheld gamma camera for detection of sentinel lymph nodes in melanoma.* Nuclear medicine and molecular imaging, 2015. **49**(4): p. 318-320.

121. Ghosh, D.B., et al., *Sentinella: Portable gamma camera versus conventional scintigram for intraoperative sentinel lymph node detection in breast cancer*. 2012, American Society of Clinical Oncology.

122. Bertsch, D., Burak, WE., Young, DC., Arnold, MW., Martin, EW. , *Radioimmunoguided Surgery system improves survival for patients with recurrent colorectal cancer Surgery.* Surgery, 1995. **118**(4): p. 634-638.

123. *CCD97-00-Back illuminated 2-phase IMO series peltier pack electron multiplying CCD sensor, E2V Technologies Limited, Chelmsford, Essex, CM1 2QU, England, A1A-CCD97.*

124. Bugby, S.L., et al., *Characterisation of a high resolution small field of view portable gamma camera.* Phys. Med, 2014 **30**(3): p. 331-9.

125. Lawson, R.S., in *The Gamma Camera: A comprehensive guide*. 2013, Institute of Physics and Engineering in Medicine: Manchester,Englang. p. 80-82. ISNB: 9781903613535.

126. *Ultimate Metals, L.R., Chingford, London, E4 7HZ, UK.*

127. Cheol-Ha Baek, S.-J.L., Yong Choi,and and Y.H. Chung, *Optimization of Large-Angle Pinhole Collimator for Environmental Monitoring System.* IEEE T. Nucl Sci,, 2010. **57**(3): p. 1404-1408.

128. Bugby, S.L., J.E. Lees, and A.C. Perkins, *Modelling image profiles produced with a small field of view gamma camera with a single pinhole collimator.* Journal of Instrumentation, 2012. **7**(11): p. 1-16.

129. Bugby, S.L., *Development of a hybrid portable medical gamma camera*, in *Physics Department*. 2015, University of Leicester: Leicester, UK.

130. Szabo, Z. and J. Buchanan, *Principles of Nuclear Medicine*. Philadelphia,W B Saunders. 1995. 292-297.

131. Cherry, S.R., J.A. Sorenson, and M.E. Phelps, *Physics in Nuclear Medicine*. 3rd ed. Elsevier, PA, USA, 3rd edition. 2003. 325-359.

132. Paix, D., *pinhole imaging of gamma rays.* Phys Med Biol, 1967. **12**(4): p. 489-500.

133. *XCOM: photon cross sections database. NIST Standard reference database, Gaithersburg. 1998.* http://www.physics.nist.gov/PhysRefData/Xcom/html/xcom1.html, Accessed 20 September 2017.

134. Metzler, S.D., K.L. Greer, and R.J. Jaszczak, *Helical Pinhole SPECT for Small-Animal Imaging: A Method for Addressing Sampling Completeness.* IEEE Trans. Nucl. Sci, 2003. **50**(5): p. 1575-1583.

135. Bugby, S.L., L.K. Jambi, and J.E. Lees, *A comparison of CsI:Tl and GOS in a scintillator-CCD detector for nuclear medicine imaging.* Journal of Instrumentation, 2016. **11**(9): p. 1-14.

136. Ferreira, T., Rasband W,, *ImageJ User Guide*. 2012.

137. *IDL (Interactive Data Language)* 8.2.2. Exelis Visual Information Solutions, B., CO,2013.

138. Mejia, J., et al., *A clinical gamma camera-based pinhole collimated system for high resolution small animal SPECT imaging.* Brazilian Journal of Medical and Biological Research, 2010. **43**(12): p. 1160-1166.

139. Li, Z., et al., *Depth of tumor invasion and tumor-occupied portions of stomach are predictive factors of intra-abdominal metastasis.* Chin J Cancer Res, 2017. **29**(2): p. 109-117.

140. Wendler, T., et al., *First demonstration of 3-D lymphatic mapping in breast cancer using freehand SPECT.* European journal of nuclear medicine and molecular imaging, 2010. **37**(8): p. 1452-1461.

141. Mihaljevic, A., et al., *Transferring innovative freehand SPECT to the operating room: first experiences with sentinel lymph node biopsy in malignant melanoma.* European Journal of Surgical Oncology (EJSO), 2014. **40**(1): p. 42-48.

142. Bafford, A., et al., *Diminishing morbidity with the increased use of sentinel node biopsy in breast carcinoma.* The American Journal of Surgery, 2010. **200**(3): p. 374-377.

143. Heuveling, D.A., et al., *Evaluation of the use of freehand SPECT for sentinel node biopsy in early stage oral carcinoma.* Oral oncology, 2015. **51**(3): p. 287-290.

144. Bluemel, C., et al., *Freehand SPECT for image-guided sentinel lymph node biopsy in breast cancer.* European journal of nuclear medicine and molecular imaging, 2013. **40**(11): p. 1656-1661.

145. Wendler, T., et al., *First demonstration of 3-D lymphatic mapping in breast cancer using freehand SPECT.* Eur J Nucl Med Mol Imaging, 2010. **37**(8): p. 1452-61.

146. Mathelin, C., et al., *Optimization of sentinel lymph node biopsy in breast cancer using an operative gamma camera.* World J Surg Oncol, 2007. **17**(5): p. 132-137.

147. Grischke, E.-M., et al., *ICG fluorescence technique for the detection of sentinel lymph nodes in breast cancer: results of a prospective open-label clinical trial.* Geburtshilfe und Frauenheilkunde, 2015. **75**(9): p. 935-940.

148. Kang, J., et al., *Real-time sentinel lymph node biopsy guidance using combined ultrasound, photoacoustic, fluorescence imaging: in vivo proof-of-principle and validation with nodal obstruction.* Scientific Reports, 2017. **7**: p. 1-9.

149. Brouwer, O.R., et al., *Comparing the hybrid fluorescent–radioactive tracer indocyanine green–99mTc-nanocolloid with 99mTc-nanocolloid for sentinel node identification: a validation study using lymphoscintigraphy and SPECT/CT.* Journal of Nuclear Medicine, 2012. **53**(7): p. 1034-40.

150. Brouwer, O.R., et al., *Feasibility of sentinel node biopsy in head and neck melanoma using a hybrid radioactive and fluorescent tracer.* Annals of surgical oncology, 2012. **19**(6): p. 1988-1994.

151. Lewis-Jones, H., S. Colley, and D. Gibson, *Imaging in head and neck cancer: United Kingdom national multidisciplinary guidelines.* The Journal of Laryngology & Otology, 2016. **130**(2): p. 28-31.

152. Daiko, H., et al., *The role of pulmonary resection in tumors metastatic from head and neck carcinomas.* Japanese journal of clinical oncology, 2010. **40**(7): p. 639-644.

153. Bluemel, C., et al., *EANM practice guidelines for lymphoscintigraphy and sentinel lymph node biopsy in melanoma.* European journal of nuclear medicine and molecular imaging, 2015. **42**(11): p. 1750-1766.

154. Amersi, F. and N.M. Hansen, *The benefits and limitations of sentinel lymph node biopsy.* Current treatment options in oncology, 2006. **7**(2): p. 141-151.

155. Cox, C.E., et al., *Sentinel lymph node biopsy for breast cancer: combined dye-isotope technique.* Breast Cancer, 2000. **7**(4): p. 389-97.

156. Rice, T.W., et al., *Role of clinically determined depth of tumor invasion in the treatment of esophageal carcinoma.* The Journal of thoracic and cardiovascular surgery, 2003. **125**(5): p. 1091-1102.

157. Munz, Y., et al., *The benfits of stereoscopic vision in robotic-assisted performance on bench models.* Surgical Endoscopy And Other Interventional Techniques, 2004. **18**(4): p. 611-616.

158. Singh, V.P. and N.M. Badiger, *Effective atomic numbers of some tissue substitutes by different methods: A comparative study.* J Med Phys, 2014. **39**(1): p. 24-31.

159. Ferreira, C.C., et al., *Total mass attenuation coefficient evaluation of ten materials commonly used to simulate human tissue.* Journal of Physics: Conference Series 249 012029, 2010: p. 1-5.

160. *The-Phantom-Laboratory. RSVP Phantom™ Head II with Bite Feature Manual - Radiosurgery Verification Phantom. Salem, NY 12865-0511: The Phantom Laboratory.* 2015.

161. Berger, M.J., et al., *XCOM: photon cross sections database.* NIST Standard reference database, 1998. **8**(1): p. 3587-3597.

162. Roy, M., et al., *Incidence and localization of ectopic parathyroid adenomas in previously unexplored patients.* World J Surg, 2013. **37**(1): p. 102-6.

163. Tardelli, E., et al., *Sentinel Lymph Node Biopsy in Cutaneous Melanoma: Standard and New Technical Procedures and Clinical Advances. A Systematic Review of the Literature.* Clinical Nuclear Medicine, 2016. **41**(12): p. 498-507.

164. Morton, D.L., et al., *Technical details of intraoperative lymphatic mapping for early stage melanoma.* Arch Surg, 1992. **127**(4): p. 392-9.

165. Uren, R.F., R. Howman-Giles, and J.F. Thompson, *Patterns of lymphatic drainage from the skin in patients with melanoma.* The Journal of Nuclear Medicine, 2003. **44**(4): p. 570.

166. Medina-Franco, H., et al., *Sentinel node biopsy for cutaneous melanoma in the head and neck.* Ann Surg Oncol, 2001. **8**(9): p. 716-9.

167. Sulzbacher, L., et al., *Clinical Usefulness of a Novel Freehand 3D Imaging Device for Radio-Guided Intraoperative Sentinel Lymph Node Detection in Malignant Melanoma.* Clin Nucl Med, 2015. **40**(9): p. 436-440.

168. Iraj Mohammad, et al., *Detection and evalution of patient motion in myocardial SPECT imaging using modeling of projection by polynomial curves and 2D curve fitting.* U.P.B. Sci. Bull, 2014. **76**(3): p. 63-76.

169. Beach, R.D., et al., *Feasibility of Stereo-Infrared Tracking to Monitor Patient Motion During Cardiac SPECT Imaging.* IEEE Trans Nucl Sci, 2004. **51**(5 II): p. 2693-2698.

170. Beyer, T., et al., *Respiration artifacts in whole-body (18)F-FDG PET/CT studies with combined PET/CT tomographs employing spiral CT technology with 1 to 16 detector rows.* Eur J Nucl Med Mol Imaging, 2005. **32**(12): p. 1429-39.

171. Chun, S.Y., *The use of anatomical information for molecular image reconstruction algorithms: attenuation/scatter correction, motion compensation, and noise reduction.* Nuclear medicine and molecular imaging, 2016. **50**(1): p. 13-23.

172. Razifar, P., et al., *Noise correlation in PET, CT, SPECT and PET/CT data evaluated using autocorrelation function: a phantom study on data, reconstructed using FBP and OSEM.* BMC medical imaging, 2005. **5**(5): p. 1-23.

173. Dawood, M., et al., *Respiratory gating in positron emission tomography: a quantitative comparison of different gating schemes.* Medical Physics, 2007. **34**(7): p. 3067-3076.

174. Nehmeh, S., et al., *Effect of respiratory gating on reducing lung motion artifacts in PET imaging of lung cancer.* Medical physics, 2002. **29**(3): p. 366-371.

175. Burrell, S. and A. MacDonald, *Artifacts and Pitfalls in Myocardial Perfusion Imaging.* J. Nucl. Med. Technol, 2006. **34** (4): p. 193-211.

176. Guy Shechter, C.O., Jon R. Resar, and Elliot R. McVeigh, *Respiratory Motion of the Heart From Free Breathing Coronary Angiograms.* IEEE TRANSACTIONS ON MEDICAL IMAGING,, 2004. **23**(8): p. 1046–1056. .

177. Lindh, W.Q., et al., *Comprehensive Medical Assisting: Administrative and Clinical Competencies [5th Edition]* Stamford: DelmarCengage Learning. 2013. P. 1246 . ISBN: 113360286X, 9781133602866

178. Zhu YY, B.E., O'Connell WJ, Dae MW, *Accuracy and Precision of Radioactivity Quantification in Nuclear Medicine Images.* Semin Nucl Med 2012. **42**(3): p. 208–218.

179. Stevens, C.W., et al., *Respiratory-driven lung tumor motion is independent of tumor size, tumor location, and pulmonary function.* Int J Radiat Oncol Biol Phys, 2001. **51**(1): p. 62-8.

180. Korreman, S., *Image-guided radiotherapy and motion management in lung cancer.* The British journal of radiology, 2015. **88**(1051): p. 1-12.

181. Siman, W., et al., *Effects of image noise, respiratory motion, and motion compensation on 3D activity quantification in count-limited PET images.* Phys Med Biol, 2017. **62**(2): p. 448-464.

182. Erlandsson, K., et al. *Reduction of CT artifacts due to respiratory motion in a slowly rotating SPECT/CT*. in *Nuclear Science Symposium Conference Record, 2008. NSS'08. IEEE*. 2008. Dresden, Germany, Germany IEEE. p. 3775-3778. .

183. S. A. Nehmeh, et al., *Quantitation of respiratory motion during 4D-PET/CT acquisition.* Med. Phys., 2004. **31**(6): p. 1333-1338.

184. Lu. W, et al., *A comparison between amplitude sorting and phase-angle sorting using external respiratory measurement for 4D CT* Med. Phys., 2006. **33**(8): p. 2964–74.

185. Boon-Keng Teo, et al., *The effect of breathing irregularities on quantitative accuracy of respiratory gated PET/CT.* Med. Phys., 2012. **39**(12): p. 7390-7397.

186. Gnanasegaran, G., et al., *Patterns, variants, artifacts, and pitfalls in conventional radionuclide bone imaging and SPECT/CT.* Seminars in nuclear medicine, 2009. **39**(6): p. 380-395.

187. V. Bettinardi, E. Rapisarda, and M.C. Gilardi, *Number of partitions (gates) needed to obtain motion-free images in a respiratory gated 4D-PET/CT study as a function of the lesion size and motion displacement.* Med.Phys., 2009. **36**(12): p. 5547-5558.

188. Guang Li, et al., *Assessing and accounting for the impact of respiratory motion on FDG uptake and viable volume for liver lesions in free-breathing PET using respiration-suspended PET images as reference.* Med. Phys., 2014. **41**(9): p. 1-10.

189. Zacho, H.D., et al., *Three-minute SPECT/CT is sufficient for the assessment of bone metastasis as add-on to planar bone scintigraphy: prospective head-to-head comparison to 11-min SPECT/CT.* EJNMMI research, 2017. **7**(1): p. 1-7.